# Ligand-Capped Gold Nanoparticles as a Platform for Controlled Drug Delivery

## Ruixue Chen

Department of Chemistry

McGill University

Montréal, Québec, Canada

February 2025

A thesis submitted to McGill University

in partial fulfillment of the requirement for the degree of Doctor of Philosophy

To my father Jian Chen, my moth	er Yalan Xue, for th	eir unwavering love and
	support	

### **Abstract**

Traditional pharmaceutical delivery systems, such as tablets and capsules, often encounter challenges such as poor solubility, instability, nonspecific distribution, and physiological barriers. Spherically symmetric gold nanoparticles (AuNPs) have emerged as promising stable nanoscale carriers, offering the potential for multifunctional capabilities within a single entity. In short, ligand capped AuNP have long been recognized as possible platforms for the long sought after triple capability in a "theranostic", where one carrier simultaneously has targeting, diagnostics, and drug delivery capability. This Thesis has thus focused on developing one of these three capabilities (drug delivery) for AuNP as examples of the other two capabilities have been well established.

The initial phase of the research involved setting out the design and syntheses of thermally responsive release linkers utilizing the retro-Diels-Alder (rDA) reaction. Optimization of these linkers enabled investigation of two complementary methods to load the AuNP capping layers with desired molecules: ligand exchange and interfacial esterification reactions of pre-existing ligands. These methods indeed provide versatility in the attachment of drug analogues to 2 nm diameter AuNPs that are then released through thermally activated retro Diels-Alder reactions.

Additionally, the photothermal heating that results from NIR irradiation of nanorods (NRs) potentially can trigger capping layer DA adduct-associated cargo release in these relatives to AuNP in the absence of externally applied heat stimuli. The synthesis of these NRs, especially with localized surface plasmon resonance (LSPR) extinctions greater than 850 nm, often suffers from poor reproducibility using traditional seed-mediated methods. Recognizing the need for a reproducible synthetic process that also accesses NR whose LSPR maxima are in the 1200 nm

range and beyond, synthetic optimization efforts were focused on enhancing the solubility of the limiting intermediate (CTA-Ag-Br) in the synthesis of AuNRs and AgNRs.

### Résumé

Les systèmes traditionnels de délivrance de médicaments, tels que les comprimés et les capsules, rencontrent souvent des défis tels que la faible solubilité, l'instabilité, la distribution non spécifique et les barrières physiologiques. Les nanoparticules d'or (AuNPs) symétriques sphériques ont émergé comme des vecteurs nanométriques stables prometteurs, offrant le potentiel pour des capacités multifonctionnelles au sein d'une seule entité. En bref, les AuNP avec ligands cappés sont reconnus depuis longtemps comme des plateformes possibles pour la triple capacité tant recherchée dans un "théranostic", où un seul vecteur possède simultanément des capacités de ciblage, de diagnostic et de livraison de médicament. Cette thèse s'est donc concentrée sur le développement de l'une de ces trois capacités (la livraison de médicament) pour les AuNP, les exemples des deux autres capacités étant bien établis.

La phase initiale de la recherche a consisté à définir la conception et la synthèse de liens de libération thermiquement réactifs utilisant la réaction rétro-Diels-Alder (rDA). L'optimisation de ces liens a permis l'étude de deux méthodes complémentaires pour charger les couches de cappage des AuNP avec les molécules souhaitées : l'échange de ligands et les réactions d'esterification interfaciale des ligands préexistants. Ces méthodes offrent en effet une polyvalence dans l'attachement d'analogues de médicaments à des AuNP de 2 nm de diamètre qui sont ensuite libérables par des réactions rétro Diels-Alder activées thermiquement.

De plus, le chauffage photothermique résultant de l'irradiation NIR de nanotiges (NRs) peut potentiellement déclencher la libération de la charge associée aux adduits de cappage DA dans ces apparentés des AuNP en l'absence de stimuli de chaleur externe. La synthèse de ces NRs, en particulier avec des extinctions de résonance plasmonique de surface localisée (LSPR)

supérieures à 850 nm, souffre souvent d'une mauvaise reproductibilité avec les méthodes traditionnelles à médiation de semences. Reconnaissant le besoin d'un processus synthétique reproductible qui accède également à des NR dont les maxima LSPR sont dans la gamme de 1200 nm et au-delà, les efforts d'optimisation synthétique ont été axés sur l'amélioration de la solubilité de l'intermédiaire limitant (CTA-Ag-Br) dans la synthèse des AuNRs et AgNRs.

## Acknowledgment

First and foremost, I would like to express my special gratitude to my supervisors, Dr. Lennox and Dr. Li. Throughout my doctoral studies, they have provided immense support in my research. Whenever I encountered difficulties in research, Dr. Lennox patiently found out the specifics and offered practical solutions. His support extended beyond academic research; he also deeply understands the challenges faced by international students. Part of my research involved organic synthesis, and whenever I faced challenges in the lab or even specific chemical reactions, Dr. Li always patiently discussed solutions and alternative reaction pathways with me. His professional guidance has been crucial to the progress of my research.

Thanks also to my advisory committee members, Dr. Reven and Dr. van de Ven. They have provided valuable comments and guidance during my yearly review, significantly enriching the content and depth of my research. Dr. Reven's professional advice helped me optimize my experimental design, while Dr. van de Ven insights deepened my understanding of the research topic. Their support and expertise have been invaluable in completing my doctoral degree.

Additionally, I am very grateful to our research associate in Lennox Group, Dr. Zhu. Whether it was research directions or experimental steps, Dr. Zhu provided tremendous assistance throughout my PhD studies. I remember my first day in the lab when Dr. Zhu patiently guided me through the preparation of my first silica gel column, marking a significant milestone in my experimental operations.

I also want to express my special thanks to my colleagues, staff, partners, and friends at McGill University who have worked alongside me and supported my research efforts behind the scenes. This includes, but is not limited to, the staff at the McGill Chemistry Characterization

Facility, who have made significant contributions to the characterization of compounds in this thesis. Specific mentions include Dr. Robin Stein for his expert assistance with NMR, Mr. Nadim Saadeh and Dr. Alexander Wahba for their help with HRMS, and Dr. Hatem Titi for his support with TGA.

Next, I would like to express my deep gratitude to my friends in Montreal: Qiyang Zhang, Zhenzhe Zhang, Anqi Chen, Laiyi Xu, Fangzhou Zhao, Shi Yin, Hu Zhou, and Siting Ni. Their constant support throughout my research journey made my life in Montreal truly enjoyable. I also extend my thanks to Danning Zhang, Tianchen Jing, and Xiaoyu Zhang; although not in Montreal, they were always there whenever I needed support.

I especially want to thank my family, particularly my parents, Mr. Jian Chen and Ms. Yalan Xue, for their endless understanding and support throughout my educational journey. From the time I was in middle school, they began planning and preparing, which enabled me to attend an international high school and ultimately pursuing my undergraduate and doctoral degrees at McGill University. Over the last eight years, despite spending little time with my family and often being far from home, they have consistently provided me with persistent support and understanding. Without their dedication, I cannot imagine how I could have reached where I am today.

Lastly, I would also like to thank myself. Reflecting on the beginning of my doctoral journey, I was not fully aware of the challenges I would face. After all these years, I learned to adjust my mindset and draw lessons from each setback. These experiences have shaped me into a more resilient individual. I am grateful to myself for not giving up and persevering to this point.

## **Contribution of Authors**

Chapter 2: All the experiments described in Chapter 2, unless otherwise specified, were conducted by Ruixue Chen, with discussion and feedback from Dr. Jun Zhu, Dr. R. Bruce Lennox, and Dr. Chao-Jun Li. The foundational ideas and inspiration for this work were derived from previous research conducted in Dr. R. Bruce Lennox's laboratory. The design of the linker structure was developed by Dr. Jun Zhu. A manuscript based on this work is in preparation and will be submitted to the journal *ACS Applied Materials & Interfaces*.

Chapter 3: All the experiments described in Chapter 3, unless specified otherwise, were conducted by Ruixue Chen, with discussions and feedback from Dr. Jun Zhu, Dr. R. Bruce Lennox, and Dr. Chao-Jun Li. A manuscript based on this work is in preparation and will be submitted to the journal *ACS Applied Materials & Interfaces*.

Chapter 4: All the experiments described in Chapter 4, unless specified otherwise, were conducted by Ruixue Chen, with discussions and feedback from Dr. Jun Zhu, Dr. R. Bruce Lennox, and Dr. Chao-Jun Li. A manuscript based on this work is in preparation and will be submitted to the journal *ACS Applied Materials & Interfaces*.

Chapter 5: All the experiments described in Chapter 5, unless specified otherwise, were conducted by Ruixue Chen, with discussions and feedback from Dr. Jun Zhu, Dr. R. Bruce Lennox, and Dr. Chao-Jun Li. A manuscript based on this work is in preparation and will be submitted to the journal *Chemical Communication*.

## **Contributions to Fundamental Knowledge**

This thesis introduces several novel advancements in the field of nanotechnology with a focus on drug delivery systems using gold nanoparticles. Initially, Chapter 1 sets the foundation by offering a critical review of traditional drug delivery methods used in drug delivery, identifying key challenges such as poor solubility and instability of traditional delivery vehicles. It then proposes the use of AuNPs, highlighting their inherent biocompatibility, consistent reproducibility in synthesis, and adaptable surface chemistry.

Chapter 2 establishes a framework for employing thermally dependent release mechanisms, featuring a novel linker inspired by retro Diels-Alder reactions. This method leverages the reversible nature of this reaction to facilitate controlled drug release at targeted temperatures, as exemplified through the use of maleimide and furfuryl alcohol derivatives.

Chapters 3 and 4 further develop innovative cargo-loading approaches on AuNPs. Chapter 3 delves into ligand exchange with thiolate ligands to achieve precise functionalization of AuNPs, while Chapter 4 introduces an interfacial esterification technique for attaching drug molecules to nanoparticles. These techniques provide flexible tools for binding a broad array of therapeutic molecules, thus broadening the functional applicability of AuNPs in drug delivery.

Moreover, I have successfully synthesized and characterized a thermal release system that operates under physiological conditions, showcasing its utility through kinetic studies and NMR monitoring. This system supports multi-stage drug release, presenting substantial advantages for complex treatment protocols such as those in pain management and chemotherapy.

Chapter 5 investigates the unique properties of anisotropic nanorods, particularly focusing on their photothermal characteristics activated by near-infrared light. This chapter delves into the

synthesis of NIR-responsive nanorods, showcasing a scalable and reproducible method. Additionally, this chapter addresses the implementation of solubility enhancement strategies that are crucial for maintaining the reproducibility of the nanorod synthesis process. These advancements are significant as they improve the practical application of nanorods in photothermal-triggered drug delivery systems.

# Contents

bstractii
ésumé
cknowledgmentvi
Contribution of Authorsix
Contributions to Fundamental Knowledge
ist of Abbreviationsxvi
ist of Figuresxix
ist of Schemesxxii
ist of Tablesxxiv
Chapter 1. General Introduction
1.1 Introduction
1.2 Synthesis of Gold Nanoparticles and Gold Nanorods
1.2.1 Synthesis of Gold Nanoparticles
1.2.2 Synthesis of Gold Nanorods
1.2.3 Characterization of Gold Nanoparticles
1.3 Surface Modification on Gold Nanoparticles
1.3.1 Approaches to the Surface Functionalization of Ligand-Capped Gold Nanoparticle
12

1.3.2 Types of Interfacial Reactions Used on Gold Nanoparticles Ligand Layers 14
1.4 Biomedical Applications of Gold Nanoparticles through Surface Modification 16
1.5 Controlled Drug Release for Therapeutic Applications
1.6 Context and Scope of Thesis Research
1.7 References
Chapter 2. Design and Synthesis of a Thermal Release Linker Based on a Retro- Diels-Alder
Reaction
2.1 Preface
2.2 Abstract
2.3 Introduction
2.4 Results and Discussion
2.4.1 Design of a Thermally Releasable Linker
2.4.2 Synthesis of a Thermally Releasable Linker
2.5 Conclusions and Perspective
2.6 Experimental
2.6.1 Material
2.6.2 Synthesis of Linker
2.7 References 61
Chapter 3. Development of a Thermally Releasing Gold Nanoparticle Template for Drug Delivery
62

3.1 Preface
3.2 Abstract
3.3 Introduction64
3.4 Result and Discussion
3.4.1 Synthesis and Characterization of 2 nm Water-Soluble AuNPs
3.4.2 Synthesis of NBD-Linker Thiol
3.4.3 Synthesis and Characterization of NBD-Linker-AuNPs
3.4.4 Kinetic Analysis of NBD Release from AuNPs
3.5 Conclusion and Perspective
3.6 Experimental
3.6.1 Materials
3.6.2 Synthesis of Fluorophore-Linker Conjugate
Synthesis of 2 nm PEGylated AuNPs
3.7 References
Chapter 4. A Controlled 'Load and Release' Reaction on Water-Soluble Gold Nanoparticles 93
4.1 Preface
4.2 Abstract
4.3 Introduction
4.4 Result and Discussion
4.4.1 Synthesis and Characterization and Linker-AuNPs

4.4.2 Interfacial Esterification Coupling Reaction of 10-AuNP with Small Molecules 1	.00
4.4.3 Kinetic Study of Acridine-AuNPs	07
4.5 Conclusion and Perspective	10
4.6 Experimental	11
4.6.1 Material	11
4.6.2 Synthesis of Acridine Derivative	11
4.7 References	26
Chapter 5. An Improved Method for the Synthesis of Gold and Silver Nanorods 1	28
5.1 Preface	28
5.2 Abstract	29
5.3 Introduction	30
5.4 Result and Discussion	32
5.4.1 Improved Aspect Ratio of AuNR using the Silver-Assisted Seed-Mediated Method1	132
5.4.2 Improved Synthesis of AgNRs using the Seed-Mediated Method 1	134
5.5 Conclusion and Perspective	40
5.6 Experimental	41
5.7 References	44
Chapter 6. Conclusions	47
6.1 Summary and Conclusions	47
6.2 Discussion and Future Work	153

6.3 Reference	155
Appendix	156
A NMR spectroscopic data from Chapter 2	156
B NMR spectroscopic data from Chapter 3	165
C NMR spectroscopic data from Chapter 4	173

## **List of Abbreviations**

AFM Atomic force microscopy

AgNRs Silver nanorods

AR Aspect ratio

AuNPs Gold nanoparticles

AuNRs Gold nanorods

CTAB Cetyltrimethylammonium bromide

CuAAC Cu(I)-catalyzed 1,3-dipolar cycloaddition of azides and alkynes

DLS Dynamic light scattering

Dox Doxorubicin

EPR Enhanced permeability and retention

FTIR Fourier transform infrared spectroscopy

GEM Gemcitabine

GSH Glutathione

HRTEM High-resolution transmission electron microscopy

IEDDA Inverse electron-demand Diels-Alder cycloaddition

LSPR Longitudinal surface plasmon resonance

NBD Nitrobenzofurazan

NIR Near-infrared

NMR Nuclear magnetic resonance

NRs Nanorods

PAA Polyacrylic acid

PEG Poly (ethylene glycol)

PET Positron emission tomography

rDA retro-Diels-Alder

SEM Scanning electron microscopy

SPAAC Strain-promoted alkyne-azide cycloaddition

SPR Polyacrylic acid

TCO Trans-cyclooctene

TEM Transmission electron microscopy

TGA Thermogravimetric analysis

TOAB Tetraocytlammonium bromide

XPS X-ray photoelectron spectroscopy

# **List of Figures**

Figure 1.1: The application of nanomaterials in various fields, Reprinted with permission from
Ref. 7
Figure 1.2: (A)Representation of ligand- stabilized AuNP; (B) High-Resolution Transmission
Electron Microscopy (HRTEM) images of the dodecanethiolate -capped 4.1 nm AuNPs sample.
(a) fcc clusters, (b and c) decahedra, (d-f) multidomain particles. Reprinted with permission
from Ref. 15
Figure 1.3: (A) SPR spectra of spherical AuNP of 9, 22, 48, and 99 nm diameter in water,
reprinted with permission from Ref.16 (B)AuNPs with different shapes and corresponding
different SPR bands, reprinted with permission from Ref.18
Figure 1.4: Methods for synthesizing AuNPs. ( <b>Method 1</b> ) Turkevich method to generate 20-50
nm; (Method 2) Brust-Schiffrin method for synthesizing 1-5 nm thiolated AuNPs; (Method 3)
One-phase modified Brust-Schiffrin method for synthesizing 1-5 nm PEGylated AuNPs
Figure 1.5: <sup>1</sup> H NMR spectra of (top) tetrahydrophthalimide linker and (bottom) linker modified
AuNPs
Figure 2.1: Illustration of release of cargo via a thermal-mediated rDA reaction through the
designed tetrahydrophthalimide linkage
Figure 2.2: Monitoring the retro Diels-Alder reaction of endo-compound 7 at different times at
45 °C, by <sup>1</sup> H NMR
Figure 2.3: Monitoring the retro-Diels-Alder reaction of exo-7 at different times, at 80 °C by <sup>1</sup> H
NMR
Figure 2.4: Kinetics of module compounds; endo-(left) at (37°C, 40 °C, 42 °C, 45 °C, 50°C) and
exo- right at (50 °C, 60 °C, 70 °C, 80 °C, 90 °C)

Figure 2.5: Arrhenius plots of the module compounds; endo- (up) and exo-(bottom) of 7 50
Figure 2.6: Illustration of orbital overlap differences between the two isomers of 7
Figure 2.7: Energy profile of endo-7 and exo-7.
Figure 3.1: Characterizations of HO-EG <sub>4</sub> -AuNPs. (A) <sup>1</sup> H NMR spectrum of HO-EG <sub>4</sub> -SH in
CDCl <sub>3</sub> and HO-EG <sub>4</sub> -AuNPs in D <sub>2</sub> O, (B) TEM image of HO-EG <sub>4</sub> -AuNPs (C) TGA scan of HO-
EG <sub>4</sub> -AuNPs. 68
Figure 3.2: Illustration of NBD derivative releasing via thermal-mediated rDA reaction of the
designed NBD-AuNPs. 71
Figure 3.3: Characterization of endo- and exo- NBD-AuNPs; <sup>1</sup> H NMR spectra of endo (A) and
exo- 4 (B) with corresponding NBD-AuNPs in CD <sub>3</sub> OD solvent. * is assigned to the solvent
(CDCl <sub>3</sub> and CH <sub>2</sub> Cl <sub>2</sub> )
Figure 3.4: Release behavior of endo-NBD-AuNPs at 37°C monitored through fluorescence
spectra (excitation wavelength at 467 nm).
Figure 3.5: Results of the first-order model fit of the endo- and exo-NBD-AuNPs at different
temperatures; endo-(left) at (37°C, 40 °C, 42 °C, 45 °C, 50°C) and exo-(right) NBD-AuNPs at
(55 °C, 60 °C, 65 °C, 70 °C, 75 °C)
Figure 3.6: Monodispersity of AuNPs confirmation through TEM analysis; (A) TEM images of
endo-NBD-AuNPs (left) and Ma-AuNPs right); (B) TEM images of exo-NBD-AuNPs (left) and
Ma-AuNPs (right)
Figure 4.1: Characterizations of MeO-EG <sub>4</sub> -AuNPs and Thp-AuNPs (A)Stacked <sup>1</sup> H NMR of
MeO-EG <sub>4</sub> -SH, MeO-EG <sub>4</sub> -AuNPs, tetrahydrophthalimide linker thiol and Thp-AuNPs; (B) TEM
image of Thp-AuNPs; (C) TGA scan of MeO-EG <sub>4</sub> -AuNPs and Thp-AuNPs

Figure 4.2: Characterizations of Acr-AuNPs; Stacked <sup>1</sup> H NMR of Thp-AuNPs, Acridine-Linker
conjugate and Acr-AuNPs. 103
Figure 4.3: Characterizations of Chr-AuNPs and; (A) The stack <sup>1</sup> H NMR of Chr-AuNPs (top)
and Sun-AuNPs (bottom)
Figure 4.4: Monitoring the retro Diels-Alder reaction of (A) Chr-AuNPs and (B) Sun-AuNPs at
different heating times at 45 °C. * was assigned to peak of the solvent dichloromethane 107
Figure 4.5: Release behavior of Acr-AuNPs monitored through fluorescence spectroscopy. (A)
Emission spectrum of Acr-AuNPs at 37 °C; (B) Results of the first-order model fitting of Acr-
AuNPs at different temperatures at (37°C, 40 °C, 42 °C, 45 °C, 50°C)
Figure 4.6: Confirmation of preserved monodispersity in AuNPs after heating at (37°C, 40 °C,
42 °C, 45 °C, 50°C); (A)TEM images of Thp-AuNP, (B) Acr-AuNPs and (C) Ma-AuNP 109
Figure 5.1: The solubility of the CTA-Ag-Br complex as a function of AgNO <sub>3</sub> in a 2% v/v
acetonitrile/ 100mM CTAB mixture. Plot of the peak intensity at 237 nm with a quantity of
AgNO <sub>3</sub> added
Figure 5.2: AuNRs synthesized as a function of AgNO <sub>3</sub> concentration (a) UV-vis spectra of
AuNRs synthesized using different amounts of AgNO <sub>3</sub> . An increased AgNO <sub>3</sub> leads to AuNRs
with a greater AR and an LSPR shifted to higher wavelengths. (b) TEM images AuNRs prepared
from different added amounts of AgNO <sub>3.</sub>
Figure 5.3: UV-vis spectra of AgNRs at different stages (A) UV-vis spectra and inserted
photograph of the silver seed stock solution after 40 minutes aging. (B) UV-vis spectra of the
AgNRs at different stages and inserted photographs of the AgNRs
Figure 5.4: TEM images of purified AgNRs made from a 0.2 mL seed stock solution (left) and a
0.1 mL seed stock solution (right).

Figure 5.5: AgNRs synthesized as a function of seed quantity added. UV-vis spect	ra of (A) crude
(B) centrifuged (C) supernatant (D) redispersed AgNRs.	139
Figure 6.1: Schematic overview of the designed thermal releasing tetrahydrophtha	limide linker
in controlled release system	148

# **List of Schemes**

Scheme 1.1: Illustration of seed growth method for AuNRs synthesis
Scheme 1.2: Illustration of AuNPs surface modification reactions
Scheme 1.3: Generalized reaction scheme of different types of interfacial reactions on AuNPs. 15
Scheme 1.4: (A) Schematic Illustration for tumor inhibition by tetrazine-mediated bioorthogonal
reaction and photothermal therapy. Reprinted with permission from Ref. 120
Scheme 1.5: (A) Schematic illustration of doxorubicin tethered AuNPs. (B) Schematic
illustration of the cooperation between enhanced doxorubicin cellular entry and a responsive
intracellular release of doxorubicin into the cells to overcome drug resistance. Reprinted with
permission from Ref. 132
Scheme 2.1: The synthesis of the tetrahydrophthalimide linker 8
Scheme 3.1: Synthetic scheme of PEG oligomer thiol (HO-EG <sub>4</sub> -SH) and <b>HO-EG<sub>4</sub>-AuNPs</b> 68
Scheme 3.2: Synthesis scheme of linker-NBD conjugate thiol 4
Scheme 4.1: The synthetic scheme of a short PEG oligomer thiol ((MeO-EG <sub>4</sub> -SH) and water-
soluble Thp-AuNPs
Scheme 4.2: Synthesis of Acr-AuNPs, Chr-AuNPs and Sun-AuNPs
Scheme 5.1: Schematic of the modified AgNRs synthesis steps. AA, ascorbic acid; CTAB =
$cetyl\ trimethylammonium\ bromide;\ CTAC = cetyltrimethylammonium\ chloride\ where\ cetyl = n-$
C16

# **List of Tables**

Table 2.1: Calculated half-lives for endo- (left) and exo-(right) of 7 as a function of temperature	
	49
Table 2.2: Eac of <b>3</b> , <b>5</b> , and <b>7</b>	50
Table 3.1: The half-life values calculated for endo- (left) and exo-(right) NBD-AuNPs at	
different temperatures.	75
Table 4.1: Coupling conditions of Thp-AuNPs with chlorambucil, sulindac, and acridine	
derivative.	104
Table 4.2: Calculated half-lives for endo-Acr-AuNPs as a function of temperature	110

## **Chapter 1. General Introduction**

#### 1.1 Introduction

Nanomaterials are a diverse class of materials characterized by having at least one dimension in the range from 1 to 100 nm. These materials possess exceptionally high surface areas, which can be finely tuned through rational design. As an emerging technology, nanotechnology has enabled the engineering of nanomaterials that exhibit superior performance compared to their bulk counterparts due to their unique properties. These properties originate from synthetic approaches that yield nanostructures such as particles (or dots), clusters, rods, prisms, and wires. Such nanostructures can be capable of: 1) efficient light absorption and conversion of energy into localized heat; 2) serving as carriers for drugs, imaging probes, and biomolecules, either on their surface or internally; 3) semiconductor properties; 4) physical properties which differ from their macroscopic analogs such as tensile strength, high surface area, and low density. These properties can be precisely controlled by manipulating the size, shape, synthesis conditions, and functionalization compared to their macroscopic analogs.

In recent years, the use of nanomaterials has expanded significantly across various sectors, including biomedical and healthcare, textiles, environmental management, agriculture, electronics, energy, and construction.<sup>7</sup> This diversification has been driven by the unique properties of nanomaterials that enable innovative applications in each of these fields, as shown in Figure 1.1.

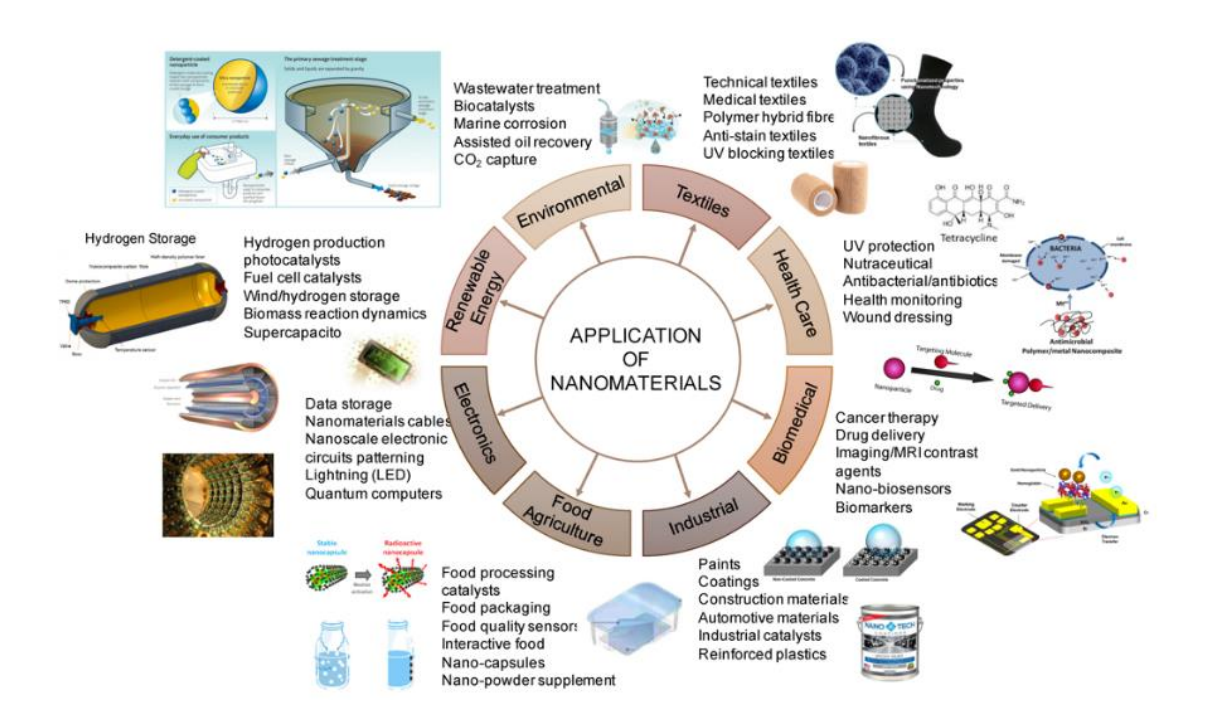


Figure 1.1: The application of nanomaterials in various fields, Reprinted with permission from Ref. 7.

Considerable attention has been drawn to metallic nanomaterials such as silver, gold, platinum, and iron due to the unique optical properties, catalytic activities, and thermal conductivities, <sup>8,9</sup> they exhibit, offering new opportunities and enhanced functionalities in a number of applications. <sup>10</sup> For example, magnetic iron oxide nanoparticles have been explored for biomedical applications such as MRI contrast agents, offering enhanced imaging quality. <sup>11</sup> In comparison, noble metal nanoparticles like silver have broad antibacterial properties and are used in water purification systems to provide safe drinking water. <sup>12</sup> Low-cost antibacterial filters, coated with silver nanoparticles, have proven effective in removing pathogens like *E. coli* in emergency applications. <sup>13</sup>

Gold nanomaterials have been the subject of a vast quantity of research over the past three decades because of their stability, accessibility through synthetic methods which yield a range of

morphologies, and novel physicochemical properties. When gold particles have at least one dimension and are between 1 nm and ca. 100 nm, they are classified as AuNPs. Most methods for synthesizing AuNPs involve the reduction of aqueous Au (I) or Au (III) salts in the presence of a surface coordinating ligand. This ligand coats the gold core and prevents their aggregation from forming macroscopic gold. (Figure 1.2.A).<sup>14</sup> Although often represented as being spherical, because spherically-symmetric AuNPs are in crystalline with a face-centered cubic lattice structure, they are in fact polyhedral (Figure 1.2.B).<sup>15</sup> By changing the quantities and concentrations of the precursor gold salt, reducing agent, and surfactants, the size of the particles can be precisely adjusted.

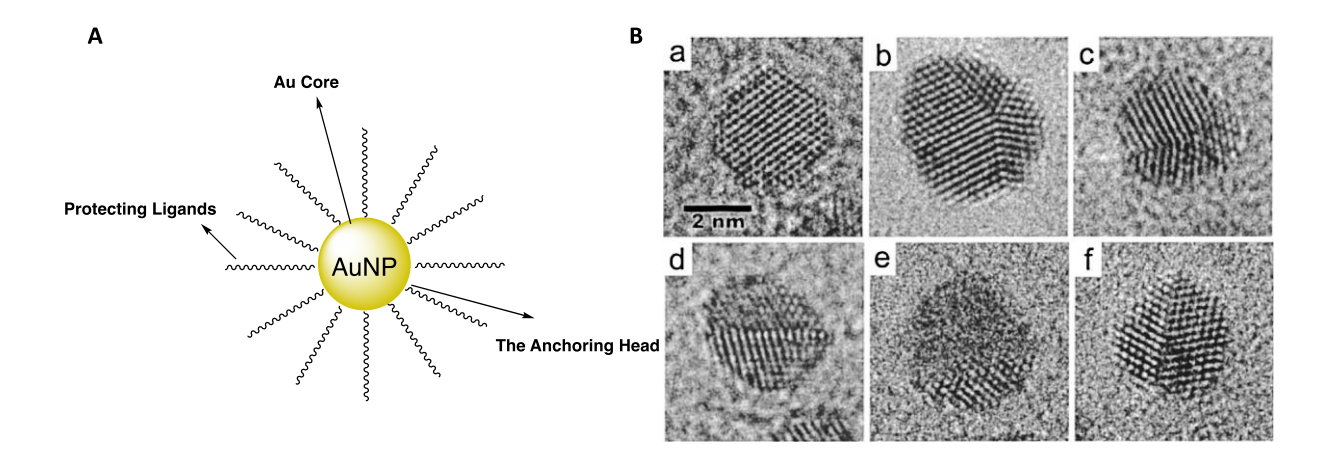


Figure 1.2: (A) Representation of ligand- stabilized AuNP; (B) High-Resolution Transmission Electron Microscopy (HRTEM) images of the dodecanethiolate -capped 4.1 nm AuNPs sample. (a) fcc clusters, (b and c) decahedra, (d-f) multidomain particles. Reprinted with permission from Ref. 15

Many of the applications of AuNP originate from their remarkable optical properties. For spherically-symmetric particles larger than 3 nm, the UV-vis absorption spectrum features a distinct peak in 530–570 nm range, known as the surface plasmon resonance (SPR) band (Figure

1.3.B). <sup>16</sup> This band arises from the collective oscillation of free conduction electrons upon their interaction with light, and accounts for the intense color of AuNPs. <sup>17</sup> The position of the SPR band depends on factors including NP size, shape, surface chemistry, and the dielectric constant of the surrounding medium. As the diameter of a sample of AuNPs increases from 20 nm to 100 nm, the wavelength of maximum absorption shifts accordingly, extending into the near-infrared (> 900nm; NIR) region for larger nanoparticles (Figure 1.3.A). <sup>18</sup> Rod-shaped NP (nanorods, or NR) that are 5 to 25nm in width exhibit an SPR band in 500-600 region (referred to as the transverse or TSPR band) as well as a long wavelength band (referred to as the longitudinal or LSPR band) that can range from 600 nm to 850 nm depending on the NR length. AuNPs can also convert absorbed light into heat through non-radiative processes, and in doing so significantly increase the NP's lattice temperature. This photothermal effect has led to the development of therapeutic applications. <sup>19</sup>

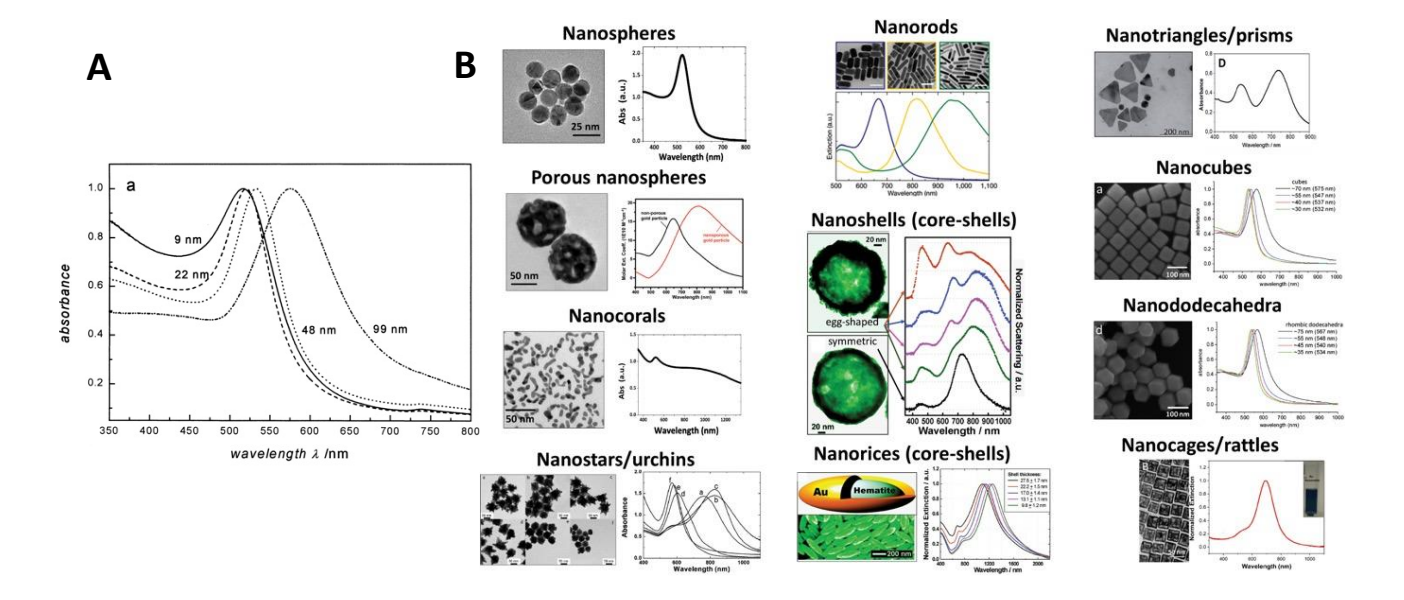


Figure 1.3: (A) SPR spectra of spherical AuNP of 9, 22, 48, and 99 nm diameter in water, reprinted with permission from Ref.16 (B) AuNPs with different shapes and corresponding different SPR bands, reprinted with permission from Ref.18

The surface functionalization of AuNPs with designed ligands can alter the metal core's chemical and physical properties. Ligands that have been extensively studied in this regard include such as thiols, <sup>20</sup> phosphines, <sup>21</sup> and amines. <sup>22</sup> Thiols however have been the most studied due to the robust gold-sulfur bond they form (ca. 200-300 kJ/mol)<sup>23</sup> which is nearly as strong as a C-C covalent (ca. 350 kJ/mol) bond, <sup>24</sup> facilitating both stabilization and functionalization of AuNPs. <sup>25</sup> The strong affinity of sulfur for Au(0), combined with van der Waals and dipole interactions between thiolated ligands, generally make AuNPs relatively stable to oxidation and thermal degradation below 90 °C and can be effectively stored under fairly simple conditions (4 °C, in the dark) without significant degradation over months. <sup>26</sup> pH values below 6 or above 11 <sup>27</sup> or high temperatures can however destabilize the thiolate-Au bond leading to ligand loss, and eventually nanoparticle aggregation. <sup>28</sup> The ligand capping layer can also be removed by exposure to I<sub>2</sub> or CN-<sup>29,30,31</sup>

The following section presents a contemporary review of the synthesis, characterization, and application of gold nanoparticles and gold nanorods.

#### 1.2 Synthesis of Gold Nanoparticles and Gold Nanorods

Gold has always fascinated people with its beautiful shine, ability to be cast and shaped in innumerable forms, and stability against oxidation. For a long time, because gold is relatively chemically inert and expensive, until the 19<sup>th</sup> C little was known about its chemistry. AuNPs are particularly valued as a template for biomedical uses due to their distinct physical and chemical properties including: (i) high chemical stability, especially toward oxidation (ii) a large surface area-to-volume ratio, (iii) low toxicity, and (iv) size and shape-dependent optical properties.<sup>32</sup>

AuNPs have been explored for a range of biomedical applications. For instance, they are used in medical diagnostics and therapeutics, serving as advanced drug delivery systems<sup>33</sup> and as imaging agents in CT.<sup>34</sup> Although a variety of three-dimensional shapes of gold nanomaterials have been synthesized,<sup>35,36</sup> including rods,<sup>37</sup> prisms,<sup>38</sup> and bipyramids,<sup>39</sup> spherical AuNPs and AuNRs are the most commonly used due to their well-studied surface functionalization and the relatively straightforward conditions required for their synthesis.

## 1.2.1 Synthesis of Gold Nanoparticles

Several protocols for the synthesis of ligand-capped AuNPs have been developed since Faraday's landmark work in the 1850s. The principal methods most often used today are the 1959 Turkevich method and the 1985 Brust-Schiffrin method.<sup>40</sup>

The Turkevich method<sup>41</sup> involves the reduction of a heated (75°C) aqueous HAuCl<sub>4</sub> solution in a 34 mM trisodium citrate solution. Citrate serves as both the reducing agent and the AuNPs stabilizing ligand. This process involves the rapid initial formation of nuclei followed by gradual growth, involving the reduction of the Au (III) to Au (0). The size of the NP thus produced depends on the HAuCl<sub>4</sub>: citrate ratio and the reaction temperature.<sup>42,43</sup> Products are usually in range of 20 nm to 50 nm in diameter. The AuNPs formed are water-soluble due to the hydrophilicity of the physiosorbed citrate ions. The relatively weak gold-citrate interaction leads to a kinetic lability where the citrate capping ligand can be readily replaced or exchanged by adsorbates with stronger gold-adsorbate interactions as is the case for thiol-containing molecules. This method thus offers a means to prepare either simply or elaborately- functionalized AuNPs directly from citrate-capped

AuNPs. Despite its limitations, including relatively low stability and poor solubility in organic solvents, the Turkevich method is often used to produce stabilized 20-50nm diameter AuNPs. 44,45

The Brust-Schiffrin method addresses many of the limitations of the Turkevich method. <sup>46</sup> It involves a two-phase process where AuCl<sub>4</sub> is transferred into an organic phase (i.e. toluene) using the phase transfer agent tetraocytlammonium bromide (TOAB). Addition of an alkylthiol to the organic phase reduces the Au (III) to Au (I), visually monitored by the disappearance of the orange color of Au (III). Subsequent addition of NaBH<sub>4</sub> quickly converts the Au(I) to Au(0), which aggregates to form spherically symmetric Au nanocrystals. <sup>47</sup> This protocol uses readily controlled reaction conditions to produce morphologically uniform (spherically symmetric) 1 nm to 5 nm AuNPs. <sup>48</sup> The product NP diameter is a function of gold-to-thiol molar ratio used, the reaction temperature, and the rate of reduction. <sup>49,50</sup> The Brust-Schiffrin method generates more stable AuNPs than the citrate-capped Turkevich NPs, as the gold-thiol bond is quite stable and kinetically robust. These AuNPs can be treated as a stable reaction precursor when further elaboration for the ligand capping layer is sought either through modification of the thiolate ligand itself, or through replacement of the entire ligand via an exchange reaction. They can be dried and re-dissolved in organic or polar solvents depending on the chemical nature of the ligand capping agents.

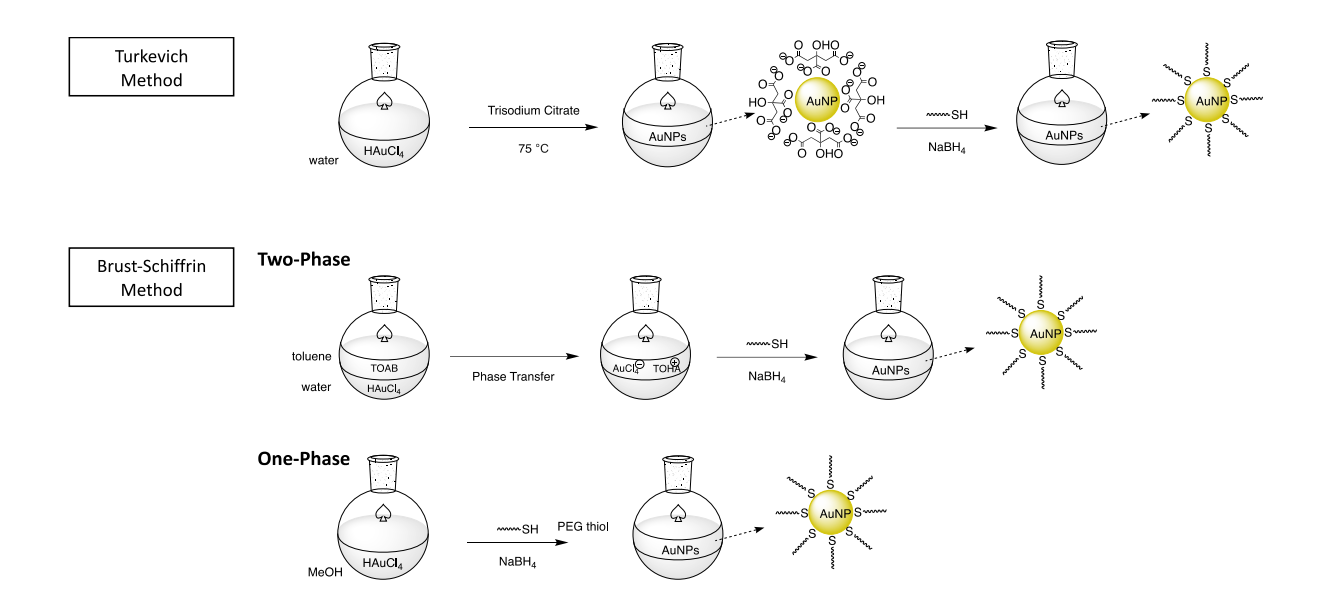


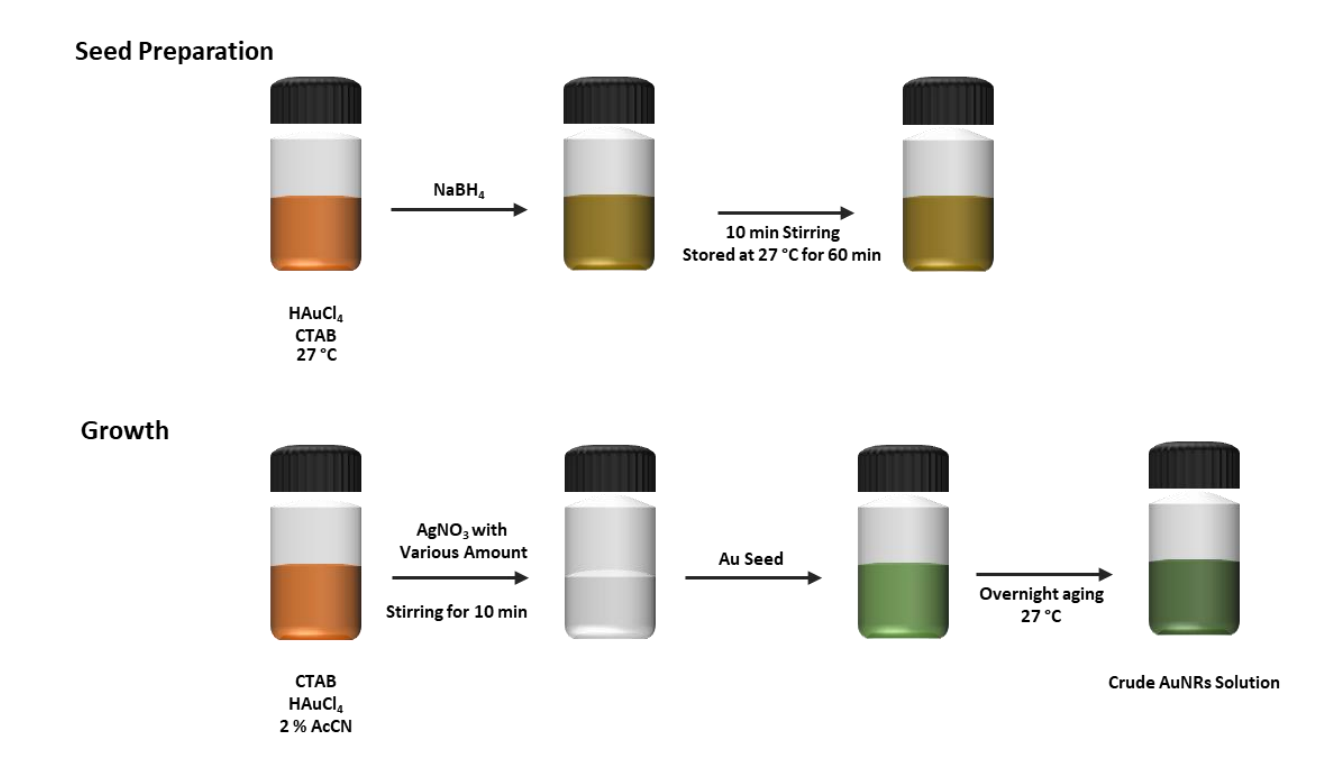
Figure 1.4: Methods for synthesizing AuNPs. (**Method 1**) Turkevich method to generate 20- 50 nm; (**Method 2**) Brust-Schiffrin method for synthesizing 1-5 nm thiolated AuNPs; (**Method 3**) One-phase modified Brust-Schiffrin method for synthesizing 1-5 nm PEGylated AuNPs.

Despite its advantages, the original Brust-Schiffrin method has some limitations, including the hydrophobicity of the alkanethiolate-stabilized AuNPs and TOAB contamination making the resulting NP incompatible in some biological applications. <sup>51</sup> To address these limitations, a one-phase synthesis method has been developed for the synthesis of water soluble thiolate-protected AuNPs. <sup>51</sup> In particular, replacing alkanethiol ligands with PEG (poly(ethylene glycol))-terminated thiol ligands enhances the water solubility of the resulting AuNPs (Figure 1.4). Murray et al first introduced the synthesis of thiol-terminated oligo (ethylene glycol)-protected AuNPs. <sup>52</sup> In recent years, the Lennox group has further elaborated this synthetic approach and reported monodisperse, water-soluble 3nm maleimide-tethered AuNPs coated with thiol-terminated PEG oligomers as a template with potential for use in biological applications. <sup>31,53</sup>

#### 1.2.2 Synthesis of Gold Nanorods

Metal nanorods, characterized by their unique physical and chemical properties, are a particularly interesting nanomaterial morphology. These rod-shaped nanoparticles are differentiated from spherical nanoparticles by length-to-width aspect ratios (AR) which can be as large as 23.<sup>54</sup> Their distinct optical, electrical, and magnetic properties compared to other nanoparticle morphologies such as spheres, prisms, stars, and cubes introduces possibilities for catalysis,<sup>55</sup> biomedical imaging,<sup>56</sup> and photothermal therapy applications.<sup>57</sup> Of particular note, as referred to above, is the presence of two size-dependent surface plasmon bands – the TSPR band in the 500-600nm region, the LSPR band in the 600nm-1500nm region of the spectrum vis-NIR.

AuNRs have been synthesized using a variety of methods, including chemical reduction,<sup>58</sup> electrochemical reduction,<sup>59</sup> and photochemical reduction.<sup>60</sup> The synthesis of nanomaterials using wet chemical methods is popular because it offers the opportunity for the facile control of the nanoparticle composition, geometry, and eventual functionality. Moreover, wet chemical methods are often amendable to scale-up.<sup>61</sup> The well documented seed-mediated method developed by Murphy<sup>54</sup> and El-Sayed<sup>56</sup> involves initial reduction of HAuCl<sub>4</sub> by NaBH<sub>4</sub> in the presence of a stabilizer (citrate or CTAB) to form gold seeds. These seeds are then added to a growth solution containing HAuCl<sub>4</sub>, ascorbic acid, and CTAB, followed by incubation at elevated temperatures (27 °C) several hours to produce the desired AuNR products, as per the general scheme shown in Scheme 1.1. Adjustments to this method, including varying the surfactant ratios and introducing binary surfactant systems, yielding LSPRs with maxima in the region of 850 nm for NRs whose lengths are 125 nm, demonstrating the ability to rationally tune the optical properties of AuNRs.<sup>62</sup>



Scheme 1.1: Illustration of seed growth method for AuNRs synthesis.

However, the reported synthetic methods of AuNR result in limited controllability over the LSPR wavelength (up to 850 nm) whereas access to the NIR-II window (1000-1700 nm) is highly desired given its potential for use in biomedical applications.<sup>56</sup> Recent advances have sought to access LSPR wavelengths in the NIR-II window<sup>63,61</sup> by making NR much longer than has been possible to date.

## 1.2.3 Characterization of Gold Nanoparticles

The characterization of AuNPs depends on different analytical needs and properties and often begins with determining the NP morphology. Transmission electron microscopy (TEM) and its high-resolution variant, HRTEM provide significant insight into the size, shape, and morphology of the NP or NR metal core.<sup>64</sup> When TEM is impractical or the focus of the research

shifts to surface morphology, atomic force microscopy (AFM) and scanning electron microscopy (SEM) provide valuable complementary information.<sup>65</sup> For investigations into the hydrodynamic behavior of ligand-coated AuNPs, dynamic light scattering (DLS) is essential, offering critical data on NP movement in fluids.<sup>66</sup> X-ray photoelectron spectroscopy (XPS) is utilized to determine the oxidation states of the surface and subsurface gold atoms, and those within core.<sup>67</sup> UV-vis spectroscopy is commonly used to determine the characteristics of the SPR peak(s) and their relationship to NP dimensions.

When AuNPs are coated with chemically elaborate organic ligands (compared to n-alkyl thiols), a variety of analytical methods can be employed to characterize their composition and structure. Thermogravimetric analysis (TGA) is a key technique that quantifies the mass ratio of organic ligands to metal, tracking weight loss as a function of temperature. <sup>68</sup> When TEM-derived NP size(s) are converted to provide average surface areas, the weight loss on heating and knowledge of the average area per ligand yields average coverage data. Fourier transform infrared spectroscopy (FTIR) data also contributes to an understanding of fate of the ligand functional groups. <sup>69</sup> A more direct analysis of the composition and structure of attached organic ligands can be accessed using nuclear magnetic resonance (NMR). <sup>70</sup> The densely packed assembly of ligands on the AuNP surface significantly decreases the dynamics of the ligand chains, which is then manifested in the characteristics of the <sup>1</sup>H resonances. For examples, the slow rotational diffusion of the bulky nanoparticles and broadened <sup>1</sup>H resonances of AuNP ligands combine to indicate successful ligand attachment (Figure 1.5).71,72 <sup>1</sup>H resonances from terminal functional groups, being farther from the core, tend to be sharper because of the enhanced mobility of the termini relative to methylenes closer to the thiolate tether point. Overall, <sup>1</sup>H NMR provides considerable information regarding the molecular environment of a ligand tethered to the nanoparticle surface.

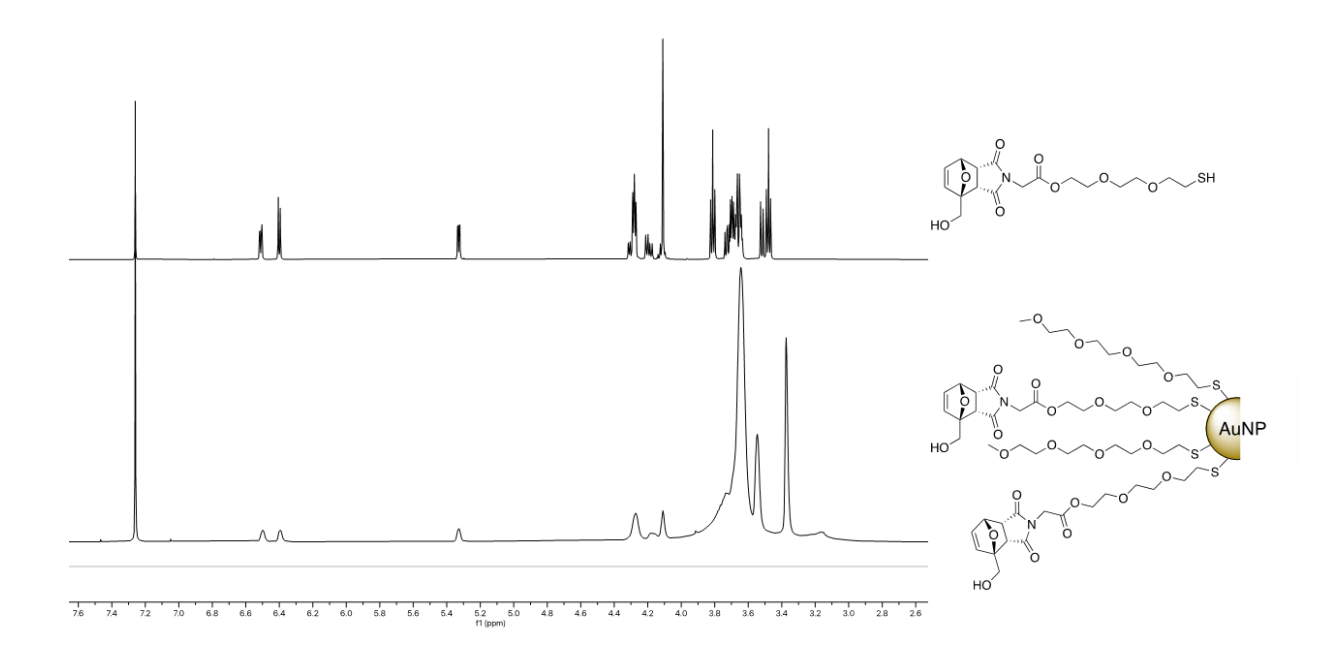


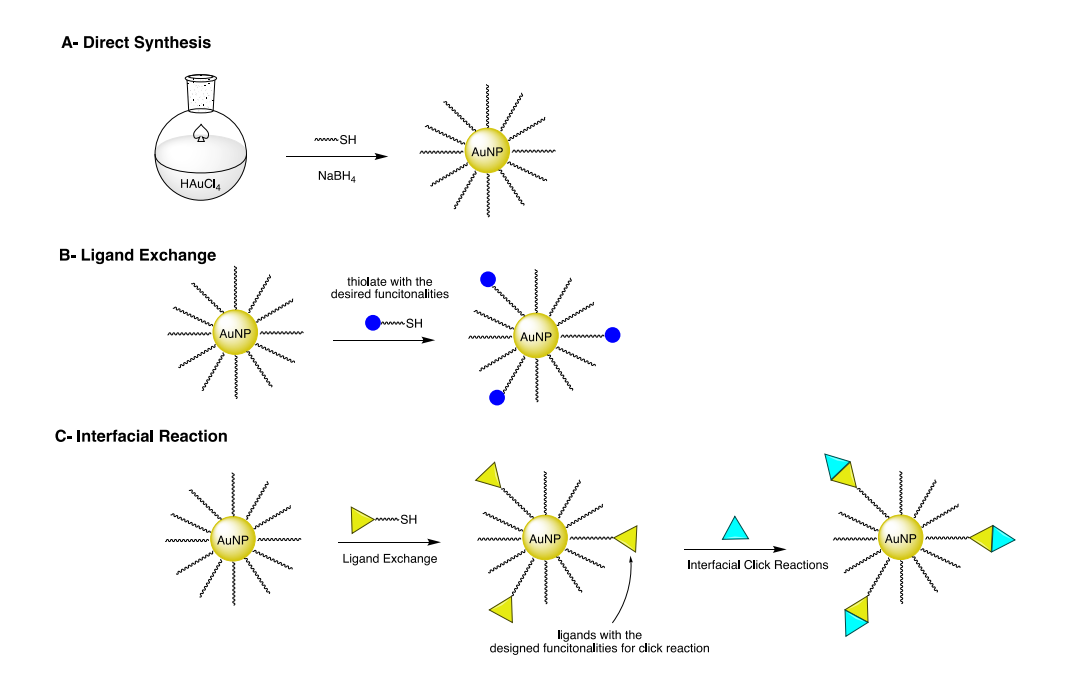
Figure 1.5: <sup>1</sup>H NMR spectra of (top) tetrahydrophthalimide linker and (bottom) linker modified AuNPs.

## 1.3 Surface Modification on Gold Nanoparticles

## 1.3.1 Approaches to the Surface Functionalization of Ligand-Capped Gold Nanoparticles

In addition to the applications described in the previous section, new applications of AuNPs are developed. The chemistry of the ligand functionalities dictates how AuNPs interact with and respond to their target environments, influencing their stability and overall properties. While amine- and phosphine-based can serve as ligands because of their affinity for gold surfaces, thiolates are the most commonly used and extensively studied due to the stronger affinity of thiols for gold.<sup>73</sup> This affinity and the fact that n-alkyl chains can align and form close packed structures facilitates the formation of stable monolayers that can be relatively defect-free.

The Brust-Schiffrin synthesis method introduced in Section 1.2.1 effectively incorporates thiol-based molecules onto AuNPs and offers a direct approach to introducing a particular desired functional group to the capping layer.<sup>74</sup> This direct synthesis method can involve the use of a thiol-containing complex ligand during the synthesis of a AuNP sample (Scheme 1.2). Functional groups that have been successfully incorporated into NP capping layers include alkyl moieties that differ from the predominant alkyl group,<sup>75</sup> as well as hydroxyl,<sup>31</sup> amine,<sup>76</sup> and carboxyl-terminated alkyl thiols.<sup>77</sup> However, this method encounters certain limitations. Firstly, it is limited by the incompatibility between some functional groups and NaBH<sub>4</sub>, the reducing agent that is commonly used in this synthesis. Secondly, functional groups which are susceptible to nucleophilic attack, such as Michael acceptors, cannot be incorporated.<sup>31</sup>



Scheme 1.2: Illustration of AuNPs surface modification reactions.

To address these limitations, an alternative method has been developed that involves use of an intermediate AuNP as a precursor (Scheme 1.2).<sup>78</sup> AuNPs with simple alkyl ligands are synthesized using the Brust-Schiffrin protocol and in a subsequent step, some of these are replaced

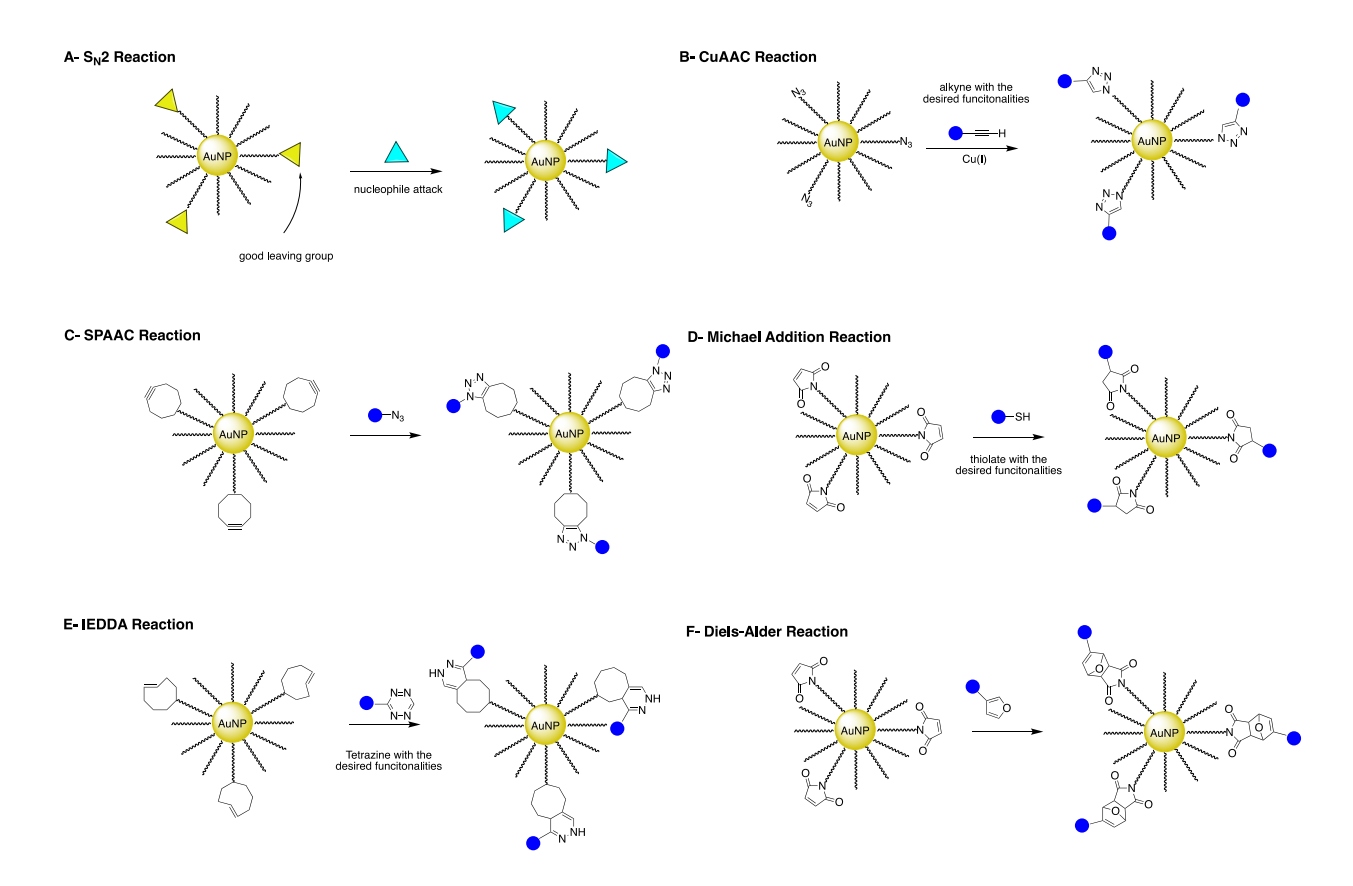
*via* an exchange with a thiolate derivative. The resulting ligand exchange results in AuNPs whose capping layer becomes a mixed monolayer from its initial single-component state. <sup>79</sup> The extent of ligand exchange can be controlled by adjusting the ratio of gold-to-thiol and the reaction time. <sup>14</sup>

A third preparation method involves post-synthetic interfacial reactions, where a reaction of some or all of the capping layer ligands is undertaken. (Scheme 1.2). This method provides a viable route to the preparation of a number of desired multifunctional AuNPs. However, the repertoire of typical reaction conditions available often involve conditions that compromise the gold-thiolate bond including high temperatures, extreme pH values (below 6)<sup>80</sup>, or the use of incompatible catalysts. Attention has therefore been directed to alternative interfacial reactions that can couple desired functional groups under mild conditions. The specifics of these reactions and their applications in creating multifunctional nanoparticles are discussed in detail in the following sections.

# 1.3.2 Types of Interfacial Reactions Used on Gold Nanoparticles Ligand Layers

S<sub>N</sub>2 reactions have been effectively used by Murray et al. in this regard.<sup>82</sup> Bromoalkanethiol-functionalized AuNPs were reacted with alkylamines where a terminal bromide reacted with amine (Scheme 1.3.A).<sup>82</sup> Mild 'click' reactions have also been used in AuNP derivatization. For example, the Cu(I)-catalyzed 1,3-dipolar cycloaddition of azides and alkynes (CuAAC) has been used to efficiently react terminal azides or alkynes on the nanoparticle surface (Scheme 1.3.B).<sup>83</sup> Finetti et al. developed a method to derivatize AuNPs with a synthetic functional copolymer via CuAAC, enhancing the NP stability toward aggregation and enabling subsequent reactions with azido-modified proteins.<sup>84</sup>

Despite the efficacy of the CuAAC reaction in NP derivatization, the cytotoxicity of residual copper ions poses a significant challenge in biomedical contexts, necessitating the complete removal of copper post-reaction. To address these concerns, catalyst-free click reactions such as like Strain-Promoted Alkyne-Azide Cycloaddition (SPAAC) have been developed offering an alternative for eventual *in vivo* use. <sup>85</sup> A further refinement in the synthesis of AuNPs involved use of an strained alkyne moiety for subsequent SPAAC reactions with azide-modified reagents (Scheme 1.3.C). <sup>86</sup>



Scheme 1.3: Generalized reaction scheme of different types of interfacial reactions on AuNPs.

Inverse electron-demand Diels-Alder cycloaddition reactions (IEDDA) have also been used to elaborate AuNPs ligand layers. This method has involved the use of tetrazine, which contains electron-rich aromatic rings that can act as diene components in IEDDA reactions

(Scheme 1.3.E). When tetrazine is incorporated into the ligand layer of a AuNP, cycloaddition reactions with cyclic alkenes such as norbornene, trans-cyclooctene, and cyclopropane can be undertaken<sup>87</sup> where these cyclic alkenes serve as electron-deficient dienophiles. The kinetics of this cycloaddition are 10<sup>6</sup> times greater than those of SPAAC reactions and thus offer an alternative to interfacial click reactions.<sup>88</sup> However, this method does encounter challenges, primarily due to the instability of tetrazine under reaction conditions used. Ongoing research has been focused on the functionalization of tetrazine to enhance its stability, recognizing that these modifications can sometimes adversely affect the efficiency of the cycloaddition reaction itself.<sup>89</sup>

Maleimide has proven to be an exceptionally stable moiety when applied to derivatization of ligand-capped AuNPs in aprotic conditions. It has been effectively used to anchor entities of interest onto AuNPs via Michael addition (Scheme 1.3.D) and Diels-Alder reactions (Scheme 1.3.F). Zhu et al. utilized maleimide-functionalized AuNPs to react with the silicon–fluorine prosthetic group [18F]SiFA-SH, achieving high radiochemical yields (60–80%) for subsequent positron emission tomography (PET) measurements *in vivo*. A commonly used coupling reaction (EDC/NHS coupling) was also reported by Bartczak et al. to couple an 8-mer peptide with terminal carboxyl groups on AuNP ligands. 91

## 1.4 Biomedical Applications of Gold Nanoparticles through Surface Modification

In contrast to the relative inertness of bulk gold, gold at the nanoscale exhibits significant catalytic activity. This property has led to the use of AuNPs in a variety of catalytic processes, including organic synthesis, <sup>92,93</sup> environmental remediation, <sup>94</sup> energy conversion. <sup>95</sup> imaging, <sup>96,97</sup> and therapeutics. <sup>98</sup> However overall this catalytic activity is reduced or negligible in the case of

the AuNPs described above, where the ligand capping layer is deliberately made stable over well documented thermal and chemical ranges. Ligand-capped AuNPs are therefore also introduced to biomedical applications where their intrinsic chemical reactivity/catalysis does present undesired effects in biological matrices. The many intrinsic properties of ligand-capped AuNP such as biocompatibility, low-toxicity, and visible-NIR optical window therefore offer the possibilities of application to biomedical sensing and delivery problems. The potential flexibility of chemistry associated with the capping layer allows researchers these AuNP as multivalent bioconjugation platforms and not simply as coated gold particles. Derivatization of the capping layer thus offers realistic opportunities to view these AuNPs as biocompatible multiplexed carriers for antibodies, peptides, drugs, and imaging agents. Throughout this section, biomedical applications of AuNPs will be discussed based on different surface modifications.

One of the most notable properties of 1-5 nm AuNPs is their intense surface plasmon, referred to above, in the visible region of the spectrum. When these NP aggregates' interparticle surface plasmon coupling occurs, to a color change from red to blue results, which can be observed visually or monitored via spectrophotometry. <sup>99</sup> The surface of AuNPs can be functionalized with various biomolecules, including oligonucleotides and antibodies, broadening their practical applications. <sup>44</sup> For example, covalent bonding often requires chemical modification of the drug and external triggers for release, noncovalent adsorption offers an alternative means to transport and efficiently release drugs. <sup>100</sup> Notably, PEG-coated AuNPs, with a core size  $\leq 5$  nm have been shown to effectively transport active hydrophobic drugs into cancer cells via membrane diffusion. <sup>101</sup> For targeted drug delivery, AuNPs are often coated with antibodies to guide them to specific sites within the body, where they can release drugs upon being triggered. The first use of antibody-functionalized AuNPs for targeted delivery was in 2008, when gemcitabine (GEM) was

specific to pancreatic adenocarcinoma cells using cetuximab-functionalized AuNPs. <sup>102</sup> Since then, AuNPs have been increasingly used to deliver a variety of chemotherapy drugs, such as doxorubicin (Dox), <sup>103,104</sup> oxaliplatin, <sup>105</sup> and docetaxel. <sup>106</sup> These drugs are attached to the AuNP core through various means including reversible gold-nitrogen (Au-N) bonds, hydrophobic interactions, and conjugation onto PEG ligands. This results in the formation of a mixed monolayer on the NP surface that includes the targeting antibody, thereby optimizing the delivery of drugs to cancer cells while reducing systemic side effects associated with whole-body rather than selective distribution of the drug.

The ligand exchange reaction, discussed in Section 1.3.1, is a technique developed by Murray et al. to replace the original ligands on AuNPs with another thiolate ligand that carries the desired functionalities. This method has been widely explored in various studies that aim to anchor different ligands with specific functionalities onto AuNPs to achieve targeted applications. In cancer treatment, small molecule anti-cancer drugs have been synthesized in their thiolate form and coated onto AuNPs. Dreaden et al. created a thiol-PEGylated derivative of the breast cancer drug tamoxifen and evaluated the efficacy of these nanoconjugates in selectively killing breast cancer cells via recognition by the membrane-estrogen receptor. Thiolated analogs of the commonly used chemotherapy agent, Doxorubicin (Dox), were synthesized by Du et al. and coated onto 35 nm AuNPs. Thang et al. reported the synthesis of a fluorescence-labeled DNA linker designed to enhance the hydrophilicity of paclitaxel. Despite these advances, the synthesis of thiolated drug conjugates remains challenging and costly due to the reactivity of the thiols, posing significant limitations to the practicality and scalability of the ligand exchange approach.

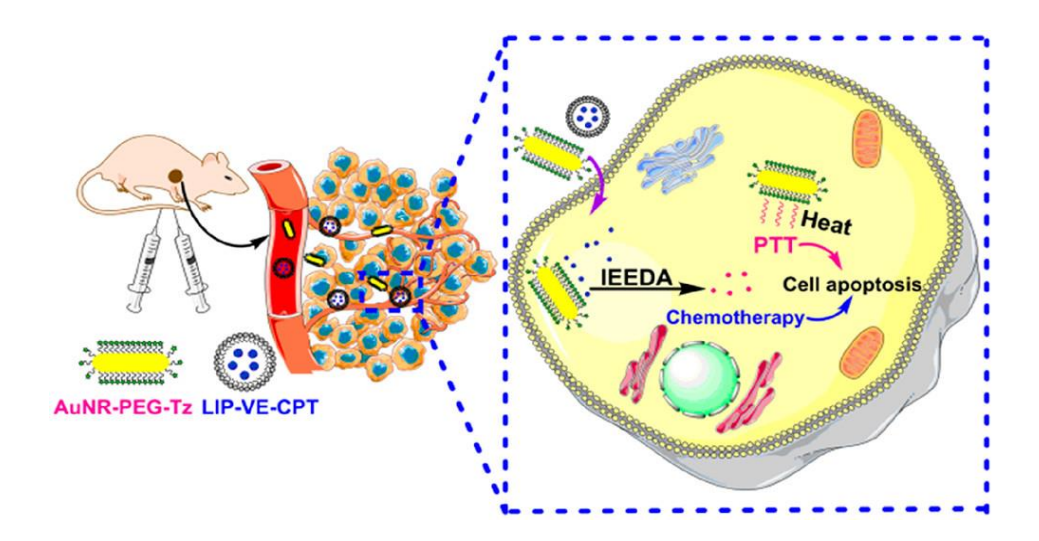
Due to the limitations of the conventional ligand exchange approach, which include the complexity of synthesizing pre-made thiolated complexes as well as the time-consuming exchange

process, researchers have explored using interfacial reactions, discussed in Section 1.3.2. These reactions enable the specific binding of designed moieties onto AuNPs, offering a relatively straightforward method to load desired functionalities onto AuNP cores.

AuNPs are also much studied in drug delivery applications, where they offer different approaches to treatment, especially in targeted therapy. 110 They provide distinct advantages in the transport and controlled release of therapeutic agents directly to disease sites compared to other delivery agents such as mineral-based materials or micelles and liposomes. A primary benefit of AuNPs in drug delivery is their highly tunable surface chemistry as per discussed in the foregoing, which facilitates the conjugation of therapeutic molecules, targeting ligands, and imaging agents all on one particle. 112 This multifunctionality enables the simultaneous execution of targeted drug delivery and controlled drug release. AuNPs can transport therapeutic agents through both covalent bonding and noncovalent attachment, with many studies demonstrating these capabilities. 113 Metallic nanorods are also considered to be good candidates for photothermal applications due to their unique optical and structural properties. The tunability of the LSPR signal 112 allows their longitudinal resonances to be extended into the NIR region by adjusting their aspect ratio. This NIR alignment is particularly advantageous for biomedical applications because NIR light (1100 -2500 nm) has much greater penetration depths into aqueous-based materials including biological tissues than do UV or visible light. 114 Moreover, nanorods can convert light into heat quite efficiently with more than 90% conversions reported, especially in the NIR. 115 This efficiency not only can facilitate targeted heating to effectively destroy cancer cells but also potentially trigger thermally-activated controlled drug release. 116

Pan et al. demonstrated the use of polyacrylic acid (PAA) coated AuNRs to target human osteosarcoma cells *in vitro*. This study highlighted that PAA-AuNRs could induce cell death by

damaging cell membranes and disrupting DNA integration, positioning these nanorods as promising agents for osteosarcoma treatment. 117 Furthermore, Park et al. modified the targeting process by using AuNRs to amplify SERS signals at tumor sites, subsequently activating NIR-triggered drug release. This method effectively localized and released chemotherapy drugs directly into tumors, enhancing treatment specificity and efficacy. 118 The high surface-to-volume ratio of AuNRs facilitates increased drug loading, which has been advantageous in cancer treatments. Fan et al. compared the chemotherapeutic efficiency of drug-coated AuNRs and AuNPs in treating gastric cancer, finding that AuNRs exhibited superior efficacy. 119 Recently, Xie et al. developed PEGylated tetrazine-functionalized AuNRs (AuNR-PEG-Tz) that facilitate bioorthogonal reaction-triggered drug release combined with photothermal therapy (Scheme 1.4). This dual approach leverages the enhanced permeability and retention effect for tumor accumulation and enables multispectral optoacoustic tomography imaging, significantly improving tumor inhibition effectiveness. 120



Scheme 1.4: Schematic Illustration for tumor inhibition by tetrazine-mediated bioorthogonal reaction and photothermal therapy. Reprinted with permission from Ref. 120.

## 1.5 Controlled Drug Release for Therapeutic Applications

The concept of controlled drug release plays a key role in therapeutic strategies. This section explores the fundamental principles governing controlled release and emphasizes the need to match drug properties with specific therapeutic requirements, including location, dosage, and rate of release.

Different drugs are optimized for action at specific sites within the body, making systems capable of targeted delivery. For instance, chemotherapeutic agents are most effective when concentrated at solid tumor sites, minimizing exposure to healthy tissues and reducing systemic side effects. Controlled release systems can be engineered to respond to local environmental triggers such as pH changes, temperature fluctuations, or specific enzymatic activity, which are indicative of the target site. This targeted approach not only enhances the efficacy of the drug but also reduces the potential for adverse reactions in healthy tissues.

The efficacy of a therapeutic agent often relies on its concentration in the bloodstream at a target site, requiring precise dosage control. Controlled release formulations are designed to maintain drug levels within a therapeutic window over an extended period, thereby avoiding the peaks and troughs associated with traditional bolus dosing. This steady-state delivery can be achieved through various mechanisms, such as encapsulating the drug in biodegradable polymers that slowly degrade and release the drug or using nanoparticle-based systems that release the drug in response to specific triggers.<sup>123</sup>

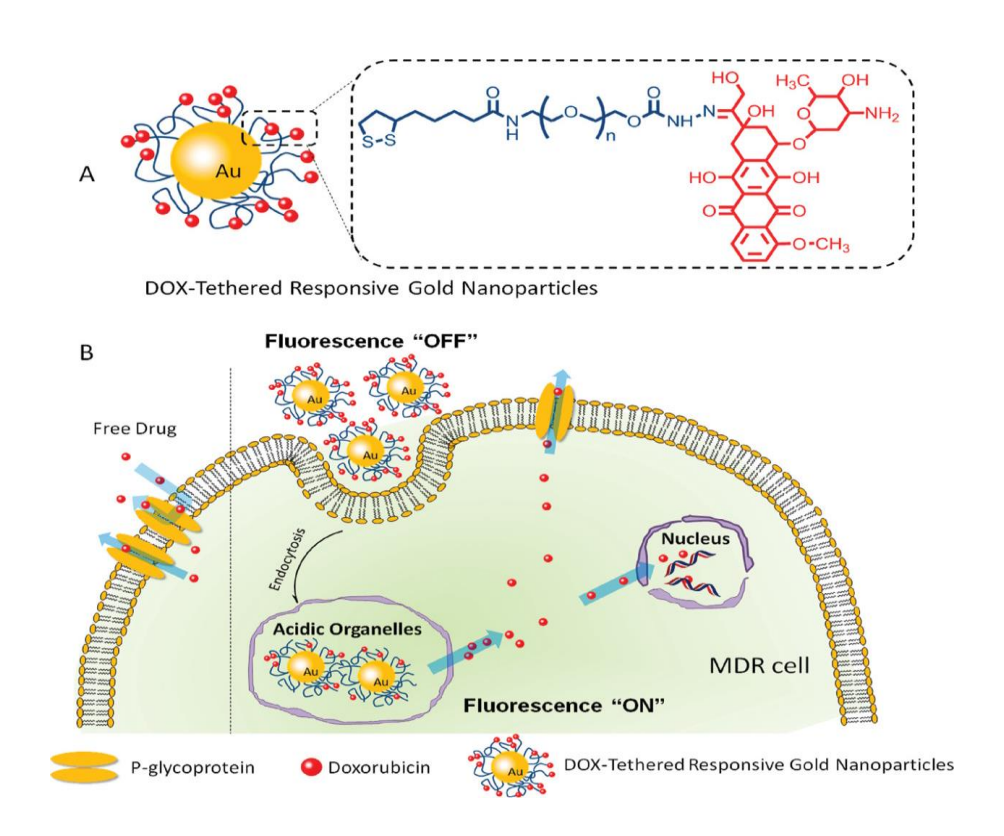
The rate at which a drug is released from its delivery system also influences its therapeutic outcomes. Controlled release systems can be fine-tuned to release drugs at a rate that matches the body's natural metabolic processes, ensuring that the local concentration of the drug is optimal for

treatment without exceeding toxicity thresholds. Technologies such as microencapsulation, <sup>124</sup> hydrogel systems, <sup>125</sup> and osmotically driven pumps <sup>126</sup> offer versatile platforms for achieving controlled release kinetics. For example, Shirakura et al. introduced a controlled release system based on hydrogel nanoparticles and analyzed its ability to deliver and release chemo-drug (cisplatin) selectively, based on thermal stimuli. <sup>125</sup> In some scenarios, a multi-stage release system is preferred for certain types of treatment. Treatments such as pain management <sup>127</sup> and cancer chemotherapy <sup>128</sup> often require an initial rapid delivery followed by a lesser but sustained release of the active ingredient. Therefore, a release system allowing for precise tuning of the release rates for different therapeutic agents is crucial for many treatments.

Finally, it is challenging to find a universal delivery system for all therapeutic applications. The following section will focus on the application of controlled release using gold nanoparticles as a carrier, aiming to address these challenges and enhance the effectiveness of drug delivery systems.

pH is one of the most studied stimuli for targeted drug release at the site of the target tissue, such as tumors. A mildly acidic to neutral environment (pH of 5.7 to 7.8) is characteristic of human cancer cells and intracellular organelles, including endosomes and vesicles. These specific pH conditions facilitate the cleavage of acid-sensitive bonds such as hydrazones, which are employed in various chemical and biological applications due to their pH sensitivity. Hydrazones have become particularly valuable in anticancer drug delivery as the acidic tumor microenvironment can trigger the cleavage of the hydrazone bond, releasing the encapsulated anticancer drug. In 2009, Aryal et al. demonstrated the effectiveness of this motif using AuNPs modified with doxorubicin through a hydrazone bond, which results in an enhanced drug release at pH 5.3. In Building on this, Wang et al. synthesized 30 nm AuNPs functionalized with PEG ligands

terminated with doxorubicin via a hydrazone bond, which facilitated the release of therapeutics under low pH conditions. These particles entered cells through endocytosis and showed enhanced drug retention in multidrug-resistant cancer cells compared to free doxorubicin as shown in Scheme 1.5.<sup>132</sup>



Scheme 1.5: (A) Schematic illustration of doxorubicin tethered AuNPs. (B) Schematic illustration of the cooperation between enhanced doxorubicin cellular entry and a responsive intracellular release of doxorubicin into the cells to overcome drug resistance. Reprinted with permission from Ref. 132.

However, the use of drug-conjugated AuNPs face challenges associated with their stability and propensity to aggregate, leading to inefficient therapy. To address these issues, Cui et al. designed a system with doxorubicin shielded by PEGylation on the surface of AuNPs. This not only enhances solubility, stability, and dispersion but also facilitates a two-step stimulus-

responsive drug release in response to the acidic environment in lysosomes followed by esterase in the cytoplasm. <sup>133</sup> Cancer cells are characterized by higher metabolic rates that lead to increased production of reactive oxygen species, resulting in elevated oxidative stress. To counteract this, cancer cells enhance their antioxidant defenses, such as elevating glutathione (GSH) levels, which are significantly higher than in normal cells. This differential has led to the development of cancer treatments that utilize the unique glutathione level within cancer cells. <sup>134</sup> Pramanik et al. developed copper complex-tethered AuNPs which are biotin coated, synthesized through interfacial amide bond formation. This design facilitates targeted delivery to tumor cells with controlled release triggered by glutathione, demonstrating an effective redox-sensitive delivery method. <sup>135</sup> Zhang et al. synthesized cysteamine AuNPs-Dox with disulfide linkages that bridge the AuNPs and doxorubicin derivatives. The breakage of these disulfide bonds and the consequent release of DOX-SH are readily induced by interaction with cellular GSH, enhancing the performance in inhibiting tumor tissues as demonstrated in vivo studies. <sup>136</sup> However, both pH- and GSH-triggered drug delivery systems face limitations, such as variations in biological systems that can impede precise control over drug release amounts. 137

Because of these challenges, research has increasingly focused on release processes based on external stimuli. Yan et al. further explored the "Click and Release" capability between prodrug iminosydnone-lonidamine and dibenzocyclooctyne, forming photothermal-active nanoaggregates with drug release. While chemically triggered release mechanisms using two-component systems such as the IEDDA reaction offer innovative drug delivery options, they also face limitations. Firstly, it is crucial to precisely synchronize or sequence the time delay between each component addition. Additionally, the instability of tetrazine/TCO (trans—cyclooctene) derivatives in biological systems often leads to inconsistent release profiles and reduced efficacy.

In response to the limitations of chemical triggers, research has expanded into external triggers, such as photo-induced release, which offers the benefits of non-invasive treatment. Luo et al. developed a light-responsive drug delivery platform utilizing AuNPs coated with a dense monolayer of hairpin DNA. Upon exposure to laser illumination at 532 nm, the photothermal effect of the AuNPs generates rapid heat, effectively triggering the release of the encapsulated molecules with high precision.<sup>139</sup>

## 1.6 Context and Scope of Thesis Research

The functionalization of nanomaterial surfaces can significantly expand their applications, which is also applicable for AuNPs. These nanoparticles, with tailored surface functionalities, find applications across a diverse range of fields including drug delivery, bioimaging, photothermal therapy, and catalysis. The conditions necessary for the derivatization of an AuNP surface should remain as mild as possible to preserve the functionality and integrity of the metal core itself. However, a major challenge in their use as drug carriers is the lack of precise control over drug release amounts, which is critical for effective disease treatment. The primary objective of this Thesis is thus to develop a drug delivery system that utilizes AuNPs. This system is designed to release drugs under mild conditions while enabling precise control over the dosage released, which aims to optimize therapeutic efficacy and minimize side effects by ensuring targeted and controlled drug release.

Chapter 2 introduces a thermal releasing linker that facilitates the conjugation and subsequent thermal release of molecular entities. It explores the design and synthesis of the linker based on the retro-Diels-Alder reaction, monitored through <sup>1</sup>H NMR. This section highlights the

linker's potential in controlled release systems, setting a foundational strategy for subsequent Chapters.

Chapter 3 describes the development of a thermal releasing AuNP template for drug delivery. It details the synthesis of a thiol ligand carrying a molecular cargo, an NBD dye derivative, and its application in modifying small water-soluble 2 nm AuNPs through a ligand exchange reaction. The Chapter outlines the methodology for determining the composition of these AuNPs and assesses the thermally triggered retro-Diels-Alder reaction via fluorescence spectroscopy, emphasizing its efficacy as a controlled drug delivery carrier.

Chapter 4 presents the development of a model controlled 'click and release' reaction, based on the retro-Diels-Alder reaction using 2 nm AuNPs. It describes the synthesis of a water-soluble acridine derivative and its incorporation onto PEGylated AuNPs through an interfacial esterification reaction. The thermally triggered reaction is examined using fluorescence spectroscopy. The Chapter also covers the successful loading of two model therapeutic agents, sulindac and chlorambucil, and monitors their release using <sup>1</sup>H NMR, demonstrating the versatility and efficiency of this platform in controlled drug delivery.

Chapter 5 addresses previous challenges in the synthesis of AuNRs and AgNRs, with an emphasis on enhancing reproducibility and purity. It discusses the improved solubility of the size-limiting agent (a silver intermediate) by introducing a co-solvent (2% v/v acetonitrile) which enables LSPR maxima to be extended to 1240 nm for the case of AuNRs. It also outlines robust methods for improving the synthesis of AgNRs, emphasizing precise chemical management and scalable production of nanorods with specific optical properties, potentially as photothermal release platforms.

Chapter 6 presents a comprehensive summary of the Conclusions drawn from this research and suggestions for Future Work.

#### 1.7 References

- (1) Baig, N.; Kammakakam, I.; Falath, W. Nanomaterials: A Review of Synthesis Methods, Properties, Recent Progress, and Challenges. *Materials Advances* **2021**, *2* (6), 1821–1871. https://doi.org/10.1039/D0MA00807A.
- (2) Burda, C.; Chen, X.; Narayanan, R.; El-Sayed, M. A. Chemistry and Properties of Nanocrystals of Different Shapes. *Chem. Rev.* **2005**, *105* (4), 1025–1102. https://doi.org/10.1021/cr030063a.
- (3) Hogan, N. J.; Urban, A. S.; Ayala-Orozco, C.; Pimpinelli, A.; Nordlander, P.; Halas, N. J. Nanoparticles Heat through Light Localization. *Nano Lett.* **2014**, *14* (8), 4640–4645. https://doi.org/10.1021/nl5016975.
- (4) Sapsford, K. E.; Algar, W. R.; Berti, L.; Gemmill, K. B.; Casey, B. J.; Oh, E.; Stewart, M. H.; Medintz, I. L. Functionalizing Nanoparticles with Biological Molecules: Developing Chemistries That Facilitate Nanotechnology. *Chem. Rev.* **2013**, *113* (3), 1904–2074. https://doi.org/10.1021/cr300143v.
- (5) Li, J.; Zhang, J. Z. Optical Properties and Applications of Hybrid Semiconductor Nanomaterials. *Coordination Chemistry Reviews* **2009**, 253 (23), 3015–3041. https://doi.org/10.1016/j.ccr.2009.07.017.
- (6) Yeo, S. J.; Oh, M. J.; Yoo, P. J. Structurally Controlled Cellular Architectures for High-Performance Ultra-Lightweight Materials. *Advanced Materials* **2019**, *31* (34), 1803670. https://doi.org/10.1002/adma.201803670.
- (7) Nizam, N. U. M.; Hanafiah, M. M.; Woon, K. S. A Content Review of Life Cycle Assessment of Nanomaterials: Current Practices, Challenges, and Future Prospects. *Nanomaterials* **2021**, *11* (12), 3324. https://doi.org/10.3390/nano11123324.
- (8) Liu, C.; Wu, T.; Lalanne, P.; Maier, S. A. Enhanced Light–Matter Interaction in Metallic Nanoparticles: A Generic Strategy of Smart Void Filling. *Nano Lett.* **2024**, *24* (15), 4641–4648. https://doi.org/10.1021/acs.nanolett.4c00810.
- (9) Khan, I.; Saeed, K.; Khan, I. Nanoparticles: Properties, Applications and Toxicities. *Arabian Journal of Chemistry* **2019**, *12* (7), 908–931. https://doi.org/10.1016/j.arabjc.2017.05.011.
- (10) R. Arvizo, R.; Bhattacharyya, S.; A. Kudgus, R.; Giri, K.; Bhattacharya, R.; Mukherjee, P. Intrinsic Therapeutic Applications of Noble Metal Nanoparticles: Past, Present and Future. *Chemical Society Reviews* **2012**, *41* (7), 2943–2970. https://doi.org/10.1039/C2CS15355F.
- (11) Lee, N.; Hyeon, T. Designed Synthesis of Uniformly Sized Iron Oxide Nanoparticles for Efficient Magnetic Resonance Imaging Contrast Agents. *Chem. Soc. Rev.* **2012**, *41* (7), 2575–2589. https://doi.org/10.1039/C1CS15248C.
- (12) Wu, J.; Li, C.; Zhang, J.; Menzies, N. W.; Bertsch, P. M.; Wang, P.; Kopittke, P. M. Release of Silver from Nanoparticle-Based Filter Paper and the Impacts to Mouse Gut Microbiota. *Environ. Sci.: Nano* **2020**, *7* (5), 1554–1565. https://doi.org/10.1039/C9EN01387C.
- (13) Praveena, S. M.; Han, L. S.; Than, L. T. L.; Aris, A. Z. Preparation and Characterisation of Silver Nanoparticle Coated on Cellulose Paper: Evaluation of Their Potential as Antibacterial Water Filter. *Journal of Experimental Nanoscience* **2016**, *11* (17), 1307–1319. https://doi.org/10.1080/17458080.2016.1209790.
- (14) Heuer-Jungemann, A.; Feliu, N.; Bakaimi, I.; Hamaly, M.; Alkilany, A.; Chakraborty, I.; Masood, A.; Casula, M. F.; Kostopoulou, A.; Oh, E.; Susumu, K.; Stewart, M. H.; Medintz, I. L.; Stratakis, E.; Parak, W. J.; Kanaras, A. G. The Role of Ligands in the Chemical

- Synthesis and Applications of Inorganic Nanoparticles. *Chem. Rev.* **2019**, *119* (8), 4819–4880. https://doi.org/10.1021/acs.chemrev.8b00733.
- (15) Zanchet, D.; Hall, B. D.; Ugarte, D. Structure Population in Thiol-Passivated Gold Nanoparticles. *J. Phys. Chem. B* **2000**, *104* (47), 11013–11018. https://doi.org/10.1021/jp0017644.
- (16) Amendola, V.; Pilot, R.; Frasconi, M.; Maragò, O. M.; Iatì, M. A. Surface Plasmon Resonance in Gold Nanoparticles: A Review. *J. Phys.: Condens. Matter* **2017**, 29 (20), 203002. https://doi.org/10.1088/1361-648X/aa60f3.
- (17) Palani, S.; Kenison, J. P.; Sabuncu, S.; Huang, T.; Civitci, F.; Esener, S.; Nan, X. Multispectral Localized Surface Plasmon Resonance (msLSPR) Reveals and Overcomes Spectral and Sensing Heterogeneities of Single Gold Nanoparticles. *ACS Nano* **2023**, *17* (3), 2266–2278. https://doi.org/10.1021/acsnano.2c08702.
- (18) Link, S.; El-Sayed, M. A. Size and Temperature Dependence of the Plasmon Absorption of Colloidal Gold Nanoparticles. *J. Phys. Chem. B* **1999**, *103* (21), 4212–4217. https://doi.org/10.1021/jp984796o.
- (19) Ali, M. R. K.; Wu, Y.; El-Sayed, M. A. Gold-Nanoparticle-Assisted Plasmonic Photothermal Therapy Advances Toward Clinical Application. *J. Phys. Chem. C* **2019**, *123* (25), 15375–15393. https://doi.org/10.1021/acs.jpcc.9b01961.
- (20) Woehrle, G. H.; Brown, L. O.; Hutchison, J. E. Thiol-Functionalized, 1.5-Nm Gold Nanoparticles through Ligand Exchange Reactions: Scope and Mechanism of Ligand Exchange. *J. Am. Chem. Soc.* **2005**, *127* (7), 2172–2183. https://doi.org/10.1021/ja0457718.
- (21) Weare, W. W.; Reed, S. M.; Warner, M. G.; Hutchison, J. E. Improved Synthesis of Small (dCORE ≈ 1.5 Nm) Phosphine-Stabilized Gold Nanoparticles. *J. Am. Chem. Soc.* **2000**, *122* (51), 12890–12891. https://doi.org/10.1021/ja002673n.
- (22) J. Rak, M.; K. Saadé, N.; Friščić, T.; Moores, A. Mechanosynthesis of Ultra-Small Monodisperse Amine-Stabilized Gold Nanoparticles with Controllable Size. *Green Chemistry* **2014**, *16* (1), 86–89. https://doi.org/10.1039/C3GC41827H.
- (23) Ferreira, V. F.; Do Prado, C. R. A.; Rodrigues, C. M.; Otubo, L.; Batista, A. A.; da Cruz, J. W.; Ellena, J.; Dinelli, L. R.; Bogado, A. L. Modified Glassy Carbon Electrode with AuNPs Using *Cis*-[RuCl(Dppb)(Bipy)(4-Vpy)]+ as Crossed Linking Agent. *Polyhedron* **2014**, 78, 46–53. https://doi.org/10.1016/j.poly.2014.04.024.
- (24) Huang, L.; Szewczyk, M.; Kancherla, R.; Maity, B.; Zhu, C.; Cavallo, L.; Rueping, M. Modulating Stereoselectivity in Allylic C(Sp3)-H Bond Arylations via Nickel and Photoredox Catalysis. *Nat Commun* **2023**, *14*, 548. https://doi.org/10.1038/s41467-023-36103-0.
- (25) Love, J. C.; Estroff, L. A.; Kriebel, J. K.; Nuzzo, R. G.; Whitesides, G. M. Self-Assembled Monolayers of Thiolates on Metals as a Form of Nanotechnology. *Chem. Rev.* **2005**, *105* (4), 1103–1170. https://doi.org/10.1021/cr0300789.
- (26) Ulman, A. Formation and Structure of Self-Assembled Monolayers. *Chem. Rev.* **1996**, *96* (4), 1533–1554. https://doi.org/10.1021/cr9502357.
- (27) Harrison, E.; Hamilton, J. W. J.; Macias-Montero, M.; Dixon, D. Peptide Functionalized Gold Nanoparticles: The Influence of pH on Binding Efficiency. *Nanotechnology* **2017**, 28 (29), 295602. https://doi.org/10.1088/1361-6528/aa77ac.
- (28) Kim, H. J.; Wang, W.; Mallapragada, S. K.; Vaknin, D. The Effects of Temperature on the Assembly of Gold Nanoparticle by Interpolymer Complexation. *J. Phys. Chem. Lett.* **2021**, 12 (5), 1461–1467. https://doi.org/10.1021/acs.jpclett.0c03749.

- (29) Wei, S.-C.; Hsu, P.-H.; Lee, Y.-F.; Lin, Y.-W.; Huang, C.-C. Selective Detection of Iodide and Cyanide Anions Using Gold-Nanoparticle-Based Fluorescent Probes. *ACS Appl. Mater. Interfaces* **2012**, *4* (5), 2652–2658. https://doi.org/10.1021/am3003044.
- (30) Templeton, A. C.; Hostetler, M. J.; Kraft, C. T.; Murray, R. W. Reactivity of Monolayer-Protected Gold Cluster Molecules: Steric Effects. *J. Am. Chem. Soc.* **1998**, *120* (8), 1906–1911. https://doi.org/10.1021/ja973863+.
- (31) Zhu, J.; Waengler, C.; Lennox, R. B.; Schirrmacher, R. Preparation of Water-Soluble Maleimide-Functionalized 3 Nm Gold Nanoparticles: A New Bioconjugation Template. *Langmuir* **2012**, *28* (13), 5508–5512. https://doi.org/10.1021/la300316j.
- (32) Dykman, L. A.; Khlebtsov, N. G. Gold Nanoparticles in Biology and Medicine: Recent Advances and Prospects. *Acta Naturae* **2011**, *3* (2), 34–55.
- (33) Kumar, A.; Zhang, X.; Liang, X.-J. Gold Nanoparticles: Emerging Paradigm for Targeted Drug Delivery System. *Biotechnology Advances* **2013**, *31* (5), 593–606. https://doi.org/10.1016/j.biotechadv.2012.10.002.
- (34) Debouttière, P.-J.; Roux, S.; Vocanson, F.; Billotey, C.; Beuf, O.; Favre-Réguillon, A.; Lin, Y.; Pellet-Rostaing, S.; Lamartine, R.; Perriat, P.; Tillement, O. Design of Gold Nanoparticles for Magnetic Resonance Imaging. *Advanced Functional Materials* **2006**, *16* (18), 2330–2339. https://doi.org/10.1002/adfm.200600242.
- (35) Fabris, L. Gold Nanostars in Biology and Medicine: Understanding Physicochemical Properties to Broaden Applicability. *J. Phys. Chem. C* **2020**, *124* (49), 26540–26553. https://doi.org/10.1021/acs.jpcc.0c08460.
- (36) Stangherlin, S.; Cathcart, N.; Sato, F.; Kitaev, V. Gold Nanoprisms: Synthetic Approaches for Mastering Plasmonic Properties and Implications for Biomedical Applications. *ACS Appl. Nano Mater.* **2020**, *3* (8), 8304–8318. https://doi.org/10.1021/acsanm.0c01741.
- (37) Chen, H.; Shao, L.; Li, Q.; Wang, J. Gold Nanorods and Their Plasmonic Properties. *Chemical Society Reviews* **2013**, *42* (7), 2679–2724. https://doi.org/10.1039/C2CS35367A.
- (38) Millstone, J. E.; Métraux, G. S.; Mirkin, C. A. Controlling the Edge Length of Gold Nanoprisms via a Seed-Mediated Approach. *Advanced Functional Materials* **2006**, *16* (9), 1209–1214. https://doi.org/10.1002/adfm.200600066.
- (39) Chateau, D.; Desert, A.; Lerouge, F.; Landaburu, G.; Santucci, S.; Parola, S. Beyond the Concentration Limitation in the Synthesis of Nanobipyramids and Other Pentatwinned Gold Nanostructures. *ACS Appl. Mater. Interfaces* **2019**, *11* (42), 39068–39076. https://doi.org/10.1021/acsami.9b12973.
- (40) C. Dreaden, E.; M. Alkilany, A.; Huang, X.; J. Murphy, C.; A. El-Sayed, M. The Golden Age: Gold Nanoparticles for Biomedicine. *Chemical Society Reviews* **2012**, *41* (7), 2740–2779. https://doi.org/10.1039/C1CS15237H.
- (41) Kimling, J.; Maier, M.; Okenve, B.; Kotaidis, V.; Ballot, H.; Plech, A. Turkevich Method for Gold Nanoparticle Synthesis Revisited. *J. Phys. Chem. B* **2006**, *110* (32), 15700–15707. https://doi.org/10.1021/jp061667w.
- (42) Daniel, M.-C.; Astruc, D. Gold Nanoparticles: Assembly, Supramolecular Chemistry, Quantum-Size-Related Properties, and Applications toward Biology, Catalysis, and Nanotechnology. *Chem. Rev.* **2004**, *104* (1), 293–346. https://doi.org/10.1021/cr030698+.
- (43) Xia, H.; Xiahou, Y.; Zhang, P.; Ding, W.; Wang, D. Revitalizing the Frens Method To Synthesize Uniform, Quasi-Spherical Gold Nanoparticles with Deliberately Regulated Sizes from 2 to 330 Nm. *Langmuir* **2016**, *32* (23), 5870–5880. https://doi.org/10.1021/acs.langmuir.6b01312.

- (44) Liu, S.; Lämmerhofer, M. Functionalized Gold Nanoparticles for Sample Preparation: A Review. *ELECTROPHORESIS* **2019**, 40 (18–19), 2438–2461. https://doi.org/10.1002/elps.201900111.
- (45) Frens, G. Controlled Nucleation for the Regulation of the Particle Size in Monodisperse Gold Suspensions. *Nature Physical Science* **1973**, 241 (105), 20–22. https://doi.org/10.1038/physci241020a0.
- (46) Brust, M.; Walker, M.; Bethell, D.; J. Schiffrin, D.; Whyman, R. Synthesis of Thiol-Derivatised Gold Nanoparticles in a Two-Phase Liquid–Liquid System. *Journal of the Chemical Society, Chemical Communications* **1994**, 0 (7), 801–802. https://doi.org/10.1039/C39940000801.
- (47) G. Booth, S.; Uehara, A.; Chang, S.-Y.; Fontaine, C. L.; Fujii, T.; Okamoto, Y.; Imai, T.; M. Schroeder, S. L.; W. Dryfe, R. A. The Significance of Bromide in the Brust–Schiffrin Synthesis of Thiol Protected Gold Nanoparticles. *Chemical Science* **2017**, *8* (12), 7954–7962. https://doi.org/10.1039/C7SC03266H.
- (48) Perala, S. R. K.; Kumar, S. On the Mechanism of Metal Nanoparticle Synthesis in the Brust–Schiffrin Method. *Langmuir* **2013**, *29* (31), 9863–9873. https://doi.org/10.1021/la401604q.
- (49) Whetten, R. L.; Khoury, J. T.; Alvarez, M. M.; Murthy, S.; Vezmar, I.; Wang, Z. L.; Stephens, P. W.; Cleveland, C. L.; Luedtke, W. D.; Landman, U. Nanocrystal Gold Molecules. *Advanced Materials* **1996**, *8* (5), 428–433. https://doi.org/10.1002/adma.19960080513.
- (50) Hosseini, S.; Alsiraey, N.; Riley, A. J.; Zubkov, T.; Closson, T.; Tye, J.; Bodappa, N.; Li, Z. Variable Growth and Characterizations of Monolayer-Protected Gold Nanoparticles Based on Molar Ratio of Gold and Capping Ligands. *Langmuir* **2018**, *34* (50), 15517–15525. https://doi.org/10.1021/acs.langmuir.8b02623.
- (51) A. Waters, C.; J. Mills, A.; A. Johnson, K.; J. Schiffrin, D. Purification of Dodecanethiol Derivatised Gold Nanoparticles. *Chemical Communications* **2003**, *0* (4), 540–541. https://doi.org/10.1039/B211874B.
- (52) Wuelfing, W. P.; Gross, S. M.; Miles, D. T.; Murray, R. W. Nanometer Gold Clusters Protected by Surface-Bound Monolayers of Thiolated Poly(Ethylene Glycol) Polymer Electrolyte. *J. Am. Chem. Soc.* **1998**, *120* (48), 12696–12697. https://doi.org/10.1021/ja983183m.
- (53) Fam, S. Y.; Chee, C. F.; Yong, C. Y.; Ho, K. L.; Mariatulqabtiah, A. R.; Tan, W. S. Stealth Coating of Nanoparticles in Drug-Delivery Systems. *Nanomaterials* **2020**, *10* (4), 787. https://doi.org/10.3390/nano10040787.
- (54) Gao, J.; Bender, C. M.; Murphy, C. J. Dependence of the Gold Nanorod Aspect Ratio on the Nature of the Directing Surfactant in Aqueous Solution. *Langmuir* **2003**, *19* (21), 9065–9070. https://doi.org/10.1021/la034919i.
- (55) Bai, X.; Gao, Y.; Liu, H.; Zheng, L. Synthesis of Amphiphilic Ionic Liquids Terminated Gold Nanorods and Their Superior Catalytic Activity for the Reduction of Nitro Compounds. *J. Phys. Chem. C* **2009**, *113* (41), 17730–17736. https://doi.org/10.1021/jp906378d.
- (56) Huang, X.; Neretina, S.; El-Sayed, M. A. Gold Nanorods: From Synthesis and Properties to Biological and Biomedical Applications. *Advanced Materials* **2009**, *21* (48), 4880–4910. https://doi.org/10.1002/adma.200802789.
- (57) Liao, S.; Yue, W.; Cai, S.; Tang, Q.; Lu, W.; Huang, L.; Qi, T.; Liao, J. Improvement of Gold Nanorods in Photothermal Therapy: Recent Progress and Perspective. *Front. Pharmacol.* **2021**, *12*. https://doi.org/10.3389/fphar.2021.664123.

- (58) Wei, M.-Z.; Deng, T.-S.; Zhang, Q.; Cheng, Z.; Li, S. Seed-Mediated Synthesis of Gold Nanorods at Low Concentrations of CTAB. *ACS Omega* **2021**, *6* (13), 9188–9195. https://doi.org/10.1021/acsomega.1c00510.
- (59) Yu; Chang, S.-S.; Lee, C.-L.; Wang, C. R. C. Gold Nanorods: Electrochemical Synthesis and Optical Properties. *J. Phys. Chem. B* **1997**, *101* (34), 6661–6664. https://doi.org/10.1021/jp971656q.
- (60) Jain, P. K.; Huang, X.; El-Sayed, I. H.; El-Sayed, M. A. Noble Metals on the Nanoscale: Optical and Photothermal Properties and Some Applications in Imaging, Sensing, Biology, and Medicine. *Acc. Chem. Res.* **2008**, *41* (12), 1578–1586. https://doi.org/10.1021/ar7002804.
- (61) Vigderman, L.; Khanal, B. P.; Zubarev, E. R. Functional Gold Nanorods: Synthesis, Self-Assembly, and Sensing Applications. *Advanced Materials* **2012**, *24* (36), 4811–4841. https://doi.org/10.1002/adma.201201690.
- (62) González-Rubio, G.; Kumar, V.; Llombart, P.; Díaz-Núñez, P.; Bladt, E.; Altantzis, T.; Bals, S.; Peña-Rodríguez, O.; Noya, E. G.; MacDowell, L. G.; Guerrero-Martínez, A.; Liz-Marzán, L. M. Disconnecting Symmetry Breaking from Seeded Growth for the Reproducible Synthesis of High Quality Gold Nanorods. *ACS Nano* **2019**, *13* (4), 4424–4435. https://doi.org/10.1021/acsnano.8b09658.
- (63) Hinman, S. S.; McKeating, K. S.; Cheng, Q. Surface Plasmon Resonance: Material and Interface Design for Universal Accessibility. *Anal Chem* **2018**, *90* (1), 19–39. https://doi.org/10.1021/acs.analchem.7b04251.
- (64) Carenco, S.; Moldovan, S.; Roiban, L.; Florea, I.; Portehault, D.; Vallé, K.; Belleville, P.; Boissière, C.; Rozes, L.; Mézailles, N.; Drillon, M.; Sanchez, C.; Ersen, O. The Core Contribution of Transmission Electron Microscopy to Functional Nanomaterials Engineering. *Nanoscale* **2016**, *8* (3), 1260–1279. https://doi.org/10.1039/C5NR05460E.
- (65) Ma, Y. Characterization of Nanomaterials in Nanotoxicological Analyses. In *Toxicology of Nanomaterials*; John Wiley & Sons, Ltd, 2016; pp 1–21. https://doi.org/10.1002/9783527689125.ch1.
- (66) Piella, J.; Bastús, N. G.; Puntes, V. Size-Dependent Protein—Nanoparticle Interactions in Citrate-Stabilized Gold Nanoparticles: The Emergence of the Protein Corona. *Bioconjugate Chem.* **2017**, 28 (1), 88–97. https://doi.org/10.1021/acs.bioconjchem.6b00575.
- (67) Battocchio, C.; Porcaro, F.; Mukherjee, S.; Magnano, E.; Nappini, S.; Fratoddi, I.; Quintiliani, M.; Russo, M. V.; Polzonetti, G. Gold Nanoparticles Stabilized with Aromatic Thiols: Interaction at the Molecule–Metal Interface and Ligand Arrangement in the Molecular Shell Investigated by SR-XPS and NEXAFS. *J. Phys. Chem. C* **2014**, *118* (15), 8159–8168. https://doi.org/10.1021/jp4126057.
- (68) Colangelo, E.; Comenge, J.; Paramelle, D.; Volk, M.; Chen, Q.; Lévy, R. Characterizing Self-Assembled Monolayers on Gold Nanoparticles. *Bioconjugate Chem.* **2017**, 28 (1), 11–22. https://doi.org/10.1021/acs.bioconjchem.6b00587.
- (69) Handali, P. R.; Webb, L. J. Quantifying Bound Proteins on Pegylated Gold Nanoparticles Using Infrared Spectroscopy. *ACS Appl. Bio Mater.* **2024**, *7* (4), 2338–2345. https://doi.org/10.1021/acsabm.4c00012.
- (70) Kohlmann, O.; Steinmetz, W. E.; Mao, X.-A.; Wuelfing, W. P.; Templeton, A. C.; Murray, R. W.; Johnson, C. S. NMR Diffusion, Relaxation, and Spectroscopic Studies of Water Soluble, Monolayer-Protected Gold Nanoclusters. *J. Phys. Chem. B* **2001**, *105* (37), 8801–8809. https://doi.org/10.1021/jp0111230.

- (71) Hostetler, M. J.; Wingate, J. E.; Zhong, C.-J.; Harris, J. E.; Vachet, R. W.; Clark, M. R.; Londono, J. D.; Green, S. J.; Stokes, J. J.; Wignall, G. D.; Glish, G. L.; Porter, M. D.; Evans, N. D.; Murray, R. W. Alkanethiolate Gold Cluster Molecules with Core Diameters from 1.5 to 5.2 Nm: Core and Monolayer Properties as a Function of Core Size. *Langmuir* **1998**, *14* (1), 17–30. https://doi.org/10.1021/la970588w.
- (72) Badia, A.; Singh, S.; Demers, L.; Cuccia, L.; Brown, G. R.; Lennox, R. B. Self-Assembled Monolayers on Gold Nanoparticles. *Chemistry A European Journal* **1996**, 2 (3), 359–363. https://doi.org/10.1002/chem.19960020318.
- (73) Vericat, C.; E. Vela, M.; Corthey, G.; Pensa, E.; Cortés, E.; H. Fonticelli, M.; Ibañez, F.; E. Benitez, G.; Carro, P.; C. Salvarezza, R. Self-Assembled Monolayers of Thiolates on Metals: A Review Article on Sulfur-Metal Chemistry and Surface Structures. *RSC Advances* **2014**, *4* (53), 27730–27754. https://doi.org/10.1039/C4RA04659E.
- (74) Borsley, S.; Edwards, W.; Mati, I. K.; Poss, G.; Diez-Castellnou, M.; Marro, N.; Kay, E. R. A General One-Step Synthesis of Alkanethiyl-Stabilized Gold Nanoparticles with Control over Core Size and Monolayer Functionality. *Chem. Mater.* **2023**, *35* (15), 6168–6177. https://doi.org/10.1021/acs.chemmater.3c01506.
- (75) Cadoni, E.; Rosa-Gastaldo, D.; Manicardi, A.; Mancin, F.; Madder, A. Exploiting Double Exchange Diels-Alder Cycloadditions for Immobilization of Peptide Nucleic Acids on Gold Nanoparticles. *Front. Chem.* **2020**, *8*. https://doi.org/10.3389/fchem.2020.00004.
- (76) Sardar, R.; Shumaker-Parry, J. S. Asymmetrically Functionalized Gold Nanoparticles Organized in One-Dimensional Chains. *Nano Lett.* **2008**, 8 (2), 731–736. https://doi.org/10.1021/nl073154m.
- (77) Oh, E.; Susumu, K.; Goswami, R.; Mattoussi, H. One-Phase Synthesis of Water-Soluble Gold Nanoparticles with Control over Size and Surface Functionalities. *Langmuir* **2010**, *26* (10), 7604–7613. https://doi.org/10.1021/la904438s.
- (78) Hostetler, M. J.; Templeton, A. C.; Murray, R. W. Dynamics of Place-Exchange Reactions on Monolayer-Protected Gold Cluster Molecules. *Langmuir* **1999**, *15* (11), 3782–3789. https://doi.org/10.1021/la981598f.
- (79) Woehrle, G. H.; Brown, L. O.; Hutchison, J. E. Thiol-Functionalized, 1.5-Nm Gold Nanoparticles through Ligand Exchange Reactions: Scope and Mechanism of Ligand Exchange. *J. Am. Chem. Soc.* **2005**, *127* (7), 2172–2183. https://doi.org/10.1021/ja0457718.
- (80) Harrison, E.; Hamilton, J. W. J.; Macias-Montero, M.; Dixon, D. Peptide Functionalized Gold Nanoparticles: The Influence of pH on Binding Efficiency. *Nanotechnology* **2017**, *28* (29), 295602. https://doi.org/10.1088/1361-6528/aa77ac.
- (81) Corma, A.; Garcia, H. Supported Gold Nanoparticles as Catalysts for Organic Reactions. *Chemical Society Reviews* **2008**, *37* (9), 2096–2126. https://doi.org/10.1039/B707314N.
- (82) Templeton, A. C.; Hostetler, M. J.; Kraft, C. T.; Murray, R. W. Reactivity of Monolayer-Protected Gold Cluster Molecules: Steric Effects. *J. Am. Chem. Soc.* **1998**, *120* (8), 1906–1911. https://doi.org/10.1021/ja973863+.
- (83) Taiariol, L.; Chaix, C.; Farre, C.; Moreau, E. Click and Bioorthogonal Chemistry: The Future of Active Targeting of Nanoparticles for Nanomedicines? *Chem. Rev.* **2022**, *122* (1), 340–384. https://doi.org/10.1021/acs.chemrev.1c00484.
- (84) Finetti, C.; Sola, L.; Pezzullo, M.; Prosperi, D.; Colombo, M.; Riva, B.; Avvakumova, S.; Morasso, C.; Picciolini, S.; Chiari, M. Click Chemistry Immobilization of Antibodies on Polymer Coated Gold Nanoparticles. *Langmuir* **2016**, *32* (29), 7435–7441. https://doi.org/10.1021/acs.langmuir.6b01142.

- (85) C. Jewett, J.; R. Bertozzi, C. Cu-Free Click Cycloaddition Reactions in Chemical Biology. *Chemical Society Reviews* **2010**, *39* (4), 1272–1279. https://doi.org/10.1039/B901970G.
- (86) Gobbo, P.; Mossman, Z.; Nazemi, A.; Niaux, A.; C. Biesinger, M.; R. Gillies, E.; S. Workentin, M. Versatile Strained Alkyne Modified Water-Soluble AuNPs for Interfacial Strain Promoted Azide–Alkyne Cycloaddition (I-SPAAC). *Journal of Materials Chemistry B* **2014**, 2 (13), 1764–1769. https://doi.org/10.1039/C3TB21799J.
- (87) L. Oliveira, B.; Guo, Z.; L. Bernardes, G. J. Inverse Electron Demand Diels—Alder Reactions in Chemical Biology. *Chemical Society Reviews* **2017**, *46* (16), 4895–4950. https://doi.org/10.1039/C7CS00184C.
- (88) Idiago-López, J.; Moreno-Antolín, E.; Fuente, J. M. de la; M. Fratila, R. Nanoparticles and Bioorthogonal Chemistry Joining Forces for Improved Biomedical Applications. *Nanoscale Advances* **2021**, *3* (5), 1261–1292. https://doi.org/10.1039/D0NA00873G.
- (89) Anderson, E. D.; Boger, D. L. Inverse Electron Demand Diels–Alder Reactions of 1,2,3-Triazines: Pronounced Substituent Effects on Reactivity and Cycloaddition Scope. *J. Am. Chem. Soc.* **2011**, *133* (31), 12285–12292. https://doi.org/10.1021/ja204856a.
- (90) Zhu, J.; Chin, J.; Wängler, C.; Wängler, B.; Lennox, R. B.; Schirrmacher, R. Rapid 18F-Labeling and Loading of PEGylated Gold Nanoparticles for in Vivo Applications. *Bioconjugate Chem.* **2014**, 25 (6), 1143–1150. https://doi.org/10.1021/bc5001593.
- (91) D, B.; Ag, K. Preparation of Peptide-Functionalized Gold Nanoparticles Using One Pot EDC/Sulfo-NHS Coupling. *Langmuir*: the ACS journal of surfaces and colloids **2011**, 27 (16). https://doi.org/10.1021/la2022177.
- (92) S. Takale, B.; Bao, M.; Yamamoto, Y. Gold Nanoparticle (AuNPs) and Gold Nanopore (AuNPore) Catalysts in Organic Synthesis. *Organic & Biomolecular Chemistry* **2014**, *12* (13), 2005–2027. https://doi.org/10.1039/C3OB42207K.
- (93) Corma, A.; Garcia, H. Supported Gold Nanoparticles as Catalysts for Organic Reactions. *Chemical Society Reviews* **2008**, *37* (9), 2096–2126. https://doi.org/10.1039/B707314N.
- (94) Perera, M.; A. Wijenayaka, L.; Siriwardana, K.; Dahanayake, D.; Silva, K. M. N. de. Gold Nanoparticle Decorated Titania for Sustainable Environmental Remediation: Green Synthesis, Enhanced Surface Adsorption and Synergistic Photocatalysis. *RSC Advances* **2020**, *10* (49), 29594–29602. https://doi.org/10.1039/D0RA05607C.
- (95) Wang, C.; Astruc, D. Nanogold Plasmonic Photocatalysis for Organic Synthesis and Clean Energy Conversion. *Chemical Society Reviews* **2014**, *43* (20), 7188–7216. https://doi.org/10.1039/C4CS00145A.
- (96) Wu, Y.; Ali, M. R. K.; Chen, K.; Fang, N.; El-Sayed, M. A. Gold Nanoparticles in Biological Optical Imaging. *Nano Today* **2019**, 24, 120–140. https://doi.org/10.1016/j.nantod.2018.12.006.
- (97) Murphy, C. J.; Gole, A. M.; Stone, J. W.; Sisco, P. N.; Alkilany, A. M.; Goldsmith, E. C.; Baxter, S. C. Gold Nanoparticles in Biology: Beyond Toxicity to Cellular Imaging. *Acc. Chem. Res.* **2008**, *41* (12), 1721–1730. https://doi.org/10.1021/ar800035u.
- (98) Mieszawska, A. J.; Mulder, W. J. M.; Fayad, Z. A.; Cormode, D. P. Multifunctional Gold Nanoparticles for Diagnosis and Therapy of Disease. *Mol. Pharmaceutics* **2013**, *10* (3), 831–847. https://doi.org/10.1021/mp3005885.
- (99) Aldewachi, H.; Chalati, T.; N. Woodroofe, M.; Bricklebank, N.; Sharrack, B.; Gardiner, P. Gold Nanoparticle-Based Colorimetric Biosensors. *Nanoscale* **2018**, *10* (1), 18–33. https://doi.org/10.1039/C7NR06367A.

- (100) Zhang, J.; Mou, L.; Jiang, X. Surface Chemistry of Gold Nanoparticles for Health-Related Applications. *Chemical Science* **2020**, *11* (4), 923–936. https://doi.org/10.1039/C9SC06497D.
- (101) Fratoddi, I.; Venditti, I.; Cametti, C.; V. Russo, M. Gold Nanoparticles and Gold Nanoparticle-Conjugates for Delivery of Therapeutic Molecules. Progress and Challenges. *Journal of Materials Chemistry B* **2014**, 2 (27), 4204–4220. https://doi.org/10.1039/C4TB00383G.
- (102) Patra, C. R.; Bhattacharya, R.; Wang, E.; Katarya, A.; Lau, J. S.; Dutta, S.; Muders, M.; Wang, S.; Buhrow, S. A.; Safgren, S. L.; Yaszemski, M. J.; Reid, J. M.; Ames, M. M.; Mukherjee, P.; Mukhopadhyay, D. Targeted Delivery of Gemcitabine to Pancreatic Adenocarcinoma Using Cetuximab as a Targeting Agent. *Cancer Research* **2008**, *68* (6), 1970–1978. https://doi.org/10.1158/0008-5472.CAN-07-6102.
- (103) Spadavecchia, J.; Movia, D.; Moore, C.; Maguire, C. M.; Moustaoui, H.; Casale, S.; Volkov, Y.; Prina-Mello, A. Targeted Polyethylene Glycol Gold Nanoparticles for the Treatment of Pancreatic Cancer: From Synthesis to Proof-of-Concept in Vitro Studies. *International Journal of Nanomedicine* **2016**, *11*, 791–822. https://doi.org/10.2147/IJN.S97476.
- (104) Das, A.; Soehnlen, E.; Woods, S.; Hegde, R.; Henry, A.; Gericke, A.; Basu, S. VEGFR-2 Targeted Cellular Delivery of Doxorubicin by Gold Nanoparticles for Potential Antiangiogenic Therapy. *J Nanopart Res* **2011**, *13* (12), 6283–6290. https://doi.org/10.1007/s11051-011-0300-8.
- (105) Tummala, S.; Kumar, M. N. S.; Pindiprolu, S. K. Improved Anti-Tumor Activity of Oxaliplatin by Encapsulating in Anti-DR5 Targeted Gold Nanoparticles. *Drug Delivery* **2016**, 23 (9), 3505–3519. https://doi.org/10.1080/10717544.2016.1199606.
- (106) Tan, H.; Hou, N.; Liu, Y.; Liu, B.; Cao, W.; Zheng, D.; Li, W.; Liu, Y.; Xu, B.; Wang, Z.; Cui, D. CD133 Antibody Targeted Delivery of Gold Nanostars Loading IR820 and Docetaxel for Multimodal Imaging and Near-Infrared Photodynamic/Photothermal/Chemotherapy against Castration Resistant Prostate Cancer. *Nanomedicine: Nanotechnology, Biology and Medicine* **2020**, 27, 102192. https://doi.org/10.1016/j.nano.2020.102192.
- (107) Dreaden, E. C.; Mwakwari, S. C.; Sodji, Q. H.; Oyelere, A. K.; El-Sayed, M. A. Tamoxifen–Poly(Ethylene Glycol)–Thiol Gold Nanoparticle Conjugates: Enhanced Potency and Selective Delivery for Breast Cancer Treatment. *Bioconjugate Chem.* **2009**, *20* (12), 2247–2253. https://doi.org/10.1021/bc9002212.
- (108) Du, Y.; Xia, L.; Jo, A.; Davis, R. M.; Bissel, P.; Ehrich, M. F.; Kingston, D. G. I. Synthesis and Evaluation of Doxorubicin-Loaded Gold Nanoparticles for Tumor-Targeted Drug Delivery. *Bioconjugate Chem.* **2018**, 29 (2), 420–430. https://doi.org/10.1021/acs.bioconjchem.7b00756.
- (109) Zhang, X.-Q.; Xu, X.; Lam, R.; Giljohann, D.; Ho, D.; Mirkin, C. A. Strategy for Increasing Drug Solubility and Efficacy through Covalent Attachment to Polyvalent DNA–Nanoparticle Conjugates. *ACS Nano* **2011**, *5* (9), 6962–6970. https://doi.org/10.1021/nn201446c.
- (110) Bouché, M.; Hsu, J. C.; Dong, Y. C.; Kim, J.; Taing, K.; Cormode, D. P. Recent Advances in Molecular Imaging with Gold Nanoparticles. *Bioconjugate Chem.* **2020**, *31* (2), 303–314. https://doi.org/10.1021/acs.bioconjchem.9b00669.
- (111) Mitchell, M. J.; Billingsley, M. M.; Haley, R. M.; Wechsler, M. E.; Peppas, N. A.; Langer, R. Engineering Precision Nanoparticles for Drug Delivery. *Nat Rev Drug Discov* **2021**, *20* (2), 101–124. https://doi.org/10.1038/s41573-020-0090-8.

- (112) Paul, S.; Mukherjee, S.; Banerjee, P. Recent Advancement in Nanomaterial-Encapsulated Drug Delivery Vehicles for Combating Cancer, COVID-19, and HIV-like Chronic Diseases. *Materials Advances* **2023**, *4* (9), 2042–2061. https://doi.org/10.1039/D2MA01075E.
- (113) Huang, H.; Liu, R.; Yang, J.; Dai, J.; Fan, S.; Pi, J.; Wei, Y.; Guo, X. Gold Nanoparticles: Construction for Drug Delivery and Application in Cancer Immunotherapy. *Pharmaceutics* **2023**, *15* (7), 1868. https://doi.org/10.3390/pharmaceutics15071868.
- (114) Cai, K.; Zhang, W.; Zhang, J.; Li, H.; Han, H.; Zhai, T. Design of Gold Hollow Nanorods with Controllable Aspect Ratio for Multimodal Imaging and Combined Chemo-Photothermal Therapy in the Second Near-Infrared Window. *ACS Appl. Mater. Interfaces* **2018**, *10* (43), 36703–36710. https://doi.org/10.1021/acsami.8b12758.
- (115) Paściak, A.; Marin, R.; Abiven, L.; Pilch-Wróbel, A.; Misiak, M.; Xu, W.; Prorok, K.; Bezkrovnyi, O.; Marciniak, Ł.; Chanéac, C.; Gazeau, F.; Bazzi, R.; Roux, S.; Viana, B.; Lehto, V.-P.; Jaque, D.; Bednarkiewicz, A. Quantitative Comparison of the Light-to-Heat Conversion Efficiency in Nanomaterials Suitable for Photothermal Therapy. *ACS Appl. Mater. Interfaces* **2022**, *14* (29), 33555–33566. https://doi.org/10.1021/acsami.2c08013.
- (116) Mackey, M. A.; Ali, M. R. K.; Austin, L. A.; Near, R. D.; El-Sayed, M. A. The Most Effective Gold Nanorod Size for Plasmonic Photothermal Therapy: Theory and In Vitro Experiments. *J. Phys. Chem. B* **2014**, *118* (5), 1319–1326. https://doi.org/10.1021/jp409298f.
- (117) Pan, S.; Xing, H.; Fu, X.; Yu, H.; Yang, Z.; Yang, Y.; Sun, W. The Effect of Photothermal Therapy on Osteosarcoma With Polyacrylic Acid—Coated Gold Nanorods. *Dose-Response* **2018**, *16* (3), 1559325818789841. https://doi.org/10.1177/1559325818789841.
- (118) Park, J.-H.; von Maltzahn, G.; Ong, L. L.; Centrone, A.; Hatton, T. A.; Ruoslahti, E.; Bhatia, S. N.; Sailor, M. J. Cooperative Nanoparticles for Tumor Detection and Photothermally Triggered Drug Delivery. *Adv Mater* **2010**, *22* (8), 880–885. https://doi.org/10.1002/adma.200902895.
- (119) Fan, L.; Wang, W.; Wang, Z.; Zhao, M. Gold Nanoparticles Enhance Antibody Effect through Direct Cancer Cell Cytotoxicity by Differential Regulation of Phagocytosis. *Nat Commun* **2021**, *12* (1), 6371. https://doi.org/10.1038/s41467-021-26694-x.
- (120) xie, X.; Li, B.; Wang, J.; Zhan, C.; Huang, Y.; Zeng, F.; Wu, S. Tetrazine-Mediated Bioorthogonal System for Prodrug Activation, Photothermal Therapy, and Optoacoustic Imaging. *ACS Appl. Mater. Interfaces* **2019**, *11* (45), 41875–41888. https://doi.org/10.1021/acsami.9b13374.
- (121) Krukiewicz, K.; Zak, J. K. Biomaterial-Based Regional Chemotherapy: Local Anticancer Drug Delivery to Enhance Chemotherapy and Minimize Its Side-Effects. *Materials Science and Engineering: C* **2016**, 62, 927–942. https://doi.org/10.1016/j.msec.2016.01.063.
- (122) Kamaly, N.; Yameen, B.; Wu, J.; Farokhzad, O. C. Degradable Controlled-Release Polymers and Polymeric Nanoparticles: Mechanisms of Controlling Drug Release. *Chem. Rev.* **2016**, *116* (4), 2602–2663. https://doi.org/10.1021/acs.chemrev.5b00346.
- (123) Dubey, R. Controlled-Release Injectable Microemulsions: Recent Advances and Potential Opportunities. *Expert Opinion on Drug Delivery* **2014**, *11* (2), 159–173. https://doi.org/10.1517/17425247.2014.870151.
- (124) Yan, C.; Kim, S.-R. Microencapsulation for Pharmaceutical Applications: A Review. *ACS Appl. Bio Mater.* **2024**, *7* (2), 692–710. https://doi.org/10.1021/acsabm.3c00776.
- (125) Shirakura, T.; Kelson, T. J.; Ray, A.; Malyarenko, A. E.; Kopelman, R. Hydrogel Nanoparticles with Thermally Controlled Drug Release. *ACS Macro Lett.* **2014**, *3* (7), 602–606. https://doi.org/10.1021/mz500231e.

- (126) Verma, R. K.; Mishra, B.; Garg, S. Osmotically Controlled Oral Drug Delivery\*. *Drug Development and Industrial Pharmacy* **2000**, *26* (7), 695–708. https://doi.org/10.1081/DDC-100101287.
- (127) Martin, C.; De Baerdemaeker, A.; Poelaert, J.; Madder, A.; Hoogenboom, R.; Ballet, S. Controlled-Release of Opioids for Improved Pain Management. *Materials Today* **2016**, *19* (9), 491–502. https://doi.org/10.1016/j.mattod.2016.01.016.
- (128) Yang, Y.; Wang, Y.; Zhu, M.; Chen, Y.; Xiao, Y.; Shen, Y.; Xie, A. RGO/AuNR/HA-5FU Nanocomposite with Multi-Stage Release Behavior and Efficient Antitumor Activity for Synergistic Therapy. *Biomaterials Science* **2017**, *5* (5), 990–1000. https://doi.org/10.1039/C7BM00007C.
- (129) Gao, W.; Chan, J. M.; Farokhzad, O. C. pH-Responsive Nanoparticles for Drug Delivery. *Mol. Pharmaceutics* **2010**, *7* (6), 1913–1920. https://doi.org/10.1021/mp100253e.
- (130) Zhuo, S.; Zhang, F.; Yu, J.; Zhang, X.; Yang, G.; Liu, X. pH-Sensitive Biomaterials for Drug Delivery. *Molecules* **2020**, *25* (23), 5649. https://doi.org/10.3390/molecules25235649.
- (131) Aryal, S.; J. Grailer, J.; Pilla, S.; A. Steeber, D.; Gong, S. Doxorubicin Conjugated Gold Nanoparticles as Water -Soluble and pH-Responsive Anticancer Drug Nanocarriers. *Journal of Materials Chemistry* **2009**, *19* (42), 7879–7884. https://doi.org/10.1039/B914071A.
- (132) Wang, F.; Wang, Y.-C.; Dou, S.; Xiong, M.-H.; Sun, T.-M.; Wang, J. Doxorubicin-Tethered Responsive Gold Nanoparticles Facilitate Intracellular Drug Delivery for Overcoming Multidrug Resistance in Cancer Cells. *ACS Nano* **2011**, *5* (5), 3679–3692. https://doi.org/10.1021/nn200007z.
- (133) Cui, T.; Liang, J.-J.; Chen, H.; Geng, D.-D.; Jiao, L.; Yang, J.-Y.; Qian, H.; Zhang, C.; Ding, Y. Performance of Doxorubicin-Conjugated Gold Nanoparticles: Regulation of Drug Location. *ACS Appl. Mater. Interfaces* **2017**, *9* (10), 8569–8580. https://doi.org/10.1021/acsami.6b16669.
- (134) Perillo, B.; Di Donato, M.; Pezone, A.; Di Zazzo, E.; Giovannelli, P.; Galasso, G.; Castoria, G.; Migliaccio, A. ROS in Cancer Therapy: The Bright Side of the Moon. *Exp Mol Med* **2020**, 52 (2), 192–203. https://doi.org/10.1038/s12276-020-0384-2.
- (135) Pramanik, A. K.; Siddikuzzaman; Palanimuthu, D.; Somasundaram, K.; Samuelson, A. G. Biotin Decorated Gold Nanoparticles for Targeted Delivery of a Smart-Linked Anticancer Active Copper Complex: In Vitro and In Vivo Studies. *Bioconjugate Chem.* **2016**, 27 (12), 2874–2885. https://doi.org/10.1021/acs.bioconjchem.6b00537.
- (136) Zhang, Q.; Gong, Y.; Guo, X.; Zhang, P.; Ding, C. Multifunctional Gold Nanoparticle-Based Fluorescence Resonance Energy-Transfer Probe for Target Drug Delivery and Cell Fluorescence Imaging. *ACS Appl. Mater. Interfaces* **2018**, *10* (41), 34840–34848. https://doi.org/10.1021/acsami.8b12897.
- (137) Lou, J.; Duan, H.; Qin, Q.; Teng, Z.; Gan, F.; Zhou, X.; Zhou, X. Advances in Oral Drug Delivery Systems: Challenges and Opportunities. *Pharmaceutics* **2023**, *15* (2), 484. https://doi.org/10.3390/pharmaceutics15020484.
- (138) Yan, X.; Li, K.; Xie, T.-Q.; Jin, X.-K.; Zhang, C.; Li, Q.-R.; Feng, J.; Liu, C.-J.; Zhang, X.-Z. Bioorthogonal "Click and Release" Reaction-Triggered Aggregation of Gold Nanoparticles Combined with Released Lonidamine for Enhanced Cancer Photothermal Therapy. *Angewandte Chemie International Edition* **2024**, *63* (13), e202318539. https://doi.org/10.1002/anie.202318539.

(139) Luo, Y.-L.; Shiao, Y.-S.; Huang, Y.-F. Release of Photoactivatable Drugs from Plasmonic Nanoparticles for Targeted Cancer Therapy. *ACS Nano* **2011**, *5* (10), 7796–7804. https://doi.org/10.1021/nn201592s.

# Chapter 2. Design and Synthesis of a Thermal Release Linker Based on a Retro-Diels-Alder Reaction

## 2.1 Preface

This chapter introduces a novel thermal release linker based on a retro Diels-Alder (rDA) reaction, an eventual cornerstone for the development of controlled drug delivery systems. The focus is on the synthesis of a tetrahydrophthalimide linker, assessing its kinetic properties, and establishing its potential for application in controlled release. By exploring the stability and reactivity of *endo* and *exo* adducts under different temperatures, this Chapter establishes the foundational knowledge required for a nanoparticle-based therapeutic system, emphasizing access to a controlled release.

#### 2.2 Abstract

This Chapter introduces the design of a thermal release linker based on a rDA reaction between maleimide and furfuryl alcohol. A tetrahydrophthalimide linker was synthesized and its kinetic properties were studied using <sup>1</sup>H NMR spectroscopy at various temperatures (37 °C – 50 °C for the *endo* linker, and 55 °C – 90 °C for the *exo* linker). The rDA reaction followed first order kinetics. The *endo* adducts have a half-life of 38 hours at 37 °C whereas the *exo* adducts have a half-life of 131.6 hours at 55 °C or, by extrapolation, 810 hours at 37 °C. These results demonstrate that the differential thermal stabilities of the *endo* and *exo* adducts can provide the basis of an efficient system for controlled release drug delivery under physiological temperatures.

## 2.3 Introduction

The development of smart and controllable molecular linkers has attracted attention for application in drug delivery, <sup>1</sup> materials science, <sup>2</sup> and bioconjugation. <sup>3,4</sup> The linkers in question are often associated with the attachment and subsequent release of molecular entities, often referred to as payloads or cargos under precise release conditions. Such systems find application in sectors such as the pharmaceutical, <sup>5,6</sup> agriculture, <sup>7</sup> cosmetic, <sup>8</sup> and food industries. <sup>9</sup> Controlled release has particularly attracted attention in drug delivery systems, with the intention to optimize efficacy and minimize toxicity of therapeutic agents by controlling the rate, duration, and location of release. <sup>10</sup> Conventional drug delivery methods, such as tablets and capsules, can suffer from poor bioavailability and inconsistent plasma drug levels, necessitating the development of more complex approaches to delivery, where controlled drug delivery systems offer promising solutions to those challenges. <sup>4</sup> Nanocarriers, including lipid, polymeric, and metallic nanomaterials, have thus emerged as versatile platforms for controlled drug delivery. <sup>11</sup> Among these, gold

nanomaterials are particularly prominent due to their functional flexibility and compatibility with surface modification techniques. Early gold nanoparticle (AuNP) - based delivery strategies have typically relied on mechanisms such as noncovalent hydrophobic entrapment, where drugs were encapsulated within polymeric surfactants on AuNPs to protect them from degradation while enabling release *via* diffusion processes. Kim et al. demonstrated how hydrophobic dyes and drugs could be entrapped in a hydrophobic pocket of AuNPs and released into the cell by membrane-mediated diffusion without uptake of the carrier nanoparticles. However, the noncovalent interactions governing drug encapsulation often face stability issues, leading to possible premature drug release during storage or circulation. On the other hand, the stability of the Au-S bond on the surface of thiol-protected AuNPs makes them suitable for further modification, prompting research into the covalent linkage of drug molecules with thiol-modified AuNPs. However, the non-

The approach reported here involves the development of reactive linkers that can enable precise control over bond-forming and bond-breaking reactions. Various strategies have been studied for the release of molecular cargos, including pH stimuli, <sup>15</sup> click and release reactions, <sup>16</sup> bioconjugation methods <sup>17</sup>, and photo-triggered release. <sup>18</sup> For example, a pH-sensitive hydrazone bond was designed and used to modify AuNPs with the chemotherapy molecule, doxorubicin. *In vitro* results suggested that use of this hydrazone as the linker leads to a relatively rapid release of the drug at pH 5.5 (i.e. a cancer cell environment), while almost no release was observed over 20 hours at a normal cell environment) of pH 7.4. <sup>15</sup> "Click and release" reactions, involving for example, iminosydnone-lonidamine (ImLND) as a prodrug and dibenzocyclooctyne as a trigger, have been utilized in AuNP-based drug delivery systems, leading to the release of the chemotherapy drug, lonidamine. Through a [3+2] cycloaddition reaction, photothermally active nanoaggregates of AuNPs were formed. <sup>16</sup> Similarly, bioorthogonal bond cleavage reactions have

been extensively studied due to their compatibility with various biological environments, offering significant potential for enhancing the safety of drug delivery systems. In this regard, Luo et al. reported a controlled release system involving water-soluble 5 nm AuNPs via bioorthogonal Staudinger-Bertozzi ligation. A Rhodamine B dye derivative was attached to a thiol which serves as an AuNP ligand. The release was monitored using fluorescence emission once the azide reacted with triphenylphosphine on the thiolated ligand. 19 Xin et al. developed a system based on a tetrazine-mediated bioorthogonal reaction and tested its application to tumor inhibition in mice. The trigger was designed by immobilizing PEGylated tetrazine on the gold nanorods (AuNRs), and the bioorthogonal prodrug camptothecin was synthesized by attaching the drug with vinyl ether, followed by encapsulating it in phospholipid liposomes. This report demonstrated that the nanoscale liposomal prodrug and AuNR-tetrazine accumulate in the tumor region and then undergo a bioorthogonal reaction to release the active camptothecin.<sup>20</sup> Photocleavable systems have been explored by a number of researchers as they offer several advantages over other modes of cleavage, primarily due to the ease of handling and precise control of the timing and location of drug release. For example, Qiao et al. developed micelle-drug conjugates where the anticancer drug 5-fluorouracil (5-FU) was covalently bound to coumarin under UV irradiation at wavelengths > 310 nm. In vitro drug release experiments demonstrate release of the anticancer drug 5-FU from the micelle-drug conjugates under irradiation at 254 nm. <sup>21</sup> However, each of these approaches lack the specificity or stability needed for adoption in therapeutic protocols, requiring the need for the development of efficient and stable molecular delivery systems that can be precisely controlled at the molecular level. More specifically, pH variations in biological systems can lead to an incomplete control of the quantity of drug released. In the case of chemically-triggered release that involves two components, it is important that the defined time delay between each component

addition be synchronized. Photoinduced release suffers from tissue penetration issues and potential phototoxicity, leading to cell damage or undesired side effects in surrounding tissues when using high-intensity light sources or prolonged exposure times.<sup>22</sup>

The Diels-Alder reaction has attracted attention due to its mild reaction conditions and the of problematic metal catalysts.  $^{23}$  Moreover, D-A reactions are capable of undergoing retro-DA reactions under thermal conditions, facilitating controlled release. For example, Bakhtiari et al. developed a controlled release system based on retro- DA reactions where a fluorescein dye was anchored onto the surface of  $200 \pm 10$  nm silica shell -gold core nanoparticles using a hydrophobic DA linker. The fluorescence emission of the fluorescein was efficiently quenched by the gold layer of the nanoparticles when it was conjugated to the core-shell material. Illumination at 532 nm resulted in an increase in the observed fluorescence intensity as the fluorescence is no longer quenched when it is released from proximity to the gold.  $^{24}$  The success of this design suggests potential for its application to controlled release of therapeutic agents. However, the system as described has limitations including the use of large size nanoparticles and the lack of precise control over the amount of cargo released. To address some of these limitations, a thermally triggered release system based on a rDA reaction is explored in this work.

## 2.4 Results and Discussion

## 2.4.1 Design of a Thermally Releasable Linker

Previous investigations in our research group have focused on the synthesis of watersoluble, maleimide-terminated AuNPs which use furan to protect the maleimide from undesired Michael addition side reactions with the AuNP thiol ligands. The *endo* form of the furan-protected maleimide undergoes a retro-DA cleavage reaction under thermally mild conditions without affecting the properties of the AuNPs can the protective ligands that remain on their surfaces.

The following criteria were applied to the design of the linker structure:

- The stability of a linker under various synthetic conditions should enable further modification
- The linker's length should be compatible with the length of the protecting surfactant ligands on the gold surface
- The linker should be capable of being incorporated onto surfaces to expand its application to other systems in materials science and nanotechnology and
- The linker should be synthesized from relatively accessible materials to ensure its scalability and reproducibility

By addressing these considerations, the utility of a 3,6-endoxo- $\Delta^4$ -tetrahydrophthalimide linker was assessed (Figure 2.1) where a triethylene glycol was used to enhance the water-solubility of the linker system. The length of the linker was sufficiently long for the terminal hydroxyl group to be effective in further coupling reactions, while being short enough that the fluorophore emission is quenched by the adjacent AuNP. The hydroxyl group on the linker facilitates the attachment of a desired molecular entity *via* Steglich esterification. Finally, a terminal thiol anchors the linker to the Au surface through an Au-S bond. Overall, this design ensures an optimization of the water-solubility, loading capability, and surface-anchoring ability of the linker.

Figure 2.1: Illustration of release of cargo via a thermal-mediated rDA reaction through the designed tetrahydrophthalimide linkage.

## 2.4.2 Synthesis of a Thermally Releasable Linker

The synthesis of the designed linker (Scheme 2.1) starts with condensing malic anhydride  $\mathbf{1}$  with glycine to form carboxyalkyl maleimide  $\mathbf{2}$ . Furan was used to protect the double bond via a [4+2] cycloaddition to prevent Michael addition in the next step. Furan-protected maleimide  $\mathbf{3}$  was subjected to an esterification reaction with mono-bromo substituted triethylene glycol  $\mathbf{4}$  using DCC and DMAP as coupling reagents. Intermediate  $\mathbf{5}$  was then deprotected by heating, followed by a DA reaction with an excess of furfuryl alcohol as the diene, at room temperature, to form the DA adduct as a mixture of *endo* and *exo* products (*endo*: exo = 3:1). Pure *endo* adduct  $\mathbf{7}$  was separated by liquid column chromatography. Finally, the *endo* adduct  $\mathbf{7}$  was converted to thiol  $\mathbf{8}$  after treated with bis(trimethylsilyl) sulfide in the presence of tetra-n-butylammonium fluoride. The final product was stable for months under Argon at  $-20\,^{\circ}$ C.

Scheme 2.1: The synthesis of the tetrahydrophthalimide linker **8**.

## 2.4.3 Kinetic Properties of the Thermally Releasable Linker

The kinetics of the rDA reaction of the tetrahydrophthalimide linkage were studied. The reaction was monitored in CDCl<sub>3</sub> by <sup>1</sup>H NMR spectroscopy. From Figure 2.2, the rDA reaction of 7 resulted in the formation of maleimide (evidenced by a singlet at 6.83 ppm) and furfuryl alcohol (evidenced by a doublet of doublets at 6.25 ppm, a doublet at 6.32 ppm, and a doublet at 4.59 ppm). Spectral analysis revealed a decrease in the signal at 5.39 ppm (proton 3 in 7) followed by the appearance of a singlet at 6.83 ppm due to the recovery of maleimide (Figure 2.2). The rate of the rDA reaction of 7 was studied at five different temperatures, ranging from 37 °C to 50 °C. The kinetic data provided a best fit to a first order kinetics rate law (Figure 2.4), where

$$\ln\left[\frac{A0}{A}\right] = kt$$
(1)

where  $A_0$  represents the concentration of the starting material (calculated by the sum of integration of 7 and maleimide). To analyze the rate of consumption of 7, the integration value of maleimide was held constant at 2. The reaction rate constant was plotted as a function of temperature, from

37 °C to 50 °C. The half-lives for both the *exo-* and *endo-*products were calculated at different temperatures *via* the corresponding rate constants determined (Table 2.1). These half-lives provided preliminary insight into the stability of the designed tetrahydrophthalimide linkage and its potential in controlled release systems. Similarly, the stability of the *exo-*isomer of 7 was also studied in toluene- $d_8$ , but over a greater temperature range (55 °C – 90 °C) in order to achieve measurable extents of conversion (Figure 2.3).

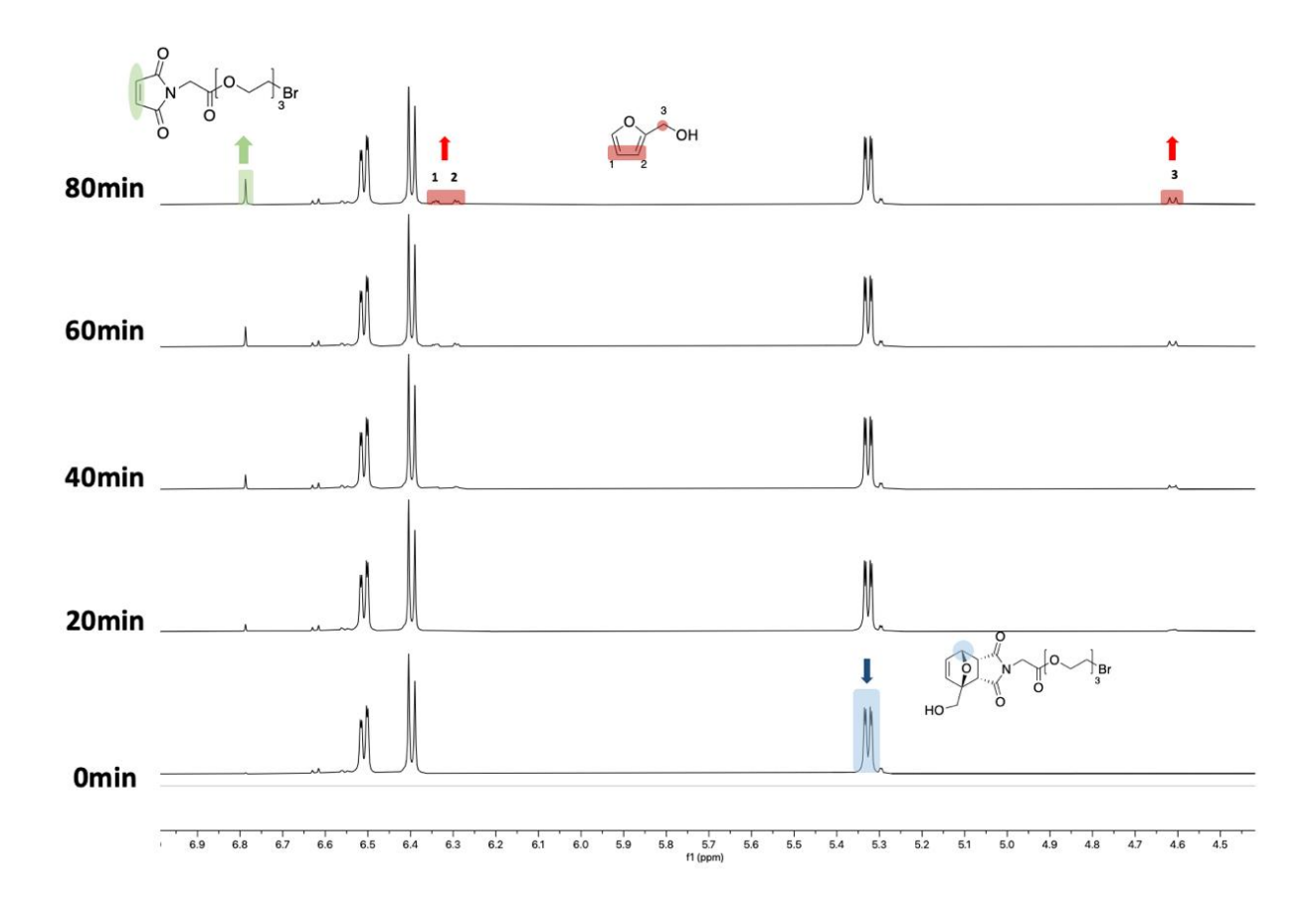


Figure 2.2: Monitoring the retro Diels-Alder reaction of endo-compound 7 at different times at 45 °C, by <sup>1</sup>H NMR.

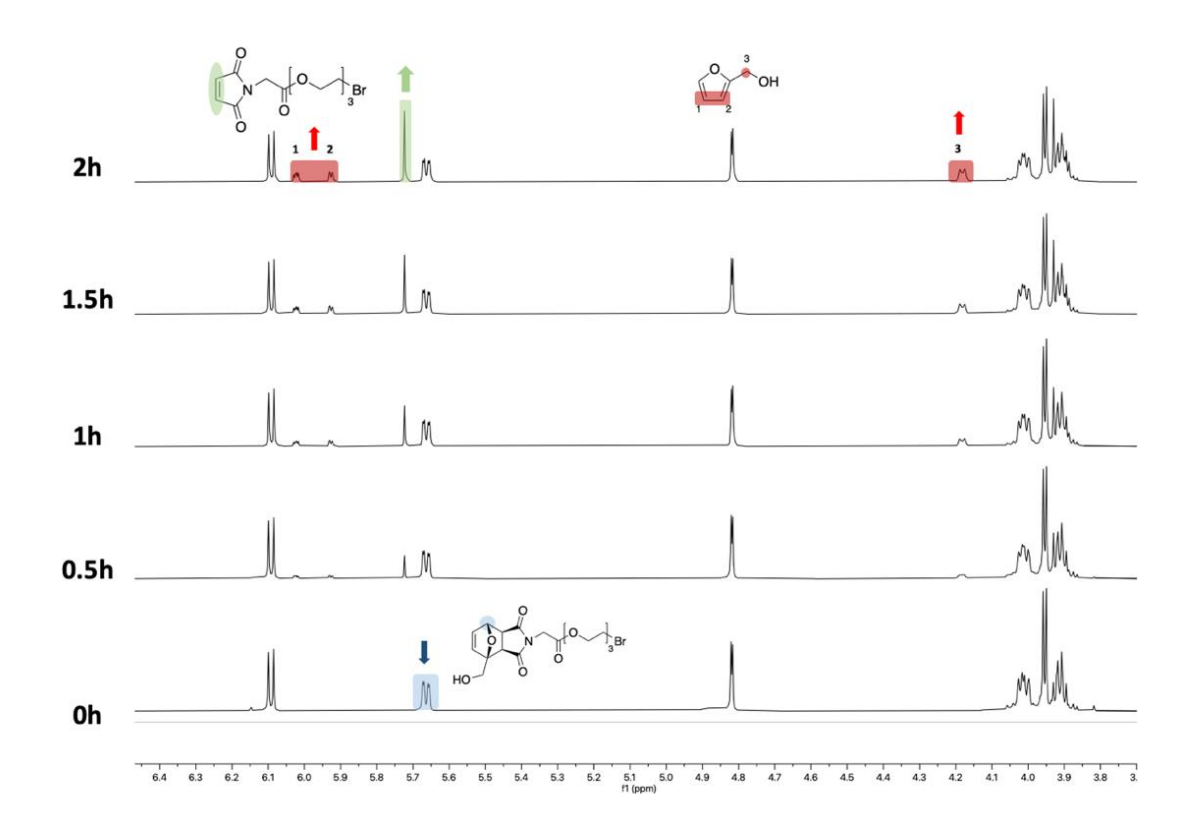


Figure 2.3: Monitoring the retro-Diels-Alder reaction of exo-7 at different times, at  $80 \, ^{\circ}\text{C}$  by  $^{1}\text{H}$  NMR.

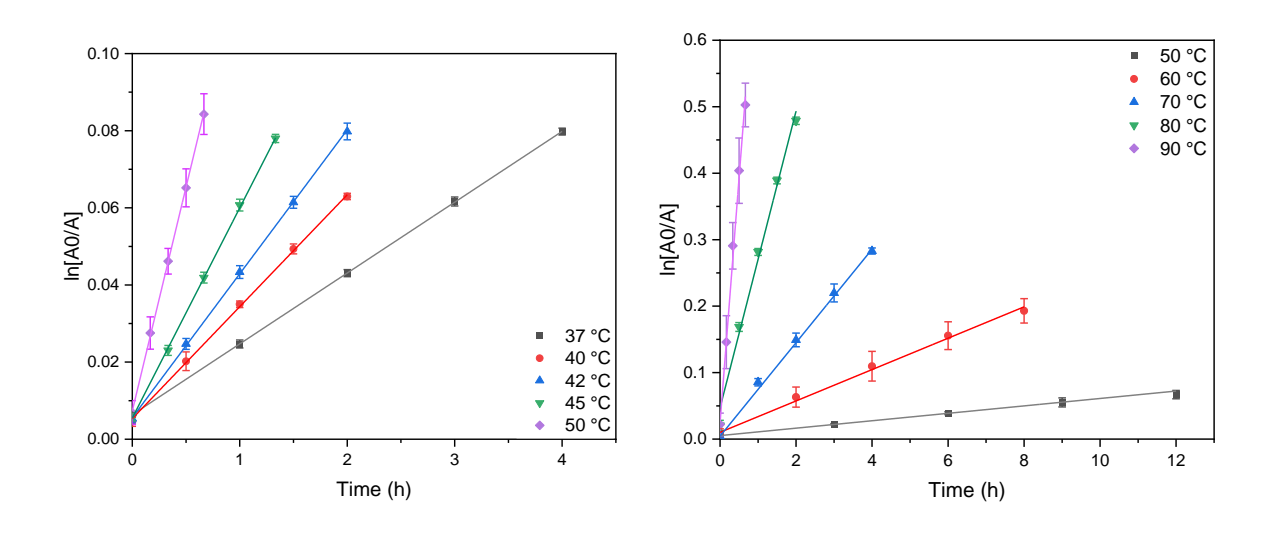
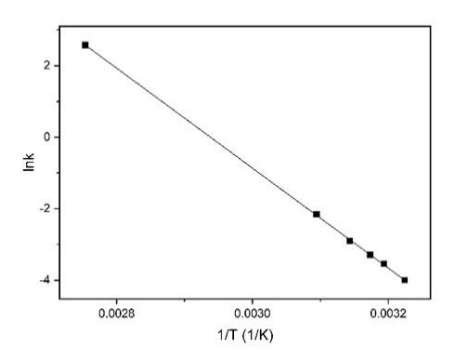


Figure 2.4: Kinetics of module compounds; *endo-*(left) at  $(37^{\circ}\text{C}, 40^{\circ}\text{C}, 42^{\circ}\text{C}, 45^{\circ}\text{C}, 50^{\circ}\text{C})$  and *exo-* right at  $(50^{\circ}\text{C}, 60^{\circ}\text{C}, 70^{\circ}\text{C}, 80^{\circ}\text{C}, 90^{\circ}\text{C})$ .

Table 2.1: Calculated half-lives for *endo-* (left) and *exo-*(right) of 7 as a function of temperature.

Temperature/°C	Half-life /(h)	•	Temperature/°C	Half-life /(h)
37	37.7	•	50	131.6
40	23.8		60	30.1
42	18.7		70	10.0
45	12.7		80	3.04
50	6.00		90	0.97

The calculated Arrhenius activation energies (Eac) of the rDA reaction are summarized in Table 2.2. Compounds 3 and 5 were also studied using the same method in order to identify the effect of the TEG chain and the methylene alcohol side chain on the rDA kinetics. As expected, the TEG chain does not introduce a significant change in the Eac, whereas the presence of the alcohol side chain increases the Eac by approximately 6 kJ/mol. This is likely because of hydrogen bonding between the carbonyl oxygen and the hydroxyl group on the bridge-head side chain. The effect was notably only observed in the *endo* case and not in the *exo* case, consistent with the carbonyl being in close proximity to the hydroxyl group only in its *endo* isomer. Overall, the *exo* adducts manifest a greater Eac than the *endo* by 2 to 9 kJ/mol, consistent with the *exo* being more thermodynamically stable.



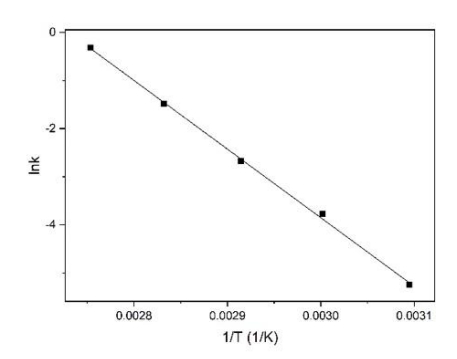


Figure 2.5: Arrhenius plots of the module compounds; *endo-* (up) and *exo-*(bottom) of 7.

Table 2.2: Eac of **3**, **5**, and **7** 

Compound	Eac(kJ/mol)		
	endo	exo	
3	107.2	115.5	
5	109.6	118.9	
7	116.2	118.7	

A DA reaction is a [4 + 2] cycloaddition involving a diene and a dienophile, where the product is formed through a six  $\pi$ -electron cyclic transition state. In the case studied here, a cyclic diene (furfuryl alcohol) and dienophile (maleimide derivative) are involved, a bridged [2.2.1] bicyclic system is formed and can adopt either an *endo* or *exo* configuration. Typically, the *endo* product is favored due to secondary orbital interactions, as illustrated in Figure 2.6. However, the *endo* to *exo* ratio can vary depending on whether the reaction is performed under kinetically or thermodynamically controlled conditions. The DA reaction is reversible, and the reverse process (rDA) is favored at higher temperatures. During the linker synthesis process, several *endo-* and *exo-* isomers were generated and isolated (Scheme 2.1). <sup>1</sup>H NMR was used to differentiate *endo* and *exo-* isomers. For example, in the case of 7, the proton at position 3 in the *endo* product appears as a doublet of doublets, while in its *exo* form, appears as a simple doublet, owing to changes in

dihedral angles between proton 3 and 4. As illustrated in Figure 2.7, the rDA of *endo* **7** is more kinetically favored, and the Eac required to undergo ae rDA reaction should be lower compared to the *exo* adduct. These results indicate that under heating at 50 °C, the *endo* -**7** undergoes the rDA reaction with an 8% conversion within 40 minutes, whereas the *exo*- **7** requires 1 hour to achieve the same conversion at 60 °C. Overall, the temperature dependence study suggests that the *endo* linker will be more suitable in controlled drug delivery applications at physiological temperatures.

Figure 2.6: Illustration of orbital overlap differences between the two isomers of 7.

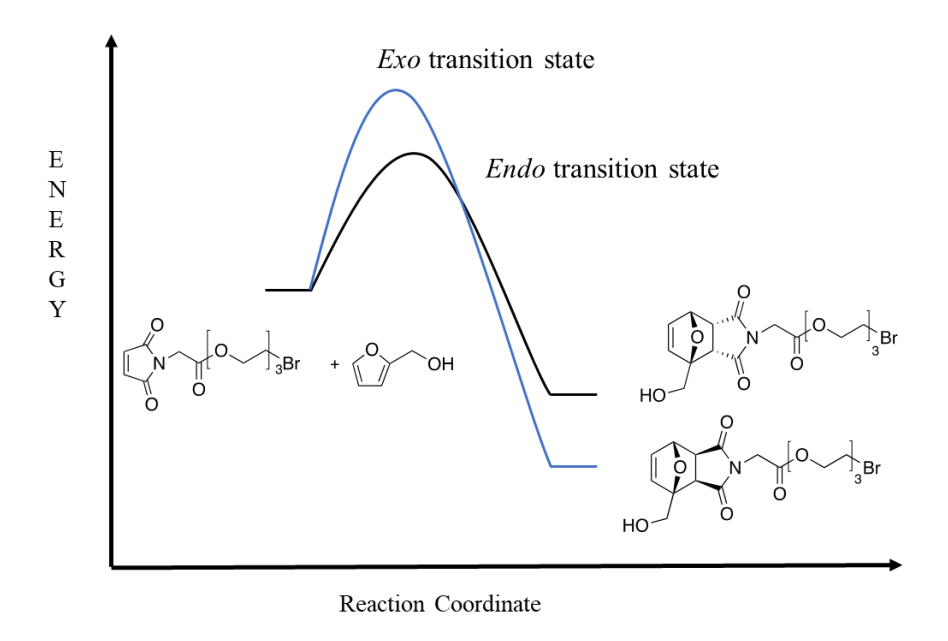


Figure 2.7: Energy profile of *endo-7* and *exo-7*.

## 2.5 Conclusions and Perspective

In this Chapter, an effective thermal release linker based on the rDA reactions of maleimide and furfuryl alcohol derivatives was developed and incorporated to a water-soluble PEG oligomer thiol for attachment to gold nanoparticles. The kinetic properties of the linker molecules conclude that the *endo* adducts can undergo the rDA reaction under relatively mild heating conditions (37 °C to 42 °C), whereas the *exo* adducts require high temperatures (70 °C - 90 °C) to achieve similar extents of conversion. These results demonstrate the potential of the designed linker for use in controlled release systems. In the subsequent Chapter, this panel of linker modules is incorporated onto PEGylated AuNPs through a ligand exchange reaction. By studying the kinetics of thermal release products on the as-prepared water-soluble AuNPs, we seek to further validate the effectiveness and applicability of the linker in applications, particularly in controlled drug delivery systems.

### 2.6 Experimental

#### 2.6.1 Material

Chemicals and solvents were purchased from Sigma Aldrich and were used as received without further purification. Proton nuclear magnetic resonance ( $^{1}$ H NMR) spectra and carbon nuclear magnetic resonance ( $^{13}$ C NMR) spectra were acquired using Bruker Ascend 500 MHz or 400 MHz spectrometers. Chemical shifts ( $\delta$ ) are reported in parts per million (ppm) and are calibrated to the residual solvent peak. Coupling constant (J) is reported in Hertz (Hz). Multiplicities are reported using the following abbreviations: s = singlet; d = doublet; t = triplet; q = quartet; br = broad; m = multiplet; dd = doublet of doublet.

# 2.6.2 Synthesis of Linker

## **Compound 2**

A 250 mL round bottom flask, equipped with a magnetic stirring bar, was charged with maleic anhydride (5.636 g, 5.75 ×10<sup>-2</sup> mol) and glycine (4.324 g, 5.76 ×10<sup>-2</sup> mol). Acetic acid (150 mL) was added to dissolve all starting materials. The mixture was stirred at room temperature for 3 days and then refluxed at 120°C for 8 hours. The flask was subsequently cooled to room temperature, and all solvent was then removed under high vacuum. After that, the crude product was purified by column chromatography, yielding 2 as a white solid (3.77 g, 41 % yield).

<sup>1</sup>H NMR (500 MHz, CDCl<sub>3</sub>):δ 6.80 (s, 2H), 4.34 (s, 2H).

<sup>13</sup>C NMR (126 MHz, CDCl3):δ 171.9, 169.6, 134.6, 38.2.

HRMS (ESI) m/z: [M+H] + calculated for C<sub>6</sub>H<sub>4</sub>NO<sub>4</sub>:154.0140, found 154.01381.

**2** (1.02 g,  $6.598 \times 10^{-3}$  mol) and furan (0.90 g,  $1.3196 \times 10^{-2}$  mol) were dissolved in 50 mL toluene. The mixture was heated in a 15 mL pressure tube at 120 °C overnight. The crude product was washed by cold hexane and ether. The remaining solvent was removed by high vacuum to yield **3** (1.326 g, 90% yield) as white solids.

 $^{1}$ H NMR (400 MHz, CDCl<sub>3</sub>):  $\delta$  6.54 (s, 2H), 5.31 (s, 2H), 4.29 (s, 2H), 2.96 (s, 2H).

 $^{13}$ C NMR (126 MHz, CDCl<sub>3</sub>):  $\delta$ 175.3, 136.8, 81.1, 47.9.

HRMS (ESI) m/z: [M+H] + calculated for C<sub>10</sub>H<sub>8</sub>NNa<sub>2</sub>O<sub>5</sub>: 268.0197, found 268.0182.

To a stirred toluene solution of triethylene glycol (30.99 g, 0.159 mol), HBr (12.9 mL, 0.238 mol) was added. The mixture was then heated at 120 °C for 3 days. The flask was cooled to room temperature and the top layer was diluted with 100 mL dichloromethane. The organic layer was subsequently washed with 1M NaOH 2 times and 40 mL brine 4 times. The crude product was then purified by column chromatography to afford pale yellow oil (17.496 g, 40% yield).

<sup>1</sup>H NMR (500 MHz, CDCl<sub>3</sub>): δ 3.82 (t, J = 6.2 Hz, 2H), 3.74 (t, J = 4.1 Hz, 2H), 3.69 (s, 4H), 3.62 (t, J = 4.9 Hz, 2H), 3.48 (t, J = 6.2 Hz, 2H).

<sup>13</sup>C NMR (126 MHz, CDCl<sub>3</sub>): δ 72.6, 71.3, 70.7, 70.5, 62.0, 30.4.

HRMS (ESI) m/z: [M+H] + calculated for C<sub>6</sub>H<sub>13</sub>BrNaO<sub>3</sub>: 234.9946, found 234.9940.

3 (0.5878 g,  $2.6 \times 10^{-3}$  mol) was dissolved in dry THF. DCC (0.543 g,  $2.6 \times 10^{-3}$  mol) and DMAP (0.016 g,  $1.382 \times 10^{-4}$  mol) were then dissolved in dry THF in another round bottom flask. Then, two mixtures were combined in one flask with addition of **4** (0.3988 g,  $1.3 \times 10^{-3}$  mol). The mixture was allowed to stir overnight and then filtration to get rid of the white principate. After that, the crude product was purified by column chromatography to afford a colorless oil (0.2931g, 40 % yield).

<sup>1</sup>H NMR (500 MHz, CDCl<sub>3</sub>)  $\delta$  6.50 (s, 2H), 5.27 (s, 2H), 4.27 - 4.26 (m, 2H), 4.22 (s, 2H), 3.79 (t, J = 6.2 Hz, 2H), 3.71-3.60 (m, 6H), 3.46 (t, J = 6.2 Hz, 2H), 2.93 (s, 2H).

<sup>13</sup>C NMR (126 MHz, CDCl<sub>3</sub>) δ 175.3, 166.6, 136.7, 80.9, 71.3, 70.6, 70.5, 68.9, 64.9, 47.7, 39.7, 30.5.

HRMS (ESI) m/z:  $[M+H]^+$  calculated for  $C_{16}H_{20}O_7NBrNa$ : 440.0321, found 440.01368.

A 250 mL round bottom flask equipped with a magnetic stirring bar was charged with 5 (0.488 g,  $1.166 \times 10^{-3}$  mol). 5 was then fully dissolved in dry toluene. After that, the mixture was refluxed at 110 °C overnight. Remove the solvent by rotary evaporation and leave the final product as a clear yellow oil with quantitative yield (0.396 g, >97% yield).

<sup>1</sup>H NMR (400 MHz, CDCl<sub>3</sub>)  $\delta$  6.79 (s, 2H), 4.31 (s, 4H), 3.82 (t, J = 6.3 Hz, 2H), 3.71 (s, 2H), 3.67 (m, 4H), 3.49 (t, J = 6.3 Hz, 2H).

<sup>13</sup>C NMR (126 MHz, CDCl<sub>3</sub>) δ 169.9, 167.3, 134.7, 71.43, 70.8, 70.7, 69.0, 65.0, 38.8, 30.5.

HRMS (ESI) m/z:  $[M+H]^+$  calculated for  $C_{12}H_{16}O_6NBrNa$ : 372.0059, found 372.00518.

2-furanmethanol (1.09 mL,  $1.2 \times 10^{-2}$  mol) and compound 6 (0.443 g,  $1.2 \times 10^{-3}$  mol) were mixed in 30 mL ethyl acetate. The mixture was left to react at room temperature for three days. The completion of the reaction was monitored by TLC. After removing the solvent, the crude product was purified by column chromatography to afford 0.295 g of endo-7 with a yield of 52 % and 0.1028 g of exo-7 with a yield of 19%.

<sup>1</sup>H NMR (500 MHz, CDCl<sub>3</sub>)  $\delta$  6.51 (dd, J = 5.8, 1.6 Hz, 1H), 6.40 (d, J = 5.8 Hz, 1H), 5.33 (dd, J = 5.5, 1.6 Hz, 1H), 4.33 – 4.25 (m, 3H), 4.19 (dd, J = 12.5, 7.0 Hz, 1H), 4.11 (s, 2H), 3.81 (t, J = 6.3 Hz, 2H), 3.76 – 3.62 (m, 7H), 3.51 (d, J = 7.7 Hz, 2H), 3.48 (t, J = 6.3 Hz, 2H).

<sup>13</sup>C NMR (126 MHz, CDCl<sub>3</sub>) δ 174.3, 173.9, 166.4, 136.1, 135.0, 92.3, 79.7, 71.4, 70.7, 70.7, 69.0, 64.9, 61.7, 48.6, 46.5, 39.4, 30.5.

HRMS (ESI) m/z:  $[M+H]^+$  calculated for  $C_{17}H_{22}O_8NBrNa$ : 470.0427, found 470.0407.

<sup>1</sup>H NMR (500 MHz, CDCl<sub>3</sub>) δ 6.62 (d, J = 5.7 Hz, 1H), 6.55 (dd, J = 5.7, 1.7 Hz, 1H), 5.29 (d, J = 1.7 Hz, 1H), 4.35 – 4.25 (m, 4H), 4.11 (d, J = 7.1 Hz, 2H), 3.81 (t, J = 6.3 Hz, 2H), 3.75 – 3.61 (m, 6H), 3.48 (t, J = 6.3 Hz, 2H), 3.10 (d, J = 6.5 Hz, 1H), 3.04 (d, J = 6.5 Hz, 1H).

<sup>13</sup>C NMR (126 MHz, CDCl<sub>3</sub>) δ 175.1, 166.5, 138.6, 137.2, 91.7, 81.0, 71.4, 70.7, 70.6, 69.0, 65.1, 60.8, 50.4, 48.5, 39.8, 30.5.

HRMS (ESI) m/z:  $[M+H]^+$  calculated for  $C_{17}H_{22}O_8NBrNa$ : 470.0427, found 470.0411.

0.103 g compound **7** (2.29×10<sup>-4</sup> mol) was dissolved in 10 mL of anhydrous THF under Ar in an ice bath. 0.053 mL of hexamethyldisilathiane (2.52×10<sup>-4</sup> mol) was added, followed by the addition of 0.026 mL of 1M TBAF solution in THF (2.52×10<sup>-4</sup> mol). After reaction for 1 hour, the reactants were diluted in 50 mL DCM and then washed with 20 mL brine 5 times and 20 mL of NH<sub>4</sub>Cl solution. The organic layer was collected and dried with MgSO4, filtered, the rotary evaporated to remove the solvent to afford 0.085 g of compounds **8** as a colorless oil (93% yield).

<sup>1</sup>H NMR (400 MHz, CDCl<sub>3</sub>) δ 6.51 (dd, J = 5.8, 1.6 Hz, 1H), 6.40 (d, J = 5.8 Hz, 1H), 5.32 (dd, J = 1.6 Hz, 1H), 4.33 – 4.25 (m, 3H), 4.23 – 4.15 (m, 1H), 4.11 (s, 2H), 3.76 – 3.62 (m, 10H), 3.52 (d, J = 7.7 Hz, 1H), 2.70 (q, J = 8.3 Hz, 2H), 1.59 (t, J = 8.4 Hz, 1H).

<sup>13</sup>C NMR (101 MHz, CDCl<sub>3</sub>) δ 174.3, 173.9, 166.4, 136.0, 135.0, 125.7, 92.3, 79.7, 73.1, 70.7, 70.3, 69.0, 64.9, 61.6, 48.6, 46.4, 39.4, 30.5, 24.4.

HRMS (ESI) m/z: [M+H] + calculated for C<sub>17</sub>H<sub>23</sub>O<sub>8</sub>NNaS: 424.1042, found 424.1037.

#### 2.7 References

- (1) Ji, X.; Zhou, C.; Ji, K.; Aghoghovbia, R. E.; Pan, Z.; Chittavong, V.; Ke, B.; Wang, B. Click and Release: A Chemical Strategy toward Developing Gasotransmitter Prodrugs by Using an Intramolecular Diels–Alder Reaction. *Angewandte Chemie International Edition* **2016**, *55* (51), 15846–15851. https://doi.org/10.1002/anie.201608732.
- (2) Zhao, H.; Sterner, E. S.; Coughlin, E. B.; Theato, P. O-Nitrobenzyl Alcohol Derivatives: Opportunities in Polymer and Materials Science. *Macromolecules* **2012**, *45* (4), 1723–1736. https://doi.org/10.1021/ma201924h.
- (3) Versteegen, R. M.; Rossin, R.; ten Hoeve, W.; Janssen, H. M.; Robillard, M. S. Click to Release: Instantaneous Doxorubicin Elimination upon Tetrazine Ligation. *Angewandte Chemie International Edition* **2013**, *52* (52), 14112–14116. https://doi.org/10.1002/anie.201305969.
- (4) Ji, X.; Pan, Z.; Yu, B.; Cruz, L. K. D. L.; Zheng, Y.; Ke, B.; Wang, B. Click and Release: Bioorthogonal Approaches to "on-Demand" Activation of Prodrugs. *Chemical Society Reviews* **2019**, *48* (4), 1077–1094. https://doi.org/10.1039/C8CS00395E.
- (5) Bio, M.; Nkepang, G.; You, Y. Click and Photo-Unclick Chemistry of Aminoacrylate for Visible Light-Triggered Drug Release. *Chemical Communications* **2012**, *48* (52), 6517–6519. https://doi.org/10.1039/C2CC32373G.
- (6) Hebels, E. R.; Dietl, S.; Timmers, M.; Hak, J.; van den Dikkenberg, A.; Rijcken, C. J. F.; Hennink, W. E.; Liskamp, R. M. J.; Vermonden, T. Versatile Click Linker Enabling Native Peptide Release from Nanocarriers upon Redox Trigger. *Bioconjugate Chem.* **2023**, *34* (12), 2375–2386. https://doi.org/10.1021/acs.bioconjchem.3c00484.
- (7) Vejan, P.; Khadiran, T.; Abdullah, R.; Ahmad, N. Controlled Release Fertilizer: A Review on Developments, Applications and Potential in Agriculture. *Journal of Controlled Release* **2021**, *339*, 321–334. https://doi.org/10.1016/j.jconrel.2021.10.003.
- (8) Lee, H. S.; Sung, D. K.; Kim, S. H.; Choi, W. I.; Hwang, E. T.; Choi, D. J.; Chang, J. H. Controlled Release of Astaxanthin from Nanoporous Silicified-Phospholipids Assembled Boron Nitride Complex for Cosmetic Applications. *Applied Surface Science* **2017**, *424*, 15–19. https://doi.org/10.1016/j.apsusc.2017.03.036.
- (9) Almasi, H.; Jahanbakhsh Oskouie, M.; Saleh, A. A Review on Techniques Utilized for Design of Controlled Release Food Active Packaging. *Critical Reviews in Food Science and Nutrition* **2021**, *61* (15), 2601–2621. https://doi.org/10.1080/10408398.2020.1783199.
- (10) Kamaly, N.; Yameen, B.; Wu, J.; Farokhzad, O. C. Degradable Controlled-Release Polymers and Polymeric Nanoparticles: Mechanisms of Controlling Drug Release. *Chem. Rev.* **2016**, *116* (4), 2602–2663. https://doi.org/10.1021/acs.chemrev.5b00346.
- (11) Xue Zhang, R.; Ahmed, T.; Yi Li, L.; Li, J.; Z. Abbasi, A.; Yu Wu, X. Design of Nanocarriers for Nanoscale Drug Delivery to Enhance Cancer Treatment Using Hybrid Polymer and Lipid Building Blocks. *Nanoscale* **2017**, *9* (4), 1334–1355. https://doi.org/10.1039/C6NR08486A.
- (12) Nurita Kurniasih, I.; Keilitz, J.; Haag, R. Dendritic Nanocarriers Based on Hyperbranched Polymers. *Chemical Society Reviews* **2015**, *44* (12), 4145–4164. https://doi.org/10.1039/C4CS00333K.
- (13) Kim, C. K.; Ghosh, P.; Pagliuca, C.; Zhu, Z.-J.; Menichetti, S.; Rotello, V. M. Entrapment of Hydrophobic Drugs in Nanoparticle Monolayers with Efficient Release into Cancer Cells. *J. Am. Chem. Soc.* **2009**, *131* (4), 1360–1361. https://doi.org/10.1021/ja808137c.

- (14) Anik, M. I.; Mahmud, N.; Al Masud, A.; Hasan, M. Gold Nanoparticles (GNPs) in Biomedical and Clinical Applications: A Review. *Nano Select* **2022**, *3* (4), 792–828. https://doi.org/10.1002/nano.202100255.
- (15) A. Swiech, O.; J. Opuchlik, L.; Wojciuk, G.; M. Stepkowski, T.; Kruszewski, M.; Bilewicz, R. Doxorubicin Carriers Based on Au Nanoparticles Effect of Shape and Gold-Drug Linker on the Carrier Toxicity and Therapeutic Performance. *RSC Advances* **2016**, *6* (38), 31960–31967. https://doi.org/10.1039/C6RA00177G.
- (16) Yan, X.; Li, K.; Xie, T.-Q.; Jin, X.-K.; Zhang, C.; Li, Q.-R.; Feng, J.; Liu, C.-J.; Zhang, X.-Z. Bioorthogonal "Click and Release" Reaction-Triggered Aggregation of Gold Nanoparticles Combined with Released Lonidamine for Enhanced Cancer Photothermal Therapy. *Angewandte Chemie International Edition* **2024**, *63* (13), e202318539. https://doi.org/10.1002/anie.202318539.
- (17) Rossin, R.; van Duijnhoven, S. M. J.; ten Hoeve, W.; Janssen, H. M.; Kleijn, L. H. J.; Hoeben, F. J. M.; Versteegen, R. M.; Robillard, M. S. Triggered Drug Release from an Antibody—Drug Conjugate Using Fast "Click-to-Release" Chemistry in Mice. *Bioconjugate Chem.* **2016**, 27 (7), 1697–1706. https://doi.org/10.1021/acs.bioconjchem.6b00231.
- (18) Xue, Y.; Bai, H.; Peng, B.; Fang, B.; Baell, J.; Li, L.; Huang, W.; Hans Voelcker, N. Stimulus-Cleavable Chemistry in the Field of Controlled Drug Delivery. *Chemical Society Reviews* **2021**, *50* (8), 4872–4931. https://doi.org/10.1039/D0CS01061H.
- (19) Luo, W.; Gobbo, P.; Gunawardene, P. N.; Workentin, M. S. Fluorogenic Gold Nanoparticle (AuNP) Substrate: A Model for the Controlled Release of Molecules from AuNP Nanocarriers via Interfacial Staudinger–Bertozzi Ligation. *Langmuir* **2017**, *33* (8), 1908–1913. https://doi.org/10.1021/acs.langmuir.6b03647.
- (20) xie, X.; Li, B.; Wang, J.; Zhan, C.; Huang, Y.; Zeng, F.; Wu, S. Tetrazine-Mediated Bioorthogonal System for Prodrug Activation, Photothermal Therapy, and Optoacoustic Imaging. *ACS Appl. Mater. Interfaces* **2019**, *11* (45), 41875–41888. https://doi.org/10.1021/acsami.9b13374.
- (21) Jin, Q.; Mitschang, F.; Agarwal, S. Biocompatible Drug Delivery System for Photo-Triggered Controlled Release of 5-Fluorouracil. *Biomacromolecules* **2011**, *12* (10), 3684–3691. https://doi.org/10.1021/bm2009125.
- (22) Deng, X.; Shao, Z.; Zhao, Y. Solutions to the Drawbacks of Photothermal and Photodynamic Cancer Therapy. *Advanced Science* **2021**, 8 (3), 2002504. https://doi.org/10.1002/advs.202002504.
- (23) Becer, C. R.; Hoogenboom, R.; Schubert, U. S. Click Chemistry beyond Metal-Catalyzed Cycloaddition. *Angewandte Chemie International Edition* **2009**, *48* (27), 4900–4908. https://doi.org/10.1002/anie.200900755.
- (24) Bakhtiari, A. B. S.; Hsiao, D.; Jin, G.; Gates, B. D.; Branda, N. R. An Efficient Method Based on the Photothermal Effect for the Release of Molecules from Metal Nanoparticle Surfaces. *Angewandte Chemie* **2009**, *121* (23), 4230–4233. https://doi.org/10.1002/ange.200805303.

# Chapter 3. Development of a Thermally Releasing Gold Nanoparticle Template for Drug Delivery

### 3.1 Preface

Chapter 3 explores the development and characterization of a gold nanoparticle (AuNP) system that is designed to create a controlled release platform for drug delivery applications. It details the integration of a retro Diels-Alder (rDA) linker with AuNPs, highlighting the synthesis of a thiol ligand conjugated with fluorescent dye and its attachment to the nanoparticles. This study demonstrates the feasibility of using rDA reactions for controlled drug release from AuNPs and reveals the potential of nanoparticle-based systems to precisely control the timing and dosage of molecular release, potentially enhancing the efficacy and specificity of therapeutic delivery.

#### 3.2 Abstract

The precise control of the release of small molecules from the ligand capping layer of metal nanoparticles has considerable potential for applications in medical imaging, biosensing, and drug delivery. In this Chapter, a novel and highly specific release methodology from gold nanoparticle (AuNP) surfaces based on a retro Diels-Alder (rDA) reaction is reported. A thiol ligand conjugated with a nitrobenzofurazan (NBD) fluorescence dye derivative was synthesized and used to modify water soluble 2 nm diameter AuNPs. This dye-AuNP system serves as a model system for the characterization of rDA release kinetics of NP-associated conjugates. Incorporation of the NBD derivative on the AuNP surface leads to quantitative quenching of the dye fluorescence emission, providing a baseline for monitoring eventual chromophore release. The kinetics of the release of the dye from the AuNPs are observed to follow a first order rate law. This system provides an entry into the use of AuNPs as programmable delivery devices for applications in drug delivery, biosensing, and materials science.

#### 3.3 Introduction

Nanomaterials have emerged as key elements of drug delivery systems owing to their capacity to simultaneously bind or encapsulate therapeutic molecules, cell/tissue recognition molecules, and imaging tags – all coupled to their adaptable physical and chemical properties. Conventional pharmaceutical delivery vehicles, such as tablets and capsules, often encounter practical challenges such as poor solubility, instability, nonspecific biological distribution, and various physiological barriers. In response to these limitations, AuNPs have garnered considerable attention as versatile nanocarriers for drug delivery. The inherent biocompatibility afforded by the gold core, reproducible syntheses, scalability, and well-understood surface

chemistry make them highly attractive for transporting a diverse array of substances, including drugs, genetic materials, proteins, and small molecules.<sup>2</sup> Regulating the release of therapeutic payloads from AuNPs typically employs two main approaches: endogenous and exogenous activation. Endogenous activation strategies involve specific physiochemical characteristics of the biological microenvironment of interest, such as glutathione (GSH)-mediated release,<sup>3</sup> pHresponsive release, <sup>4</sup> and enzyme-responsive release. <sup>5</sup> For example, Zhang et al. developed a novel drug delivery system that employs cysteamine-modified AuNPs conjugated with doxorubicin for targeted cancer therapy and enhanced imaging capabilities. Doxorubicin (DOX) is attached to the cysteamine-AuNPs via disulfide bonds, which are specifically cleavable by the GSH present in higher concentrations found in cancer cells. Upon cleavage, the released DOX-SH serves in a dual role both as a fluorescent marker of the cancer cell and as an active agent in stimulus-responsive therapeutics. This design enhances the internalization of the drug into cancer cells when compared to free doxorubicin, which significantly improves the efficiency of delivering the therapeutic agent into cancer cells.<sup>6</sup> Similarly, Nam et al. reported a combination cancer therapy platform that consists of pH-responsive 10 nm AuNPs that are conjugated with doxorubicin. These AuNPs are engineered to aggregate in mildly acidic conditions which is common in some tumor environments. Upon aggregation, the nanoparticles not only serve as photothermal agents but also facilitate the controlled release of doxorubicin. This dual functionality enhances therapeutic efficacy toward tumors in an animal model study. The AuNPs induced apoptosis in tumor cells while sparing surrounding healthy tissues, indicating that they have minimal side effects. However, endogenous activation methods for drug release, such as those relying on specific physiological triggers within the body, are prone to individual variations that can result in inconsistent drug delivery profiles. In contrast, exogenous activation techniques, which utilize external stimuli like photo-triggered

and thermal-triggered release, offer a complementary and perhaps more general strategy.<sup>8,9</sup> Nonetheless, exogenous stimuli such as high-intensity light present their own challenges such as phototoxicity that has the potential to cause cellular damage or inflammation at the site of irradiation.<sup>10</sup> Consequently, there is an need to develop more general and efficient delivery systems that offer greater control and lower potential for complications at the molecular level.

In this regard, previous research identified PEGylated AuNPs as being excellent candidates for deliberate thermal release of co-ligands, given the qualities that the PEGylated ligands provide including solubility as well as thermal stability in forming the capping layer. Chapter 2 introduced a linker that undergoes a thermally triggered retro-Diels-Alder (rDA) reaction under relatively mild heating conditions. The rDA reaction of the linker follows temperature-dependent first-order dissociation kinetics of the Diels-Alder adduct, allowing for precise temporal control of the quantity of released molecule. In this Chapter, an *endo/exo* linker was incorporated onto the capping layer of AuNPs and model compounds were also attached onto the linker for the development of a thermal release template.

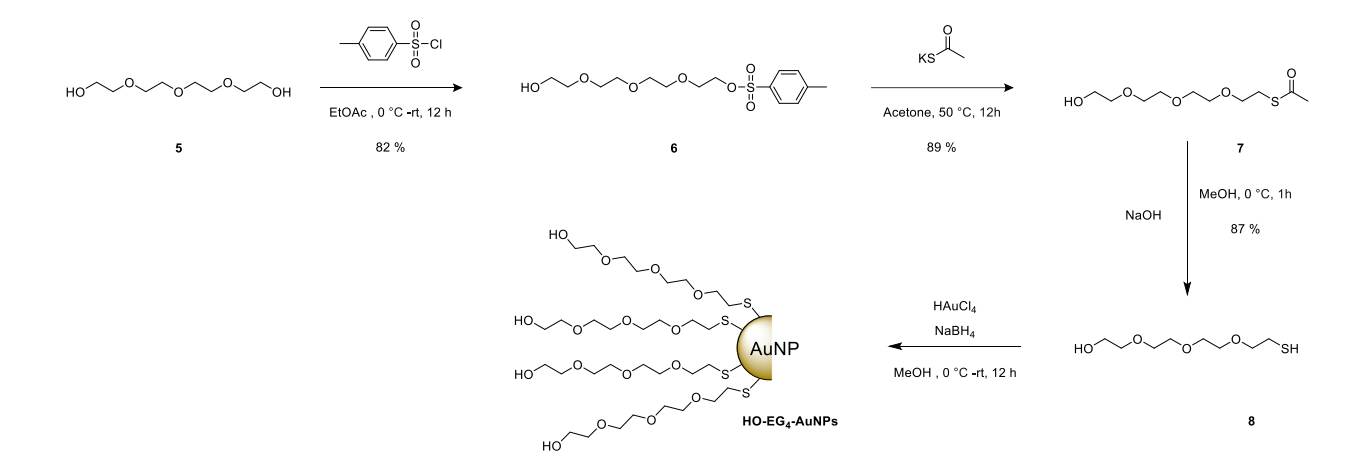
#### 3.4 Result and Discussion

### 3.4.1 Synthesis and Characterization of 2 nm Water-Soluble AuNPs

AuNP sizes can be controlled by synthesis over a moderately small (+/- 20%) size range. Coating the gold core with PEG (polyethylene glycol) derivatives reduces opsonization or aggregation, potentially prolongs circulation time in the bloodstream, and enables the nanoparticles to reach tumor tissues via the enhanced permeability and retention (EPR) effect.<sup>12</sup> The hydrophilicity conferred by PEG enhances an AuNP's ability to circulate readily through the

bloodstream and interact effectively with biological tissues and cells with an enhanced biocompatibility. Therefore, AuNPs coated with a PEG oligomer were synthesized here to form the basis of a model drug carrier. Small AuNPs (2 nm diameter) were selected as smaller particles are often taken up in cells and tissues to a greater extent than ones in the 10 nm – 50 nm ranges. We have previously studied 3 nm PEG-coated maleimide AuNPs, observing negligible toxicity toward HeLa cells at low to moderate concentrations (< 0.1 mM) and only limited toxicity at higher concentrations (0.1–1.0 mM). Given this, small water-soluble AuNPs were synthesized and utilized as a distributable source of a releasable model small molecule drug.

PEG thiol (HO-EG<sub>4</sub>-SH) and the corresponding PEGylated HO-EG<sub>4</sub>-AuNPs were synthesized as demonstrated in Scheme 3.1. AuNP were synthesized by a one phase method where HAuCl<sub>4</sub>.3H<sub>2</sub>O (1eq) was dissolved in a mixture of methanol and glacial acetic acid (6:1) leading to a bright yellow solution. A subsequent color change to black results from the quick addition of freshly prepared NaBH<sub>4</sub> solution in methanol (10 eq.) to yield the AuNP sample. The resulting AuNP were purified and characterized by TEM, UV-Vis spectroscopy, <sup>1</sup>H NMR, and TGA. The resulting HO-EG<sub>4</sub>-AuNPs were confirmed by <sup>1</sup>H NMR spectroscopy, as shown in Figure 3.1, with an average diameter of 1.8 ± 0.4 nm revealed by TEM. Furthermore, TGA provided direct information about the quantity of organic components on the HO-EG<sub>4</sub>-AuNPs, revealing a total weight loss of 28 % attributable to the PEG ligands, as illustrated in Figure 3.1. The composition of HO-EG<sub>4</sub>-AuNPs was thus calculated as being Au<sub>200</sub>[HO-EG<sub>4</sub>-S<sup>-</sup>]<sub>70</sub>, using the average gold core diameter and the approximation that the gold cores are monodisperse and spherical. The resulting amphiphilic AuNPs, distinguished by their high solubility in both aqueous and organic media, provide a versatile nanoplatform for their study as a small molecule thermal release system.



Scheme 3.1: Synthetic scheme of PEG oligomer thiol (HO-EG<sub>4</sub>-SH) and HO-EG<sub>4</sub>-AuNPs.

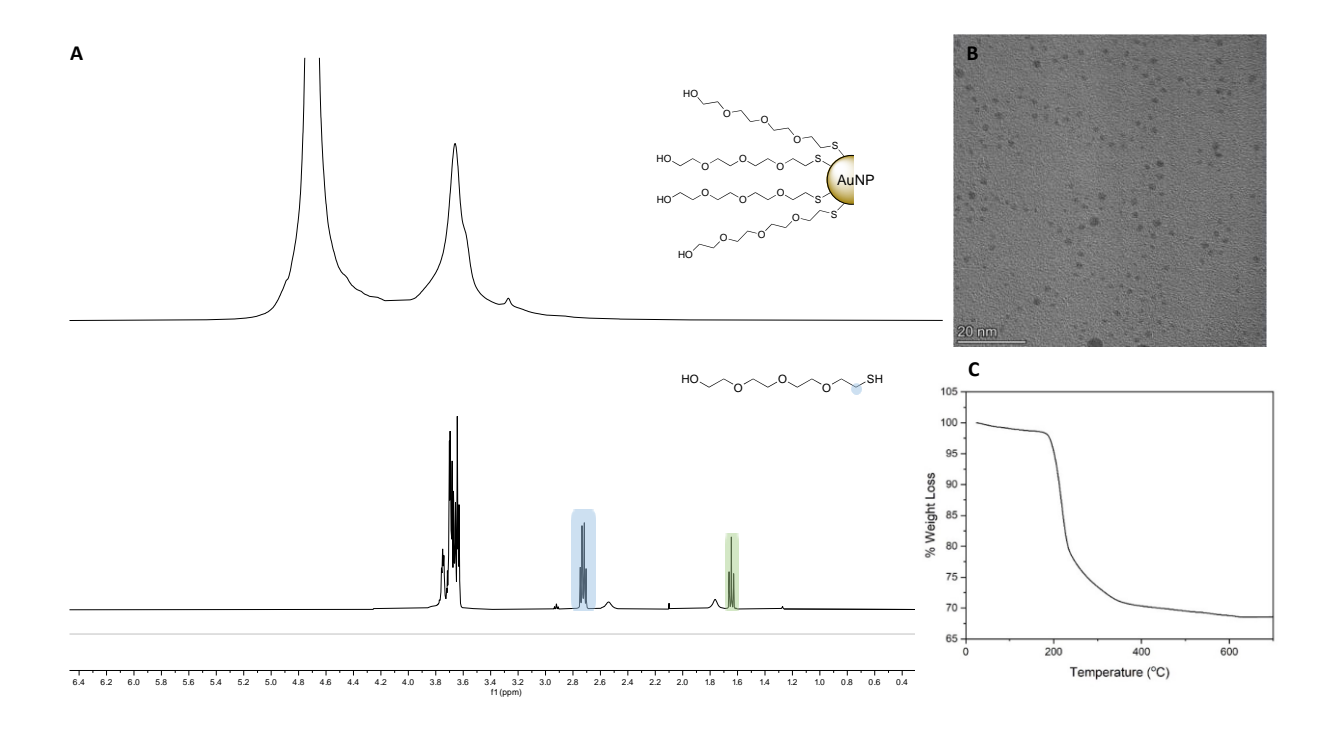


Figure 3.1: Characterizations of HO-EG<sub>4</sub>-AuNPs. (A) $^1$ H NMR spectrum of HO-EG<sub>4</sub>-SH in CDCl<sub>3</sub>and HO-EG<sub>4</sub>-AuNPs in D<sub>2</sub>O, (B) TEM image of HO-EG<sub>4</sub>-AuNPs (C) TGA scan of HO-EG<sub>4</sub>-AuNPs.

#### 3.4.2 Synthesis of NBD-Linker Thiol

Following the demonstration of controlled dissociation by the tetrahydrophthalimide thermal linker in Chapter 2, this Chapter explores its application when associated with AuNP surfaces. The fluorescence signal of a fluorophore is quenched after attachment to a AuNP surface provided the surface-fluorophore distance does not exceed 10 nm and the fluorescence is recovered after it is detached from the NP surface. For instance, Bhatt et al. used two fluorophore-labeled and thiol-modified DNA strands attached to AuNPs to study the dissociation and degradation of these DNA constructs by monitoring the recovery of the signal of the fluorophore. Similarly, Han et al. investigated a light-regulated release of DNA using a fluorescein-labeled DNA to track DNA delivery and release *in vivo*. In this Chapter, a fluorophore was covalently attached to AuNPs *via* this linker to study its controlled release properties as a function of heating. NBD was selected as a model fluorophore over rhodamine B, coumarin derivatives, and fluorescein due to the low thermal stability of Rhodamine B and coumarin derivatives and the tedious purification required of fluorescein derivatives.

NBD ( $\lambda_{\rm ex}$  = 467 nm and  $\lambda_{\rm em}$  = 538 nm) derivatized thiol with the DA linker was thus synthesized (Scheme 3.2). Compound **1** reacted with of 6-aminohexanoic acid via a nucleophilic aromatic substitution to yield **2**. **2** which underwent EDC/DMAP coupling with the bromide-substituted linkers (*endo* or *exo*) to form **3** with a yield of 70 %. Finally, *endo*- and *exo*-**3** were mixed with bis(trimethylsilyl)sulfide in the presence of tetra-n-butylammonium fluoride to generate **4**. The final products, *endo* and *exo*-**4**, demonstrated good stability over 180 days of storage at -20 °C under Ar.

Scheme 3.2: Synthesis scheme of linker-NBD conjugate thiol 4.

# 3.4.3 Synthesis and Characterization of NBD-Linker-AuNPs

Here, the synthesized thiols (endo- or exo-4) were introduced to PEGylated AuNPs using a place-exchange reaction (Figure 3.2). The reaction conditions were optimized to improve the loading of 4 onto HO-EG<sub>4</sub>-AuNPs. The  $^{1}$ H NMR spectrum of the resulting NBD-AuNPs was collected after purification (Figure 3.3A, bottom). Compared to the thiol 4 (Figure 3.3A, top), the absence of sharp peaks in the spectrum of NBD-AuNPs indicated effective removal of unbound thiols and disulfides after purification. The appearance of the broad peaks whose chemical shift is the same as the free ligands confirms that the ligands had been successfully attached to the AuNPs. TEM images showed no sign of aggregation of the NP post-ligand attachment, with an average size of  $1.9 \pm 0.3$  nm (Figure 3.6). The presence of nitrogen in the post-reaction EDX spectra post-reaction confirmed the successful incorporation of compound 4 onto the AuNPs. Finally, the extent of NBD loading on the AuNPs was determined after complete release of NBD via the thermally triggered rDA reaction. The NBD concentration can be measured using fluorescence spectroscopy after comparison to the standard calibration curve of compound 2.

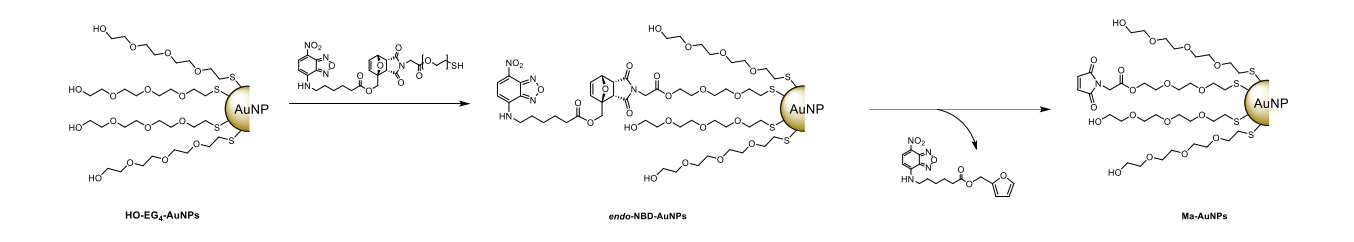
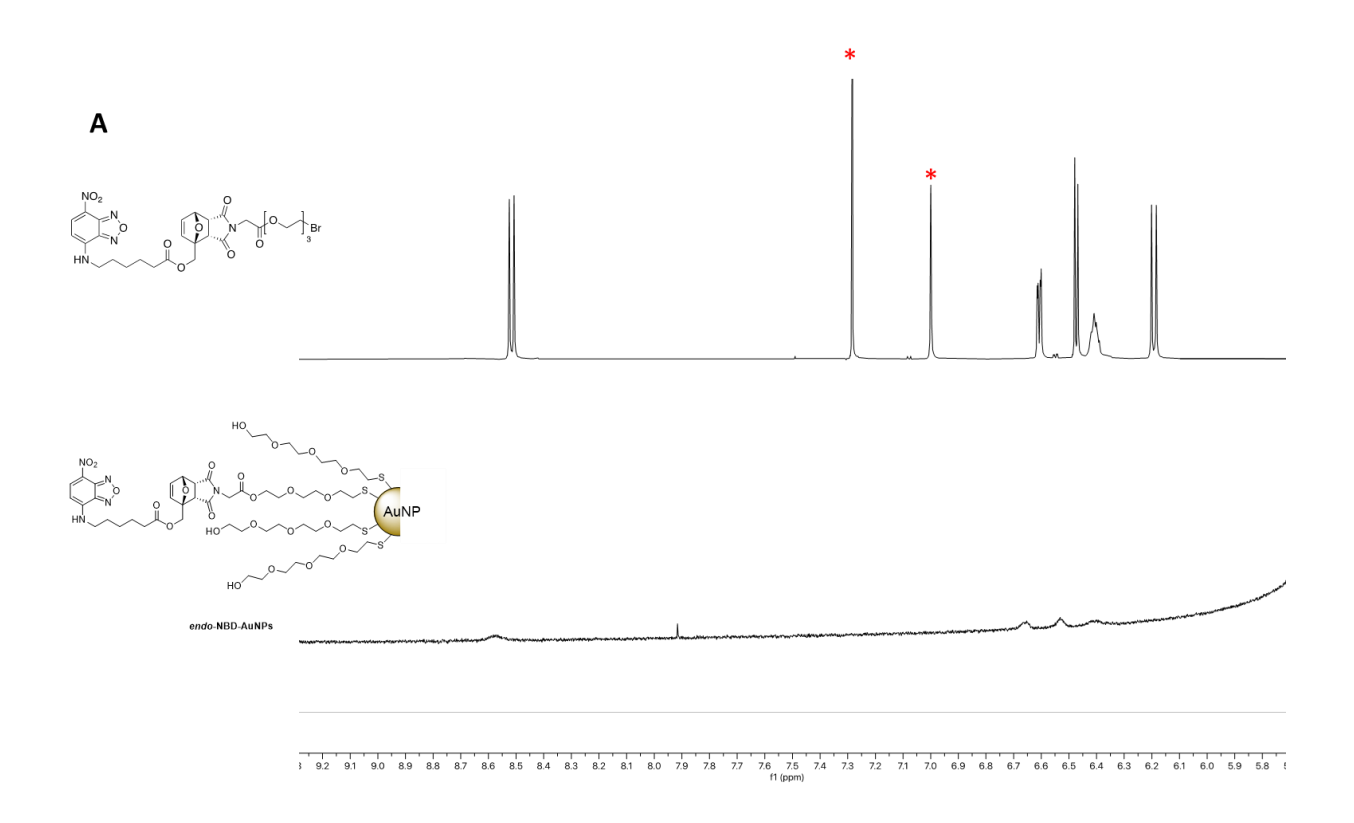


Figure 3.2: Illustration of NBD derivative releasing via thermal-mediated rDA reaction of the designed NBD-AuNPs.



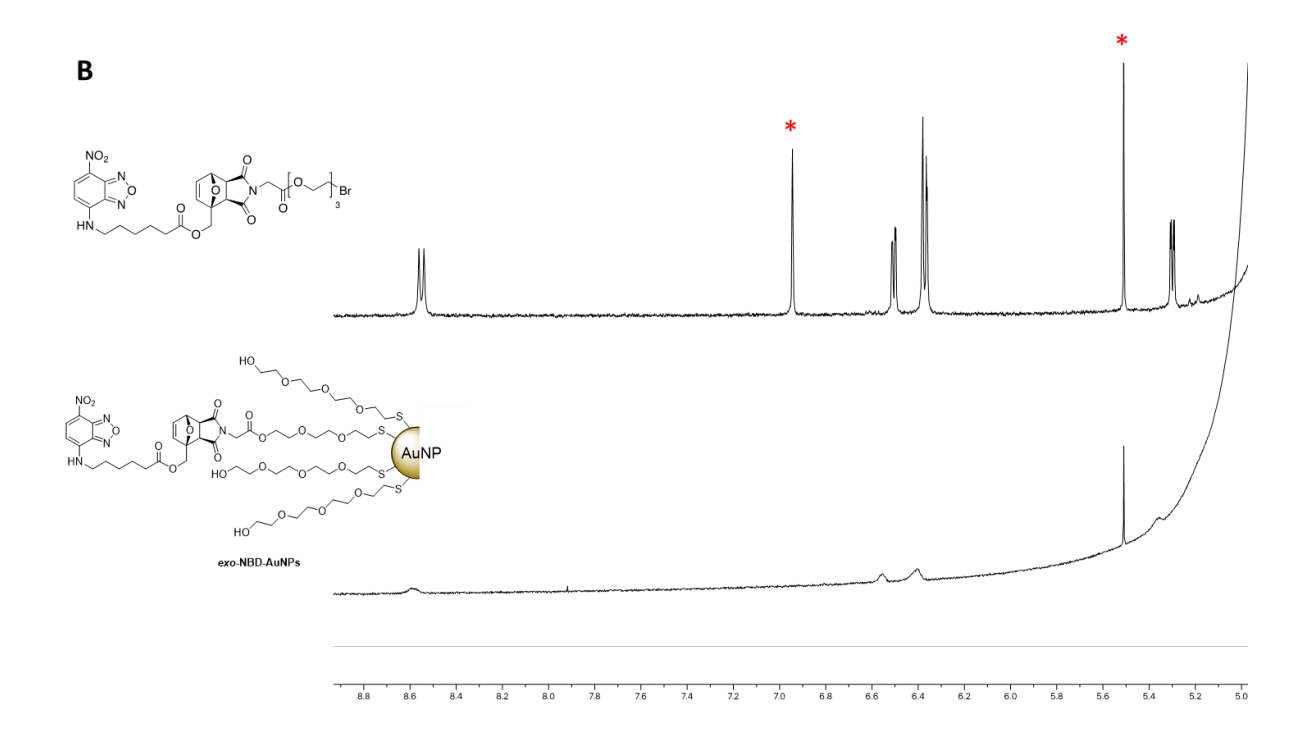


Figure 3.3: Characterization of *endo-* and *exo-* NBD-AuNPs; <sup>1</sup>H NMR spectra of *endo* (A) and *exo-* 4 (B) with corresponding NBD-AuNPs in CD<sub>3</sub>OD solvent. \* is assigned to the solvent (CDCl<sub>3</sub> and CH<sub>2</sub> Cl<sub>2</sub>).

# 3.4.4 Kinetic Analysis of NBD Release from AuNPs

The quenching of an AuNP-linked fluorophore is attributed to a combination of energy and electron transfer from the photoexcited species to the NP core. <sup>18</sup> The regeneration of fluorescence after release from the AuNP can thus be used to study the kinetics of the rDA release process. For example, Chaudhary et al. reported a one-pot synthesis of doxorubicin-AuNP conjugates, which can be used for drug delivery without further processing. Under basic conditions, the terminal hydroxyl group of doxorubicin participated in the formation of the AuNP. The release profile, alongside cell viability and cellular uptake efficiency data, revealed that the as-prepared conjugates

have significant potential for use as an efficient drug delivery system, even within complex biological matrices. Chompoosor et al. explored the charge- and time-dependent release kinetics by analyzing the detachment of fluorescein from AuNPs. <sup>19</sup> Montalti et al. employed an approach by using a non-fluorescent thiol to replace a pyrene-labeled aliphatic thiol on AuNPs, a technique aimed at studying the kinetics of ligand-exchange reactions. <sup>20</sup>

In this study, the rDA kinetics of NBD-AuNPs were assessed as a function of temperature via fluorescence spectroscopy. The observed increase in fluorescence intensity upon heating confirmed the successful dissociation of NBD from the linker attached to the AuNPs, as shown in Figure 3.4. The detachment of the NBD furan-alcohol moiety was verified by HR-MS, via the signal associated with its exact mass of 373.11619 m/z.

The rDA kinetics study for the *exo*-isomer NBD-AuNPs was evaluated over a range of 55°C - 75°C, as illustrated in Figure 3.5. The rDA reaction followed a first-order kinetics rate law, consistent with the previous experimental data. The rate constants were derived from

$$kt = \ln\left[\frac{B_{\infty}}{B_{\infty} - B}\right] \tag{2}$$

where k is the rate constant,  $B_{\infty}$  is the concentration of fully formed NBD-furan derivative and B is the concentration of current NBD-furan derivative. The Eac of the rDA reaction of NBD-AuNPs was determined using the Arrhenius equation and the experimental rate constants. Eac values of 87.5 kJ/mol for *endo*-NBD-AuNPs and 117.6 kJ/mol for *exo*-NBD-AuNPs were determined. Based on the rate constant obtained at each temperature, the corresponding half-lives were calculated and summarized in Table 3.1.

Subsequent TEM analyses of both *endo-* and *exo-*Ma-AuNPs (Maleimide-EG<sub>3</sub>-AuNPs) post-heating revealed that the NP maintained their sizes and size distribution  $(1.8 \pm 0.3 \text{ nm})$ ,

demonstrating the system's resilience and the efficacy of the thermal release mechanism (Figure 3.6).

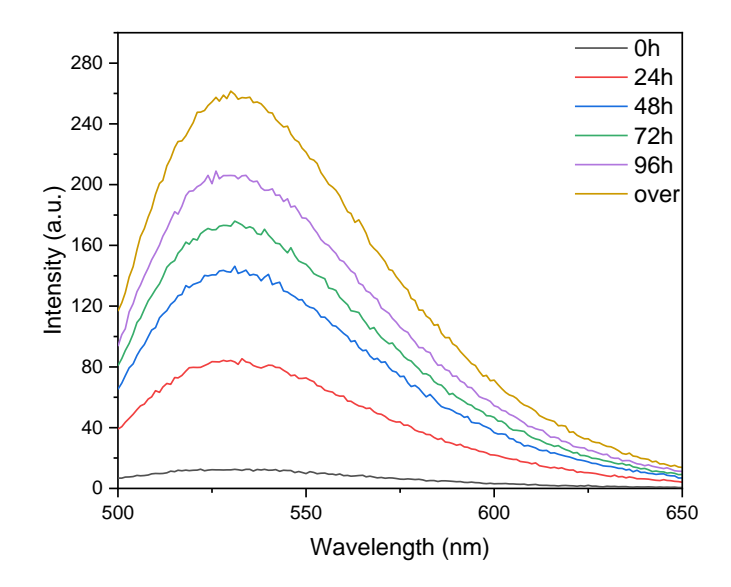


Figure 3.4: Release behavior of *endo*-NBD-AuNPs at 37°C monitored through fluorescence spectra (excitation wavelength at 467 nm).

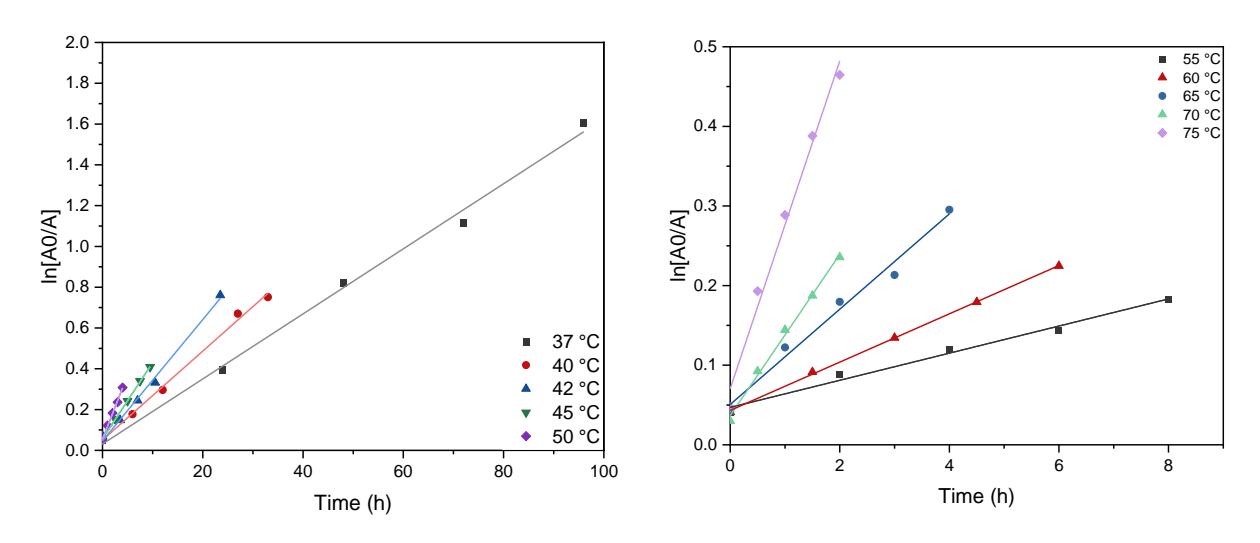


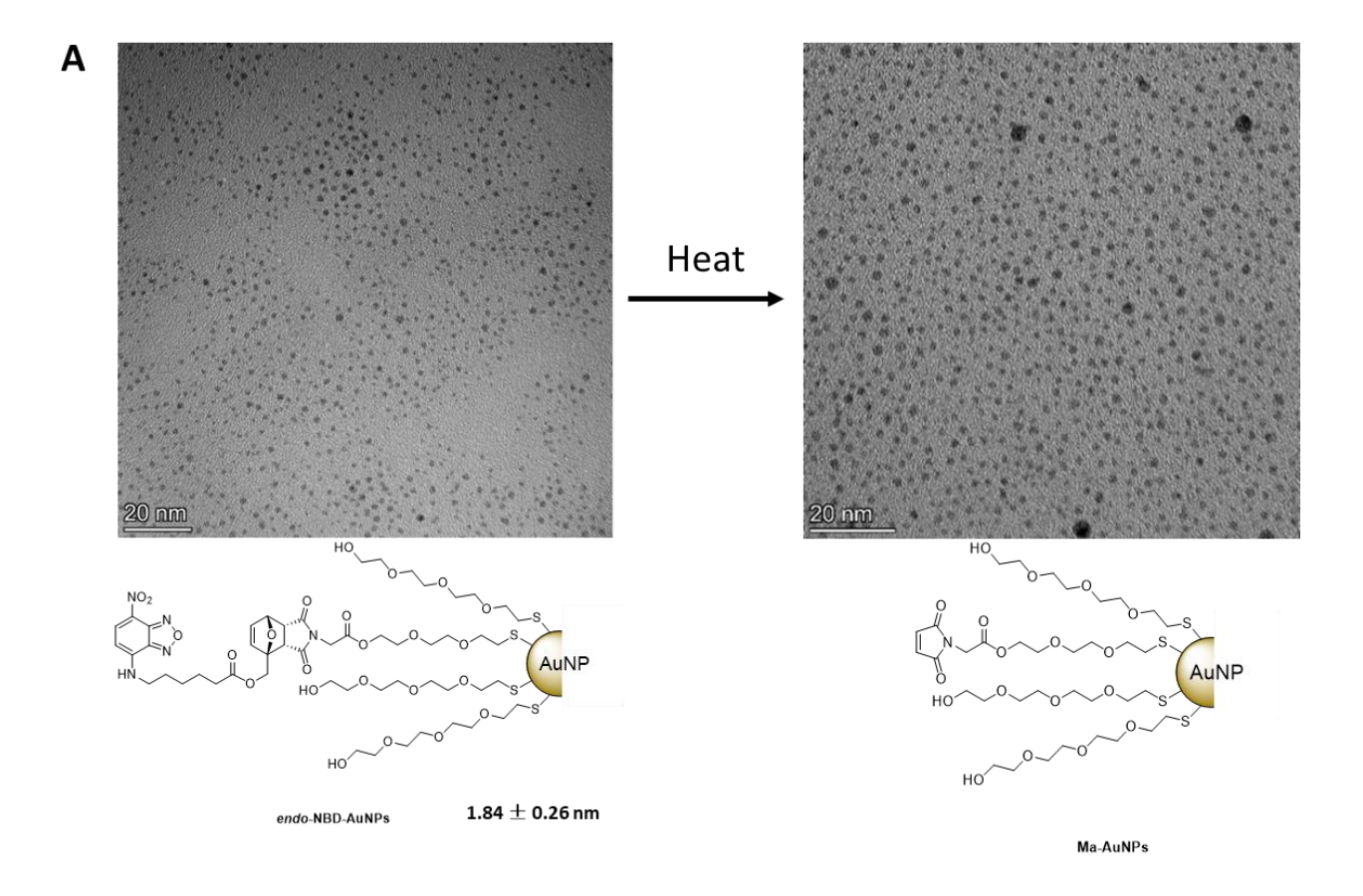
Figure 3.5: Results of the first-order model fit of the *endo-* and *exo-*NBD-AuNPs at different temperatures; *endo-*(left) at (37°C, 40 °C, 42 °C, 45 °C, 50°C) and *exo-*(right) NBD-AuNPs at (55 °C, 60 °C, 65 °C, 70 °C, 75 °C).

The half lives for both the *exo-* and *endo-*NBD-AuNPs were calculated at different temperatures using the corresponding rate constants, as shown in Table 3.1. These half-lives provide preliminary insights into the stability of the system and its potential for use in controlled release systems. It has been found that the temperature of solid tumors is typically 1.5°C higher than that of surrounding healthy tissue, which is approximately 37°C. In hyperthermia therapy, tumors are intentionally heated to higher temperatures, typically between 40°C and 45°C, using technologies such as radiofrequency, microwaves, ultrasound, or infrared heat. This temperature range is targeted to weaken or kill cancer cells more effectively while sparing normal cells, given that cancer cells are generally more sensitive to heat. Therefore, by extrapolating the half-lives to each of these temperatures, we can gain insights into the amount of drug released under different conditions. For instance, at the typical temperature of a solid tumor, the endo-NBD-AuNP exhibits a half-life of 36 hours. During hyperthermia therapy 45 °C, where the patient's tumor is intentionally heated, the *endo-*NBD-AuNPs have a reduced half-life of 18 hours. Conversely, when properly stored at normal freezer conditions (-20°C), the system's half-life extends to 10 years.

Table 3.1: The half-life values calculated for *endo-* (top) and *exo-*(bottom) NBD-AuNPs at different temperatures.

Temperature/°C	Half-life /(h)
37	38
40	24
42	19
45	13
50	6.0

Temperature/°C	Half-life /(h)
55	132
60	30
65	10
70	3.0
75	0.97



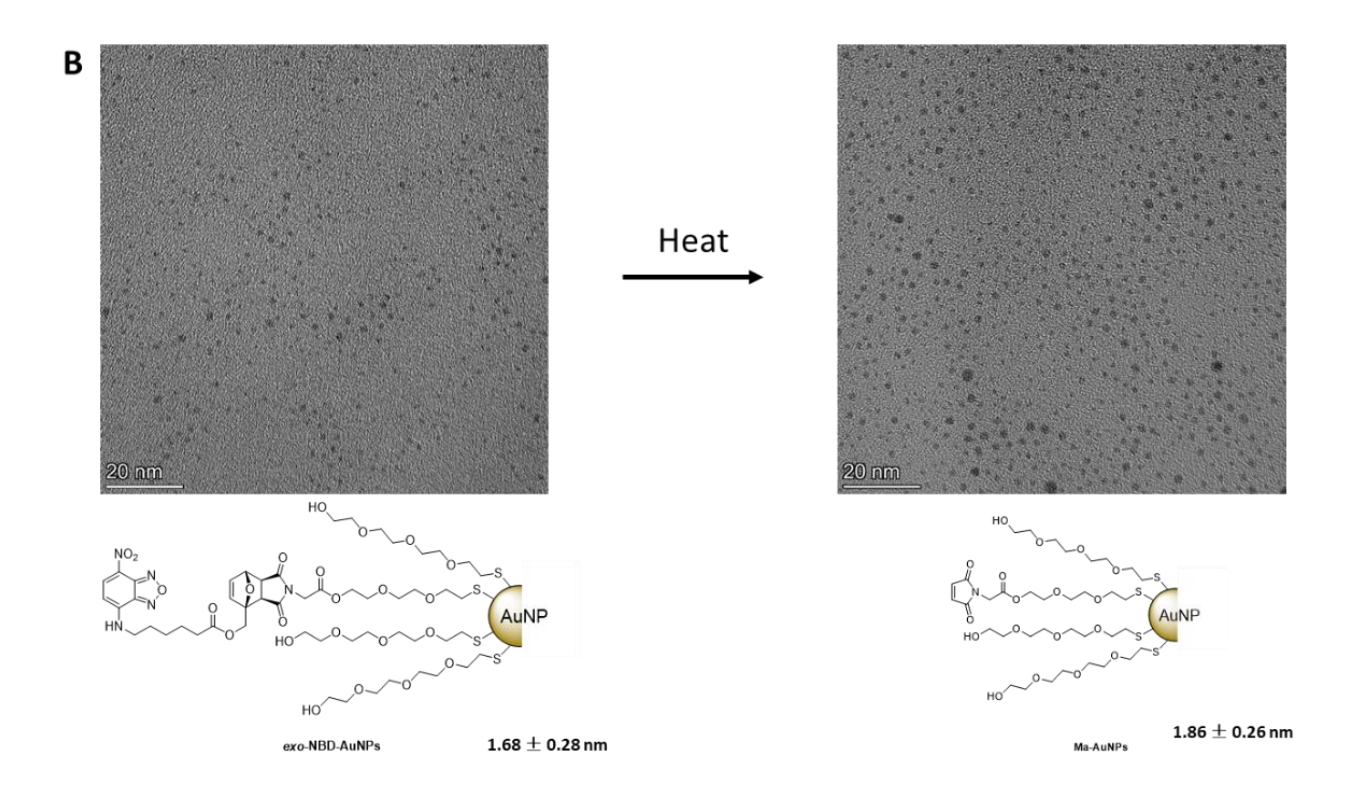


Figure 3.6: Monodispersity of AuNPs confirmation through TEM analysis; (A) TEM images of *endo*-NBD-AuNPs (left) and Ma-AuNPs right); (B) TEM images of *exo*-NBD-AuNPs (left) and Ma-AuNPs (right).

# 3.5 Conclusion and Perspective

In this Chapter, a delivery system using 2 nm diameter water soluble AuNPs was successfully synthesized and evaluated. NBD was first installed on the thiol ligands with both *endo* and *exo* DA linkers, then attached to the AuNPs through a ligand exchange reaction. The release capabilities of both *endo*- and *exo*-NBD loaded AuNPs were assessed via the increase in fluorescence intensity upon heating. The observed first-order kinetics of the rDA reaction, as per previous findings, demonstrates the system's capacity for predictable conditions for triggered release. Significant differences in reaction activation energies (87.5 kJ/mol for *endo*- NBD-AuNPs

and 117.6 kJ/mol for *exo*-NBD-AuNPs) result in a significant difference in the  $t_{1/2}$  of the two reactions at 50 °C (6 h vs 131 h) and by extrapolation, 38 h vs. 521 h at 37 °C. Post-heating TEM images confirmed that the AuNPs maintained their size and monodispersity (1.8  $\pm$  0.3 nm), demonstrating the system's resilience to changing conditions. Looking ahead, the combination of this linker system with therapeutic agents presents a promising avenue for further exploration. This approach promises not only targeted and efficient treatment options but also enhanced controllability, paving the way for the next generation of drug delivery systems.

### 3.6 Experimental

#### 3.6.1 Materials

Chemicals and solvents were purchased from Sigma Aldrich and used as received without further purification. Proton nuclear magnetic resonance ( $^{1}H$  NMR) spectra and carbon nuclear magnetic resonance ( $^{13}C$  NMR) spectra were acquired using Bruker Ascend 500 MHz or 400 MHz spectrometers. Chemical shifts ( $\delta$ ) are reported in parts per million (ppm) and are calibrated to the residual solvent peak. Coupling constants (J) are reported in Hertz (Hz). Multiplicities are reported using the following abbreviations: s = singlet; d = doublet; t = triplet; d = doublet of doublets.

## 3.6.2 Synthesis of Fluorophore-Linker Conjugate

## **Compound 2**

4-chloro-7-nitrobenzofurazan (60 mg, 0.3 mmol), 6-aminohexanoic acid (43 mg, 0.3 mmol) and NaHCO<sub>3</sub> (30 mg, 0.36 mmol) were combined in a 20 mL round bottom flask. The mixture was dissolved in 5 mL MeOH with a magnetic stir bar and heated at 50°C for 5 hours. Subsequently, the flask was cooled to room temperature, and the mixture was quenched with a 2M HCl solution. After that, the mixture was centrifuged at 2000 rpm for 3 minutes. The top aqueous layer was disposed, and the remaining orange solid was redissolved by saturated NaHCO<sub>3</sub> solution, followed by few drops of 2M HCl solution. The mixture was then centrifuged at 2000 rpm for 5 minutes. The crude product was washed with hexane to afford the orange solid (8.6×10<sup>-2</sup> g, 97% yield).

<sup>1</sup>H NMR (500 MHz, CD<sub>3</sub>CN)  $\delta$  8.48 (d, J = 8.8 Hz, 1H), 7.39 (s, 1H), 6.29 (d, J = 8.8 Hz, 1H), 3.50 (s, 2H), 2.29 (t, J = 7.4 Hz, 2H), 1.75 (p, J = 7.3 Hz, 2H), 1.63 (p, J = 7.4 Hz, 2H), 1.50 – 1.40 (m, 2H).

<sup>13</sup>C NMR (126 MHz, CD<sub>3</sub>CN) δ 175.0, 145.8, 145.4, 138.3, 99.8, 44.4, 34.0, 28.5, 27.0, 25.1.

HRMS (ESI) m/z:  $[M+H]^+$  calculated for  $C_{12}H_{14}N_4NaO_5$ : 317.0862, found 317.0863.

$$\begin{array}{c} \text{NO}_2 \\ \text{NO}_2 \\ \text{NO}_3 \\ \text{NO}_4 \\ \text{NO}_5 \\ \text{NO}_2 \\ \text{DMAP (0.1 equiv)} \\ \text{ACN , 0 °C , 8h} \\ \text{70 %} \\ \text{Chemical Formula: $C_{12}H_{14}N_4O_5$} \\ \text{Molecular Weight: $294.27} \\ \text{Chemical Formula: $C_{12}H_{14}N_4O_5$} \\ \text{Molecular Weight: $48.27} \\ \text{Chemical Formula: $C_{29}H_{34}BrN_5O_{12}$} \\ \text{Molecular Weight: $724.52$} \\ \text{Molecular Weight: $724.52$} \\ \end{array}$$

2 (79.2 mg, 2.6×10<sup>-5</sup> mol), tetrahydrophthalimide linker (59.7 mg, 1.3×10<sup>-4</sup> mol), EDC (82 mg, 5.3×10<sup>-4</sup> mol) and DMAP (1.6 mg, 1.3×10<sup>-5</sup> mol) were combined in a 20 mL round bottom flask. The reactants were dissolved in 5 mL dry acetonitrile and stirred overnight at 0 °C. The solvent was then removed by rotary evaporation, redissolved in 50 mL DCM and then washed with 20 mL brine 2 times. The organic layer was collected and dried with MgSO<sub>4</sub>, filtered, the rotary evaporated to remove the solvent. Afterwards, the crude product was purified by column chromatography to afford the yellow oil (67 mg, 70% yield).

<sup>1</sup>H NMR (400 MHz, CDCl<sub>3</sub>) δ 8.44 (d, J = 8.6 Hz, 1H), 6.59 (t, J = 5.9 Hz, 1H), 6.50 (dd, J = 5.8, 1.6 Hz, 1H), 6.35 (d, J = 5.8 Hz, 1H), 6.15 (d, J = 8.7 Hz, 1H), 5.31 (dd, J = 5.5, 1.6 Hz, 1H), 4.83 (d, J = 12.7 Hz, 1H), 4.59 (d, J = 12.7 Hz, 1H), 4.30 – 4.19 (m, 2H), 4.09 (s, 2H), 3.78 (t, J = 6.2 Hz, 2H), 3.75 – 3.60 (m, 4H), 3.55 – 3.41 (m, 5H), 2.43 (t, J = 7.2 Hz, 2H), 1.84 – 1.79 (m, 2H), 1.73 (p, J = 7.2 Hz, 2H), 1.54 – 1.48 (m, 2H).

<sup>13</sup>C NMR (101 MHz, CDCl<sub>3</sub>) δ 173.5, 173.0, 166.3, 144.3, 144.1, 144.0, 136.7, 136.0, 134.6, 89.7, 79.7, 71.3, 70.6, 70.5, 68.0, 64.9, 62.0, 48.1, 47.0, 43.8, 39.4, 33.7, 30.5, 30.4, 28.1, 26.3, 25.7, 24.2.

HRMS (ESI) m/z: [M+H] + calculated for C<sub>29</sub>H<sub>34</sub>BrN<sub>5</sub>NaO<sub>12</sub>: 746.1285, found 746.1280.

<sup>1</sup>H NMR (500 MHz, CDCl<sub>3</sub>)  $\delta$  8.49 (d, J = 8.6 Hz, 1H), 6.58 (dd, J = 5.8, 1.8 Hz, 1H), 6.45 (d, J = 5.7 Hz, 1H), 6.40 – 6.36 (m, 1H), 6.17 (d, J = 8.7 Hz, 1H), 5.31 (d, J = 1.7 Hz, 1H), 4.90 (d, J = 12.7 Hz, 1H), 4.50 (d, J = 12.7 Hz, 1H), 4.35 – 4.22 (m, 4H), 3.81 (t, J = 6.2 Hz, 2H), 3.75 – 3.62 (m, 6H), 3.54 – 3.45 (m, 4H), 3.11 (d, J = 6.5 Hz, 1H), 3.01 (d, J = 6.5 Hz, 1H), 2.42 (t, J = 7.1 Hz, 2H), 1.87 – 1.79 (m, 2H), 1.74 (q, J = 7.2 Hz, 2H), 1.58 – 1.48 (m, 2H).

<sup>13</sup>C NMR (126 MHz, CDCl<sub>3</sub>) δ 174.7, 173.5, 172.9, 166.5, 137.7, 137.4, 136.6, 135.9, 125.7, 89.6, 81.2, 71.4, 70.8, 70.6, 69.0, 65.1, 61.5, 50.4, 48.7, 43.8, 39.9, 34.4, 33.8, 30.6, 30.5, 28.2, 26.4, 24.4, 21.3.

HRMS (ESI) m/z: [M+H] + calculated for C<sub>29</sub>H<sub>34</sub>BrN<sub>5</sub>NaO<sub>12</sub>: 746.1285, found 746.1296.

$$\begin{array}{c} \text{NO}_2\\ \text{NO}$$

Either *endo*- or *exo*- **3** (32 mg,  $4 \times 10^{-5}$  mol) were dissolved in 10 mL of anhydrous THF under Ar in an ice bath. 0.01 mL of hexamethyldisilathiane ( $4.8 \times 10^{-5}$  mol) was added, followed by the addition of 0.048 mL mL of 1M TBAF solution in THF ( $4.8 \times 10^{-5}$  mol). After reaction for 1 hour, the reactants were diluted in 50 mL dichloromethane and then washed with 20 mL brine 5 times and 20 mL of NH<sub>4</sub>Cl solution. The organic layer was collected and dried with MgSO4, filtered, the rotary evaporated to remove the solvent to afford 0.0299 g of compounds **4** as a colorless oil (95% yield).

<sup>1</sup>H NMR (400 MHz, CDCl<sub>3</sub>) δ 8.46 (dd, J = 8.8, 2.3 Hz, 1H), 6.51 (d, J = 5.8 Hz, 1H), 6.36 (d, J = 5.7 Hz, 1H), 6.19 (d, J = 8.7 Hz, 1H), 5.32 (d, J = 5.4 Hz, 1H), 4.84 (d, J = 12.7 Hz, 1H), 4.61 (d, J = 12.7 Hz, 1H), 4.26 (t, J = 4.7 Hz, 2H), 4.10 (s, 2H), 3.85 – 3.46 (m, 5H), 3.38 – 3.29 (m, 1H), 3.03 – 2.93 (m, 1H), 2.69 (q, J = 6.5 Hz, 2H), 2.44 (t, J = 7.2 Hz, 2H), 1.72 (t, J = 7.3 Hz, 2H), 1.6 – 1.46(m, 4H).

<sup>13</sup>C NMR (101 MHz, CDCl<sub>3</sub>) δ 173.5, 173.5, 173.0, 166.4, 144.4, 144.0, 144.0, 136.6, 136.1, 134.7, 98.7, 89.8, 79.8, 71.4, 70.7, 70.6, 69.0, 65.0, 62.1, 48.2, 47.1, 43.8, 39.4, 33.7, 30.4, 28.2, 26.4, 24.3.

HRMS (ESI) m/z:  $[M+H]^+$  calculated for  $C_{29}H_{35}N_5NaO_{12}S$ : 700.1901, found 700.1895.

<sup>1</sup>H NMR (400 MHz, CDCl<sub>3</sub>) δ 8.49 (d, J = 8.6, 1H), 6.58 (dd, J = 5.7, 1.7 Hz, 1H), 6.45 (d, J = 5.7 Hz, 1H), 6.17 (d, J = 8.6 Hz, 1H), 5.31 (t, J = 2.0 Hz, 1H), 4.90 (d, J = 12.6 Hz, 1H), 4.50 (d, J = 12.6 Hz, 1H), 4.35 – 4.24 (m, 4H), 3.78 – 3.60 (m, 9H), 3.50 (q, J = 6.7 Hz, 2H), 3.11 (d, J = 6.5 Hz, 1H), 3.01 (d, J = 6.5 Hz, 1H), 2.70 (q, J = 6.3 Hz, 1H), 2.42 (t, J = 7.1 Hz, 2H), 1.89 – 1.65 (m, 4H), 1.63 – 1.47 (m, 2H).

<sup>13</sup>C NMR (101 MHz, CDCl<sub>3</sub>) δ 174.6, 173.4, 172.8, 166.4, 144.3, 143.9, 137.6, 137.3, 136.5, 98.6, 89.5, 81.0, 72.9, 70.6, 70.2, 68.8, 64.9, 61.3, 50.2, 48.6, 43.7, 39.8, 33.6, 28.0, 26.2, 24.3, 24.2.

HRMS (ESI) m/z: [M+H] + calculated for C<sub>29</sub>H<sub>35</sub>N<sub>5</sub>NaO<sub>12</sub>S:700.1901, found 700.1895.

Tetraethylene glycol (49.8 g, 0.256 mol) and triethylamine (3.56 mL,  $2.56 \times 10^{-2}$  mol) were combined in a 500 mL round bottom flask. The mixture was dissolved in 50 mL dichloromethane followed by the addition of 4-toluenesulfonyl chloride (4.88 g,  $2.56 \times 10^{-2}$  mol) dissolved in 5 mL dichloromethane. The reactants were capped and stirred under room temperature overnight and then diluted in 50 mL DCM. The crude product was washed by 40 mL brine three times to remove the access tetraethylene glycol. Then, the crude product was purified by column chromatography to afford the colorless oil (7.58 g, 85% yield).

<sup>1</sup>H NMR (400 MHz, CDCl<sub>3</sub>) δ 7.80 (d, J = 8.3 Hz, 2H), 7.34 (d, J = 7.9 Hz, 2H), 4.19 (t, J = 4.5 Hz, 2H), 3.75 – 3.57 (m, 14H), 2.45 (s, 3H), 2.36 (s, 1H).

 $^{13}C\ NMR\ (126\ MHz,\ CDCl_3)\ \delta\ 129.8,\ 128.0,\ 72.5,\ 70.8,\ 70.7,\ 70.5,\ 70.4,\ 69.3,\ 68.7,\ 61.8,\ 21.7.$ 

HRMS (ESI) m/z:  $[M+H]^+$  calculated for  $C_{15}H_{24}NaO_7S$ : 371.1140, found 371.1127.

Potassium thioacetate (0.4233 g,  $3.7 \times 10^{-3}$  mol) and **6** (1.1769 g,  $3.37 \times 10^{-3}$  mol) were dissolved in 20 mL acetone, and the mixture was refluxed at 50 °C overnight. After cooling to room temperature, the mixture was filtrated and washed with acetone. The mixture was diluted in 50 mL DCM, washed with brine 3 times and dried over MgSO<sub>4</sub>. Remove the solvent by rotary evaporation and leave the final product as a clear yellow oil with quantitative yield (0.758 g, 89% yield).

<sup>1</sup>H NMR (400 MHz, CDCl<sub>3</sub>)  $\delta$  3.76 – 3.56 (m, 14H), 3.10 (t, J = 6.5 Hz, 2H), 2.34 (s, 3H).

<sup>13</sup>C NMR (126 MHz, CDCl<sub>3</sub>) δ 195.6, 72.5, 70.7, 70.5, 70.4, 70.3, 69.8, 61.8, 30.6, 28.8.

HRMS (ESI) m/z:  $[M+H]^+$  calculated for  $C_{10}H_{20}NaO_5S$ : 275.0929, found 275.0992.

NaOH 1.0 equiv

HO

O

O

NaOH 1.0 equiv

HO

O

O

SH

MeOH, 0 °C, 1h

1.0 equiv

Chemical Formula: 
$$C_{10}H_{20}O_{5}S$$

Molecular Weight: 252.33

NaOH 1.0 equiv

Chemical Formula:  $C_{8}H_{18}O_{4}S$ 

Molecular Weight: 210.29

A 50 mL round bottom flask, equipped with a magnetic stirring bar, was charged with **7** (0.4943 g,  $1.95 \times 10^{-3}$  mol) and 20 mL MeOH. NaOH (0.164 g,  $4.1 \times 10^{-3}$  mol) was then dissolved in 10 mL volumetric flask of ethanol followed by 10 minutes of sonication until full dissolved. A 4.78 mL aliquot of the 0.4 M NaOH solution was added dropwise into the 50 mL round bottom flask. The mixture was allowed to stir in an ice bath for 1 hour under Ar. After that, the crude product was diluted in 50 mL and washed by 20 mL brine 2 times. The solvent was removed by rotary evaporation to afford a colorless oil. (0.358 g, 87% yield)

<sup>1</sup>H NMR (400 MHz, CDCl<sub>3</sub>)  $\delta$  3.76 – 3.59 (m, 14H), 2.71 (q, J = 8.2, 6.4 Hz, 2H), 1.63 (t, J = 8.2 Hz, 1H).

 $^{13}\text{C NMR}$  (126 MHz, CDCl<sub>3</sub>)  $\delta$  73.1, 72.6, 70.8, 70.7, 70.5, 70.4, 61.9, 24.4.

HRMS (ESI) m/z: [M+H] + calculated for C<sub>8</sub>H<sub>18</sub>NaO<sub>4</sub>S: 233.0824, found 233.08184.

## Synthesis of 2 nm PEGylated AuNPs

HO-EG<sub>4</sub>-AuNPs

 $HAuCl_4\cdot 3H_2O$  (0.2481 g,  $6.2\times 10^{-4}$  mol, 1.0 eq.) was dissolved in a mixture of methanol (30 mL) and glacial acetic acid (6 mL). Thiol **8** (0.2646 g,  $1.2\times 10^{-3}$  mol, 2.0 eq.) was added to this yellow solution. The reduction was initiated by rapidly introducing a methanol solution of NaBH<sub>4</sub> (0.2383 g,  $6.2\times 10^{-3}$ , 10.0 eq.) under vigorous stirring, resulting in an immediate color change to dark brown. The reaction mixture was then left to stir overnight at room temperature. Afterwards, the mixture was concentrated under reduced pressure to form a film of AuNPs, which was subsequently washed three times with a toluene/hexane mixture to remove the majority of the acetic acid. For further purification, the crude HO-EG<sub>4</sub>-AuNPs were redissolved in distilled water and subjected to dialysis for 3 days, ensuring the removal of residual reactants and by-products. The purity of the final HO-EG<sub>4</sub>-AuNPs was confirmed through <sup>1</sup>H NMR.

## Calculation of nanoparticle composition

Analysis of the data derived from TEM, NMR and TGA lead to an estimation of the composition of the AuNPs. To simplify the calculation, the AuNPs are assumed to be spherical, and their size is monodispersed.

The average number of gold atoms  $(N_{\text{Au}})$  per NP can be calculated from the following formula:

$$N_{Au} = \frac{\pi \rho d^3 N_A}{6 M_{Au}}$$

Where:

 $\rho$  = density of face centered cubic (fcc) gold lattice (19.3 g/cm<sup>3</sup>)

d = average diameter of nanoparticles

 $N_A$  = Avogadro constant

 $M_{Au}$  = mole atomic weight of gold (199.9665 g/mol)

The total number of ligands  $(N_L)$  per gold nanoparticle can be calculated using the following formula:

$$N_{L} = \omega \frac{N_{Au} M_{Au} / (1 - \omega)}{M W_{ligand1} \varphi + M W_{ligand2} (1 - \varphi)}$$

Where:

 $\omega$  = percentage of mass loss due to the protecting ligands

 $MW_{ligand}$  = molar weight of ligand

 $\varphi$  = molar percentage of ligand

#### Synthesis of NBD-Linker-AuNPs

The preparation of either *endo-* or *exo-*NBD-AuNPs involved a place exchange reaction, where ligand *endo-* or *exo-*4 was combined with previously prepared PEGylated AuNP. This process was conducted in methanol, where the ligand and nanoparticles were mixed at optimized 50:1 molar ratio of thiol 4 to HO-EG<sub>4</sub>-AuNPs. The reaction was allowed to proceed for two hours under inert gas to protect the reactants from oxidation. Following the reaction, the resulting NBD-AuNPs sample was purified through dialysis for 2 days at 4 °C to ensure the removal of unreacted ligands. The purity of the final NBD-AuNPs product was verified by <sup>1</sup>H NMR spectroscopy, confirming the successful incorporation of the ligands into the nanoparticle ligand layer.

# Calculation of NBD-AuNP conversion to Ma-AuNPs as monitored by fluorescence spectroscopy.

The kinetics of the dissociation reaction from NBD-AuNPs (A) to Ma-AuNPs (B) were determined via the following:

	Α -	<b>→</b> B
Initial	$A_0$	0
During the reaction	At	$A_0$ - $A_t$ = $B$
Completion of reaction	0	$A0=B_{\scriptscriptstyle \infty}$
First order kinetic equation	$ln [A_t] = -kt + ln[A_0]$	
Replacing A <sub>t</sub> with A <sub>0</sub> - B	$ln [A_0 - B] = -kt + ln[B_{\infty}]$	
Rearrangement	$ln [A_0 - B] - ln[B_{\infty}] = -kt$	
		D.

Replacing  $A_0$  with  $B_{\infty}$  and rearrangement  $\quad kt = ln[\frac{B_{\infty}}{B_{\infty}-B}]$ 

#### 3.7 References

- (1) Cao, J.; Huang, D.; Peppas, N. A. Advanced Engineered Nanoparticulate Platforms to Address Key Biological Barriers for Delivering Chemotherapeutic Agents to Target Sites. *Advanced Drug Delivery Reviews* **2020**, *167*, 170–188. https://doi.org/10.1016/j.addr.2020.06.030.
- (2) Kim, C.; Ghosh, P.; M. Rotello, V. Multimodal Drug Delivery Using Gold Nanoparticles. *Nanoscale* **2009**, *I* (1), 61–67. https://doi.org/10.1039/B9NR00112C.
- (3) Hong, R.; Han, G.; Fernández, J. M.; Kim, B.; Forbes, N. S.; Rotello, V. M. Glutathione-Mediated Delivery and Release Using Monolayer Protected Nanoparticle Carriers. *J. Am. Chem. Soc.* **2006**, *128* (4), 1078–1079. https://doi.org/10.1021/ja056726i.
- (4) Kazmi, S. A. R.; Qureshi, M. Z.; Ali, S.; Masson, J.-F. In Vitro Drug Release and Biocatalysis from pH-Responsive Gold Nanoparticles Synthesized Using Doxycycline. *Langmuir* **2019**, *35* (49), 16266–16274. https://doi.org/10.1021/acs.langmuir.9b02420.
- (5) Hu, Q.; S. Katti, P.; Gu, Z. Enzyme-Responsive Nanomaterials for Controlled Drug Delivery. *Nanoscale* **2014**, *6* (21), 12273–12286. https://doi.org/10.1039/C4NR04249B.
- (6) Zhang, Q.; Gong, Y.; Guo, X.; Zhang, P.; Ding, C. Multifunctional Gold Nanoparticle-Based Fluorescence Resonance Energy-Transfer Probe for Target Drug Delivery and Cell Fluorescence Imaging. *ACS Appl. Mater. Interfaces* **2018**, *10* (41), 34840–34848. https://doi.org/10.1021/acsami.8b12897.
- (7) Nam, J.; La, W.-G.; Hwang, S.; Ha, Y. S.; Park, N.; Won, N.; Jung, S.; Bhang, S. H.; Ma, Y.-J.; Cho, Y.-M.; Jin, M.; Han, J.; Shin, J.-Y.; Wang, E. K.; Kim, S. G.; Cho, S.-H.; Yoo, J.; Kim, B.-S.; Kim, S. pH-Responsive Assembly of Gold Nanoparticles and "Spatiotemporally Concerted" Drug Release for Synergistic Cancer Therapy. *ACS Nano* **2013**, *7* (4), 3388–3402. https://doi.org/10.1021/nn400223a.
- (8) Shiao, Y.-S.; Chiu, H.-H.; Wu, P.-H.; Huang, Y.-F. Aptamer-Functionalized Gold Nanoparticles As Photoresponsive Nanoplatform for Co-Drug Delivery. *ACS Appl. Mater. Interfaces* **2014**, *6* (24), 21832–21841. https://doi.org/10.1021/am5026243.
- (9) Yang, Z.; He, G.; Cai, D.; Ren, Z. Photothermal Heating-Induced Localized Structural Disruption in a Poly-ε-Caprolactone Nanocarrier System for Controlled Drug Delivery. *ACS Appl. Bio Mater.* **2019**, 2 (1), 464–469. https://doi.org/10.1021/acsabm.8b00662.
- (10) Klelemen, H.; Hancu, G.; Kacsó, E.; Papp, L.-A. Photosensitivity Reactions Induced by Photochemical Degradation of Drugs. *Adv Pharm Bull* **2022**, *12* (1), 77–85. https://doi.org/10.34172/apb.2022.010.
- (11) Zhu, J.; Waengler, C.; Lennox, R. B.; Schirrmacher, R. Preparation of Water-Soluble Maleimide-Functionalized 3 Nm Gold Nanoparticles: A New Bioconjugation Template. *Langmuir* **2012**, 28 (13), 5508–5512. https://doi.org/10.1021/la300316j.
- (12) Baban, D. F.; Seymour, L. W. Control of Tumour Vascular Permeability. *Advanced Drug Delivery Reviews* **1998**, *34* (1), 109–119. https://doi.org/10.1016/S0169-409X(98)00003-9.
- (13) Carnovale, C.; Bryant, G.; Shukla, R.; Bansal, V. Identifying Trends in Gold Nanoparticle Toxicity and Uptake: Size, Shape, Capping Ligand, and Biological Corona. *ACS Omega* **2019**, *4* (1), 242–256. https://doi.org/10.1021/acsomega.8b03227.
- (14) Zhu, J.; Chin, J.; Wängler, C.; Wängler, B.; Lennox, R. B.; Schirrmacher, R. Rapid 18F-Labeling and Loading of PEGylated Gold Nanoparticles for in Vivo Applications. *Bioconjugate Chem.* **2014**, 25 (6), 1143–1150. https://doi.org/10.1021/bc5001593.

- (15) Goodman, C. M.; McCusker, C. D.; Yilmaz, T.; Rotello, V. M. Toxicity of Gold Nanoparticles Functionalized with Cationic and Anionic Side Chains. *Bioconjugate Chem.* **2004**, *15* (4), 897–900. https://doi.org/10.1021/bc049951i.
- (16) Bhatt, N.; Huang, P.-J. J.; Dave, N.; Liu, J. Dissociation and Degradation of Thiol-Modified DNA on Gold Nanoparticles in Aqueous and Organic Solvents. *Langmuir* **2011**, 27 (10), 6132–6137. https://doi.org/10.1021/la200241d.
- (17) Han, G.; You, C.-C.; Kim, B.-J.; Turingan, R. S.; Forbes, N. S.; Martin, C. T.; Rotello, V. M. Light-Regulated Release of DNA and Its Delivery to Nuclei by Means of Photolabile Gold Nanoparticles. *Angew Chem Int Ed Engl* **2006**, *45* (19), 3165–3169. https://doi.org/10.1002/anie.200600214.
- (18) Dulkeith, E.; Ringler, M.; Klar, T. A.; Feldmann, J.; Muñoz Javier, A.; Parak, W. J. Gold Nanoparticles Quench Fluorescence by Phase Induced Radiative Rate Suppression. *Nano Lett.* **2005**, *5* (4), 585–589. https://doi.org/10.1021/nl0480969.
- (19) Chompoosor, A.; Han, G.; Rotello, V. M. Charge Dependence of Ligand Release and Monolayer Stability of Gold Nanoparticles by Biogenic Thiols. *Bioconjugate Chem.* **2008**, *19* (7), 1342–1345. https://doi.org/10.1021/bc8000694.
- (20) Montalti, M.; Prodi, L.; Zaccheroni, N.; Baxter, R.; Teobaldi, G.; Zerbetto, F. Kinetics of Place-Exchange Reactions of Thiols on Gold Nanoparticles. *Langmuir* **2003**, *19* (12), 5172–5174. https://doi.org/10.1021/la034581s.

# Chapter 4. A Controlled 'Load and Release' Reaction on Water-Soluble Gold Nanoparticles

#### 4.1 Preface

Chapter 4 builds on the foundational work of the previous chapters by refining and enhancing a controlled release system that uses 2 nm water soluble gold nanoparticles (AuNPs). This Chapter further explores the efficacy of a tetrahydrophthalimide linker for the efficient loading and controlled (thermal) release of therapeutic agents, particularly those containing carboxyl groups by detailing the synthesis, functionalization, and characterization of these AuNPs, particularly with an acridine derivative and other therapeutic agents. A detailed kinetic analysis using fluorescence spectroscopy and <sup>1</sup>H NMR to track reaction progress reveals the system's effectiveness across a physiological relevant temperature range. These investigations mark an advancement in nanoparticle-mediated drug delivery but also demonstrate the system's versatility and adaptability to a range of therapeutic compounds, setting the stage for future applications in therapeutics.

#### 4.2 Abstract

This Chapter presents the design, synthesis, and characterization of 2 nm AuNPs for the efficient loading and controlled release of therapeutic agents. The system involves a tetrahydrophthalimide linker that facilitates the attachment of carboxyl group-bearing molecules without having to use laborious purification steps. As a test system, a water-soluble acridine derivative was specifically designed, synthesized, and conjugated to ligand-capped AuNPs to assess the load-and-release processes that occur. The release kinetics follow a first order rate law across a physiologically-relevant temperature range, using fluorescence spectroscopy to track the loss of the acridine derivative from the ligand layer. These findings were extended to two additional test cases involving known therapeutic agents, sulindac and chlorambucil. The release reactions of chlorambucil—conjugated and sulindac-conjugated AuNPs were monitored by <sup>1</sup>H NMR, and the detached furfuryl alcohol derivatives were isolated, and their composition confirmed using high resolution mass spectrometry (HRMS). Overall, the versatility and efficiency of this drug load-and-release methodology highlights its potential in controlled drug delivery applications.

#### 4.3 Introduction

The need for effective drug delivery systems has long been a concern in the field of therapeutics. The emergence of nanomaterials over the past two decades has opened new avenues for the development of sophisticated delivery vehicles capable of targeting specific biological sites and releasing therapeutic agents in a controlled manner. AuNPs, with their unique optical properties and potential for derivatization for both cargo (drug) derivatization and biocompatibility, have emerged as promising candidates in this field.<sup>1</sup>

There have been two primary approaches to covalently attaching molecules of interest onto AuNPs: ligand exchange reactions and interfacial reactions of the protecting ligands. The ligand exchange method involves synthesizing thiol derivatives that attach to the AuNPs and then using them to replace existing ligands. However, this approach often presents significant challenges in terms of synthetic accessibility, efficacy, and reproducibility. Tailored and complex synthetic pathways are often required. For example, Wang et al used an acid-labile hydrazine linkage to tether doxorubicin to AuNPs, enhancing drug accumulation and retention in cancer cells compared to free doxorubicin.<sup>2</sup> To overcome the complexities of syntheses, significant attention has shifted towards interfacial reactions for loading cargo onto AuNPs. Taking the case of doxorubicin again, Kang et al achieved the loading of doxorubicin onto AuNPs through a pH-sensitive hydrazine linkage. Upon release, a recovery of fluorescence was observed, demonstrating the release dynamics.<sup>3</sup> In a further innovation in the interfacial loading reaction, Luo et al developed reactive moieties capable of loading and releasing molecules onto/from the ligand capping layer of thiolprotected AuNPs. They utilized an electrophilic ester-bound strained cyclooctyne, which covalently captures general payloads via 1,3-dipolar cycloaddition. The attached cargo, tethered through triazole or isoxazoline linkages, can subsequently be liberated using Staudinger-Bertozzi ligation 'click-to-release' chemistry triggered by an exogenous azide.<sup>4</sup> The Diels-Alder (DA) reaction on the other hand provides another platform to achieve programmable, triggered release with its characteristic reversible and site-specific conjugation advantages. Increasing attention has therefore been directed to the use of this reaction in the surface modification and labelling of biomolecules over the last decade.<sup>5</sup> For example, Chen et al utilized a DA reaction for creating single-stranded DNA-silver nanoparticle conjugates, demonstrating the versatility of this method in complex biological matrices.<sup>6</sup> However, the reverse DA reaction has been relatively less

investigated due to the harsher reaction conditions required. Therefore, most papers on reverse DA reactions have focused on the reaction of furan and maleimide, because of the relatively mild conditions required for this rDA reaction.<sup>5</sup> For example, Zhu et al used a thermally reversible DA reaction for constructing monolayer protected AuNPs, showcasing the durability and reusability of these systems through multiple cycles without degradation. While current studies primarily focus on either click chemistry or release of conjugates via conventional methods, precise therapeutic targeting often requires the use of biomolecules like antibodies or aptamers attached to AuNPs. However, the viability of these biomolecules can often be reduced by degradation or denaturation due to proteases, pH variation, or the presence of other biomolecules. 8 Furthermore, systems designed for triggered release, such as those activated by pH, 9,10 redox conditions, 11 or light, <sup>12</sup> often lack precise control over the quantity and location of drug released. Therefore, we undertook to design a click-and-release method for attaching molecules to AuNPs through interfacial esterification and releasing them through a rDA reaction. In doing so, some limitations of traditional click chemistry methods and the achievement of precise control over the quantity of molecules released are addressed. To test the compatibility of the designed system with small molecule targets, the synthesis of a water-soluble acridine derivative was introduced with its subsequent conjugation to the AuNPs along with an assessment of the release kinetics. The introduction of small molecule drugs, chlorambucil and sulindac, into this system to analyze the compatibility of system with other therapeutically interesting small molecules.

Chlorambucil belongs to a class of drugs known as alkylating agents used in chemotherapy. It is primarily used to treat various types of cancer, including chronic lymphocytic leukemia and non-Hodgkin's lymphoma. On the other hand, Sulindac is a nonsteroidal anti-inflammatory drug which is used to treat pain, fever, and inflammation. These therapeutic agents, chosen for their

relevance in prior drug delivery studies,  $^{18,19}$  pose significant dosage/delivery challenges due to their poor aqueous solubility. This solubility is crucial for achieving effective drug concentrations under physiological conditions and remains a significant hurdle in drug development. In addressing similar challenges, Suresh et al employed a water-reactive metal-organic framework (MOF) as a carrier to enhance solubility, creating a drug@MOF composite that prevents crystallization of the amorphous phase drug, stable for over four months, and facilitates immediate release in dissolution media upon MOF decomposition.  $^{20}$  Guan et al developed an enzymeresponsive supramolecular assembly using sulfato- $\beta$ -cyclodextrin and chlorambucil, demonstrating a functional approach for controlled drug release.  $^{21}$  Our system, on the other hand, leverages the unique properties of AuNPs to enhance the water solubility of these drugs, thereby improving their delivery efficiency.

This Chapter thus reports the design and synthesis of 2 nm PEGylated AuNPs tailored for the conjugation of therapeutic cargos through an efficient esterification process. Central to the design is the incorporation of a hydroxyl-containing tetrahydrophthalimide linker, which facilitates the attachment of target molecules without the synthesis of individual thiol derivatives. Two low MW hydrophobic drugs, sulindac (MW = 356.41 g/mol) and chlorambucil (MW = 304.212 g/mol), were covalently bonded onto the AuNPs and their thermal releasing properties studied. The drug-loaded AuNPs demonstrate excellent stability in storage and effective release triggered by heating to 40 °C – conditions important to their potential use as a drug delivery system.

#### **4.4 Result and Discussion**

# 4.4.1 Synthesis and Characterization and Linker-AuNPs

2 nm methoxy-terminated PEGylated AuNPs were employed as a foundational material for conjugating small molecules of interest. The methoxy-terminated thiol (MeO-EG<sub>4</sub>-SH) was synthesized as described in Scheme 1. A one-phase method was applied to the synthesis of MeO-EG<sub>4</sub>-AuNPs by reduction of HAuCl<sub>4</sub>·3H<sub>2</sub>O by NaBH<sub>4</sub> in the presence of methoxy-terminated thiol yielded AuNPs (Scheme 4.1). The MeO-EG<sub>4</sub>-AuNPs exhibited excellent stability when stored in solution at -20 °C for extended periods. The final composition of MeO-EG<sub>4</sub>-AuNPs was determined to be Au<sub>400</sub>[MeO-EG<sub>4</sub>-S<sup>-</sup>]<sub>200</sub> from the convergence of TEM and TGA data, with a confirmed diameter of  $1.6 \pm 0.3$  nm. Thus, these AuNPs could serve as highly resilient substrates for further modification and applications. Further experimental details regarding their synthesis, characterization and calculations are provided in the Experimental Section.

The thiol tetrahydrophthalimide linker was then incorporated onto AuNPs via a ligand exchange reaction with MeO-EG<sub>4</sub>-AuNPs, to form Thp-AuNPs (tetrahydrophthalimide-AuNPs) as illustrated in Scheme 4.1. The place exchange reaction condition was optimized in order to maintain AuNP water solubility with high level of modified ligand loading. The maximum loading capacity was determined by adjusting the ratio of linker thiol to PEGylated AuNP during the ligand exchange reaction, as well as by modifying the reaction time. Thp-AuNPs was subsequently purified by dialysis at 4 °C. The <sup>1</sup>H NMR spectrum of the resulting Thp-AuNPs (Figure 4.1) exhibit broadened peaks consistent with the ligands being bound to the AuNP surface. The absence of sharp peaks in this region confirms the absence of free tetrahydrophthalimide linker in solution, thereby confirming the effectiveness of the purification process in removing unbound thiols and disulfides. New peaks were identified at 6.50, 6.39, and 5.32 ppm, which are indicative of the

successful attachment of the linker ligands to the AuNPs. These peaks are consistent with the expected chemical shifts arising from the ligand environment introduced by the linker. Additionally, a peak at 3.37 ppm is attributed to methoxy (MeO-) groups, and peaks at 3.64 and 3.54 ppm correspond to CH protons present in the PEG oligomer. Quantitative NMR data suggests that a linker thiolate-to-MeO-PEG thiolate loading ratio 1:6 or approximately 16%. Complementary thermogravimetric analysis (TGA) reveals a total weight loss of 34%, which aligns with the expected mass loss from organic components bound to the nanoparticles. (Figure 4.1). The composition of Thp-AuNPs was thus determined as being Au<sub>400</sub>[MeO-EG<sub>4</sub>-S<sup>-</sup>]<sub>184</sub>[linker]<sub>16</sub>, from the convergence of TEM, NMR and TGA data (Experimental Section)

Scheme 4.1: The synthetic scheme of a short PEG oligomer thiol (MeO-EG<sub>4</sub>-SH) and water-soluble Thp-AuNPs.

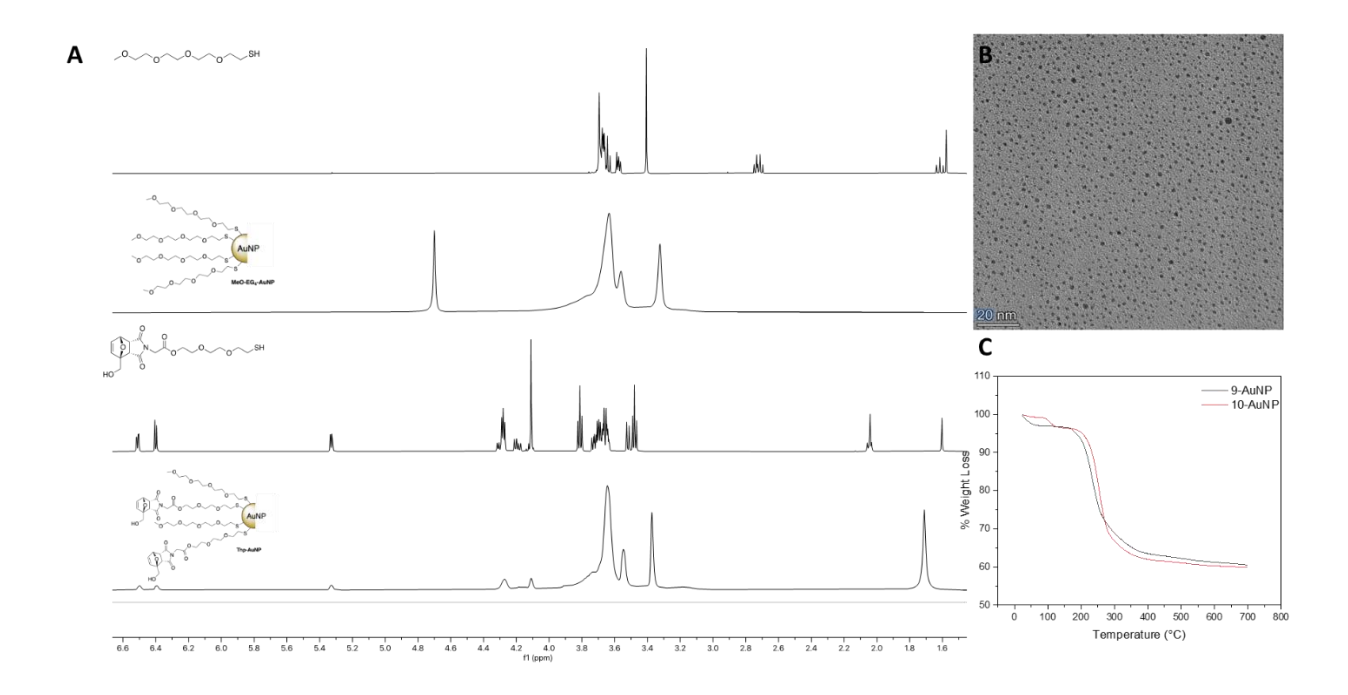


Figure 4.1: Characterizations of MeO-EG<sub>4</sub>-AuNPs and Thp-AuNPs (A)Stacked <sup>1</sup>H NMR of MeO-EG<sub>4</sub>-SH, MeO-EG<sub>4</sub>-AuNPs, tetrahydrophthalimide linker thiol and Thp-AuNPs; (B) TEM image of Thp-AuNPs; (C) TGA scan of MeO-EG<sub>4</sub>-AuNPs and Thp-AuNPs.

## 4.4.2 Interfacial Esterification Coupling Reaction of 10-AuNP with Small Molecules

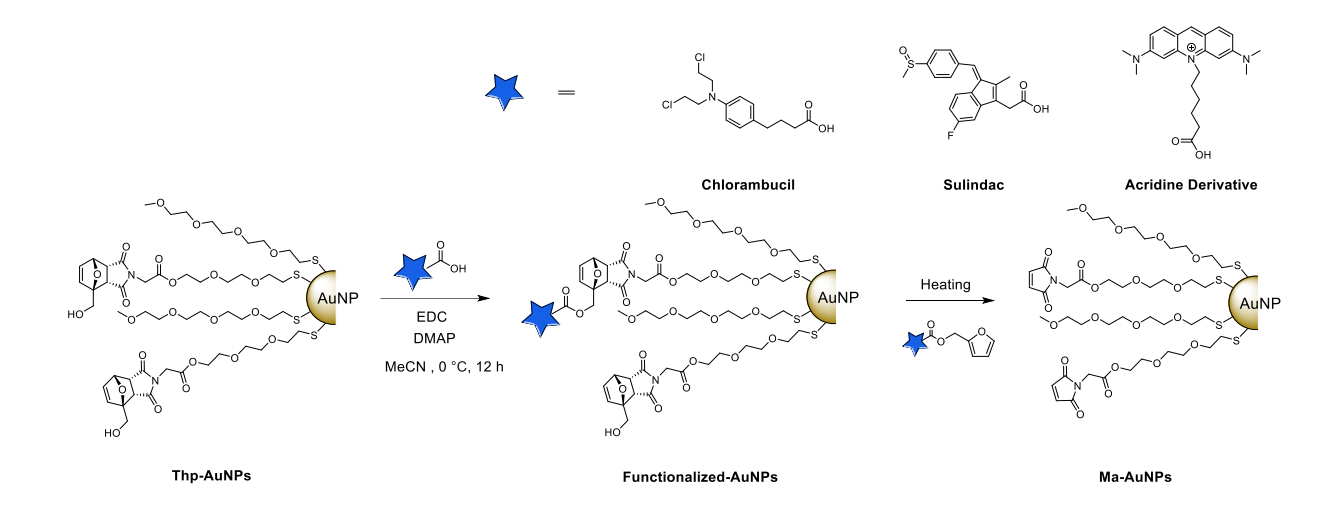
The monitoring of a NP ligand capping layer's composition as a function of conditions including time can be quite accurately determined if the ligand conjugate is fluorescent and whose fluorescence is quenchable by the AuNP core. In the system developed here, cargo is loaded onto AuNPs via an esterification reaction associated with the hydroxyl group on the linker and the cargo's carboxyl group. The reactivity of functional ligands on nanoparticles, however, can possibly be influenced by the local steric environment of the nanoparticle capping layer. Therefore, assessing the reactivity and availability of the hydroxyl end groups of Thp-AuNPs before conjugating carboxyl group-bearing compounds was crucial. Initial attempts to evaluate the

click efficiency using excess rhodamine B in a non-aqueous solvent were unsuccessful, likely due to steric hindrance from its ortho- carboxyl group. To mitigate this, 4-phenylbutyric acid was selected and successfully coupled with Thp-AuNPs and confirmed by the <sup>1</sup>H NMR spectrum. However, due to the excess amount of 4-phenylbutyric acid used, the as-prepared AuNPs become insoluble in water and are soluble only in organic solvents. Nonetheless, this result confirmed that the hydroxyl terminus in Thp-AuNPs was accessible toward the demands of the esterification reaction and was reactive for further modification.

As reported in Chapter 2, fluorophore-conjugated AuNPs have been used to monitor the release of molecular conjugates. This technique has been effectively applied by researchers to study the release kinetics through the detachment of fluorophores from AuNPs. Building on these foundational studies, we also aim to use the detachment of fluorophores to analyze the release kinetics of this system. This approach allows one to monitor the release behavior and effectiveness of our targeted delivery strategy.

Several fluorophore candidates, including rhodamine B, rosamine, a water-soluble coumarin, and NBD-X were thus evaluated. Rosamine, with its para- carboxyl group, showed less steric hindrance than rhodamine B but degrades rapidly upon mild heating. Similarly, coumarin experiences thermal stability issues likely due to the relatively reactive ester bond. Although NBD showed excellent thermal stability, its poor water solubility limits the extensive loading that is sought. Acridine was thus considered as a trial candidate as it is fluorescent with high thermal stability, good water solubility, and minimally prone to steric effects. Biver et al previously demonstrated the compatibility of acridine and ligand-capped AuNPs as they successfully incorporated an acridine derivative onto AuNPs using an Au-S bond, exploiting acridine's ability to partially intercalate with DNA. This created a multifunctional probe with specific photo-

responsive properties in both absorbance and emission, suitable for binding DNA.<sup>14</sup> The thermal stability of acridine, demonstrated in previous studies<sup>,15,16</sup> supported its choice for analyzing the thermal release kinetics of our designed system. The synthetic details resulting in access to the desired acridine derivative are presented in the Experimental Section.



Scheme 4.2: Synthesis of Acr-AuNPs, Chr-AuNPs and Sun-AuNPs.

The preparation of target compound functionalized AuNPs was conducted via an interfacial esterification reaction (Scheme 4.2), where the acridine reacted overnight with Thp-AuNPs, at a weight ratio of 1:2, to achieve the maximum loading capacity. Unlike a ligand exchange reaction, where the reaction time and the ratio of thiol/PEGylated AuNP could be used to precisely monitor the loading capacity, in this system, the extent of cargo loading can be finely adjusted by altering the starting acridine quantity. Due to the amphiphilicity of the Thp-AuNPs, the coupling could be conducted either in water or organic solvents, using various coupling reagents as summarized in Table 4.1. The protic solvent system was modified from previous studies. <sup>17</sup> This versatility enables the loading of both hydrophobic and hydrophilic cargo while preserving the amphiphilicity of the AuNP system post-incorporation. The crude AuNPs mixture was purified by overnight dialysis at 4 °C, with residual free acridine removed *via* a desalting column. It was imperative to eliminate

any unbound acridine to establish a baseline fluorescence from which the release kinetics could be accurately determined. Successful acridine loading onto the Thp-AuNPs was verified by <sup>1</sup>H NMR spectroscopy, comparing the spectra of the resulting Acr-AuNPs (Acridine-AuNPs) (Figure 4.2, bottom) with the linker-acridine conjugate (Figure 4.2, middle) and Thp-AuNPs (Figure 4.2, top). The observed spectral broadening indicated effective purification and loading, with approximately 60% of the linker conjugated with acridine based on spectral integration. The composition of Acr-AuNPs was thus determined as being Au<sub>400</sub>[MeO-EG<sub>4</sub>-S<sup>-</sup>]<sub>184</sub>[linker]<sub>5</sub>[Acridine]<sub>11</sub>, from the convergence of NMR and TGA data.

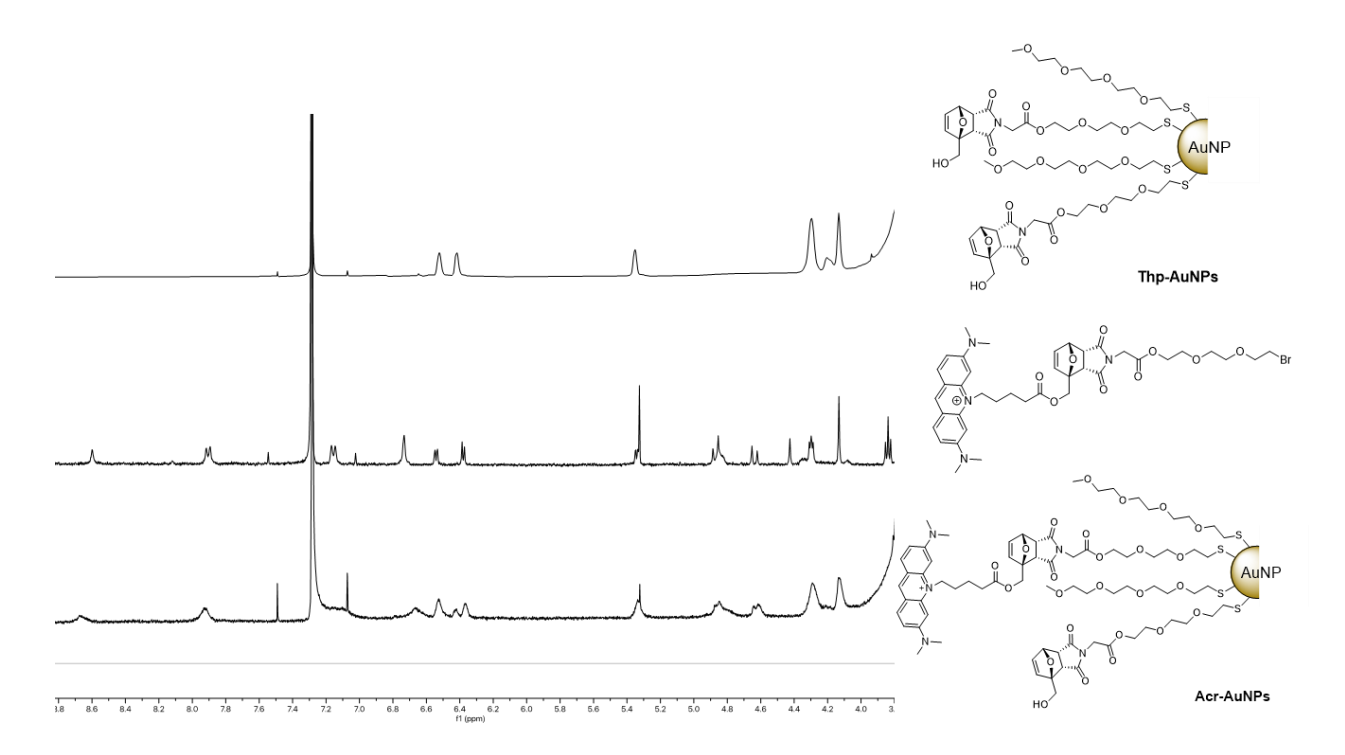


Figure 4.2: Characterizations of Acr-AuNPs; Stacked <sup>1</sup>H NMR of Thp-AuNPs, Acridine-Linker conjugate and Acr-AuNPs.

Table 4.1: Coupling conditions of Thp-AuNPs with chlorambucil, sulindac, and acridine derivative.

Solvent	Acridine/mg	10-AuNP/mg	Coupling Regents	pН
MeCN	1	3	DCC	/
9:1 MeCN: H <sub>2</sub> O	2	3	EDC NHS	4

The compatibility of Thp-AuNPs with other small molecules was also examined, as detailed in Scheme 4.2. As previously discussed, the hydroxyl group on the tetrahydrophthalimide linker was designed to couple with the carboxyl group of target therapeutic drugs through an interfacial esterification reaction. Despite the hydrophobicity of the chosen drug molecules, successful conjugation was achieved using an aprotic solvent system and EDC as the coupling agent. The drug loading onto the AuNPs was verified by <sup>1</sup>H NMR (Figure 4.3), where peak broadening in the spectra indicated effective coupling to the AuNP monolayer. To determine the maximum loading capacity of each drug on the AuNP, the quantity of model drug used as the starting material was varied. Through <sup>1</sup>H NMR integration ratio analyses, it was determined that nearly 50% of the linker molecules had successfully bonded to the model drugs, while maintaining the hydrophilicity of the system. Further characterization by TEM indicated the preservation of the AuNPs' size and size distribution and EDX spectroscopy confirmed the successful loading of each of the small molecule drugs. Specifically, the EDX spectrum reveals the presence of chlorine in Chr-AuNPs (chlorambucil-AuNPs) and fluorine in Sun-AuNPs (Sulindac-AuNPs). These findings highlight the efficiency and adaptability of the drug loading technique reported here, which are essential for optimizing drug delivery performance and enhancing therapeutic efficacy. The composition of the resulting AuNPs was thus determined as being Au<sub>400</sub>[MeO-EG<sub>4</sub>-

 $S^{\text{-}}]_{184}[linker]_{5}[Chlorambucil]_{8} \quad and \quad Au_{400}[MeO\text{-}EG_{4}\text{-}S^{\text{-}}]_{184}[linker]_{5}[Sulindac]_{8}, \quad from \quad the \\ convergence of NMR and TGA data.$ 

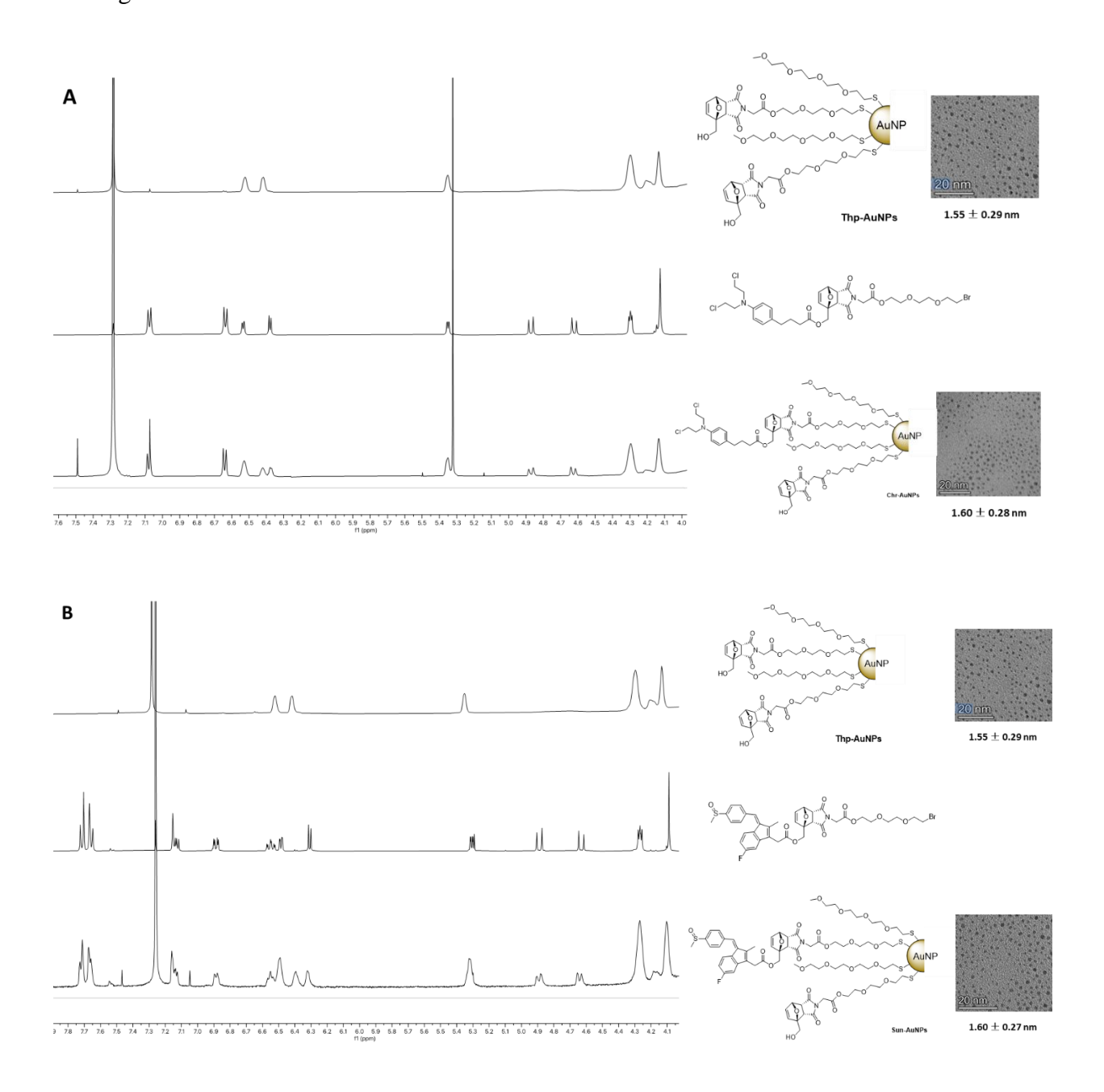
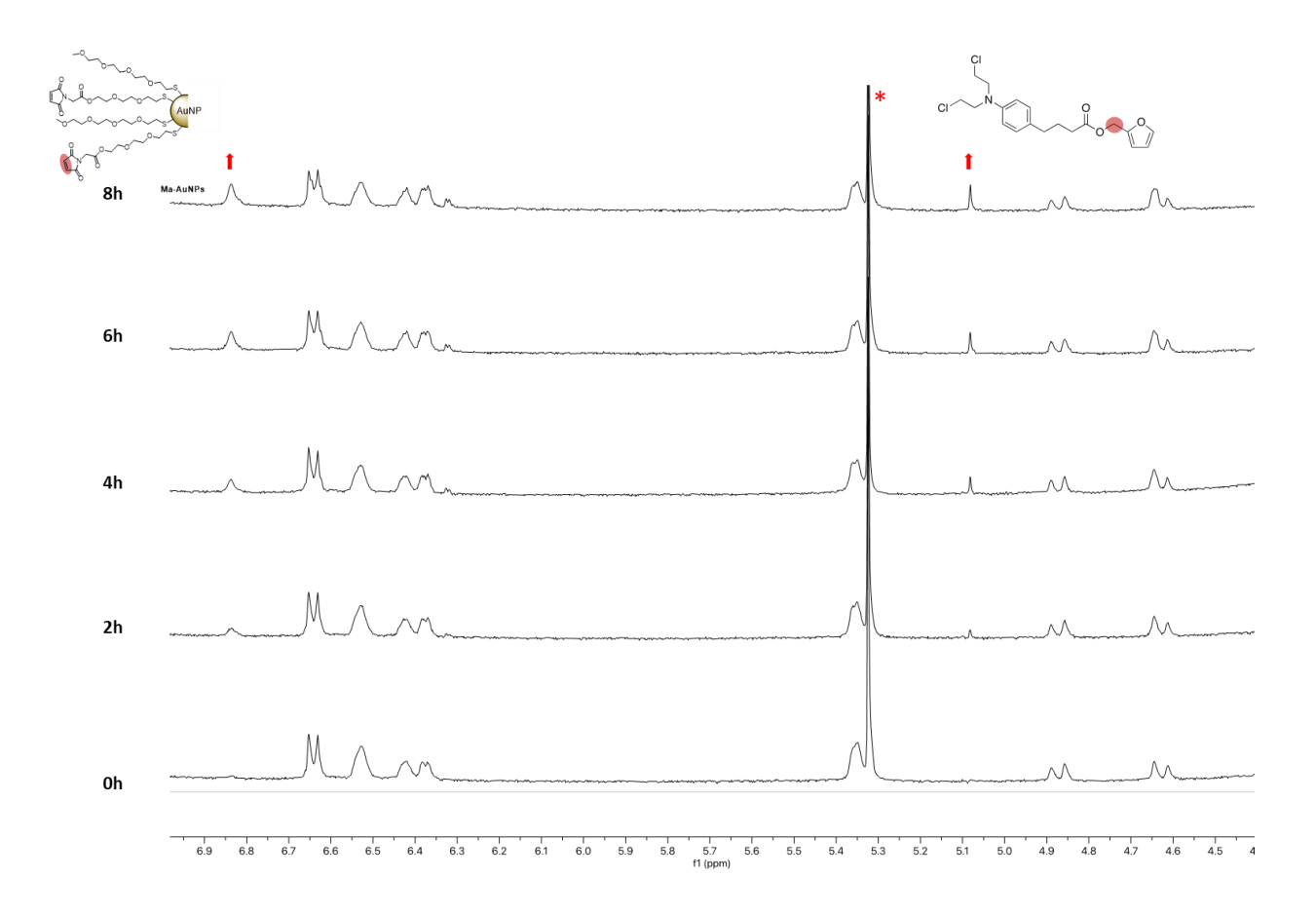


Figure 4.3: Characterizations of Chr-AuNPs and (A) The stack <sup>1</sup>H NMR of Chr-AuNPs (top) and Sun-AuNPs (bottom).

The rDA reaction of Chr-AuNP was monitored by <sup>1</sup>H NMR in CDCl<sub>3</sub> to avoid maleimide hydrolysis (Figure 4.4, top). The aromatic signals of the resulting chlorambucil-furan alcohol derivative overlapped with those of Chr-AuNP; therefore, the rDA reaction was inferred primarily from the formation of maleimide on the AuNPs and the alkyl group from the released chlorambucil-furan alcohol. This procedure was also applied to monitor the rDA reaction of Sun-AuNPs (Figure 4.4, bottom). Additionally, the presence of detachment of furfuryl derivatives in each system was confirmed by HR-MS, identifying a sulindac furfuryl at 459.1037 m/z and a chlorambucil furfuryl alcohol at 406.0947 m/z, further validating the effectiveness of the designed system.



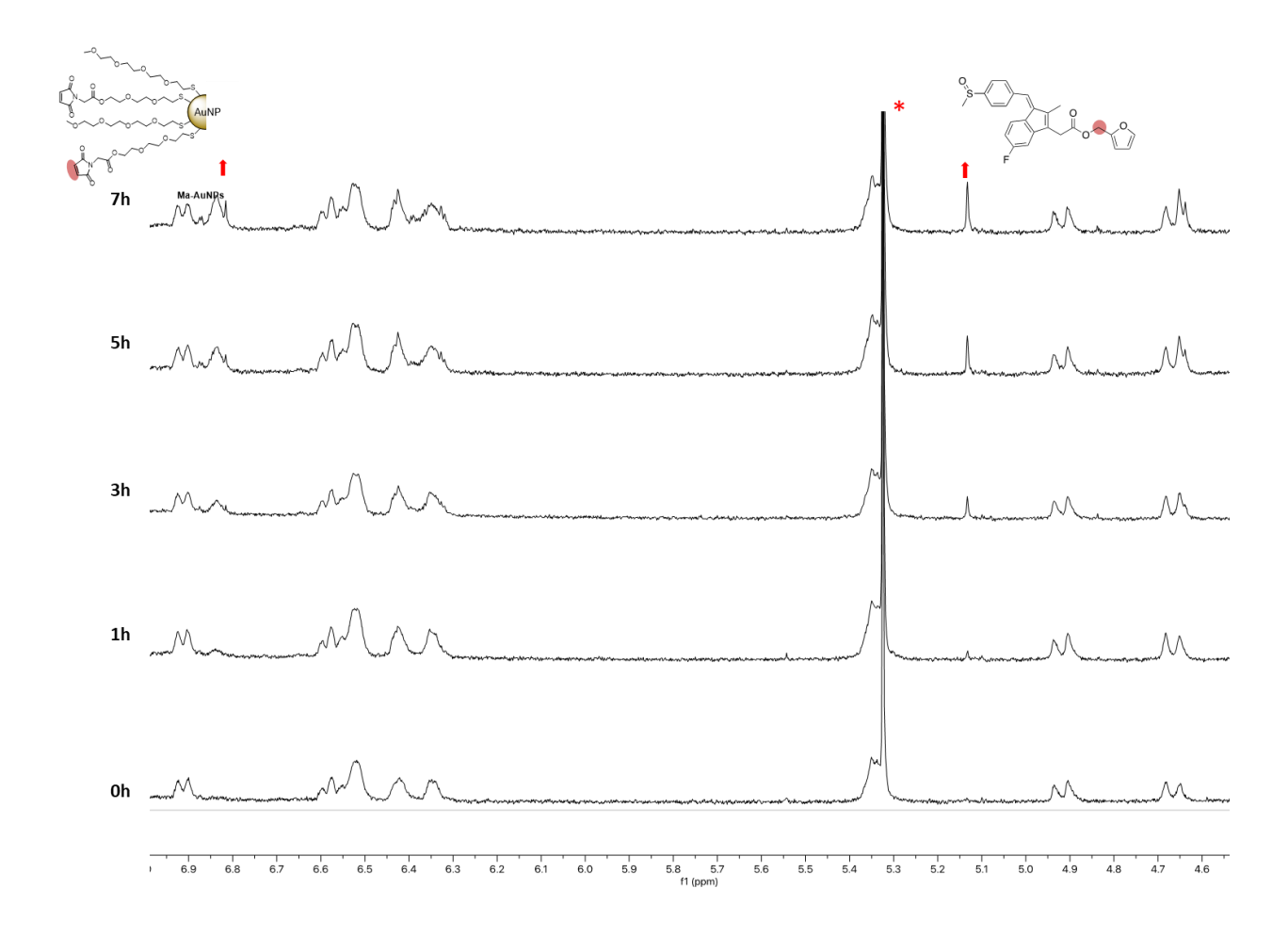


Figure 4.4: Monitoring the retro Diels-Alder reaction of (A) Chr-AuNPs and (B) Sun-AuNPs at different heating times at 45 °C. \* was assigned to peak of the solvent dichloromethane.

## 4.4.3 Kinetic Study of Acridine-AuNPs

Following the confirmation of the synthetic accessibility of the Acr-AuNP, the rate of the rDA reaction of Acr-AuNPs was monitored using fluorescence spectroscopy. Heating Acr-AuNPs to 37°C induced an rDA reaction, yielding Ma-AuNPs (maleimide-AuNPs) and an acridine-furan alcohol derivative (Scheme 4.2). Fluorescence spectra reveal a recovery in intensity upon heating at 37 °C, indicating successful acridine derivative release from the AuNP surface over 9.5 hours, as shown in Figure 4.5. The resulting acridine-furan derivative was also detected by HRMS, further

validating the progression of the desired reaction. Employing methodologies from previous chapters, the rDA reaction rate of Acr-AuNP was evaluated. An aqueous Acr-AuNP solutions was heated from 37 °C to 50 °C, with emission spectra recorded at defined intervals. Kinetic plots for each temperature confirm the first-order kinetics of the release reaction with a half lives of 67 hours at 37 °C. TEM analysis, conducted pre- and post-heating, confirmed that the size distribution of the Acr-AuNP gold cores remains unchanged and there is no evidence of aggregation (Figure 4.6), highlighting their stability and suitability as potential drug delivery systems. Finally, the detachment of the acridine furfuryl alcohol moiety was verified by HR-MS, with an exact mass of 460.2595 m/z. This further confirms the viability of the designed release system.

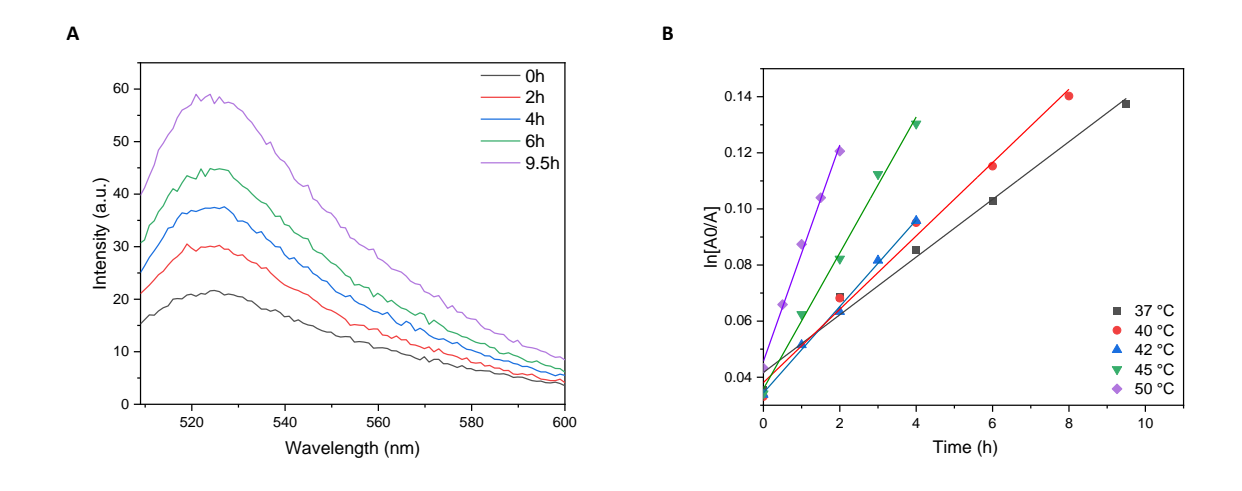


Figure 4.5: Release behavior of Acr-AuNPs monitored through fluorescence spectroscopy. (A) Emission spectrum of Acr-AuNPs at 37 °C; (B) Results of the first-order model fitting of Acr-AuNPs at different temperatures at (37°C, 40 °C, 42 °C, 45 °C, 50°C).

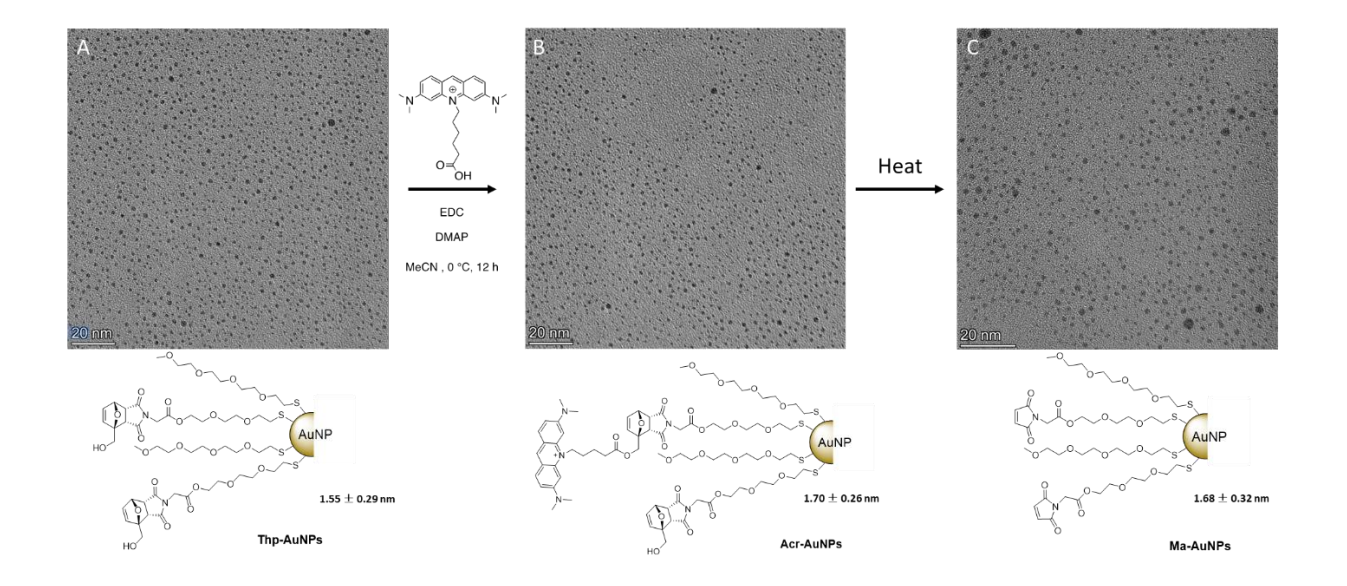


Figure 4.6: Confirmation of preserved monodispersity in AuNPs after heating at (37°C, 40 °C, 42 °C, 45 °C, 50°C); (A)TEM images of Thp-AuNP, (B) Acr-AuNPs and (C) Ma-AuNP.

The half-lives for *endo*-Acr-AuNPs were estimated at different temperatures using the corresponding rate constants, as shown in Table 4.2. These half-lives provide preliminary insights into the stability of the system and its potential for use in controlled release applications. As described in the previous chapter, the temperatures of solid tumors tend to be about 1.5°C greater than healthy tissue. Therefore, extrapolating the half lives to each of these two temperatures allows us to understand the quantity of drug released under varying background conditions. For example, at the typical temperature of a solid tumor, the endo-Acr-AuNPs exhibits a half life of 60 hours. During hyperthermia therapy, where a tumor can be intentionally heated to 45°C, the system's half life is reduced to 28 hours. Conversely, when stored at normal freezer conditions (-20 °C), the system's half life extends to 17 years.

Table 4.2: Calculated half-lives for *endo*-Acr-AuNPs as a function of temperature.

Temperature/°C	Half-life /(h)	
37	67	
40	53	
42	45	
45	29	
50	18	

#### 4.5 Conclusion and Perspective

In this Chapter, 2nm PEGylated AuNPs were designed for cargo loading, employing a mild esterification reaction between the hydroxyl group on a tetrahydrophthalimide linker and the carboxyl group on the cargo. The system was capable of efficiently coupling molecules bearing a carboxyl group without the need for laborious purification at the molecular level. A water-soluble acridine derivative was specifically synthesized and loaded onto pre-prepared AuNPs to facilitate the analysis of loading and release kinetics. The rate of the rDA reaction of the acridine-loaded AuNPs was monitored using fluorescence spectroscopy at five different temperatures, revealing a first-order kinetic release mechanism. Furthermore, TEM analysis post-heating confirms the structural integrity of the AuNPs, demonstrating their stability under elevated temperatures. The designed system's compatibility with therapeutic cargos, specifically sulindac and chlorambucil, was demonstrated, achieving a loading efficiency of nearly 50%. The rDA reactions of chlorambucil and sulindac conjugated AuNPs were monitored by <sup>1</sup>H NMR, and the presence of the detached furfuryl alcohol derivatives was confirmed by HRMS.

## 4.6 Experimental

#### 4.6.1 Material

Chemicals and solvents were purchased from Sigma Aldrich and used as received without further purification. Proton nuclear magnetic resonance ( $^{1}H$  NMR) spectra and carbon nuclear magnetic resonance ( $^{13}C$  NMR) spectra were acquired using Bruker Ascend 500 MHz or 400 MHz spectrometers. Chemical shifts ( $\delta$ ) are reported in parts per million (ppm) and are calibrated to the residual solvent peak. Coupling constant (J) are reported in Hertz (Hz). Multiplicities are reported using the following abbreviations: s = singlet; d = doublet; t = triplet; d = quartet; d = doublet of doublet.

## 4.6.2 Synthesis of Acridine Derivative

A 250 mL round bottom flask was charged with 6-bromohexanoic acid (2.543 g,  $1.29 \times 10^{-2}$  mol), DCC (3.222 g,  $1.56 \times 10^{-2}$  mol), DMAP (0.159 g,  $1.3 \times 10^{-3}$  mol) and 50 mL of dry DCM. Then, tert-butyl alcohol (6.03 mL,  $6.5 \times 10^{-2}$  mol) was added dropwisely through syringe. The mixture was allowed to stir overnight. After that, the crude product was purified by column chromatography to afford the colorless oil (0.056 g, 80% yield).

<sup>1</sup>H NMR (500 MHz, CDCl<sub>3</sub>) δ 3.40 (t, J = 6.8 Hz, 2H), 2.22 (t, J = 7.4 Hz, 2H), 1.86 (p, J = 6.9 Hz, 2H), 1.60 (dt, J = 15.2, 7.4 Hz, 2H), 1.44 (m, 11H).

<sup>13</sup>C NMR (126 MHz, CDCl<sub>3</sub>) δ 173.0, 80.3, 35.4, 33.7, 32.6, 28.2, 27.7, 24.4.

HRMS (ESI) m/z: [M+H] + calculated for  $C_{10}H_{19}BrNaO_2$ : 273.0466, found 273.4061.

**2** (2.632 g,  $1.04 \times 10^{-2}$  mol), acridine orange (0.1264 g,  $4.75 \times 10^{-4}$  mol) and  $K_2CO_3$  (0.2634 g, 1.90  $\times 10^{-3}$  mol) were combined in a 15 mL pressure tube in dry toluene. The reactants were heated at 120 °C overnight. The crude mixture was purified by column chromatography to afford the **3** (0.1414 g, 48 % yield).

<sup>1</sup>H NMR (500 MHz, CDCl<sub>3</sub>) δ 8.68 (s, 1H), 7.85 (d, J = 9.3, Hz, 2H), 6.94 (dd, J = 9.2, 2.2 Hz, 2H), 6.46 (d, J = 2.3 Hz, 2H), 4.71 (t, J = 7.9 Hz, 2H), 3.23 (s, 12H), 2.24 – 2.14 (m, 2H), 1.86 (q, J = 7.0, 6.5 Hz, 2H), 1.69 – 1.58 (m, 4H), 1.32 (s, 9H).

<sup>13</sup>C NMR (126 MHz, CDCl<sub>3</sub>) δ 172.9, 155.5, 143.3, 142.5, 133.5, 117.1, 114.0, 92.9, 80.1, 47.9, 41.1, 35.2, 28.1, 26.5, 26.1, 24.9.

HRMS (ESI) m/z:  $[M+H]^+$  calculated for  $C_{27}H_{38}N_3O_2$ : 436.2964, found 436.2959.

3 (0.157 g,  $3.596 \times 10^{-4}$  mol) was dissolved in acetonitrile with the dropwise addition of TFA (0.1295 mL,  $2.157 \times 10^{-3}$  mol) in a 25 mL round bottom flask. The mixture was heated at 60 °C overnight and then purified through a reverse phase column to yield 4 (0.0684 g, 50 % yield).

<sup>1</sup>H NMR (500 MHz, MeOD) δ 8.66 (s, 1H), 7.91 (d, J = 9.2 Hz, 2H), 7.28 (dd, J = 9.3, 2.1 Hz, 2H), 6.68 (d, J = 2.2 Hz, 2H), 4.72 – 4.65 (m, 2H), 3.33 (s, 12H), 2.33 (t, J = 7.1 Hz, 2H), 2.08 – 1.98 (m, 2H), 1.81 (t, J = 7.7 Hz, 2H), 1.70 (q, J = 7.7 Hz, 2H).

<sup>13</sup>C NMR (126 MHz, MeOD) δ 169.7, 157.4, 144.3, 144.1, 134.3, 118.6, 115.6, 93.7, 40.8, 36.3, 27.6, 26.7, 26.3.

HRMS (ESI) m/z:  $[M+H]^+$  calculated for  $C_{23}H_{30}N_3O_2$ :380.2338, found 380.2333.

Tetraethyleneglycol monomethyl ether (0.5 g,  $2.4 \times 10^{-3}$  mol) and triethylamine (0.335 mL,  $2.4 \times 10^{-3}$  mol) were combined in a 50 mL round bottom flask. The mixture was dissolved in 10 mL DCM, followed by the addition of 4-toluenesulfonyl chloride (0.503 g,  $2.64 \times 10^{-3}$  mol) dissolved in 5 mL DCM. The mixture was stirred under room temperature overnight and then the crude product was purified by column chromatography to afford the colorless oil (0.711 g, 80% yield).

<sup>1</sup>H NMR (400 MHz, CDCl<sub>3</sub>) δ 7.80 (d, J = 8.4 Hz, 2H), 7.34 (d, J = 7.8 Hz, 2H), 4.19 – 4.12 (m, 2H), 3.69 (t, J = 5.1 Hz, 2H), 3.64 – 3.52 (m, 12H), 3.37 (s, 3H), 2.45 (s, 3H).

<sup>13</sup>C NMR (126 MHz, CDCl<sub>3</sub>) δ 144.9, 133.2, 130.0, 128.1, 72.1, 70.9, 70.7, 70.8, 70.7, 70.7, 69.4, 68.8, 59.2, 21.8.

HRMS (ESI) m/z:  $[M+H]^+$  calculated for  $C_{16}H_{26}NaO_7S$ : 385.1297, found 385.1291.

Potassium thioacetate (0.12 g,  $1.02 \times 10^{-3}$  mol) and **7** (0.3381 g,  $9.32 \times 10^{-4}$  mol) were dissolved in 30 mL acetone, and the mixture was refluxed overnight. After cooling down to room temperature, the mixture was filtrated and washed with acetone. The mixture was redissolved in 50 mL DCM, washed with 20mL brine 3 times, and dried over MgSO<sub>4</sub>. Residual solvent was removed under high *vacuo* to yield the pale-yellow oil **8** (0.211 g, 85% yield).

 $^{1}$ H NMR (500 MHz, CDCl<sub>3</sub>)  $\delta$  3.70 – 3.53 (m, 14H), 3.38 (s, 3H), 3.09 (t, J = 6.5 Hz, 2H), 2.34 (s, 3H)

<sup>13</sup>C NMR (126 MHz, CDCl<sub>3</sub>) δ 195.7, 72.1, 70.8, 70.8, 70.7, 70.7, 70.5, 69.9, 59.2, 30.7, 29.0.

HRMS (ESI) m/z: [M+H] + calculated for C<sub>9</sub>H<sub>17</sub>N<sub>6</sub>O<sub>3</sub>S:289.1082, found 289.1077.

NaOH 1.0 equiv

NaOH 1.0 equiv

NaOH 1.0 equiv

MeOH, 0 °C, 1h

1.0 equiv

Chemical Formula: 
$$C_{11}H_{22}O_{5}S$$

Molecular Weight: 266.35

NaOH 1.0 equiv

Chemical Formula:  $C_{9}H_{20}O_{4}S$ 

Molecular Weight: 224.32

A 50 mL round bottom flask was charged with **8** (0.2111 g,  $7.97 \times 10^{-4}$  mol) and 20 mL MeOH. NaOH (0.12 g,  $3.0 \times 10^{-3}$  mol) was then dissolved in a 10 mL volumetric flask of ethanol followed by 10 minutes of sonication. A 2.65 mL NaOH solution was added dropwisely into the 50 mL round bottom flask. The mixture was allowed to stir at 0 °C for 1 hour. Remove the solvent by rotary evaporation and dilute the mixture with 40 mL DCM. The organic layer was washed by 20 mL brine 2 times and residual solvent was removed by high *vacuo* to afford a colorless oil (0.1422 g, 80 % yield).

<sup>1</sup>H NMR (400 MHz, CDCl<sub>3</sub>)  $\delta$  3.67 – 3.58 (m, 12H), 3.58 – 3.52 (m, 2H), 3.38 (s, 3H), 2.70 (q, J = 8.2 Hz, 2H), 1.59 (t, J = 8.2 Hz, 1H)

<sup>13</sup>C NMR (126 MHz, CDCl<sub>3</sub>) δ 73.0, 72.1, 70.8, 70.7, 70.4, 59.2, 24.4.

HRMS (ESI) m/z:  $[M+H]^+$  calculated for  $C_9H_{20}O_4SNa$ : 247.0980, found 247.0974.

**Tetrahydrophthalimide linker**  $(0.049 \text{ g}, 1.09 \times 10^{-4} \text{ mol})$ , chlorambucil  $(0.0338 \text{ g}, 1.1 \times 10^{-4} \text{ mol})$ , DCC  $(0.0252 \text{ g}, 1.2 \times 10^{-4} \text{ mol})$ , DMAP  $(0.01689 \text{ g}, 1.1 \times 10^{-5} \text{ mol})$  were dissolved in 10 mL dry acetonitrile. Then, the mixture was allowed to stir in ice bath overnight. After that, the crude product was purified by column chromatography to afford the colorless oil **10** (0.056 g, 70% yield).

<sup>1</sup>H NMR (500 MHz, CDCl<sub>3</sub>) δ 7.05 (d, J = 8.6 Hz, 2H), 6.62 (d, J = 8.4 Hz, 2H), 6.51 (dd, J = 5.8, 1.7 Hz, 1H), 6.35 (d, J = 5.8 Hz, 1H), 5.33 (dd, J = 5.4, 1.7 Hz, 1H), 4.85 (d, J = 12.7 Hz, 1H), 4.60 (d, J = 12.7 Hz, 1H), 4.30 – 4.24 (m, 2H), 4.10 (s, 2H), 3.80 (t, J = 6.2 Hz, 2H), 3.75 – 3.58 (m, 15H), 3.51 – 3.43 (m, 3H), 2.56 (t, J = 7.5 Hz, 2H), 2.39 (t, J = 7.5 Hz, 2H), 1.92 (p, J = 7.5 Hz, 2H)

<sup>13</sup>C NMR (126 MHz, CDCl<sub>3</sub>) δ 173.6, 173.4, 173.1, 166.3, 144.4, 136.0, 134.7, 130.6, 129.8, 112.3, 89.9, 79.8, 71.4,70.7, 70.6, 69.0, 64.9, 61.9, 53.7, 48.2, 47.0, 40.6, 39.4, 33.4, 30.5, 26.7.

HRMS (ESI) m/z: [M+H] + calculated for C<sub>31</sub>H<sub>39</sub>BrCl<sub>2</sub>N<sub>2</sub>NaO<sub>9</sub>: 755.1113, found 755.1108.

**Tetrahydrophthalimide Linker** (0.207 g, 4.6× 10<sup>-5</sup> mol), sulindac (8.23×10<sup>-2</sup> g, 2.3×10<sup>-5</sup> mol), EDC (0.1434 g, 9.2× 10<sup>-4</sup> mol) and DMAP (2.8×10<sup>-3</sup> g, 2.3×10<sup>-5</sup> mol) were combined in a 50 mL round bottom flask. The reactants were dissolved in 10 mL dry acetonitrile and stirred overnight at 0 °C. Then, the solvent was removed by rotary evaporation. The mixture was diluted by 40 mL DCM and washed by 20 mL brine 2 times. Afterwards, the crude product was purified by column chromatography to afford the yellow oil (0.162 g, 89% yield).

<sup>1</sup>H NMR (400 MHz, CDCl<sub>3</sub>) δ 7.71 (d, J = 8.5 Hz, 2H), 7.66 (d, J = 8.3 Hz, 2H), 7.18 – 7.09 (m, 2H), 6.89 (dd, J = 8.9, 2.7 Hz, 1H), 6.60 – 6.51 (m, 1H), 6.49 (dd, J = 5.8, 1.6 Hz, 1H), 6.31 (d, J = 5.8 Hz, 1H), 5.31 (dd, J = 5.5, 1.7 Hz, 1H), 4.89 (d, J = 12.6 Hz, 1H), 4.63 (d, J = 12.6 Hz, 1H), 4.31 – 4.23 (m, 2H), 4.09 (s, 2H), 3.80 (t, J = 6.3 Hz, 2H), 3.71 – 3.59 (m, 10H), 3.47 (t, J = 6.2 Hz, 2H), 3.37 (d, J = 7.7 Hz, 1H), 2.80 (s, 3H), 2.20 (d, J = 2.0 Hz, 3H)

<sup>13</sup>C NMR (126 MHz, CDCl<sub>3</sub>) δ 173.5, 173.5, 169.8, 164.4, 162.4, 145.7, 141.7, 139.7, 138.6, 136.0, 134.6, 131.5, 130.5, 129.6, 128.3, 123.9, 123.7, 111.0, 110.8, 106.7, 106.5, 89.7, 79.7, 71.4, 70.6, 69.0, 64.9, 62.5, 48.1, 47.2, 44.0, 39.4, 31.6, 30.5, 10.7.

HRMS (ESI) m/z: [M+H] + calculated for C<sub>37</sub>H<sub>37</sub> O<sub>10</sub>NBrFNaS: 808.1203, found 808.11872.

## Synthesis of 2 nm PEGylated AuNPs

MeO-EG<sub>4</sub>-AuNP

HAuCl<sub>4</sub>·3H<sub>2</sub>O (0.1072 g,  $2.7 \times 10^{-4}$  mol, 1.0 eq.) was dissolved in a mixture of methanol (30 mL) and glacial acetic acid (6 mL). Thol **9** (0.1221 g,  $5.4 \times 10^{-4}$  mol, 2.0 eq.) was added to this yellow solution. The reduction was initiated by rapidly introducing a methanol solution of NaBH<sub>4</sub> (0.1029 g,  $2.7 \times 10^{-3}$ , 10.0 eq.) under vigorous stirring, resulting in an immediate color change to dark brown. The reaction mixture was then left to stir overnight at room temperature. Afterwards, the mixture was concentrated under reduced pressure to form a film of AuNPs, which was subsequently washed three times with a toluene/hexane mixture to remove the majority of the acetic acid. For further purification, the crude MeO-EG<sub>4</sub>-AuNPs were redissolved in distilled water and subjected to dialysis for 3 days, ensuring the removal of residual reactants and byproducts. The purity of the final MeO-EG<sub>4</sub>-AuNPs was confirmed through <sup>1</sup>H NMR.

### Calculation of nanoparticle composition

Analysis of the data derived from TEM, NMR and TGA lead to an estimation of the composition of the AuNPs. To simply the calculation, we assume that the AuNPs are spherical, and their size is monodispersed.

The number of gold atoms (N<sub>Au</sub>) can be calculated from the following formula:

$$N_{Au} = \frac{\pi \rho d^3 N_A}{6 M_{Au}}$$

Where:

 $\rho$  = density of face centered cubic (fcc) gold lattice (19.3 g/cm<sup>3</sup>)

d = average diameter of nanoparticles

 $N_A$  = Avogadro constant

 $M_{Au}$  = mole atomic weight of gold (199.9665 g/mol)

The total number of ligands  $(N_L)$  per gold nanoparticle can be calculated using the following formula:

$$N_{L} = \omega \frac{N_{Au} M_{Au} / (1 - \omega)}{M W_{ligand1} \varphi + M W_{ligand2} (1 - \varphi)}$$

Where:

 $\omega$  = percentage of mass loss due to the protecting ligands

 $MW_{ligand}$  = molar weight of ligand

 $\varphi$  = molar percentage of ligand

### **Synthesis of Linker-MeO-AuNP**

The preparation of Thp-AuNPs involved a place-exchange reaction, where tetrahydrophthalimide linker thiol was combined with previously prepared MeO-EG<sub>4</sub>-AuNP. This process was conducted in methanol, where the ligand and nanoparticles were mixed at an optimized 5:1 molar ratio of thiol linker to MeO-EG<sub>4</sub>-AuNPs. The reaction was allowed to proceed for 15 minutes under inert gas to protect the reactants from oxidation. Following the reaction, the resulting Thp-AuNPs sample was washed six times with a toluene/hexane mixture to remove the majority of the unreacted thiol linker. Further purification was performed through dialysis for 1 days at 4 °C to ensure the removal of unreacted ligands. The purity of the final Thp-AuNPs product was verified using <sup>1</sup>H NMR spectroscopy, confirming the successful incorporation of the ligands into the nanoparticle structure.

### **Synthesis of Acr-AuNPs**

All reagents used in this synthesis were prepared as stock solution and stored in -20 °C fridge.

### In protic solvent

Acridine derivative 4 (2 mg), EDC (2 mg) and NHS (2 mg) were combined in a 5 mL round bottom flask. The mixture's pH was adjusted to 4 with 1M HCl solution. The 10-AuNP (3 mg) was added, and the reaction was allowed to proceed overnight at 0 °C. The resultant Acr-AuNPs sample was purified through dialysis for 2 days at 4 °C.

### In aprotic solvent

Thp-AuNP (3 mg), acridine derivative **4** (1 mg), DCC (3 mg 1.2 ×10<sup>-4</sup> mol), DMAP (0.01 mg, 8.0×10<sup>-8</sup> mol) were dissolved in 2 mL dry acetonitrile. Then, the mixture was stirred in ice bath overnight. After the reaction, the Acr-AuNPs sample was purified through dialysis for 2 days at 4 °C, with residual free acridine removed via a desalting column. The purity of the final Acr-AuNPs product was verified using <sup>1</sup>H NMR spectroscopy, confirming the successful incorporation of the acridine onto the nanoparticle.

Calculation of Acr-AuNPs conversion to Ma-AuNP as monitored by fluorescence spectroscopy.

It was a dissociation reaction from Acr-AuNPs (A) to Ma-AuNPs (B).

	A	<b>→</b> B
Initial	$A_0$	0
During the reaction	At	$A_0$ - $A_t$ = $B$
Completion of reaction	0	$A0=B_{\infty}$

$$First \ order \ kinetic \ equation \qquad \qquad ln \ [A_t] = \text{-}kt + ln[A_0]$$

$$\label{eq:replacing At with A_0 - B} \text{ ln } [A_0 \text{ - B}] = \text{-kt} + \text{ln}[B_\infty]$$

$$Rearrangement \hspace{1cm} ln \ [A_0 \text{ - } B] \text{ - } ln [B_{\infty}] = -kt$$

Replacing 
$$A_0$$
 with  $B_{\infty}$  and rearrangement 
$$kt = ln [\frac{B_{\infty}}{B_{\infty} - B}]$$

# Synthesis of Chr-AuNPs and Sun-AuNPs

Thp-AuNPs (3 mg), therapeutic molecules (1 mg), DCC (3 mg  $1.2 \times 10^{-4}$  mol), DMAP (0.01 mg,  $8.0 \times 10^{-8}$  mol) were dissolved in 2 mL dry acetonitrile. Then, the mixture was stirred in ice bath overnight. After the reaction, the sample was purified through dialysis for 2 days at 4 °C. The purity of the final product was verified using  $^{1}$ H NMR spectroscopy, confirming the successful incorporation of the therapeutic molecule onto the nanoparticle.

#### 4.7 References

- (1) Haniti Mohd-Zahid, M.; Mohamud, R.; Abdullah, C. A. C.; Lim, J.; Alem, H.; Hanaffi, W. N. W.; A, I. Z. Colorectal Cancer Stem Cells: A Review of Targeted Drug Delivery by Gold Nanoparticles. *RSC Advances* **2020**, *10* (2), 973–985. https://doi.org/10.1039/C9RA08192E.
- (2) Wang, F.; Wang, Y.-C.; Dou, S.; Xiong, M.-H.; Sun, T.-M.; Wang, J. Doxorubicin-Tethered Responsive Gold Nanoparticles Facilitate Intracellular Drug Delivery for Overcoming Multidrug Resistance in Cancer Cells. *ACS Nano* **2011**, *5* (5), 3679–3692. https://doi.org/10.1021/nn200007z.
- (3) Kang, B.; Afifi, M. M.; Austin, L. A.; El-Sayed, M. A. Exploiting the Nanoparticle Plasmon Effect: Observing Drug Delivery Dynamics in Single Cells via Raman/Fluorescence Imaging Spectroscopy. *ACS Nano* **2013**, *7* (8), 7420–7427. https://doi.org/10.1021/nn403351z.
- (4) Luo, W.; Luo, J.; Popik, V. V.; Workentin, M. S. Dual-Bioorthogonal Molecular Tool: "Click-to-Release" and "Double-Click" Reactivity on Small Molecules and Material Surfaces. *Bioconjugate Chem.* **2019**, *30* (4), 1140–1149. https://doi.org/10.1021/acs.bioconjchem.9b00078.
- (5) Gandini, A. The Furan/Maleimide Diels—Alder Reaction: A Versatile Click—Unclick Tool in Macromolecular Synthesis. *Progress in Polymer Science* **2013**, *38* (1), 1–29. https://doi.org/10.1016/j.progpolymsci.2012.04.002.
- (6) Chen, C.; Fruk, L. Functionalization of Maleimide-Coated Silver Nanoparticles through Diels–Alder Cycloaddition. *RSC Adv.* **2013**, *3* (6), 1709–1713. https://doi.org/10.1039/C2RA22738J.
- (7) Zhu, J.; Kell, A. J.; Workentin, M. S. A Retro-Diels—Alder Reaction to Uncover Maleimide-Modified Surfaces on Monolayer-Protected Nanoparticles for Reversible Covalent Assembly. *Org. Lett.* **2006**, *8* (22), 4993–4996. https://doi.org/10.1021/ol0615937.
- (8) Zhou, W.; Gao, X.; Liu, D.; Chen, X. Gold Nanoparticles for In Vitro Diagnostics. *Chem. Rev.* **2015**, *115* (19), 10575–10636. https://doi.org/10.1021/acs.chemrev.5b00100.
- (9) Nam, J.; La, W.-G.; Hwang, S.; Ha, Y. S.; Park, N.; Won, N.; Jung, S.; Bhang, S. H.; Ma, Y.-J.; Cho, Y.-M.; Jin, M.; Han, J.; Shin, J.-Y.; Wang, E. K.; Kim, S. G.; Cho, S.-H.; Yoo, J.; Kim, B.-S.; Kim, S. pH-Responsive Assembly of Gold Nanoparticles and "Spatiotemporally Concerted" Drug Release for Synergistic Cancer Therapy. *ACS Nano* **2013**, *7* (4), 3388–3402. https://doi.org/10.1021/nn400223a.
- (10) Lee, K. Y. J.; Lee, G. Y.; Lane, L. A.; Li, B.; Wang, J.; Lu, Q.; Wang, Y.; Nie, S. Functionalized, Long-Circulating, and Ultrasmall Gold Nanocarriers for Overcoming the Barriers of Low Nanoparticle Delivery Efficiency and Poor Tumor Penetration. *Bioconjugate Chem.* **2017**, 28 (1), 244–252. https://doi.org/10.1021/acs.bioconjchem.6b00224.
- (11) Wang, X.; Cai, X.; Hu, J.; Shao, N.; Wang, F.; Zhang, Q.; Xiao, J.; Cheng, Y. Glutathione-Triggered "Off–On" Release of Anticancer Drugs from Dendrimer-Encapsulated Gold Nanoparticles. *J. Am. Chem. Soc.* **2013**, *135* (26), 9805–9810. https://doi.org/10.1021/ja402903h.
- (12) Mathiyazhakan, M.; Yang, Y.; Liu, Y.; Zhu, C.; Liu, Q.; Ohl, C.-D.; Tam, K. C.; Gao, Y.; Xu, C. Non-Invasive Controlled Release from Gold Nanoparticle Integrated Photo-Responsive Liposomes through Pulse Laser Induced Microbubble Cavitation. *Colloids and Surfaces B: Biointerfaces* 2015, 126, 569–574. https://doi.org/10.1016/j.colsurfb.2014.11.019.

- (13) Javed, R.; Sajjad, A.; Naz, S.; Sajjad, H.; Ao, Q. Significance of Capping Agents of Colloidal Nanoparticles from the Perspective of Drug and Gene Delivery, Bioimaging, and Biosensing: An Insight. *Int J Mol Sci* **2022**, *23* (18), 10521. https://doi.org/10.3390/ijms231810521.
- (14) Biver, T.; Eltugral, N.; Pucci, A.; Ruggeri, G.; Schena, A.; Secco, F.; Venturini, M. Synthesis, Characterization, DNA Interaction and Potential Applications of Gold Nanoparticles Functionalized with Acridine Orange Fluorophores. *Dalton Trans.* **2011**, *40* (16), 4190–4199. https://doi.org/10.1039/C0DT01371D.
- (15) Géci, I.; Filichev, V. V.; Pedersen, E. B. Synthesis of Twisted Intercalating Nucleic Acids Possessing Acridine Derivatives. Thermal Stability Studies. *Bioconjugate Chem.* **2006**, *17* (4), 950–957. https://doi.org/10.1021/bc0600580.
- (16) Kostelansky, F.; Miletin, M.; Havlinova, Z.; Szotakova, B.; Libra, A.; Kucera, R.; Novakova, V.; Zimcik, P. Thermal Stabilisation of the Short DNA Duplexes by Acridine-4-Carboxamide Derivatives. *Nucleic Acids Research* **2022**, *50* (18), 10212–10229. https://doi.org/10.1093/nar/gkac777.
- (17) Wang, Y.; Aleiwi, B. A.; Wang, Q.; Kurosu, M. Selective Esterifications of Primary Alcohols in a Water-Containing Solvent. *Org. Lett.* **2012**, *14* (18), 4910–4913. https://doi.org/10.1021/ol3022337.
- (18) A. Rocha, M.; D. Petersen, P. A.; Teixeira-Neto, E.; M. Petrilli, H.; Leroux, F.; Taviot-Gueho, C.; L. Constantino, V. R. Layered Double Hydroxide and Sulindac Coiled and Scrolled Nanoassemblies for Storage and Drug Release. *RSC Advances* **2016**, *6* (20), 16419–16436. https://doi.org/10.1039/C5RA25814F.
- (19) Saha, B.; Haldar, U.; De, P. Polymer-Chlorambucil Drug Conjugates: A Dynamic Platform of Anticancer Drug Delivery. *Macromolecular Rapid Communications* **2016**, *37* (13), 1015–1020. https://doi.org/10.1002/marc.201600146.
- (20) Suresh, K.; Matzger, A. J. Enhanced Drug Delivery by Dissolution of Amorphous Drug Encapsulated in a Water Unstable Metal–Organic Framework (MOF). *Angewandte Chemie International Edition* **2019**, *58* (47), 16790–16794. https://doi.org/10.1002/anie.201907652.
- (21) Guan, X.; Chen, Y.; Wu, X.; Li, P.; Liu, Y. Enzyme-Responsive Sulfatocyclodextrin/Prodrug Supramolecular Assembly for Controlled Release of Anti-Cancer Drug Chlorambucil. *Chemical Communications* **2019**, *55* (7), 953–956. https://doi.org/10.1039/C8CC09047E.

# Chapter 5. An Improved Method for the Synthesis of Gold and Silver Nanorods

### **5.1 Preface**

Chapter 5 introduces an improved method for the synthesis of gold and silver nanorods (AuNRs and AgNRs). This Chapter refines the seed-mediated synthesis techniques used in order to achieve precise aspect ratios for each type of nanorod. We focus on the role of the CTA-Ag-Br complex in controlling nanorod growth and introducing a co-solvent system to enhance its solubility. Through UV-vis-NIR spectroscopy and TEM analysis, a reproducible protocol is established for the production of nanorods having customizable optical properties, and in doing so contribute to the use of rod-shaped nanoparticles in applications.

#### **5.2 Abstract**

The synthesis of AuNRs and AgNRs with specific aspect ratios (AR; length:width ratio) is vital to the development of their use in imaging, sensing, drug delivery, and biotechnology applications. However, traditional seed-mediated synthesis methods often suffer from unpredictable outcomes and poor reproducibility. In the silver case, this study addresses these limitations by identify the critical silver intermediate CTA-Ag-Br (where CTA = cetyltrimethylammonium) that arises during the synthesis process. By adjusting the solubility of this CTA-Ag-Br complex, reproducibility and the scope of the nanorod syntheses can be significantly improved. The localized surface plasmon resonance (LSPR) of AuNR is limited to < 900 nm using the traditional seed-mediated silver-aided AuNR synthesis but can be extended to >1200 nm via control of the reported CTA-Ag-Br intermediate, which is studied in this Chapter. A parallel approach is explored here with the aim of to improve the reproducibility and AR of seed-mediated AgNR syntheses. A depletion method applied to the purification of the assynthesized AgNRs yields highly monodisperse AgNR samples. UV-vis spectroscopy was used to characterize the formation of the AgNRs. These results not only pave the way for producing nanorods with customizable optical properties but also significantly contribute to the field of nanoparticle synthesis by providing a reproducible method to control nanoscale dimensions and purity.

#### **5.3 Introduction**

Noble metal nanoparticles, particularly AuNRs and AgNRs, exhibit remarkable localized surface plasmon resonance (SPR) properties that significantly enhance the electromagnetic field around the particles.<sup>2</sup> This enhancement leads to large resonance spectral extinctions at relatively long wavelengths in the visible and near-IR regions of the EM spectrum, making AuNRs and AgNRs of particular interest for use in many applications.<sup>3</sup> These unique optical properties, combined with their tunable size, accessible surface modification, and possible biocompatibility, make AuNRs and AgNRs highly promising for diverse applications in catalysis, 4,5 sensing, 6 imaging, <sup>7</sup> and theranostics. <sup>8</sup> The seed-mediated growth method, pioneered by Murphy et al. in 2001<sup>9</sup> and later improved by El Sayed et al. in 2003, remains the dominant technique for the synthesis of AuNRs. 10 Overall, this method involves the generation of gold seeds that are approximately 1.5 nm in diameter, followed by growth promotion using ascorbic acid under carefully designed conditions. Despite its simplicity and reproducibility, the method suffers from several limitations, including limited control over the value of the LSPR maximum (up to 850 nm) and broad size distributions in the NR width and length<sup>11</sup> The need to expand the LSPR window into the NIR-II window of 1000-1700 nm, a range increasingly vital for biomedical applications, necessitates the development of new synthetic approaches. <sup>12</sup> Murphy et al. suggested that a combination of hydroquinone and hydrochloric acid could extend the maximum LSPR wavelength to above 1300 nm with a NR diameter of 6-9 nm. 13 Lee et al. further refined the Murphy approach by adjusting the ratios of ascorbic acid and hydroquinone, achieving LSPR maxima to around 1300 nm with a NR diameter of 8.1 nm. <sup>14</sup> Liz-Marzan et al demonstrated that a CTAB:1-decanol mixture could produce AuNRs with tunable LSPR maxima that range from 600 to 1270 nm. 15 In this context, our previous research identified a CTA-Ag-Br complex as being a critical determinant in controlling the AR of AuNRs. The solubility limit of CTA-Ag-Br has been identified as the principal factor that limits the longitudinal growth of AuNRs. In this Chapter, we therefore introduce a co-solvent (acetonitrile) to the NR growth solution to enhance the solubility of the CTA-Ag-Br reaction intermediate under reaction conditions. The result is the successful synthesis of isolated AuNR samples that exhibit very narrow size distributions, a high yield of the desired NR morphology other morphologies such as spherically symmetric, cubic, or pyramidal, and an LSPR maximum of > 1200 nm associated with large AR values of 10 - 13.

In regard to the synthesis of AgNRs with different morphologies and sizes, methods that exploit the unique dielectric properties of silver in the visible-NIR range of the EM spectrum have been developed. For example, AgNRs have been prepared by different methods, including the thermal reshaping of Ag decahedra, 16 the polyol method, 17 light-assisted synthesis, 18,19 and seeded growth in water.<sup>20</sup> Among the various approaches for synthesizing AgNRs, light-assisted synthesis has been reported by Zhang et al by using plasmonic excitation of Ag seed particles with 600–750 nm light in the presence of Ag<sup>+</sup> and trisodium citrate to synthesize penta-twinned nanorods. However, this method produces nanorods with AR values that range from 30 to 37 and is relatively time consuming to perform.<sup>18</sup> Other techniques involve the use of Au or Pd nanoparticle seeds. In particular, Au bipyramids have been used as seeds for AgNRs growth, as explored by the Wang lab and the Liz-Marzan lab. 21, 22 Conversely, the wet seed-mediated method originally developed by Murphy for AuNRs synthesis has not been thoroughly applied to AgNRs. Inspired by the success of the wet seed-mediated method originally developed for AuNRs, we explored this approach for AgNR syntheses with the aim of enhancing the quality of the AgNRs produced. Recognizing that the unique photothermal properties for AuNRs and AgNRs make them ideal drug delivery/release carriers in combination of our well-developed thermally releasable linkers as

described elsewhere in this Thesis, we undertook to develop a reproducible synthetic protocol of AgNRs using a wet seed mediated reaction procedure.

#### **5.4 Result and Discussion**

### 5.4.1 Improved Aspect Ratio of AuNR using the Silver-Assisted Seed-Mediated Method

Access to the reproducible synthesis of AuNRs whose AR remains a significant challenge in seed-mediated methods. We previously reported the role of a CTA-Ag-Br complex in continuously supplying silver during the AuNR synthesis. However, the solubility limit of this complex (0.12 mM in the growth solution), restricts the extent of silver availability and thus limits the AR to < 5 and the LSPR band maximum to ca. 900 nm. Introduction of binary surfactants to enhance the solubility of the CTA-Ag-Br complex facilitates the synthesis of AuNRs whose LSPR >1000 nm. For instance, El-Sayed et al used a mixture of CTAB and benzyldimethylhexadecylammonium chloride (BDAC) in a 1:3 ratio (27 mM:75 mM), 10 while Murray et al used a 3:1 CTAB to sodium oleate blend (37 mM:12.6 mM) to achieve similar outcomes.<sup>23</sup> However, **BDAC** and sodium oleate exhibit high degrees of absorbance in the 200-250 nm range. This overlap with the absorbance of the CTA-Ag-Br complex limits the measurement of the solubility of the silver intermediate. More recently, Liz-Marzan et al reported that the use of a CTAB:1-decanol binary surfactant mixture that yield AuNRs with tunable LSPR maxima values that range from 600 to 1270 nm. Our previous studies revealed that the CTAB:1-decanol binary surfactant mixture leads to an improvement in the solubility of the silver intermediate. 15 We therefore hypothesized that addition of a water-miscible organic cosolvent could improve the solubility of the CTA-Ag-Br intermediate without interfering with the

surfactant properties of the CTAB, with the overall aim of researchers being able to use the same seed-mediated silver-aided AuNR method for the preparation of AgNRs with previously unobtainable AR values.

The solubility of the CTA-Ag-Br complex was assessed by mixing a 2% v/v acetonitrile solution with a 100 mM CTAB solution over a range of AgNO<sub>3</sub> concentrations. The UV-vis absorbance at 237 nm, characteristic of the complex formation, was measured as a function of the quantity of AgNO<sub>3</sub> (Figure 5.1). The peak intensity at 237 nm increased linearly with the concentration of AgNO<sub>3</sub>, ranging from 0.05 to 0.50 mM. Notably, the addition of AgNO<sub>3</sub> up to 0.50 mM remained within the solubility limit of the silver intermediate (Figure 5.1).

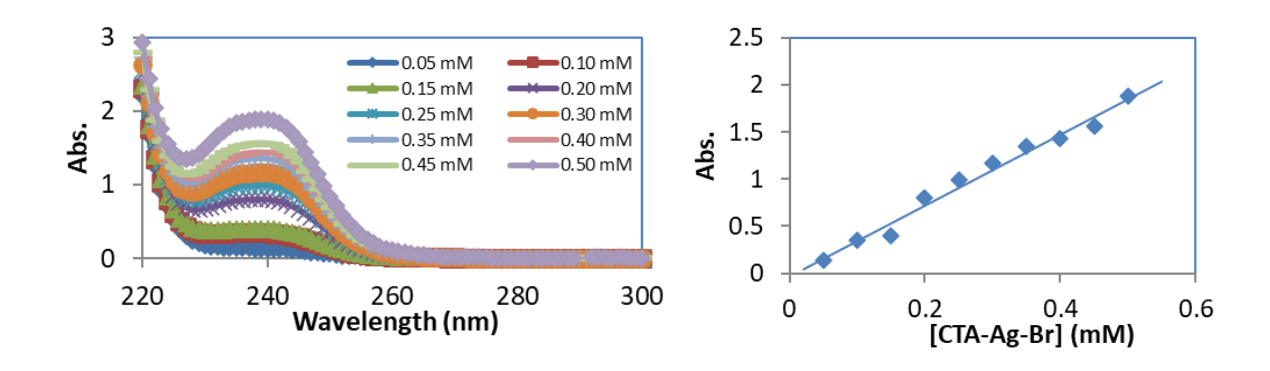


Figure 5.1: The solubility of the CTA-Ag-Br complex as a function of AgNO<sub>3</sub> in a 2% v/v acetonitrile/ 100mM CTAB mixture. Plot of the peak intensity at 237 nm with a quantity of AgNO<sub>3</sub> added.

Under the same reaction conditions as those typically employed in the conventional seed-mediated method (conducted at 28°C), addition of 2% v/v acetonitrile to 100 mM CTAB significantly enhances the AR value of the resulting AuNRs. These conditions yielded AuNRs with a tunable LSPR up to 1240 nm with an AR value of 7.5, as shown in Figure 5.2. The results demonstrate that an increase in the solubility of the intermediate CTA-Ag-Br complex in the

aqueous reaction conditions by using trace (2% v/v) acetonitrile, AuNR with LSPR bands > 1200 nm can be synthesized using the seed-mediated method.

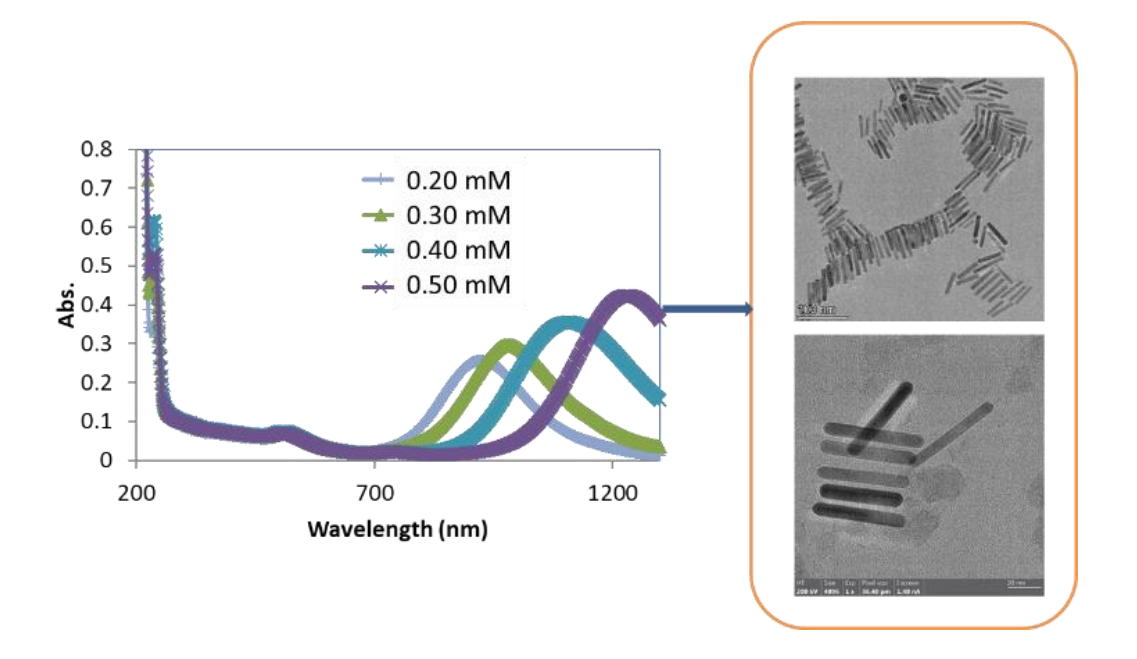


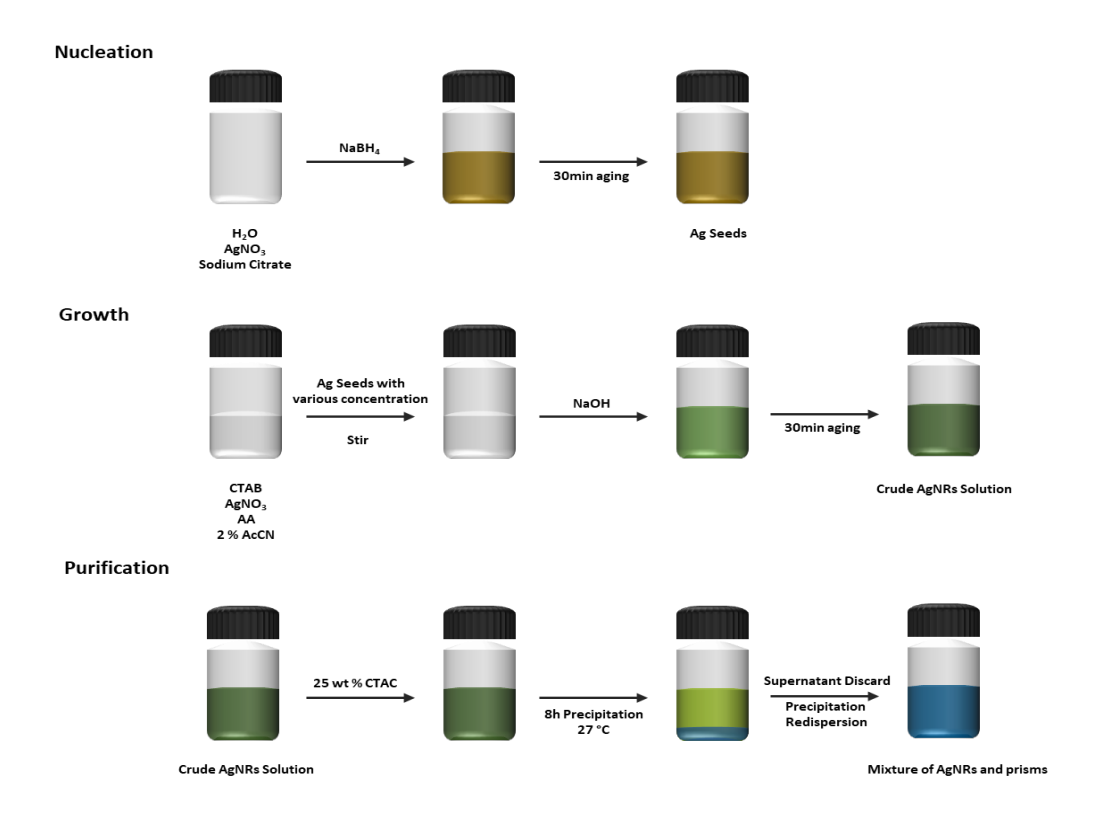
Figure 5.2: AuNRs synthesized as a function of AgNO<sub>3</sub> concentration (a) UV-vis spectra of AuNRs synthesized using different amounts of AgNO<sub>3</sub>. An increased AgNO<sub>3</sub> leads to AuNRs with a greater AR and an LSPR shifted to higher wavelengths. (b) TEM images AuNRs prepared from different added amounts of AgNO<sub>3</sub>.

### 5.4.2 Improved Synthesis of AgNRs using the Seed-Mediated Method

The number of reports of the seed-mediated synthesis of AgNRs is limited.<sup>24</sup> This is primarily due to the poor reproducibility of the method and the relatively reactive nature of silver.<sup>24</sup> As the seed-mediated AgNR and AuNR synthesis conditions are similar, the solubility of the CTA-Ag-Br complex could possibly also be key in the AgNR synthesis. In the conditions of the AgNR synthesis method reported by the Murphy et al, the silver intermediate concentration is

about 0.24 mM, about 2-fold greater than its solubility.<sup>24</sup> To ensure that the intermediate is fully soluble under the reaction conditions, 2% v/v acetonitrile was thus added.

A modified version of a published synthetic procedure is reported here (Scheme 5.1).<sup>24</sup> Spherical silver nanoparticle seeds were initially prepared via rapid reduction of AgNO<sub>3</sub> with NaBH<sub>4</sub> in a citrate solution (Figure 5.3). For the growth of nanorods, 0.2 mL of this seed solution was added to an aqueous growth solution comprising 0.25 mM AgNO<sub>3</sub>, 0.25 mM ascorbic acid, 0.1 mL acetonitrile, and 5 mL of 100 mM CTAB, maintained at 27 °C. 0.1 mL of 1 M NaOH was subsequently introduced to accelerate the deposition of silver on the AgNP seeds. This modification was based on our previous findings from AuNR syntheses, where the introduction of a 2% v/v acetonitrile solution improves the solubility of the silver intermediate significantly.<sup>1</sup>



Scheme 5.1: Schematic of the modified AgNRs synthesis steps. AA, ascorbic acid; CTAB = cetyl trimethylammonium bromide; CTAC = cetyltrimethylammonium chloride where cetyl = n-C16.

The UV-vis- NIR spectrum of the crude AgNRs solutions exhibit characteristic peaks at 420 nm (formerly assigned to the TSPR of AgNR)<sup>24</sup> and 610 nm (due to the LSPR of AgNR). The presence of these two peaks demonstrates the formation of AgNRs (Figure 5.3). The resulting AgNRs were concentrated via centrifugation (6000 rpm) and subsequently re-dispersed in a 5 mL CTAB solution (1 mM). The centrifuged AgNRs retain their distinctive plasmonic bands at 420 nm and 610 nm, and an additional peak emerges at 354 nm. The following depletion method was then applied to the crude reaction mixture in order to selectively precipitate nanoparticles with desired morphologies. After addition of 80 µL of a 25 wt % CTAC solution to the AgNR solution, an AgNR precipitate forms after 8 hours without disturbance at 27 °C. A purified AgNR solution was achieved by re-dispersing the precipitate in 5 mL of 1 mM CTAB solution. The resulting UV-vis spectra of the supernatant and purified AgNR (Figure 5.3) exhibit two plasmonic bands (354 nm, 694 nm). The supernatant exhibits a single plasmonic band at 420 nm, <sup>25</sup> which corresponds to spherical nanoparticle impurities. These observations demonstrate the efficacy of the depletion purification method in the separation of NRs from spherical NPs. We also note that TSPR of AgNRs have likely been previously misassigned due to inadequate removal of NP impurities from the sought after NR. <sup>26,27</sup>

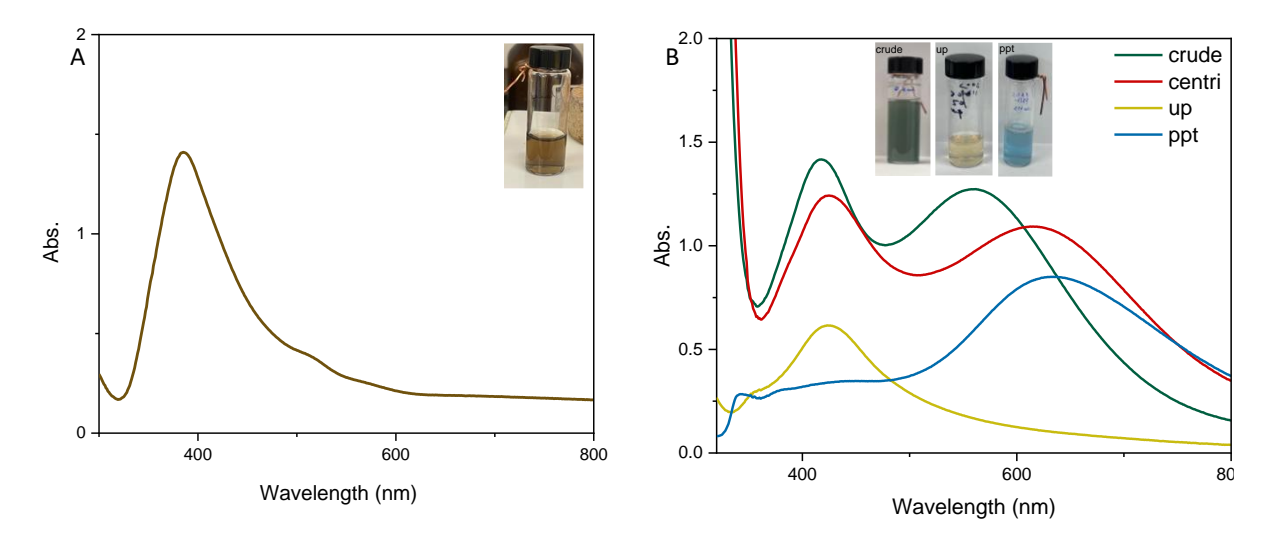


Figure 5.3: UV-vis spectra of AgNRs at different stages (A) UV-vis spectra and inserted photograph of the silver seed stock solution after 40 minutes aging. (B) UV-vis spectra of the AgNRs at different stages and inserted photographs of the AgNRs.

TEM analyses were performed on the purified AgNR samples. The AgNRs prepared using 0.2 mL seed solution with an AR of  $5.5 \pm 1.0$  (L =  $97 \pm 9$  nm, D =  $18 \pm 2$  nm) are shown in Figure 5.4. The TEM images reveal that the AgNRs were successfully separated from spherical AgNPs and about 30 % (by number density) nanoplates. Importantly, the diameters of the nanorods remain < 20 nm, which was significantly smaller than those of previously reported Ag nanorods which are typically > 30 nm in diameter. Given that TEM images only provide the projection of the particles onto the observation plane, it is plausible that the nanoplates can self-assemble in a manner that is visually mimicking two-dimensional nanorods upon gradual solvent evaporation. To confirm that AgNRs and not self-assembled nanoplates, the TEM grid was tilted. The imaged particles retain a rod shape after sample tilting. The AR of AgNR can be tuned by controlling the seed quantity used where, for example, AgNR synthesis using 0.1 mL seed solutions results in longer AgNRs (224nm) with an AR of  $7.1 \pm 3.8$  (L =  $224 \pm 77$  nm, D =  $31 \pm 6$  nm).

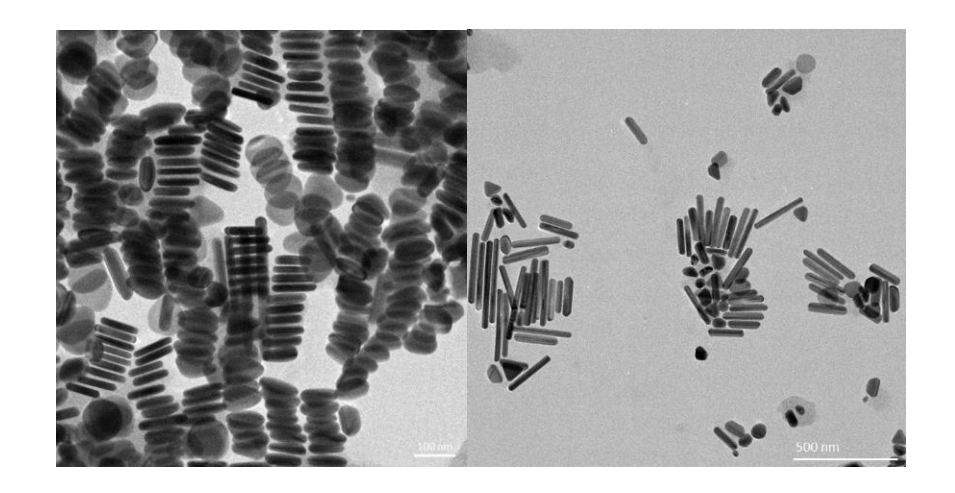


Figure 5.4: TEM images of purified AgNRs made from a 0.2 mL seed stock solution (left) and a 0.1 mL seed stock solution (right).

We have previously shown that varying the number of seeds used can serve as an effective method for the synthesis of AuNRs with different size. With the solution of the silver intermediate solubility problem in hand, a methodology to reproducibly access AgNRs with defined AR values and associated optical properties is accessible (see Experimental for details). By varying the quantity of AgNP seed used (50 µL to 300 µL of seed stock solution in 5 mL CTAB solution), the LSPR of the resulting AgNP can be tuned from 600 nm to over 800 nm (Figure 5.5). The batches of longer AgNP were not assessed because of the limited range of the UV-Vis spectrometer available in this work (Cary 200, range from 200 - 800 nm). As previously described, a spherical AgNP by-product with a peak at 420nm, can be removed *via* the depletion purification process. AgNRs exhibit an TSPR at 354 nm, consistent with the width of the resulting AgNRs being constant across the sample collection. This confirms that the synthetic procedure described effectively controls the AR value of AgNRs by controlling the seed concentration.

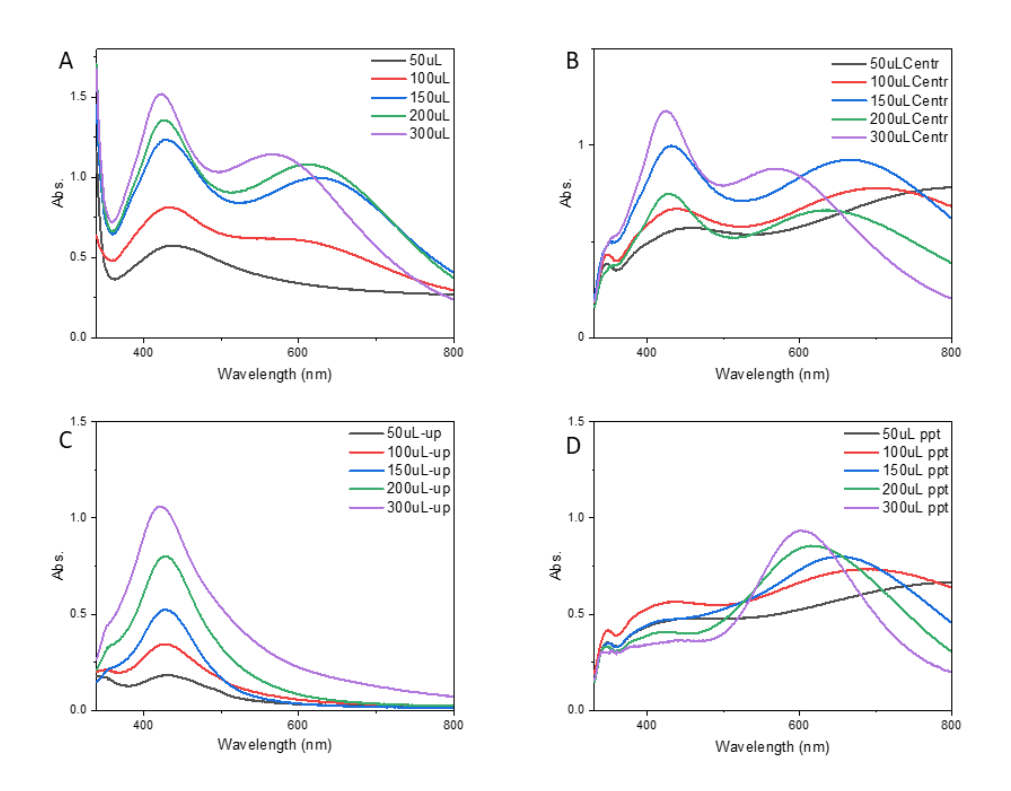


Figure 5.5: AgNRs synthesized as a function of seed quantity added. UV-vis spectra of (A) crude (B) centrifuged (C) supernatant (D) redispersed AgNRs.

### **5.5 Conclusion and Perspective**

The key silver intermediate for the synthesis of AuNR and AgNR using the seed-mediated method has been identified. Its solubility serves as the size (length) limiting factor in NR formation. Facile adjustment of the silver intermediate solubility with a co-solvent (2% v/v acetonitrile) without change any other perimeters for the well-studied NR synthesis yields a versatile and reproducible synthetic procedure. Tunable LSPR characteristics are thus accessible with LSPR maxima ranging from 620 nm to 1240 nm for AuNRs. Furthermore, a method for improving the reproducibility and (morphology) purity of AgNRs synthesis is presented. Transfer of the solubility enhancement techniques developed in the AuNR synthesis to the AgNR synthetic process leads to significantly improved reproducibility and purity of the AgNR prepared. The use of a depletion purification method and defined seed concentrations further refines the synthetic procedure, enabling the selective formation and isolation of desired nanorod morphologies. Analysis of the UV-vis spectra reveals two characteristic plasmonic peaks in the as-synthesized AgNRs: a TSPR at 354 nm and a LSPR ranging from 550 nm to >800nm, by varying the seed concentration. Spherical AgNP side products and their 420nm SPR peak were successfully removed from different AgNRs samples through precipitation. The refinement of the synthetic procedure underscores the importance of precise management of the reaction intermediates in this complex reaction system and introduces a much-desired pathway for the scalable production of nanorods with specific optical properties. The insights gained from this research could serve as a foundation for future studies aimed at optimizing and diversifying the functional capabilities of nanorod-based systems.

### **5.6 Experimental**

Commercial Reagents and General Instrumentation. Hexadecyltrimethylammonium bromide (CTAB, > 99%), hydrogen tetrachloroaurate (HAuCl<sub>4</sub>, > 99%), silver nitrate (AgNO<sub>3</sub>, > 99%), L-Ascorbic acid (99%), sodium citrate (99%), sodium borohydride (NaBH<sub>4</sub>, 98%), sodium hydroxide (NaOH, > 97%) and hexadecyltrimethylammonium chloride (CTAC, 25 wt% in water) were purchased from Aldrich and used as-received. Hydrochloric acid (37%) was purchased from Fisher Chemicals. All reagent solutions were prepared using Milli-Q water (>18.2 M $\Omega$ ). Freshly prepared solution of silver nitrate, ascorbic acid, and sodium citrate solutions were stored in the dark at 4 °C prior to use. To minimize degradation being an uncontrolled variable, these solutions were freshly prepared every 3 days. UV—vis spectra were recorded using a Cary 100 UV—vis and Cary 5000 UV—vis-NIR spectrometers (Agilent Technologies). Transmission electron microscopy (TEM) images were collected using a Philips CM200 200 kV TEM.

Solution. To examine the solubility of the *in situ* formed CTA-Ag-Br complex in 2% v/v acetonitrile / 100 mM CTAB solution, varying amounts of 10 mM AgNO<sub>3</sub> were mixed with 1 mL of 2% v/v acetonitrile / 100 mM surfactant solution to reach a final silver concentration at 0.05, 0.10, 0.15, 0.20, 0.25, 0.30, 0.35, 0.40, 0.45 and 0.50 mM at 27 °C. The *in situ* formation of the CTA-Ag-Br complex was monitored by UV- vis spectroscopy (Figure 5.1). The acetonitrile-CTAB solution does not have a UV-vis absorbance signature in the 237 nm region. The peak at 237 nm is thus attributed to the resulting CTA-Ag-Br complex, which showed an increased solubility in this solution.

General Method for Seed Mediated Synthesis of Gold Nanorods with Varying Aspect Ratios. *Preparation of Gold Nanoparticle Seeds*. Mixing 25 µL of a 50 mM HAuCl<sub>4</sub> and 4.7 mL

of 100 mM CTAB solution at 27 °C results in a clear orange solution. This mixture was then quickly treated with 0.3 mL of a freshly prepared, ice-cold 10 mM NaBH<sub>4</sub> solution under vigorous stirring; the solution instantly turned from clear to pale brown. The seed solution was continuously stirred for 10 minutes before being stored at 27 °C for 60 minutes.

Preparation of Growth Solution. 0.1 mL of 50 mM HAuCl<sub>4</sub> was mixed with 10 mL of 100 mM CTAB and 0.2 mL of acetonitrile, with varying amounts of 10 mM AgNO<sub>3</sub> added under stirring. After stirring for 10 minutes, 70 μL of 100 mM ascorbic acid was added, turning the solution from orange to a clear colorless state, which was maintained even after 8 hours of storage at 27 °C. Nanorod formation was initiated by adding 120 μL of the seed solution to the growth solution, and a color change is observed within 10 minutes. The reaction was then maintained at 27 °C in a water bath overnight and processed after 12 hours by centrifuging at 7500g for 15 minutes to collect the AuNRs. The upper clear solution was discarded, and the collected AuNR sample washed 1X with 1 mM CTAB before being dissolved in 1 mL of the same solution for future use. The resulting AuNRs were characterized using Cary 5000 UV-vis-NIR spectroscopy to assess their optical properties.

General Method for Seed Mediated Synthesis of Silver Nanorods with Varying Aspect Ratios. *Preparation of Silver Nanoparticle Seeds*. 10 μL of a 50 mM AgNO<sub>3</sub> solution and 6.66 μL of 75 mM sodium citrate solution was added to 1.983 mL water. 60 μL of a freshly prepared NaBH<sub>4</sub> solution was then quickly added under vigorous stirring. The stirring was stopped 5 seconds after the addition of the NaBH<sub>4</sub> solution. The solution turned from clear to clear yellow, ultimately converting to a dark brown solution within 40 seconds. The seed stock solution was then left to age for 30 minutes before use. Results indicate that the seeds were not viable for use after 1 hour.

Preparation of Growth Solution and Silver Nanorod Formation. 25 μL of a 50 mM AgNO<sub>3</sub> solution, 0.25 mL of 100 mM ascorbic acid solution, 0.1 mL acetonitrile and 5 mL of 80 mM CTAB solution were combined in a 10 mL vial under stirring at 27 °C. Varying quantities (50 μL to 300 μL) of an aged seed solution was added to the growth solution. The formation of AgNRs was initiated by adding 0.1 mL of 1 M NaOH solution to the reaction mixture to adjust the pH of the solution to 11. Stirring was stopped after 5 seconds. Following the addition of NaOH, a noticeable color change was observed, with the solution eventually evolving into a grey, green, blue, or dark reddish, depending on the quantity of seed used.

Purification of Silver Nanorods. After aging the crude AgNRs solution for 30 minutes, 80 μL of the 25 wt% CTAC solution was added to the 5 mL reaction mixture. Based on experimental observations, allowing the CTAC solution to remain undisturbed at the top of the mixture results in a better extent of precipitation compared to thorough mixing. The reaction mixture was then kept at 27 °C in a water bath overnight, during which the AgNRs precipitated. The supernatant was discarded, and AgNR precipitate was redispersed in 5 mL by 1 mM CTAB for further use. UV-vis spectroscopy was used to characterize the resulting AgNRs. Compared with the UV-vis spectra of crude AgNRs, the resulting AgNRs exhibited two characteristic peaks: a TSPR at 354 nm and a LSPR ranging from 550 nm into NIR. The overall synthetic scheme of the AgNRs is shown in Scheme 5.1.

#### **5.7 References**

- (1) Zhu, J.; Lennox, R. B. Insight into the Role of Ag in the Seed-Mediated Growth of Gold Nanorods: Implications for Biomedical Applications. *ACS Appl. Nano Mater.* **2021**, *4* (4), 3790–3798. https://doi.org/10.1021/acsanm.1c00230.
- (2) Zare, I.; Tavakkoli Yaraki, M.; Speranza, G.; Hassani Najafabadi, A.; Shourangiz-Haghighi, A.; Bakhshian Nik, A.; B. Manshian, B.; Saraiva, C.; J. Soenen, S.; J. Kogan, M.; Woong Lee, J.; V. Apollo, N.; Bernardino, L.; Araya, E.; Mayer, D.; Mao, G.; R. Hamblin, M. Gold Nanostructures: Synthesis, Properties, and Neurological Applications. *Chemical Society Reviews* **2022**, *51* (7), 2601–2680. https://doi.org/10.1039/D1CS01111A.
- (3) Huang, J.; Zhu, Y.; Liu, C.; Zhao, Y.; Liu, Z.; Hedhili, M. N.; Fratalocchi, A.; Han, Y. Fabricating a Homogeneously Alloyed AuAg Shell on Au Nanorods to Achieve Strong, Stable, and Tunable Surface Plasmon Resonances. *Small* **2015**, *11* (39), 5214–5221. https://doi.org/10.1002/smll.201501220.
- (4) Gao, P.; Zhang, M.; Hou, H.; Xiao, Q. A Simple Template Method for Hierarchical Dendrites of Silver Nanorods and Their Applications in Catalysis. *Materials Research Bulletin* **2008**, 43 (3), 531–538. https://doi.org/10.1016/j.materresbull.2007.06.031.
- (5) Bai, X.; Gao, Y.; Liu, H.; Zheng, L. Synthesis of Amphiphilic Ionic Liquids Terminated Gold Nanorods and Their Superior Catalytic Activity for the Reduction of Nitro Compounds. *J. Phys. Chem. C* **2009**, *113* (41), 17730–17736. https://doi.org/10.1021/jp906378d.
- (6) Ostovar, B.; Cai, Y.-Y.; Tauzin, L. J.; Lee, S. A.; Ahmadivand, A.; Zhang, R.; Nordlander, P.; Link, S. Increased Intraband Transitions in Smaller Gold Nanorods Enhance Light Emission. ACS Nano 2020, 14 (11), 15757–15765. https://doi.org/10.1021/acsnano.0c06771.
- (7) J. Murphy, C.; M. Gole, A.; E. Hunyadi, S.; W. Stone, J.; N. Sisco, P.; Alkilany, A.; E. Kinard, B.; Hankins, P. Chemical Sensing and Imaging with Metallic Nanorods. *Chemical Communications* **2008**, *0* (5), 544–557. https://doi.org/10.1039/B711069C.
- (8) Rizwan Younis, M.; He, G.; Gurram, B.; Lin, J.; Huang, P. Recent Advances in Gold Nanorods-Based Cancer Theranostics. *Advanced NanoBiomed Research* **2021**, *I* (12), 2100029. https://doi.org/10.1002/anbr.202100029.
- (9) Jana, N. R.; Gearheart, L.; Murphy, C. J. Seed-Mediated Growth Approach for Shape-Controlled Synthesis of Spheroidal and Rod-like Gold Nanoparticles Using a Surfactant Template. *Advanced Materials* **2001**, *13* (18), 1389–1393. https://doi.org/10.1002/1521-4095(200109)13:18<1389::AID-ADMA1389>3.0.CO;2-F.
- (10) Nikoobakht, B.; El-Sayed, M. A. Preparation and Growth Mechanism of Gold Nanorods (NRs) Using Seed-Mediated Growth Method. *Chem. Mater.* **2003**, *15* (10), 1957–1962. https://doi.org/10.1021/cm0207321.
- (11) Orendorff, C. J.; Murphy, C. J. Quantitation of Metal Content in the Silver-Assisted Growth of Gold Nanorods. *J. Phys. Chem. B* **2006**, *110* (9), 3990–3994. https://doi.org/10.1021/jp0570972.
- (12) Xing, W.; Tang, Y.; Ji, Y.; Cheng, D.; Wang, B.; Fu, Y.; Xu, Y.; Qian, X.; Zhu, W. Engineering Near-Infrared Laser-Activated Gold Nanorod Vesicles with Upper Critical Solution Temperature for Photothermal Therapy and Chemotherapy. *Journal of Colloid and Interface Science* **2023**, *640*, 41–51. https://doi.org/10.1016/j.jcis.2023.02.049.
- (13) Chang, H.-H.; Murphy, C. J. Mini Gold Nanorods with Tunable Plasmonic Peaks beyond 1000 Nm. *Chem. Mater.* **2018**, *30* (4), 1427–1435. https://doi.org/10.1021/acs.chemmater.7b05310.

- (14) Yoo, S.; Nam, D. H.; Singh, T. I.; Leem, G.; Lee, S. Effect of Reducing Agents on the Synthesis of Anisotropic Gold Nanoparticles. *Nano Convergence* **2022**, *9* (1), 5. https://doi.org/10.1186/s40580-021-00296-1.
- (15) González-Rubio, G.; Kumar, V.; Llombart, P.; Díaz-Núñez, P.; Bladt, E.; Altantzis, T.; Bals, S.; Peña-Rodríguez, O.; Noya, E. G.; MacDowell, L. G.; Guerrero-Martínez, A.; Liz-Marzán, L. M. Disconnecting Symmetry Breaking from Seeded Growth for the Reproducible Synthesis of High Quality Gold Nanorods. *ACS Nano* **2019**, *13* (4), 4424–4435. https://doi.org/10.1021/acsnano.8b09658.
- (16) Pietrobon, B.; McEachran, M.; Kitaev, V. Synthesis of Size-Controlled Faceted Pentagonal Silver Nanorods with Tunable Plasmonic Properties and Self-Assembly of These Nanorods. *ACS Nano* **2009**, *3* (1), 21–26. https://doi.org/10.1021/nn800591y.
- (17) Patarroyo, J.; Genç, A.; Arbiol, J.; G. Bastús, N.; Puntes, V. One-Pot Polyol Synthesis of Highly Monodisperse Short Green Silver Nanorods. *Chemical Communications* **2016**, *52* (73), 10960–10963. https://doi.org/10.1039/C6CC04796C.
- (18) Zhang, J.; Langille, M. R.; Mirkin, C. A. Synthesis of Silver Nanorods by Low Energy Excitation of Spherical Plasmonic Seeds. *Nano Lett.* **2011**, *11* (6), 2495–2498. https://doi.org/10.1021/nl2009789.
- (19) Langille, M. R.; Personick, M. L.; Mirkin, C. A. Plasmon-Mediated Syntheses of Metallic Nanostructures. *Angewandte Chemie International Edition* **2013**, *52* (52), 13910–13940. https://doi.org/10.1002/anie.201301875.
- (20) R. Jana, N.; Gearheart, L.; J. Murphy, C. Wet Chemical Synthesis of Silver Nanorods and Nanowires of Controllable Aspect ratioElectronic Supplementary Information (ESI) Available: UV–VIS Spectra of Silver Nanorods. See Http://Www.Rsc.Org/Suppdata/Cc/B1/B100521i/. *Chemical Communications* **2001**, *0* (7), 617–618. https://doi.org/10.1039/B100521I.
- (21) Zhuo, X.; Zhu, X.; Li, Q.; Yang, Z.; Wang, J. Gold Nanobipyramid-Directed Growth of Length-Variable Silver Nanorods with Multipolar Plasmon Resonances. *ACS Nano* **2015**, *9* (7), 7523–7535. https://doi.org/10.1021/acsnano.5b02622.
- (22) Sánchez-Iglesias, A.; Zhuo, X.; Albrecht, W.; Bals, S.; Liz-Marzán, L. M. Tuning Size and Seed Position in Small Silver Nanorods. *ACS Materials Lett.* **2020**, *2* (9), 1246–1250. https://doi.org/10.1021/acsmaterialslett.0c00388.
- (23) Ye, X.; Zheng, C.; Chen, J.; Gao, Y.; Murray, C. B. Using Binary Surfactant Mixtures To Simultaneously Improve the Dimensional Tunability and Monodispersity in the Seeded Growth of Gold Nanorods. *Nano Lett.* **2013**, *13* (2), 765–771. https://doi.org/10.1021/nl304478h.
- (24) R. Jana, N.; Gearheart, L.; J. Murphy, C. Wet Chemical Synthesis of Silver Nanorods and Nanowires of Controllable Aspect ratioElectronic Supplementary Information (ESI) Available: UV–VIS Spectra of Silver Nanorods. See Http://Www.Rsc.Org/Suppdata/Cc/B1/B100521i/. *Chemical Communications* **2001**, *0* (7), 617–618. https://doi.org/10.1039/B100521I.
- (25) Agnihotri, S.; Mukherji, S.; Mukherji, S. Size-Controlled Silver Nanoparticles Synthesized over the Range 5–100 Nm Using the Same Protocol and Their Antibacterial Efficacy. *RSC Adv.* **2013**, *4* (8), 3974–3983. https://doi.org/10.1039/C3RA44507K.
- (26) Sinha, R. K. Surface-Enhanced Raman Scattering and Localized Surface Plasmon Resonance Detection of Aldehydes Using 4-ATP Functionalized Ag Nanorods. *Plasmonics* **2023**, *18* (1), 241–253. https://doi.org/10.1007/s11468-022-01763-z.

(27) Rekha, C. R.; Nayar, V. U.; Gopchandran, K. G. Synthesis of Highly Stable Silver Nanorods and Their Application as SERS Substrates. *Journal of Science: Advanced Materials and Devices* **2018**, *3* (2), 196–205. https://doi.org/10.1016/j.jsamd.2018.03.003.

## **Chapter 6. Conclusions**

### **6.1 Summary and Conclusions**

Traditional pharmaceutical delivery and release vehicles, such as tablets and capsules, often face challenges including poor solubility, instability, nonspecific distribution, and various physiological barriers. In response, gold nanoparticles (AuNPs) have garnered considerable attention as possibly serving as nanoscale carriers for drug delivery and release, thanks to the inherent biocompatibility of gold,<sup>2</sup> the reproducibility of their synthesis,<sup>3</sup> scalability of synthesis,<sup>4</sup> and versatile surface chemistry and its derivatization.<sup>5</sup> Particularly due to this well-established surface functionalization capability, AuNPs have demonstrated potential to be carriers of fluorophores,<sup>6</sup> positron emission tomography ligands,<sup>7</sup> small therapeutic molecules,<sup>8</sup> and antibodies.9 Because 2nm-5nm AuNPs can have between 50-300 individual ligands in their capping layer, the possibility of a designed AuNP having truly multifunctional capabilities all in one small volume is very interesting. In short, ligand capped AuNP have long been recognized as possible platforms for the long sought after triple capability of "theranostics", where one carrier simultaneously has targeting, diagnostics, and drug delivery capabilities. This Thesis has thus focused on one of these three - exploring AuNPs for thermally dependent drug delivery. Although different stimuli-responsive delivery systems have been developed, current methods still face limitations such as phototoxicity, lack of control over dosage release, and potential toxicity of the trigger. This Thesis has presented the development and characterization of a novel release system using the retro Diels-Alder reaction on AuNPs, designed for controlled drug release under mild conditions with precise dosage control (Figure 6.1). Our findings in this Thesis demonstrate that linker-AuNPs can be effectively synthesized and functionalized to bind a fluorescence probe and therapeutic agents, providing a stable and controllable release template.

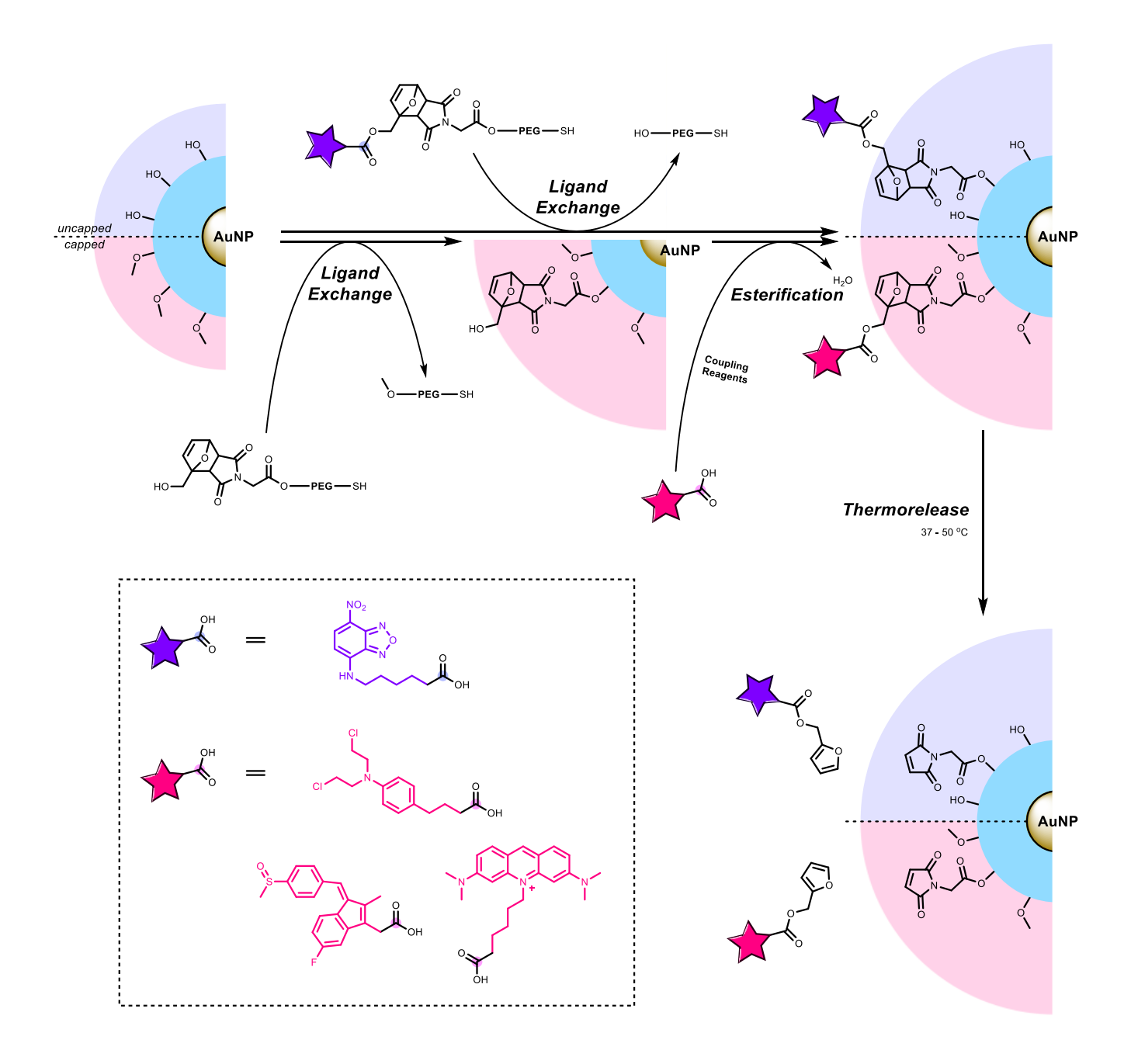


Figure 6.1: Schematic overview of the designed thermal releasing tetrahydrophthalimide linker in controlled release system

Our exploration into developing a thermally dependent releasing system began with the design and syntheses of thermally dependent release linkers, detailed in **Chapter 2**. Developing these linkers was crucial for establishing a baseline for controlled drug release, enabling the

detachment of drug analogues that respond to temperature changes. This Chapter introduced the design and synthesis of a novel thermally releasable linker based on retro Diels-Alder reactions between maleimide and furfuryl alcohol derivatives. We studied the Diels-Alder and retro Diels-Alder reactions of a series of furan derivative dienes and maleimide derivatized dienophiles. The N-derivatized maleimide and furfuryl alcohol were selected for effective Diels-Alder reactions, and especially the feasible separation of the *endo-/exo-* adducts. This linker, synthesized in both *endo-* and *exo-* forms, demonstrated first-order kinetics for its retro Diels-Alder reaction, with the *endo-*adducts displaying a half-life of 38 hours at 37 °C, and the *exo-*adducts 132 hours at 55 °C, monitored through <sup>1</sup>H NMR. These preliminary results indicate the potential of the designed linker for use in controlled release systems at physiological temperatures.

Once the linker structure was selected and its controlled retro Diels-Alder reaction capability tested, the next step involved loading the linker onto a stable carrier, AuNPs. The research focused on spherical nanoparticles, the most straightforward carriers due to their well-studied nature and ease of synthesis. However, in designing a controlled release system, two factors needed to be considered: 1) precise control over cargo loading, and 2) compatibility of the carrier with a variety of cargos, including various functional groups. The most straightforward loading approach could be a Diels-Alder reaction between dienophile-functionalized AuNPs and diene-cargo derivatives. However, steric effects between the AuNPs surface and the diene significantly slowed the Diels-Alder reaction rate. Due to the considerable diversity of functional groups in small molecules of choice, we were not able to identify a universal loading approach. Therefore, **Chapters 3** and **4** explored two different cargo loading approaches that complement one another. Ligand exchange of the capping layer ligands in **Chapter 3** provides a precise and direct method for attaching desired functionalities onto AuNPs by controlling the ratio between

AuNPs and functionalized thiolate as well as the reaction time. However, the synthesis and purification of thiolates of complex molecules can often be challenging. An interfacial esterification reaction therefore was found to offer an alternative method for incorporating such molecules onto AuNPs, as demonstrated in **Chapter 4**. Overall, these two approaches for attaching releasable drug analogues to 2 nm AuNPs are complementary and provide researchers with the choice of conditions to meet many of the outcomes that are sought.

Chapter 3 thus involved incorporating designed thiolate linker modules conjugated with the fluorescence dye derivative (NBD-X) onto 2 nm PEGylated AuNPs through a ligand exchange reaction, as illustrated in Figure 6.1. The release capabilities of this test case of both endo- and exo-NBD loaded AuNPs were assessed via the increase in fluorescence intensity upon heating. Although the AuNPs themselves are water-soluble, the hydrophobic nature of the NBD-X fluorophore results in the low water solubility of the product. The kinetic studies thus had to be conducted in ethanol to accommodate the solubility characteristics of the fluorophore. Significant differences in the reaction activation energies (87.5 kJ/mol for endo-AuNP and 117.6 kJ/mol for exo-AuNP) resulted in considerable differences in the half-lives of the two reactions at 50°C (6 h vs. 131 h), and by extrapolation, at 37°C (38 h vs. 521 h), suggesting their potential for use in multi-stage drug release systems, such as in pain management, 11 antibiotics, 12 and cancer chemotherapy. 13 Therefore, coating the AuNP carrier with controlled ratios of the endo- and exolinker could in principle achieve multi-stage release upon triggering at different temperatures. This approach would allow for precise tuning of the release rates for different therapeutic agents, enabling the multi-stage drug delivery system to be initiated at specific temperatures.

**Chapter 4** introduced an alternative approach for loading cargo onto AuNPs by using the nanoparticles themselves as starting materials in the coupling process. In this Chapter, an

interfacial esterification reaction was used to incorporate drug/probe molecules onto AuNPs, as demonstrated by incorporating water-soluble acridine derivatives and studying their release kinetics. The release kinetics followed a first-order rate law using fluorescence spectroscopy, with an activation energy of 89.9 kJ/mol for *endo*-acridine-AuNPs. This methodology was also successfully applied to two known therapeutic agents, sulindac and chlorambucil. These two molecules cannot undergo thiolate-associated synthesis due to incompatibilities with specific functional groups but can be incorporated through an esterification reaction onto AuNPs. The release reactions of chlorambucil and sulindac conjugated AuNPs were monitored by <sup>1</sup>H NMR, and the furfuryl derivatives were confirmed with HRMS, validating the system's efficiency. This method showcased the versatility of AuNPs and simplified the purification steps in drug delivery applications.

The systems developed and characterized in **Chapters 2**, **3**, and **4** established the viability of using designed rDA reactions to release desired cargo, as marker probes of therapeutic agents. If applied to therapeutics, these systems can to some extent release at a rate that is therapeutically effective. Nonetheless, as the rDA reactions are thermal in nature, there is little opportunity to control release in an off-on-off manner because there is little opportunity to apply targeted (temporally or spatially) thermal events in whole tissue.

Whereas spherical AuNPs typically exhibit a single plasmon resonance peak in the visible range, anisotropic AuNRs also have a second, tunable (LSPR) signal that ranges from the visible to NIR region depending on the length. In recent years, this tunability makes AuNRs highly valuable in therapeutic applications due to their unique optical properties, biocompatibility, and modifiability. The photothermal effect of AuNRs is triggered by exposure to light that corresponds to the LSPR maximum. The AuNRs absorb light and convert it into heat, effectively generating

and dissipating heat from the particle to its surrounding medium. This process could facilitate the diffusion and release of the drug if AuNRs are functionalized with our designed DA adducts. Research has demonstrated that under NIR, AuNRs can significantly elevate temperatures, achieving an increase from 24 °C to 50 °C within just 2 minutes of irradiation. A specific example rapid and substantial temperature rise was achieved under the following conditions: a concentration of AuNRs at 10 nM, an incident wavelength of 808 nm at an intensity of 5.8 W/cm<sup>2</sup>, and water as the medium. 14 It is noted that the temperature change can vary depending on the AR of the AuNRs and the conditions (incident wavelength, NR concentration, intensity) of the illumination. Future studies should focus on identifying the optimal conditions for each AuNRs variant with specific AR to maximize their photothermal conversion efficiency. This effective photothermal conversion shows the potential of AuNRs as a photothermal triggered drug carrier. Moreover, the ability to tune the LSPR of AuNRs across a broad range of the electromagnetic spectrum is particularly advantageous for biomedical applications, as it minimizes interference from biological tissue absorption, especially from water. The non-ionizing and low-energy characteristics of NIR light reduce potential harm to human tissues, making it a safer option for such applications. However, synthesizing AuNRs with longer wavelength LSPR (> 900 nm) using a wet seed-mediated method is challenging and therefore very limiting to reaching our desired endpoint of having a nanoplatform that can be stimulated *in situ* to release its drug or cargo.

The story thus moved forward in **Chapter 5** with approaches to the synthesis of NIR-responsive NRs. Importantly, the photothermal heating that results from NIR irradiation of NRs potentially can trigger capping layer DA adduct-associated cargo release without there being externally applied heat. By adjusting the solubility of the precursor to the NRs, the CTA-Ag-Br complex, the reproducibility of the AuNRs syntheses can be significantly improved with a tunable

LSPR beyond 850 nm. Furthermore, application of the solubility enhancement techniques developed in the AuNRs synthesis to the AgNRs synthetic process leads to significantly improved reproducibility and purity. A depletion method was then applied to remove the spherical AgNPs side products. Analysis of the UV-vis-NIR spectra of AgNRs revealed two characteristic plasmonic peaks: a TSPR at 354 nm and a LSPR ranging from 550 nm to NIR range by varying the seed concentration. Spherical AgNP side products and their 420 nm SPR peak were successfully removed from different AgNRs samples through precipitation. The refinement of the AgNRs synthetic process makes the synthetic procedure more straightforward and reproducible to those people who are not expert in nanomaterial synthesis.

Overall, this Thesis has introduced a platform that significantly contributes to the understanding of thermally dependent release systems in potential nanomaterial-based drug delivery applications. Building upon the foundational work discussed in this Thesis, the subsequent section on future work will explore advanced modifications to optimize the functionality of AuNPs to be used as a carrier for therapeutic agent.

### **6.2 Discussion and Future Work**

This Thesis has demonstrated significant advancements in nanomaterial-based drug delivery systems, particularly through the innovative use of AuNPs. It lays a strong foundation for the development of multifunctional nanocarriers designed to control drug release with high precision.

Building upon the successful development of AuNPs systems for drug delivery, future efforts will aim to integrate these systems with cutting-edge imaging and targeting technologies.

Specifically, we plan to incorporate the previous work within our group on PET imaging using radiolabeled AuNPs with the developed delivery system in this Thesis. As a result, we can track the precise location of the nanoparticles within the body, thereby enhancing the precision of drug delivery and then release the therapeutic compound upon applying heat. Antibodies have been widely used in drug delivery applications to specifically lock onto disease-associated sites. Therefore, AuNPs and AuNRs could act as theragnostic platforms by simultaneously carrying targeting, diagnostics, and delivery agents. This approach will ensure that therapeutic agents are delivered directly to the affected areas, minimizing systemic exposure and maximizing therapeutic efficacy.

Future studies should focus on the surface functionalization of the linker onto AuNRs while maintaining water solubility. Subsequent photothermal kinetic studies of linker-coated AuNRs are necessary to analyze the viability of photothermal release. Similar to the studies conducted for AuNPs, assessments of toxicity and stability in various environments should follow to ensure comprehensive evaluation of the system's efficacy and safety in vitro and in vivo.

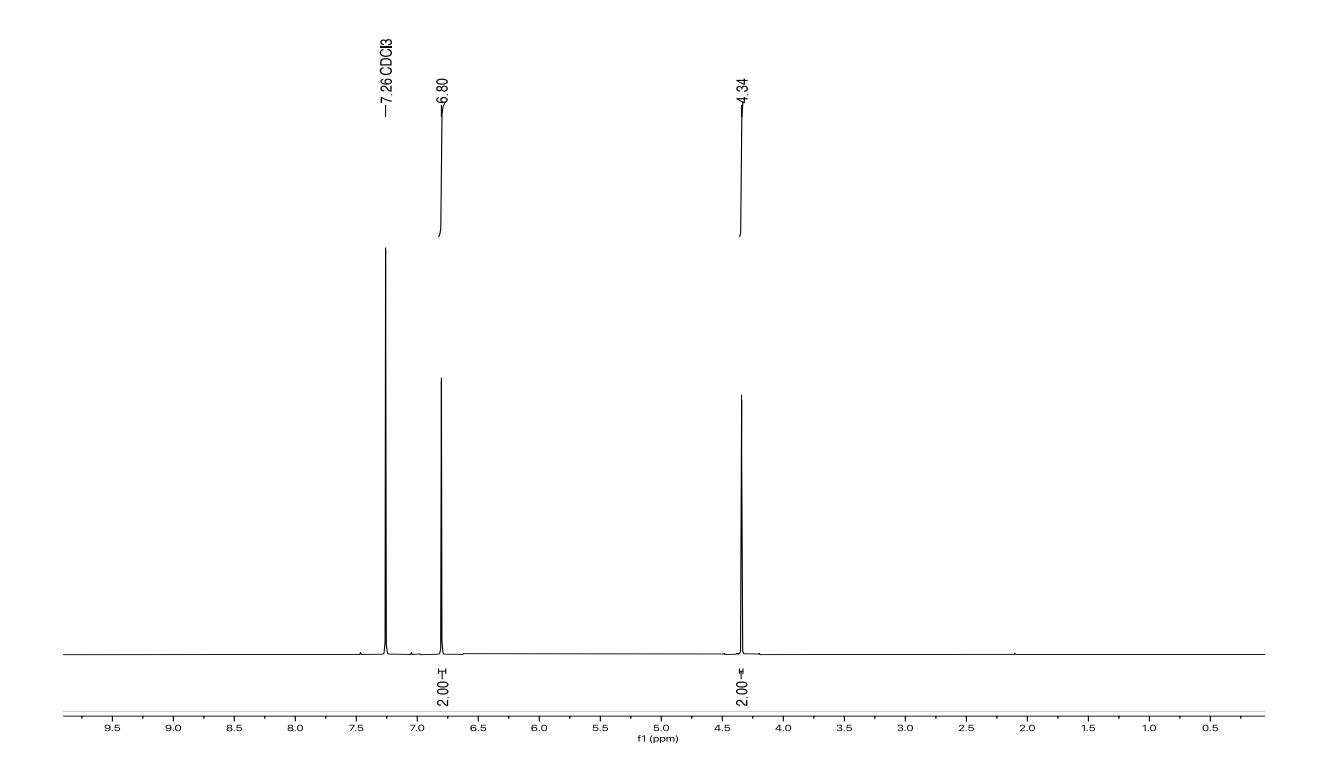
In conclusion, the research outlined in this thesis marks a significant advancement in the field of nanomaterial-based drug delivery systems, providing a robust foundation for the development of multifunctional nanocarriers with precise control over drug release. The future studies, focusing on the application of AuNRs and the further exploration of AuNPs, aim to examine the clinical applications of these systems. The successful continuation of this work could lead to new therapeutic methods that are more effective and less invasive. The findings from this research are anticipated to soon move from the lab into real-world applications, helping to fulfill the potential of nanotechnology in healthcare.

#### **6.3 Reference**

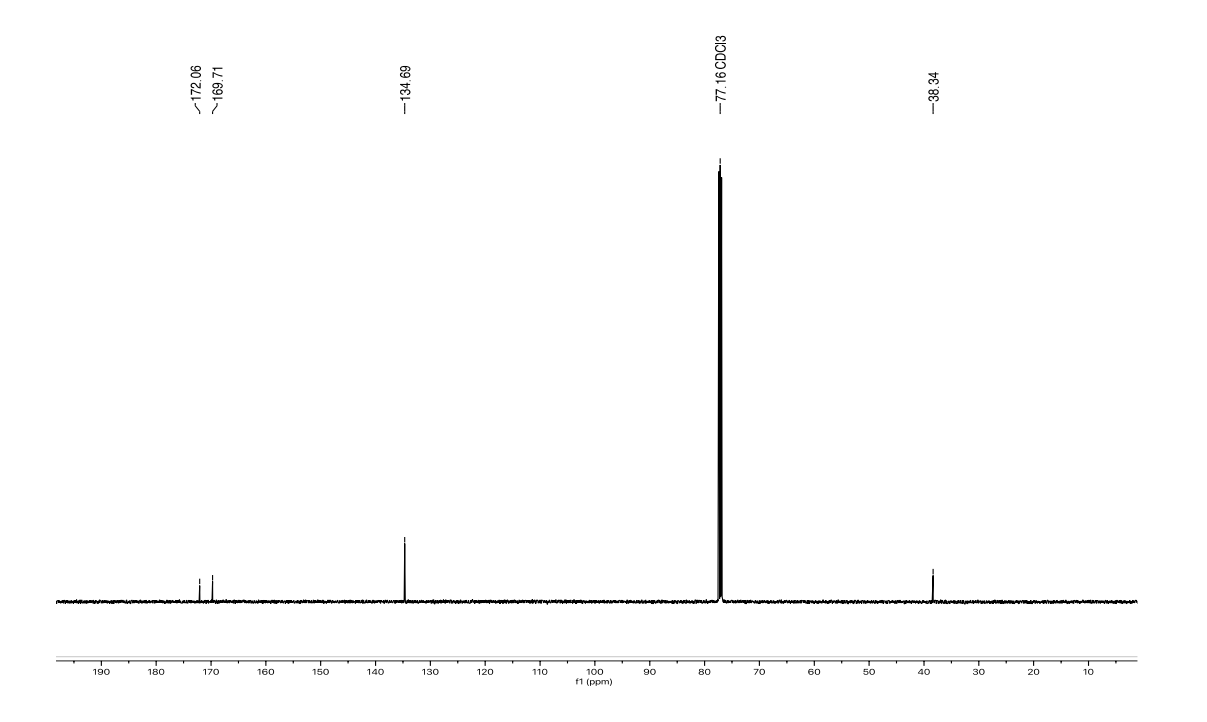
- (1) Hua, S. Advances in Oral Drug Delivery for Regional Targeting in the Gastrointestinal Tract Influence of Physiological, Pathophysiological and Pharmaceutical Factors. *Front. Pharmacol.* **2020**, *11*. https://doi.org/10.3389/fphar.2020.00524.
- (2) Shukla, R.; Bansal, V.; Chaudhary, M.; Basu, A.; Bhonde, R. R.; Sastry, M. Biocompatibility of Gold Nanoparticles and Their Endocytotic Fate Inside the Cellular Compartment: A Microscopic Overview. *Langmuir* **2005**, *21* (23), 10644–10654. https://doi.org/10.1021/la0513712.
- (3) Kimling, J.; Maier, M.; Okenve, B.; Kotaidis, V.; Ballot, H.; Plech, A. Turkevich Method for Gold Nanoparticle Synthesis Revisited. *J. Phys. Chem. B* **2006**, *110* (32), 15700–15707. https://doi.org/10.1021/jp061667w.
- (4) Ray, N. J.; Yoo, J. H.; McKeown, J. T.; Elhadj, S.; Baxamusa, S. H.; Johnson, M. A.; Nguyen, H. T.; Steele, W. A.; Chesser, J. M.; Matthews, M. J.; Feigenbaum, E. Enhanced Tunability of Gold Nanoparticle Size, Spacing, and Shape for Large-Scale Plasmonic Arrays. *ACS Appl. Nano Mater.* **2019**, *2* (7), 4395–4401. https://doi.org/10.1021/acsanm.9b00815.
- (5) Zhang, J.; Mou, L.; Jiang, X. Surface Chemistry of Gold Nanoparticles for Health-Related Applications. *Chemical Science* **2020**, *11* (4), 923–936. https://doi.org/10.1039/C9SC06497D.
- (6) Swierczewska, M.; Lee, S.; Chen, X. The Design and Application of Fluorophore– Gold Nanoparticle Activatable Probes. *Physical Chemistry Chemical Physics* **2011**, *13* (21), 9929–9941. https://doi.org/10.1039/C0CP02967J.
- (7) Zhu, J.; Chin, J.; Wängler, C.; Wängler, B.; Lennox, R. B.; Schirrmacher, R. Rapid 18F-Labeling and Loading of PEGylated Gold Nanoparticles for in Vivo Applications. *Bioconjugate Chem.* **2014**, 25 (6), 1143–1150. https://doi.org/10.1021/bc5001593.
- (8) Wang, F.; Wang, Y.-C.; Dou, S.; Xiong, M.-H.; Sun, T.-M.; Wang, J. Doxorubicin-Tethered Responsive Gold Nanoparticles Facilitate Intracellular Drug Delivery for Overcoming Multidrug Resistance in Cancer Cells. *ACS Nano* **2011**, *5* (5), 3679–3692. https://doi.org/10.1021/nn200007z.
- (9) Busch, R. T.; Karim, F.; Weis, J.; Sun, Y.; Zhao, C.; Vasquez, E. S. Optimization and Structural Stability of Gold Nanoparticle–Antibody Bioconjugates. *ACS Omega* **2019**, *4* (12), 15269–15279. https://doi.org/10.1021/acsomega.9b02276.
- (10) Li, F.; Qin, Y.; Lee, J.; Liao, H.; Wang, N.; Davis, T. P.; Qiao, R.; Ling, D. Stimuli-Responsive Nano-Assemblies for Remotely Controlled Drug Delivery. *Journal of Controlled Release* **2020**, *322*, 566–592. https://doi.org/10.1016/j.jconrel.2020.03.051.
- (11) Xie, J.; Xiao, D.; Zhao, J.; Hu, N.; Bao, Q.; Jiang, L.; Yu, L. Mesoporous Silica Particles as a Multifunctional Delivery System for Pain Relief in Experimental Neuropathy. *Advanced Healthcare Materials* **2016**, *5* (10), 1213–1221. https://doi.org/10.1002/adhm.201500996.
- (12) Li, Z.; Xu, K.; Qin, L.; Zhao, D.; Yang, N.; Wang, D.; Yang, Y. Hollow Nanomaterials in Advanced Drug Delivery Systems: From Single- to Multiple Shells. *Advanced Materials* **2023**, *35* (12), 2203890. https://doi.org/10.1002/adma.202203890.
- (13) Chen, B.; Dai, W.; He, B.; Zhang, H.; Wang, X.; Wang, Y.; Zhang, Q. Current Multistage Drug Delivery Systems Based on the Tumor Microenvironment. *Theranostics* **2017**, *7* (3), 538–558. https://doi.org/10.7150/thno.16684.

(14) Mackey, M. A.; Ali, M. R. K.; Austin, L. A.; Near, R. D.; El-Sayed, M. A. The Most Effective Gold Nanorod Size for Plasmonic Photothermal Therapy: Theory and In Vitro Experiments. <i>J. Phys. Chem. B</i> <b>2014</b> , <i>118</i> (5), 1319–1326. https://doi.org/10.1021/jp409298f.
Appendix
A NMR spectroscopic data from Chapter 2
Compound 2

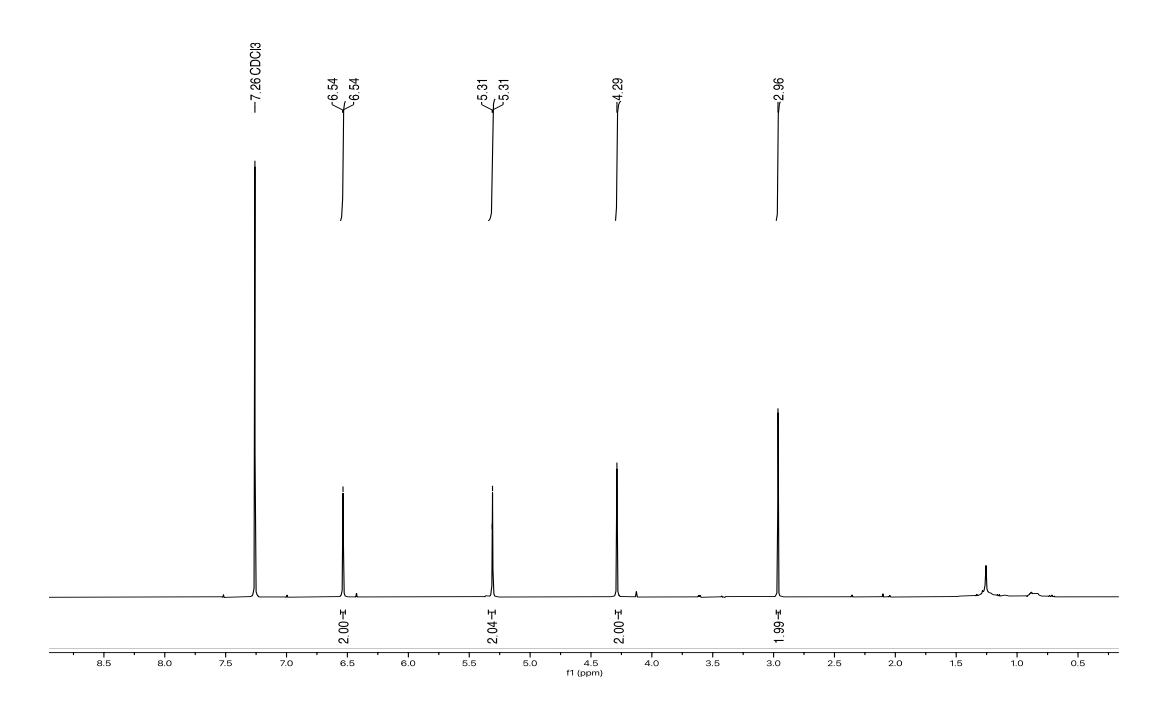
# <sup>1</sup>H NMR (500 MHz, CDCl<sub>3</sub>)



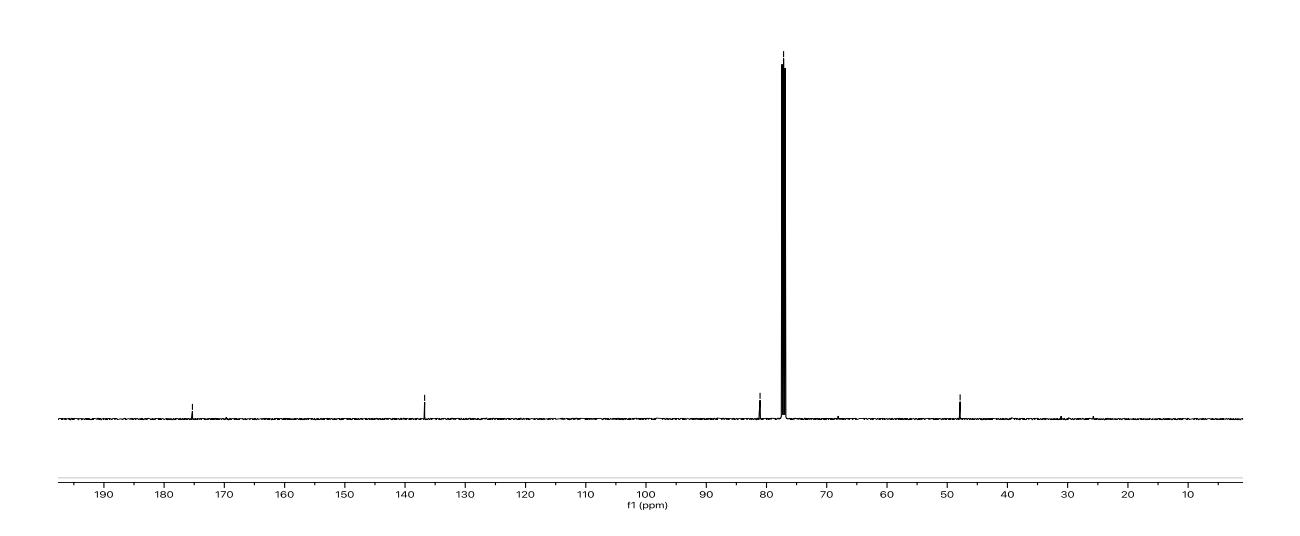
# <sup>13</sup>C NMR (126 MHz, CDCl3)



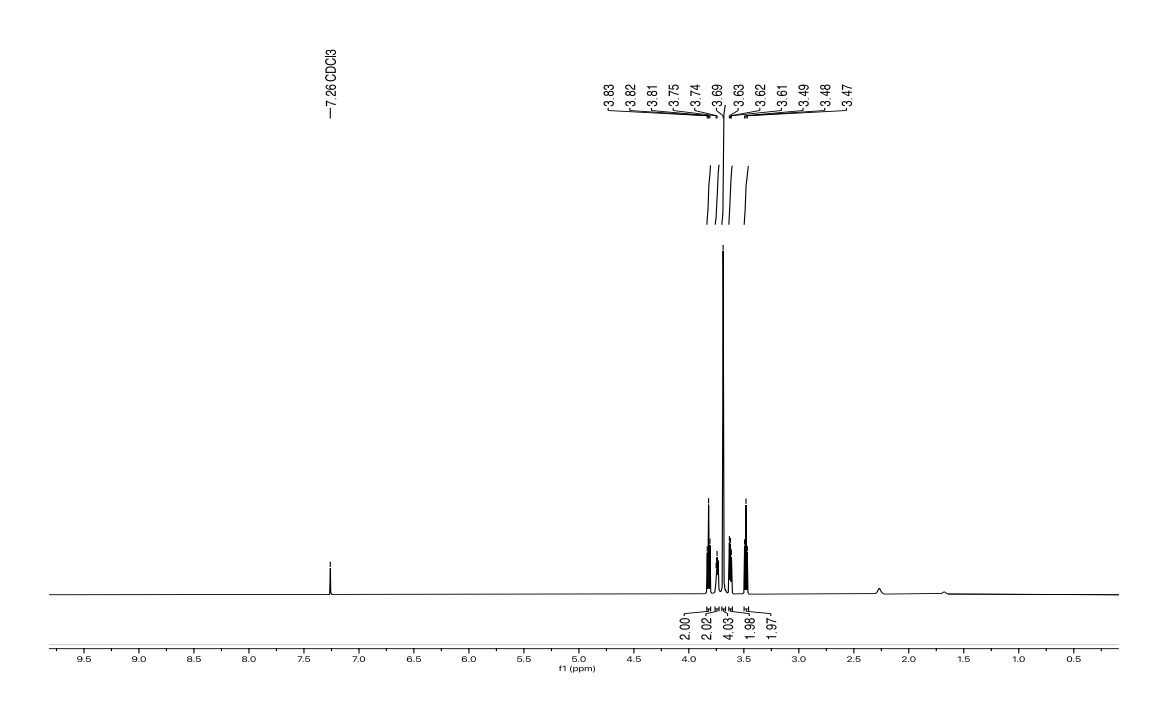
# <sup>1</sup>H NMR (400 MHz, CDCl<sub>3</sub>)

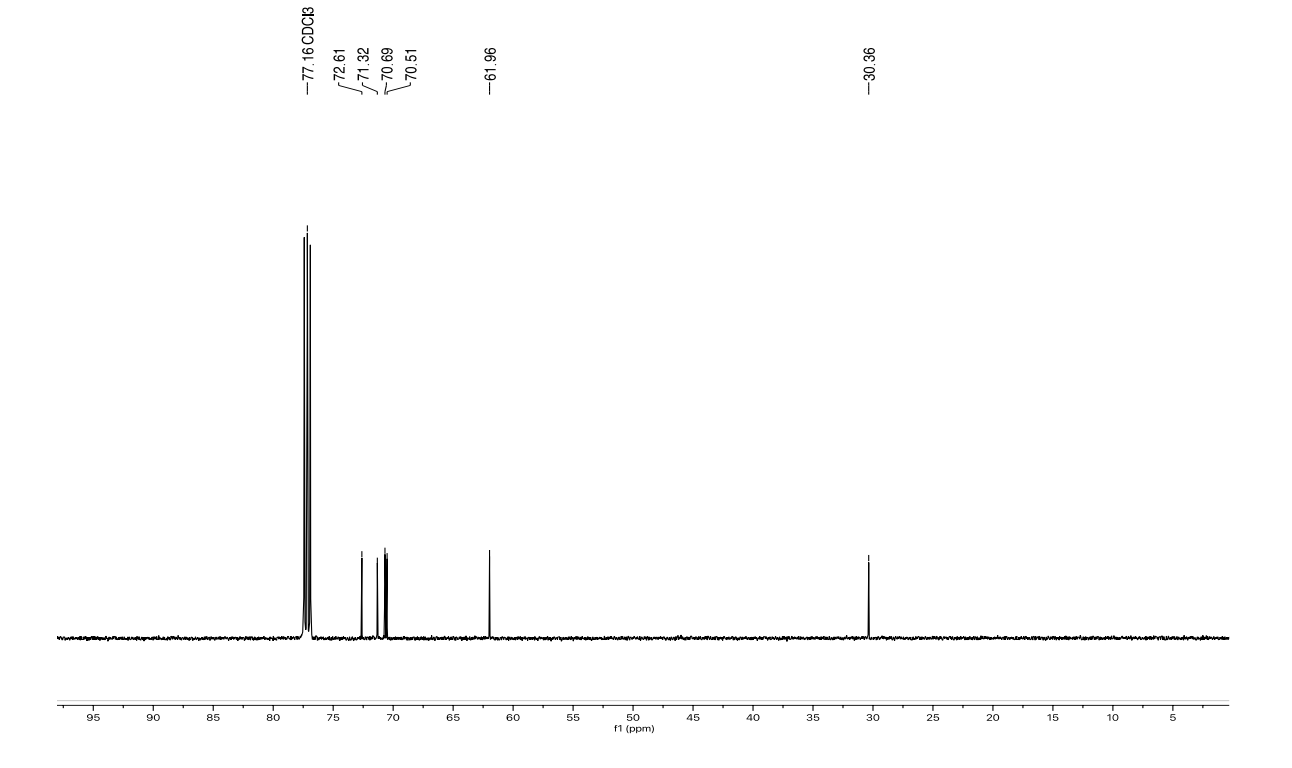




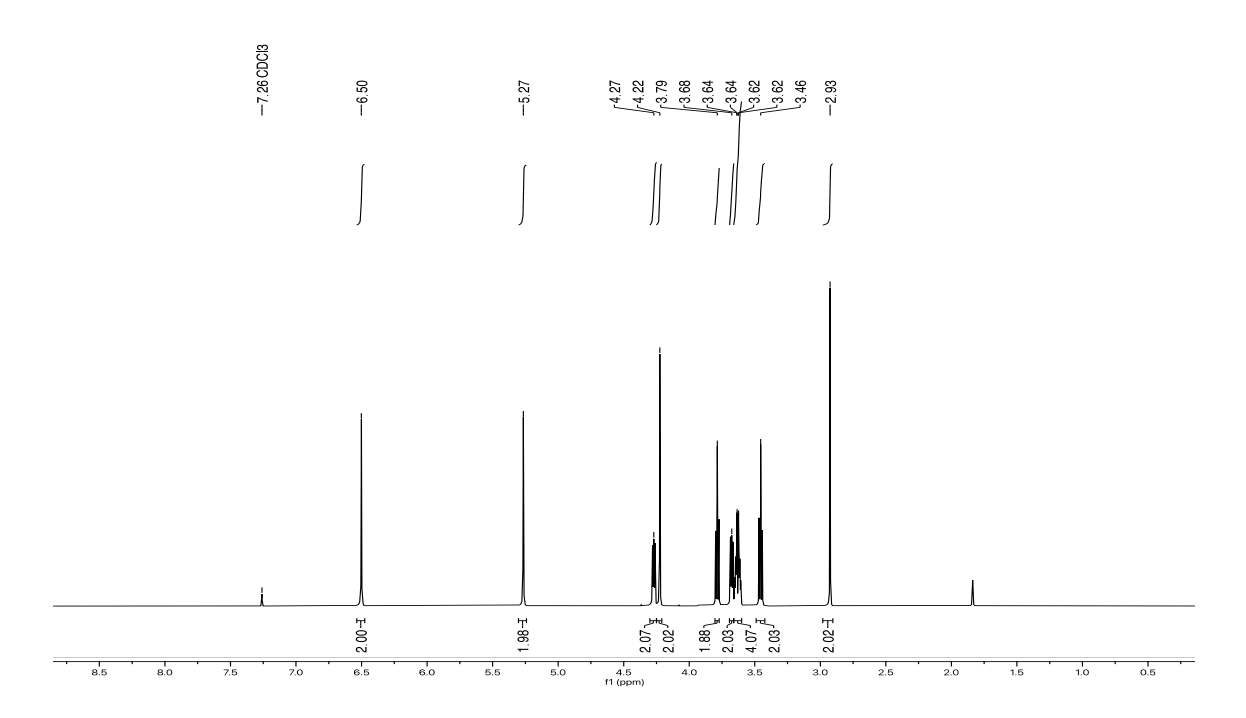


<sup>1</sup>H NMR (500 MHz, CDCl<sub>3</sub>)

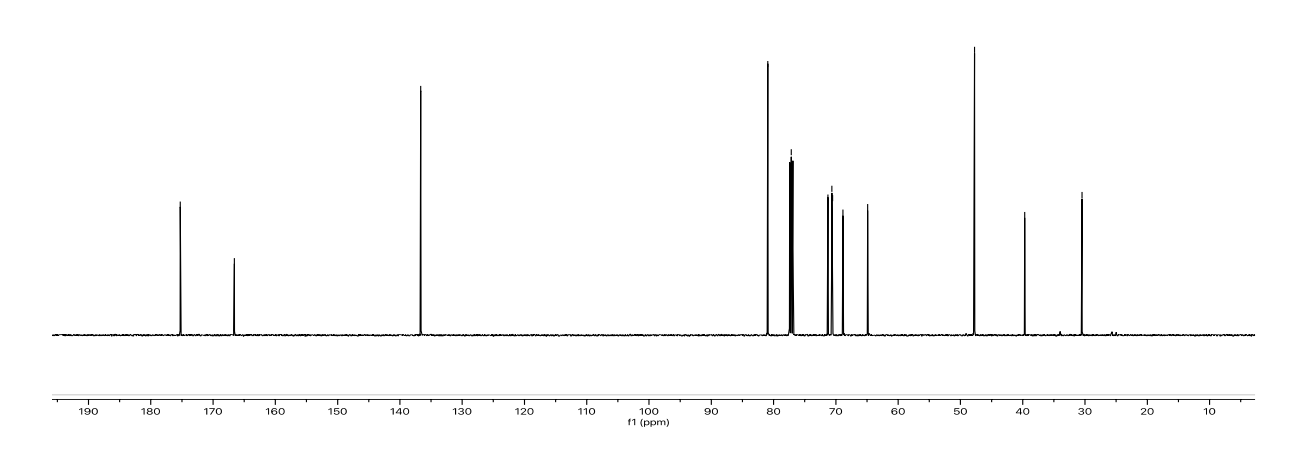




# <sup>1</sup>H NMR (500 MHz, CDCl<sub>3</sub>)

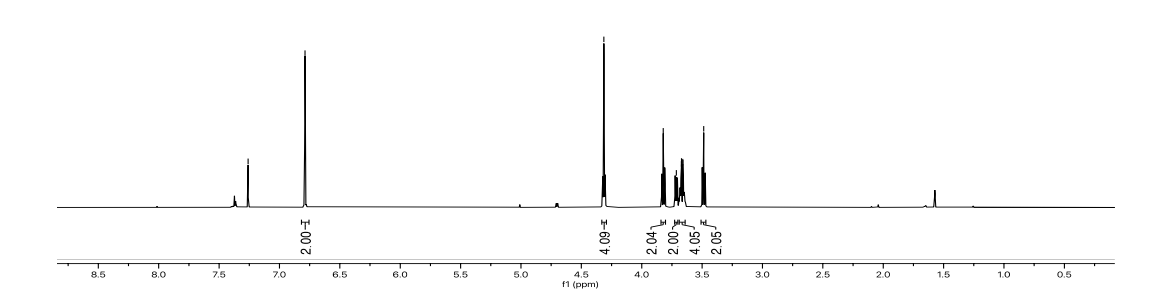




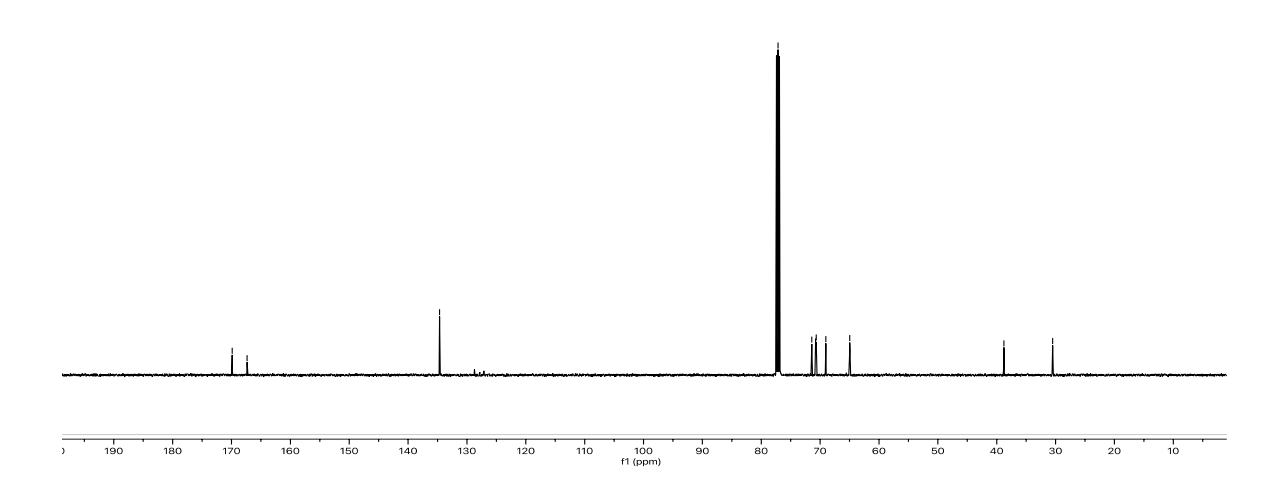


# <sup>1</sup>H NMR (400 MHz, CDCl<sub>3</sub>)



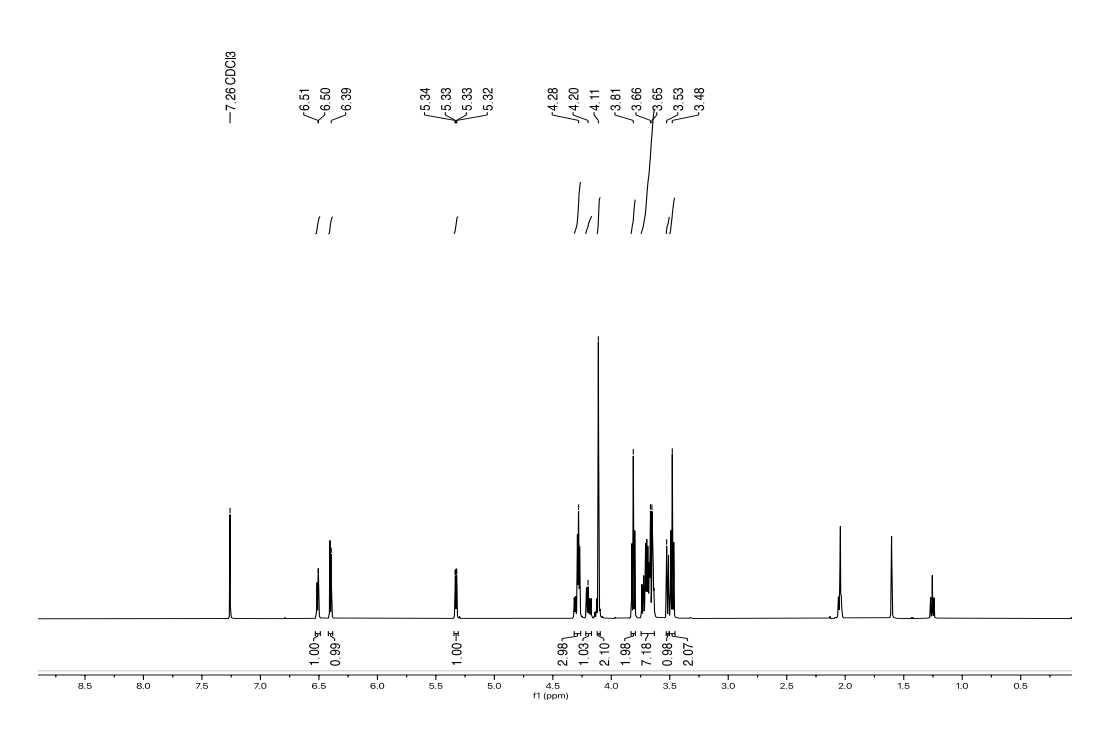


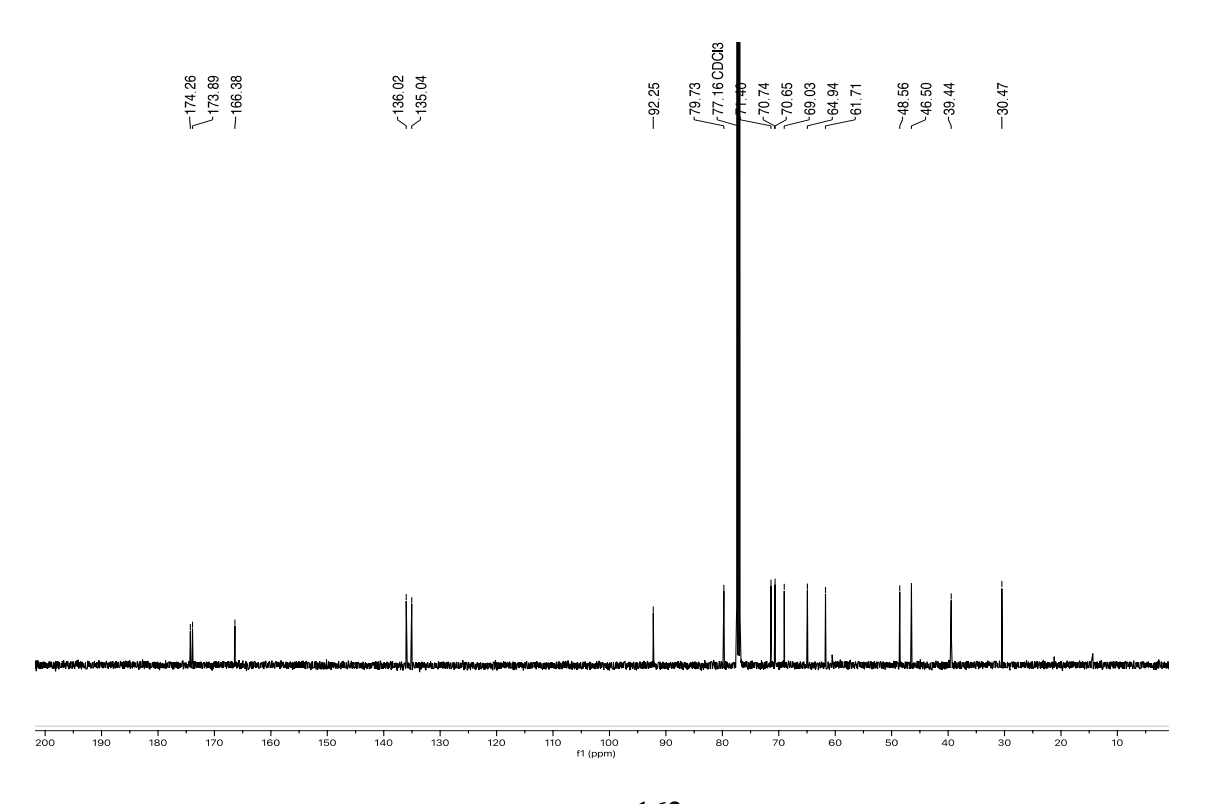




## endo-Compound 7

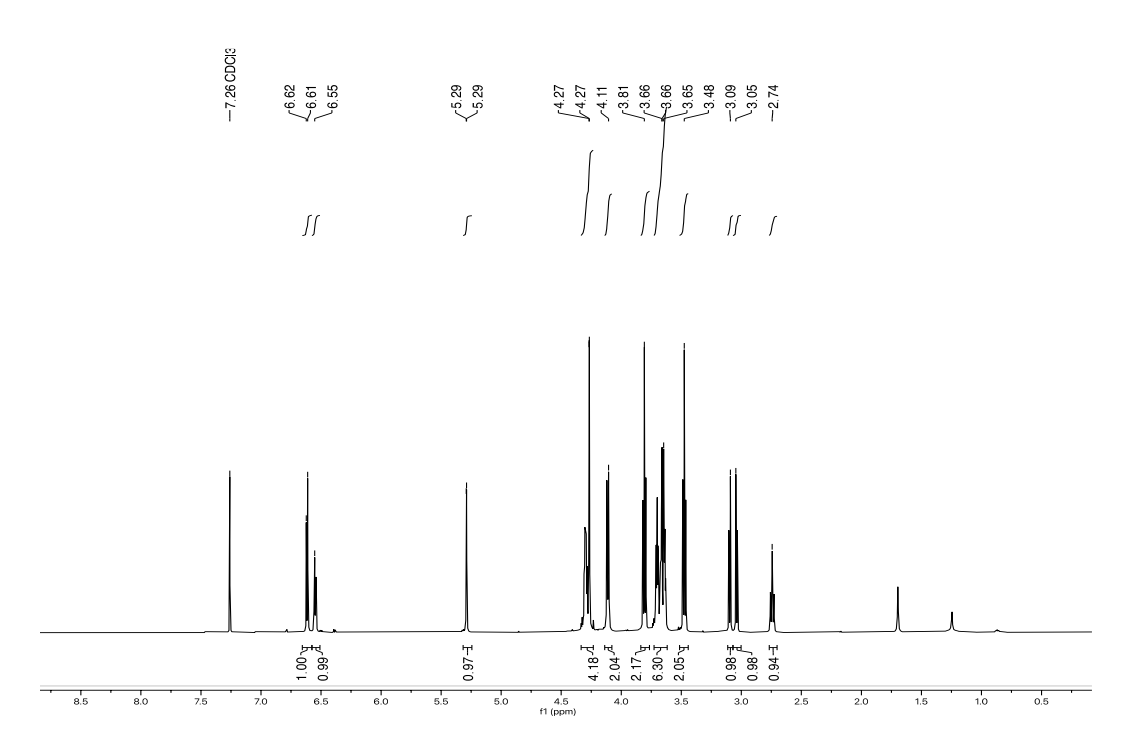
# <sup>1</sup>H NMR (500 MHz, CDCl<sub>3</sub>)

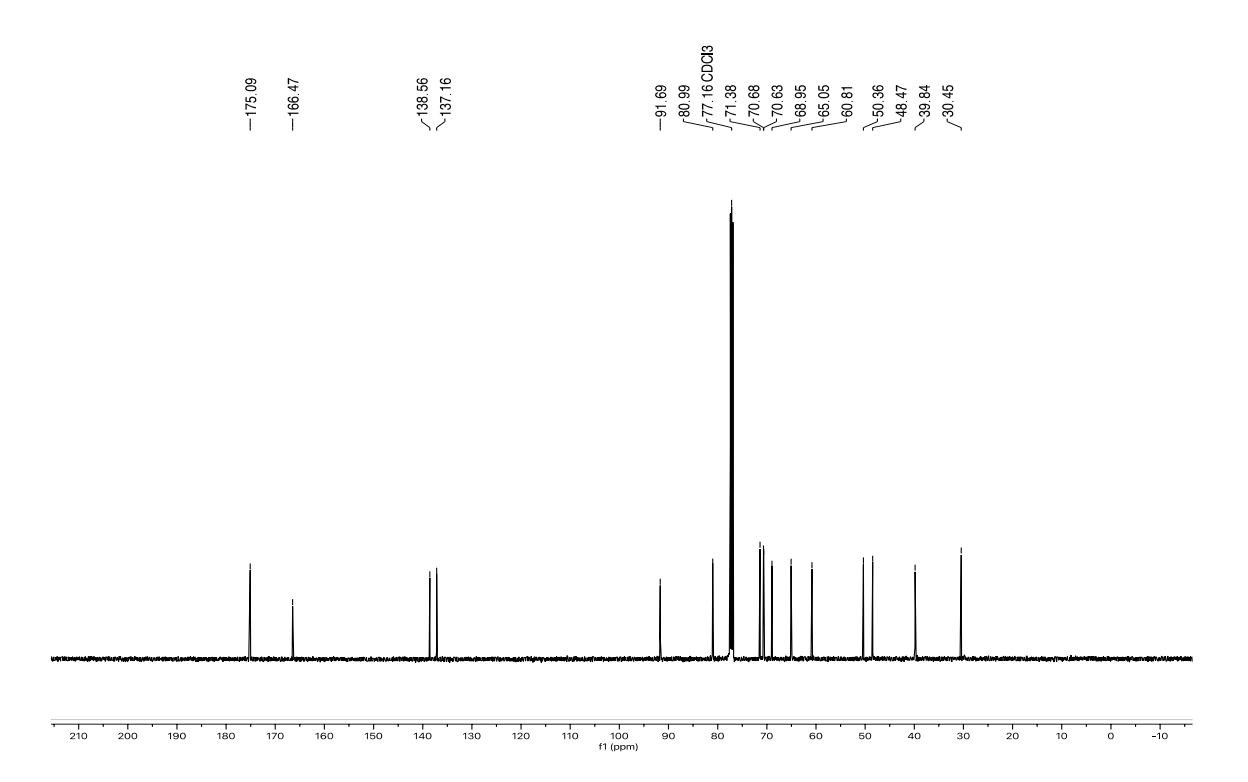




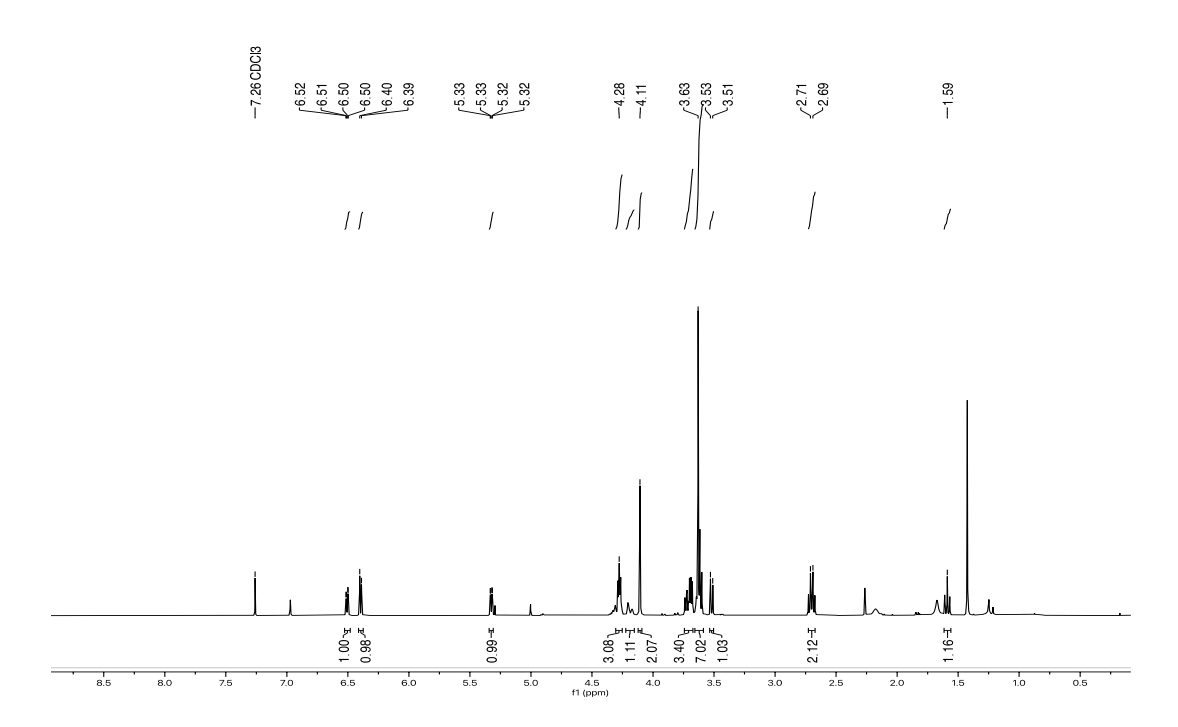
#### exo-Compound 7

# <sup>1</sup>H NMR (500 MHz, CDCl<sub>3</sub>)

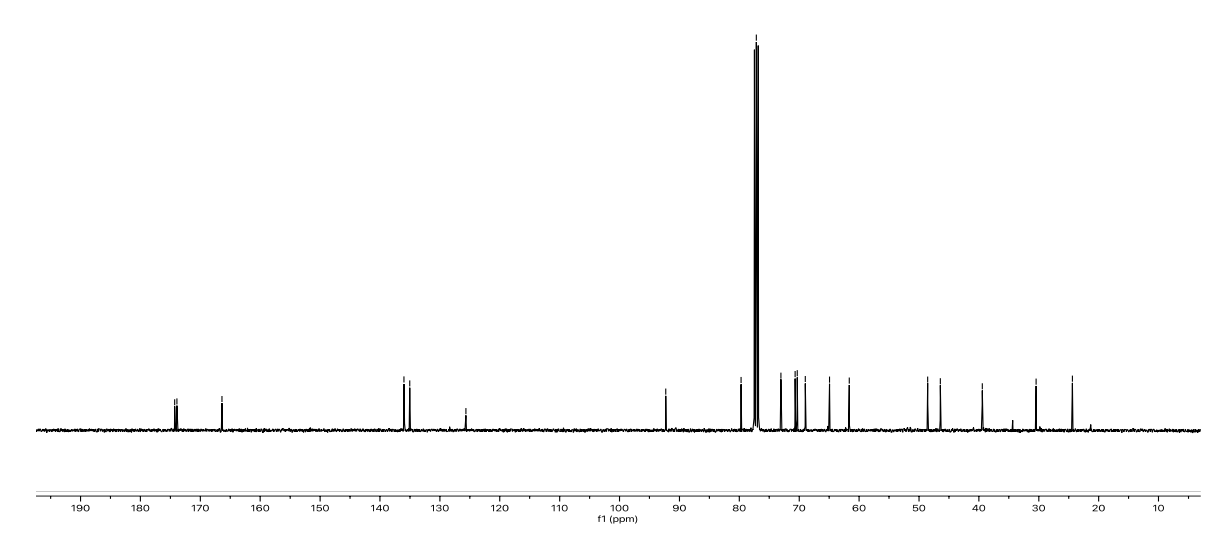




<sup>1</sup>H NMR (400 MHz, CDCl<sub>3</sub>)



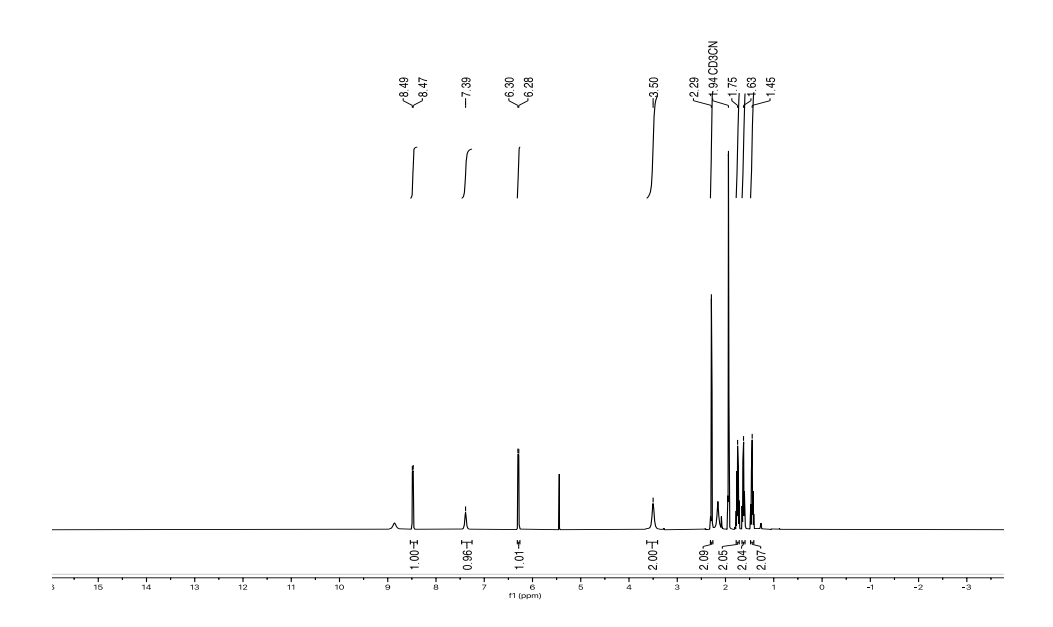


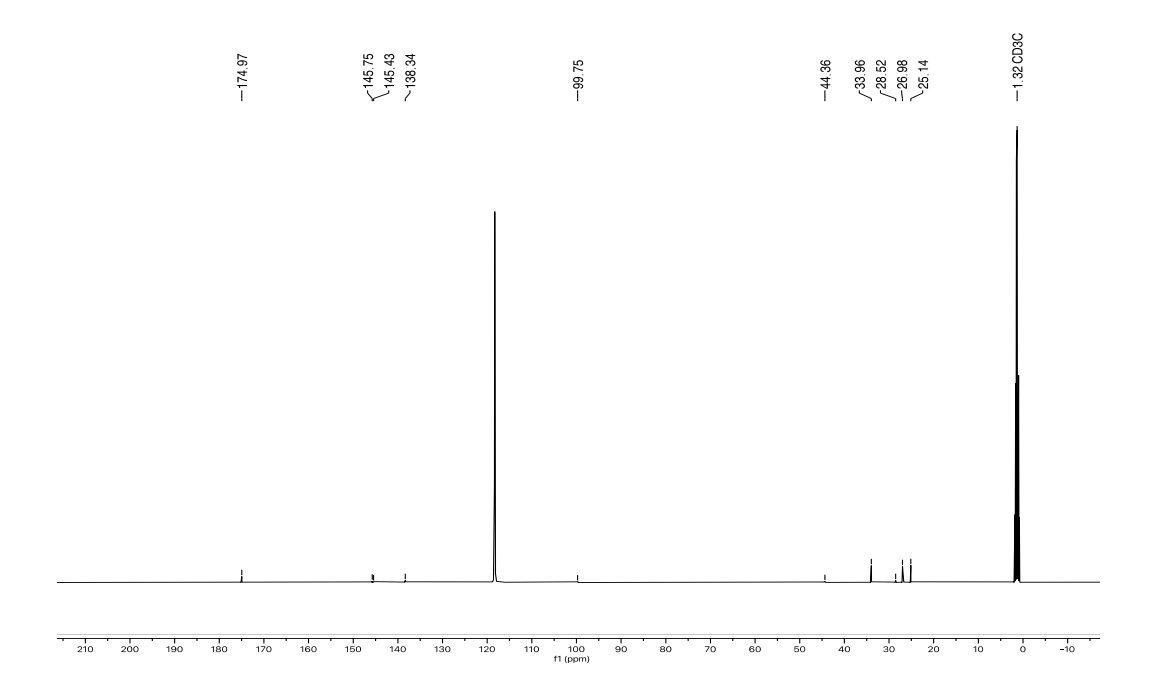


## **B NMR** spectroscopic data from Chapter 3

#### Compound 2

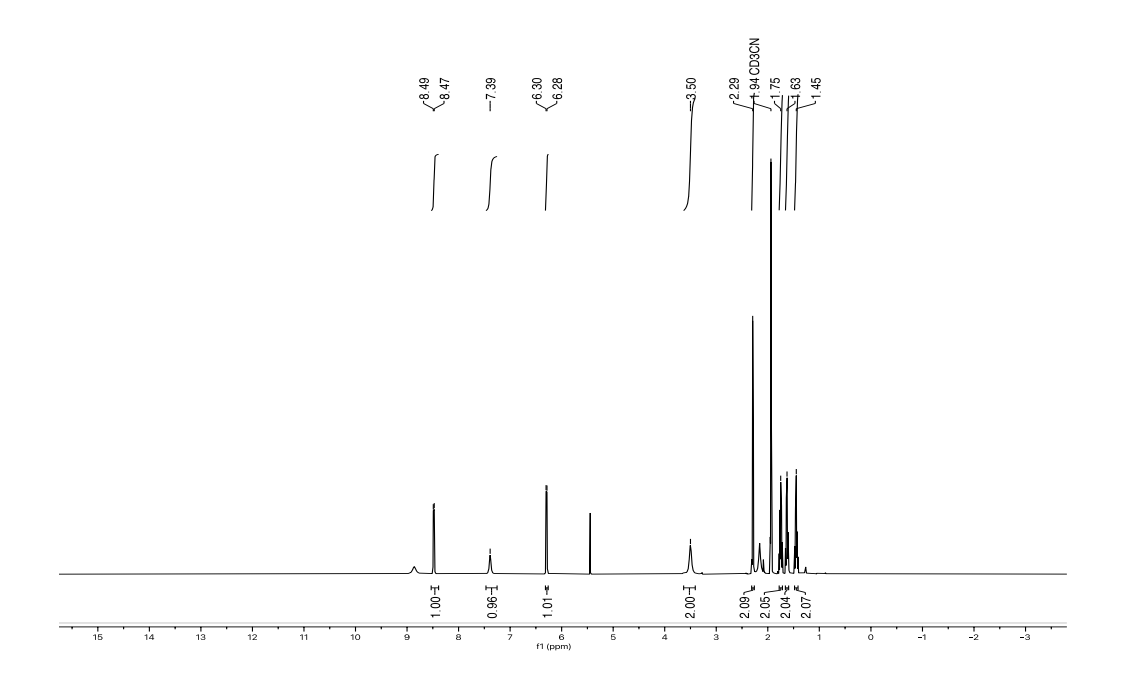
<sup>1</sup>H NMR (500 MHz, CD<sub>3</sub>CN)

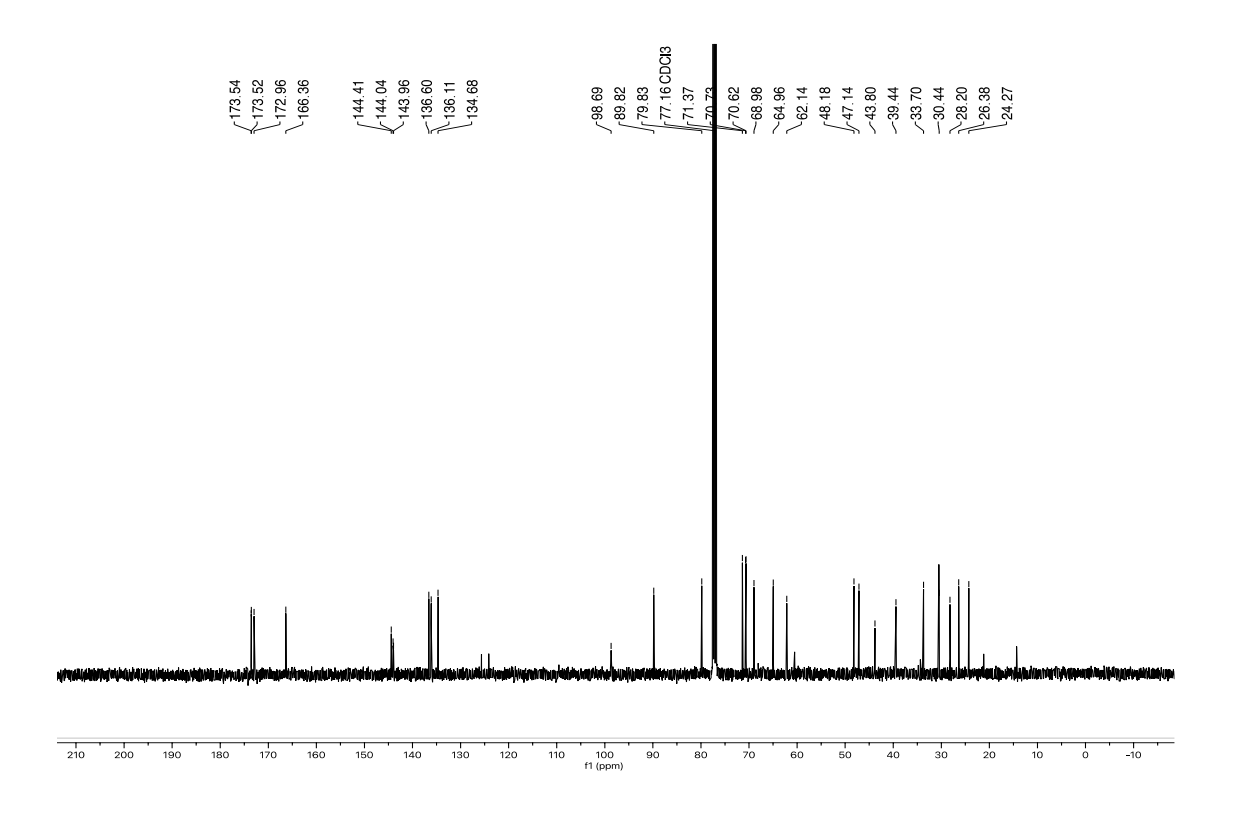




#### endo-Compound 3

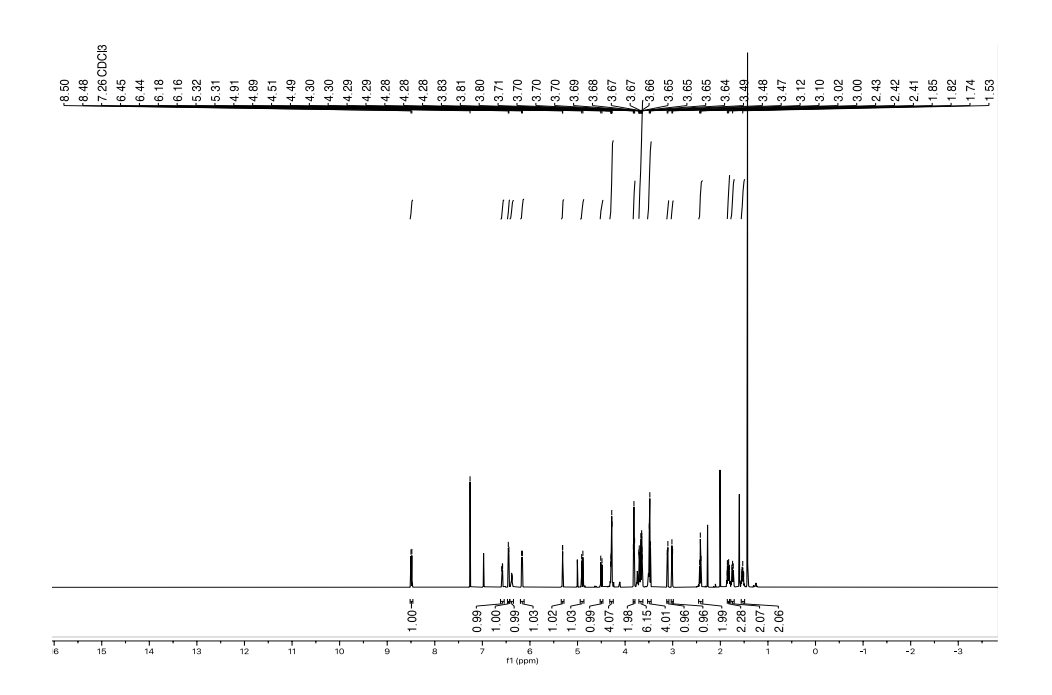
# <sup>1</sup>H NMR (400 MHz, CDCl<sub>3</sub>)

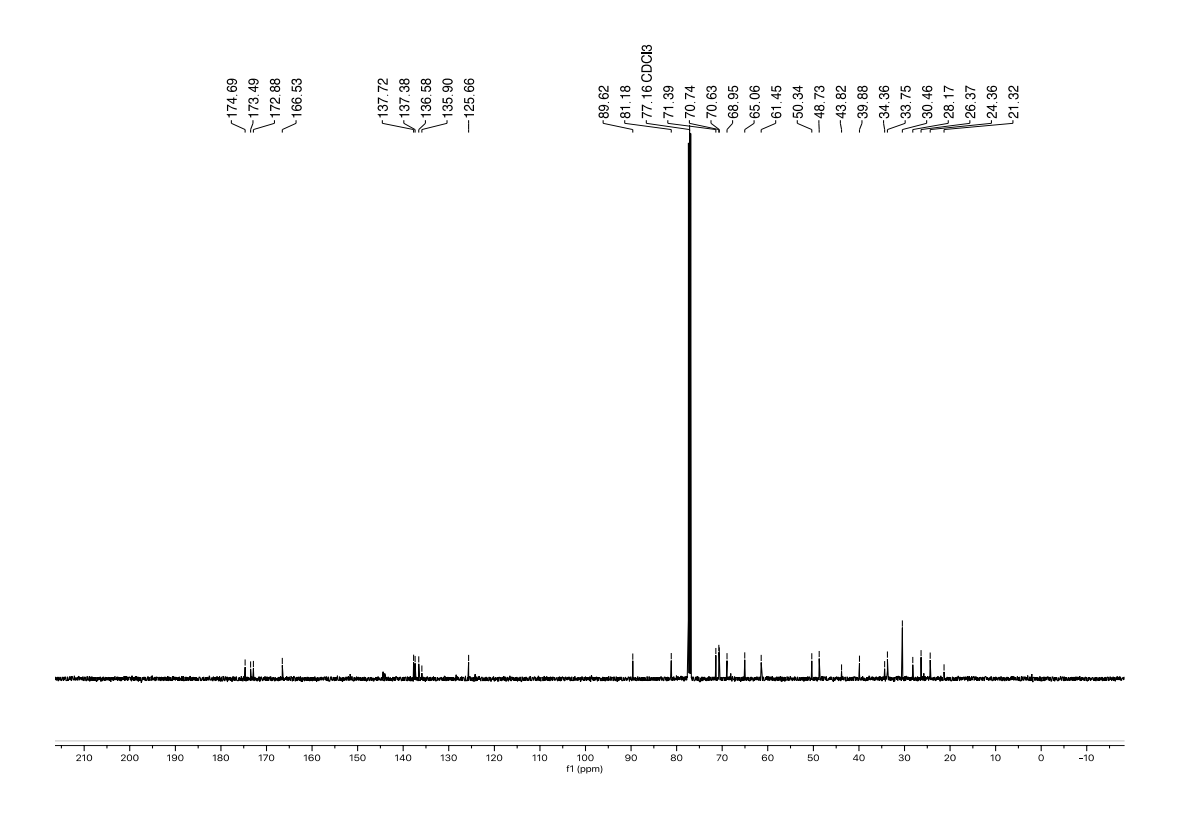




## exo-Compound 3

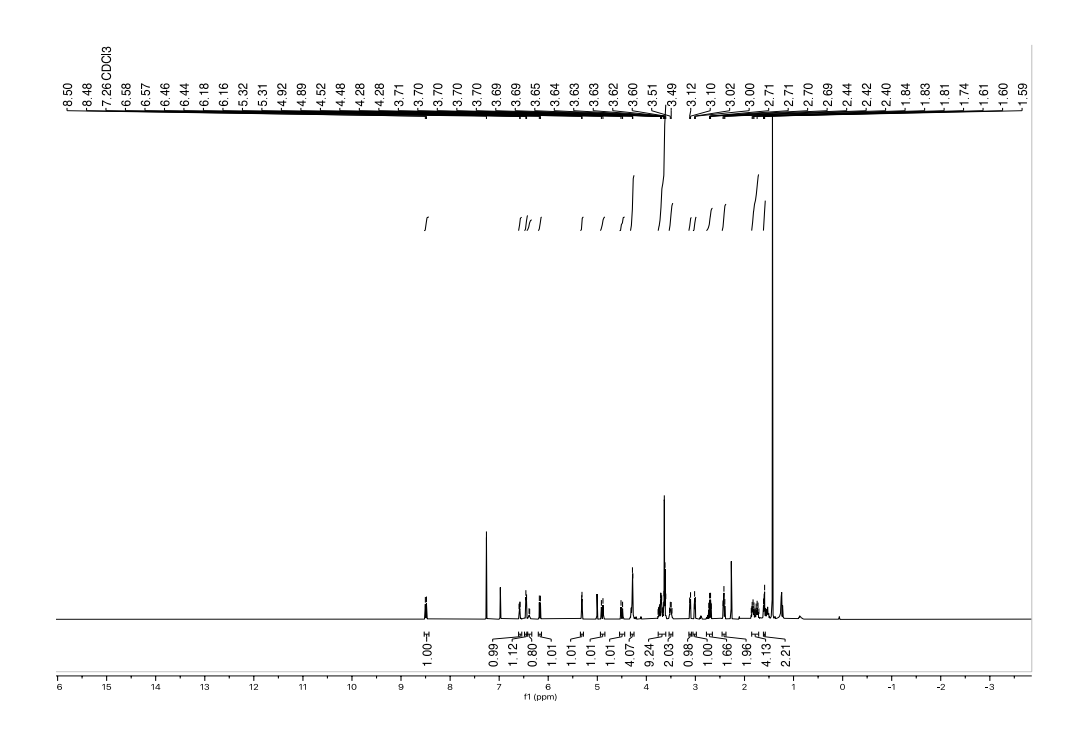
## <sup>1</sup>H NMR (400 MHz, CDCl<sub>3</sub>)

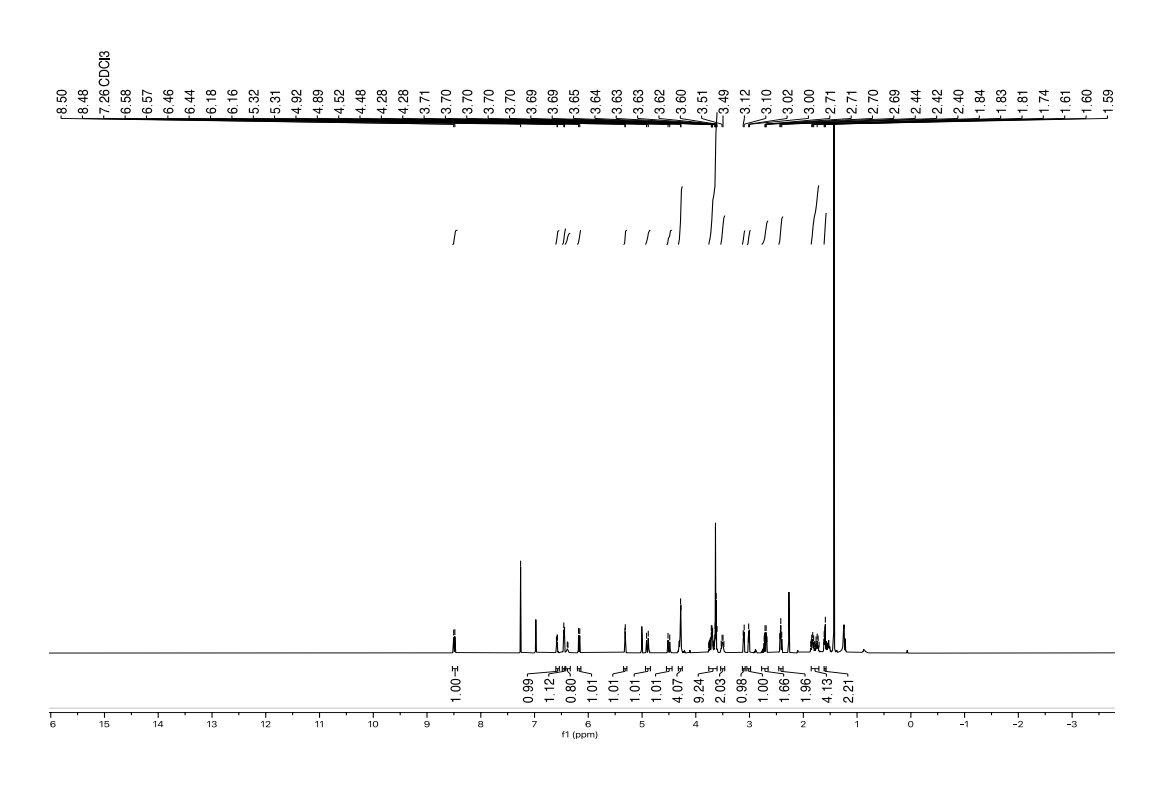




#### exo-Compound 4

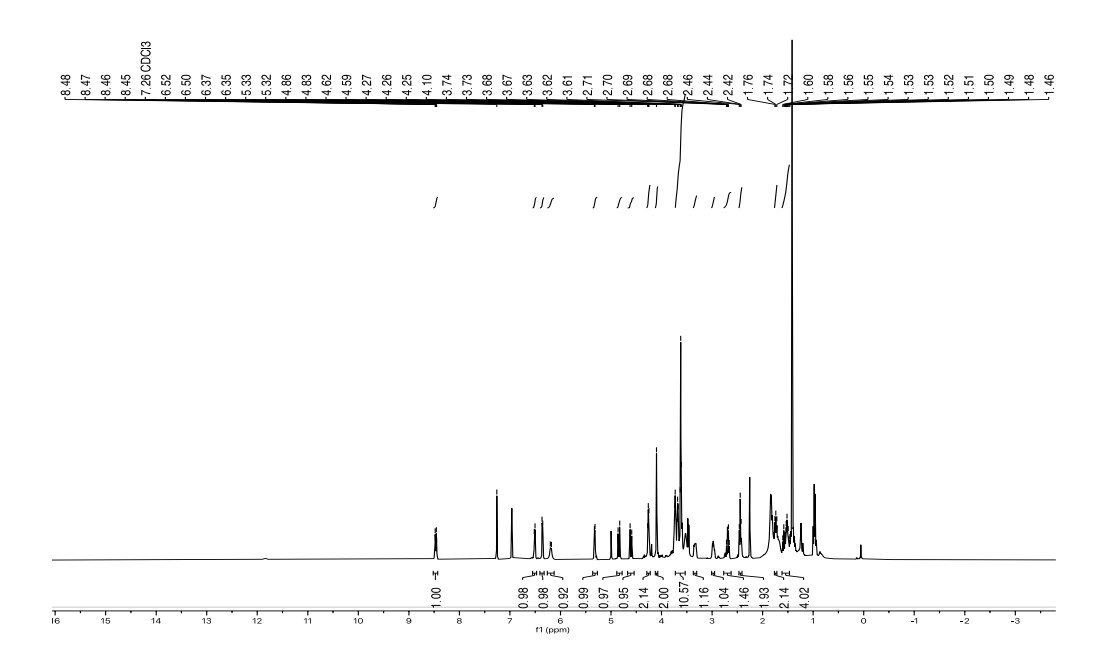
# <sup>1</sup>H NMR (400 MHz, CDCl<sub>3</sub>)

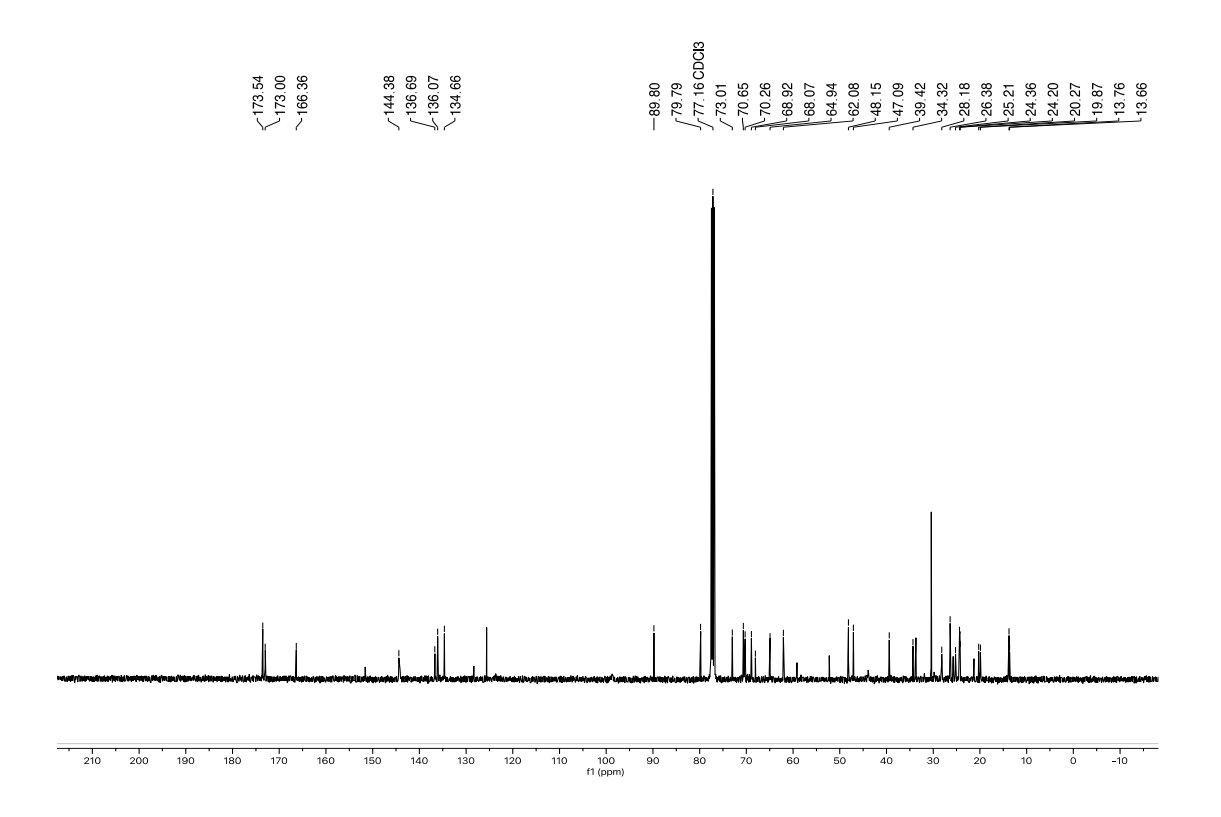




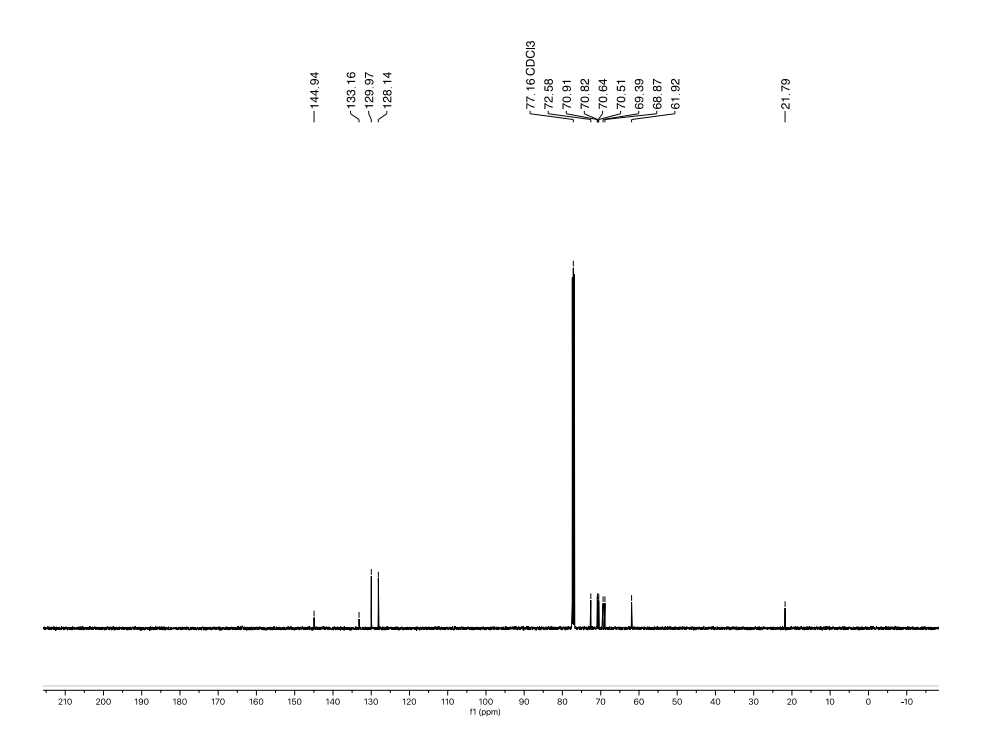
#### endo-Compound 4

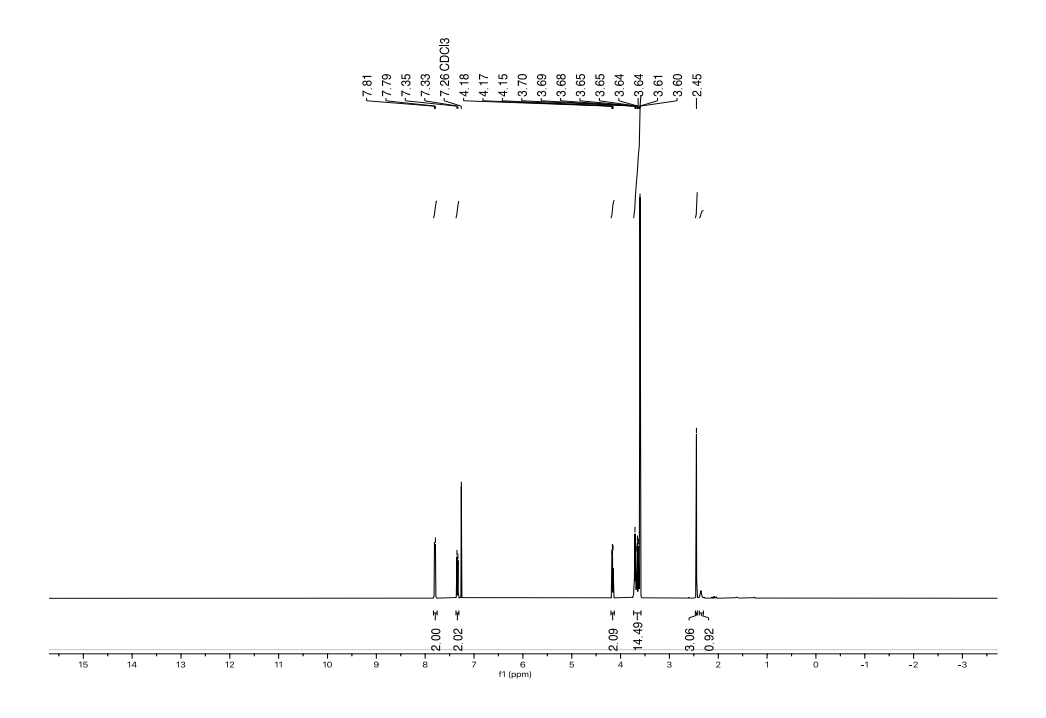
## <sup>1</sup>H NMR (400 MHz, CDCl<sub>3</sub>)



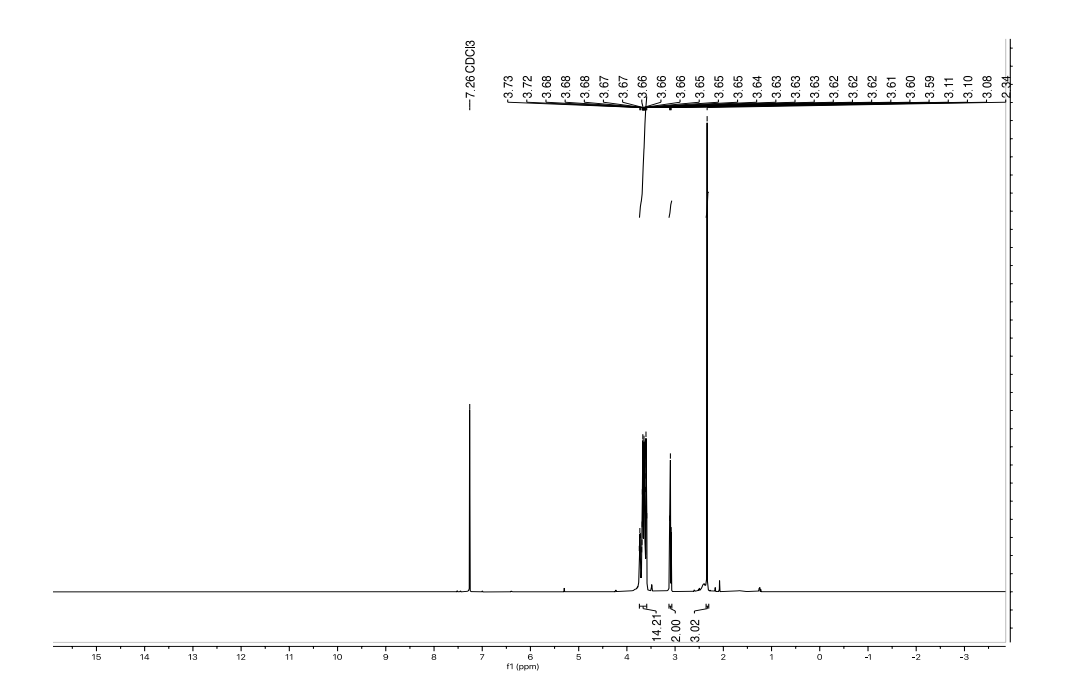


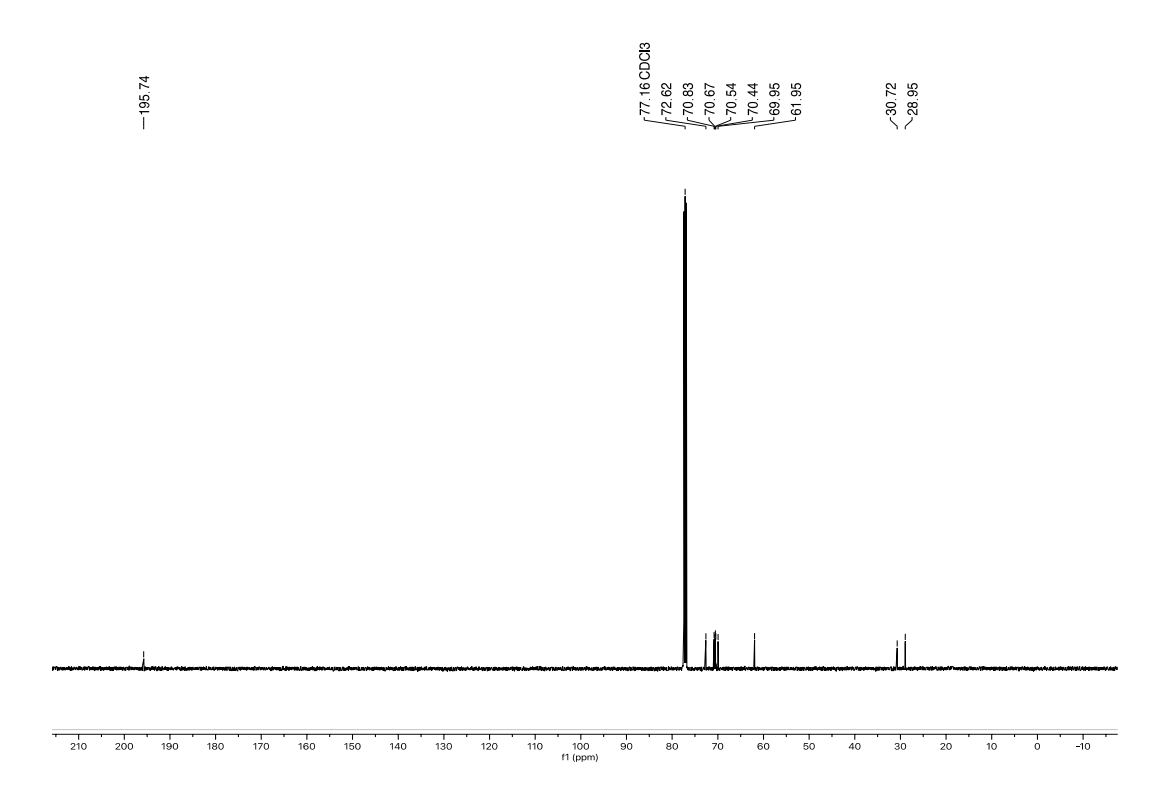
<sup>1</sup>H NMR (400 MHz, CDCl<sub>3</sub>)



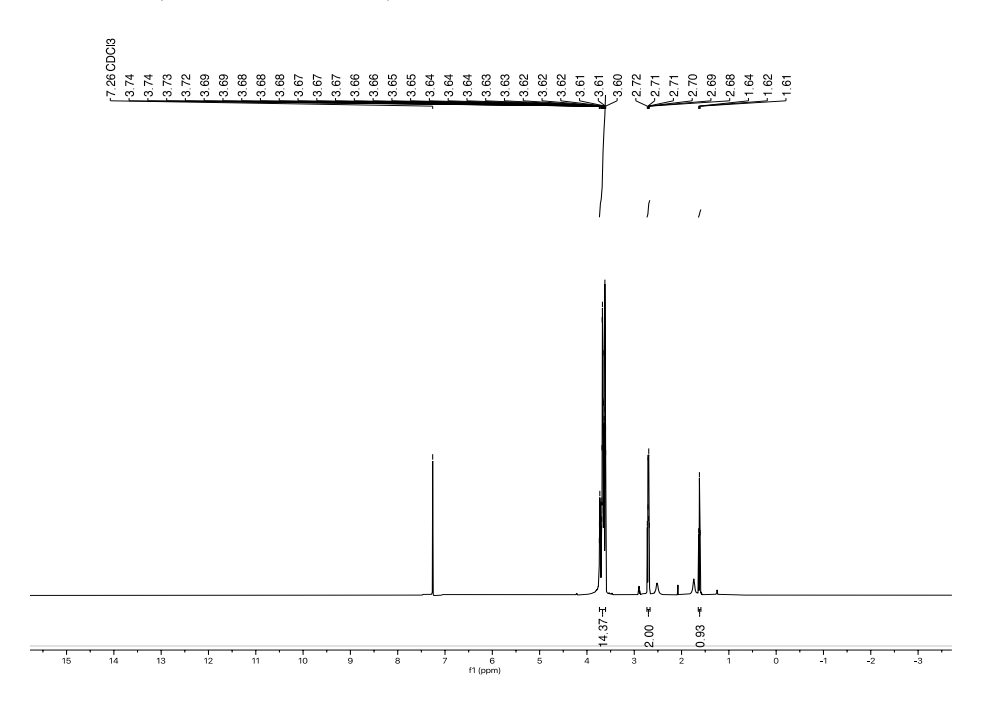


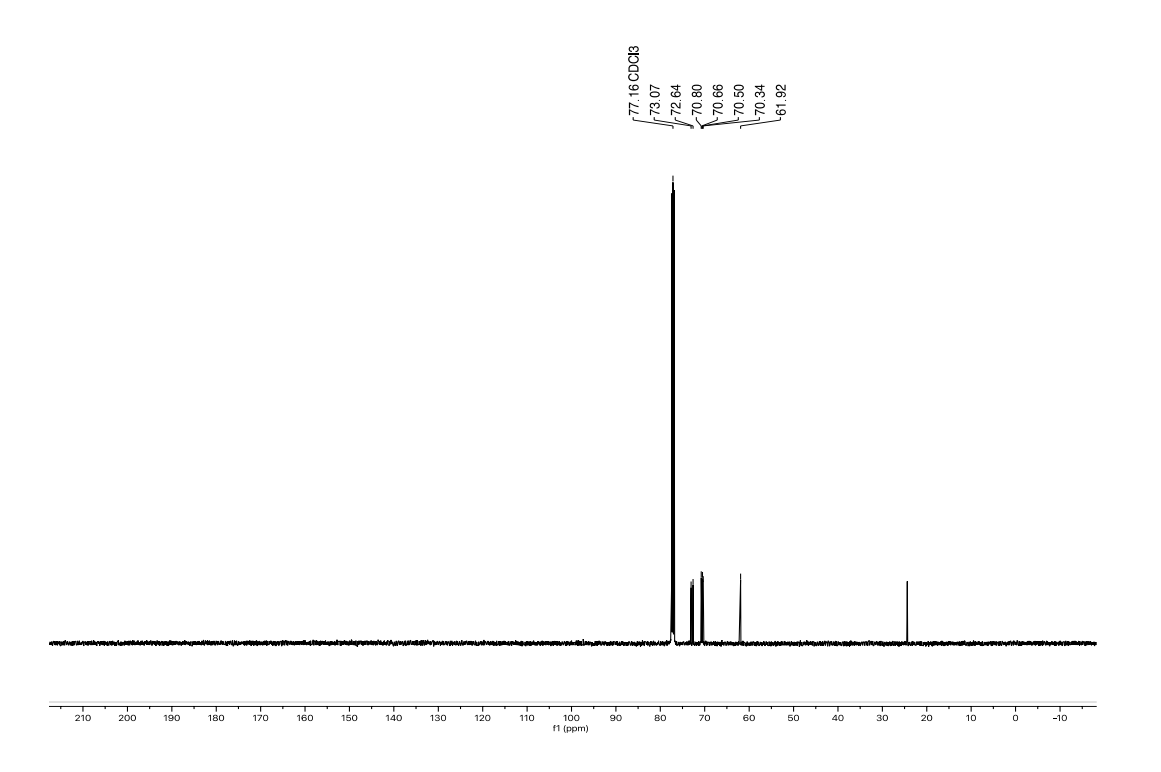
# <sup>1</sup>H NMR (400 MHz, CDCl<sub>3</sub>)





# <sup>1</sup>H NMR (400 MHz, CDCl<sub>3</sub>)

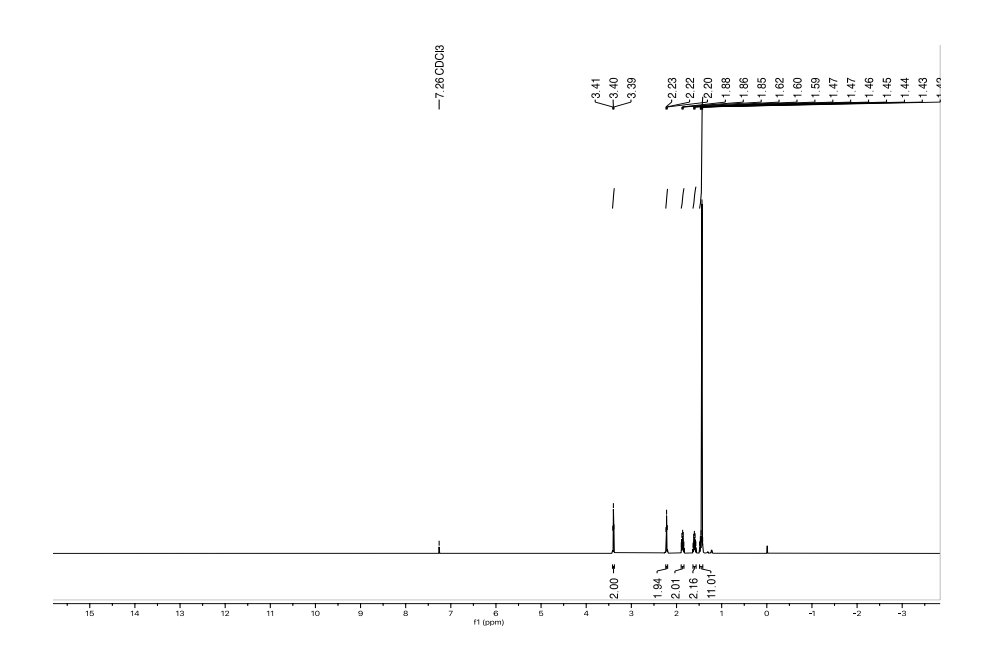


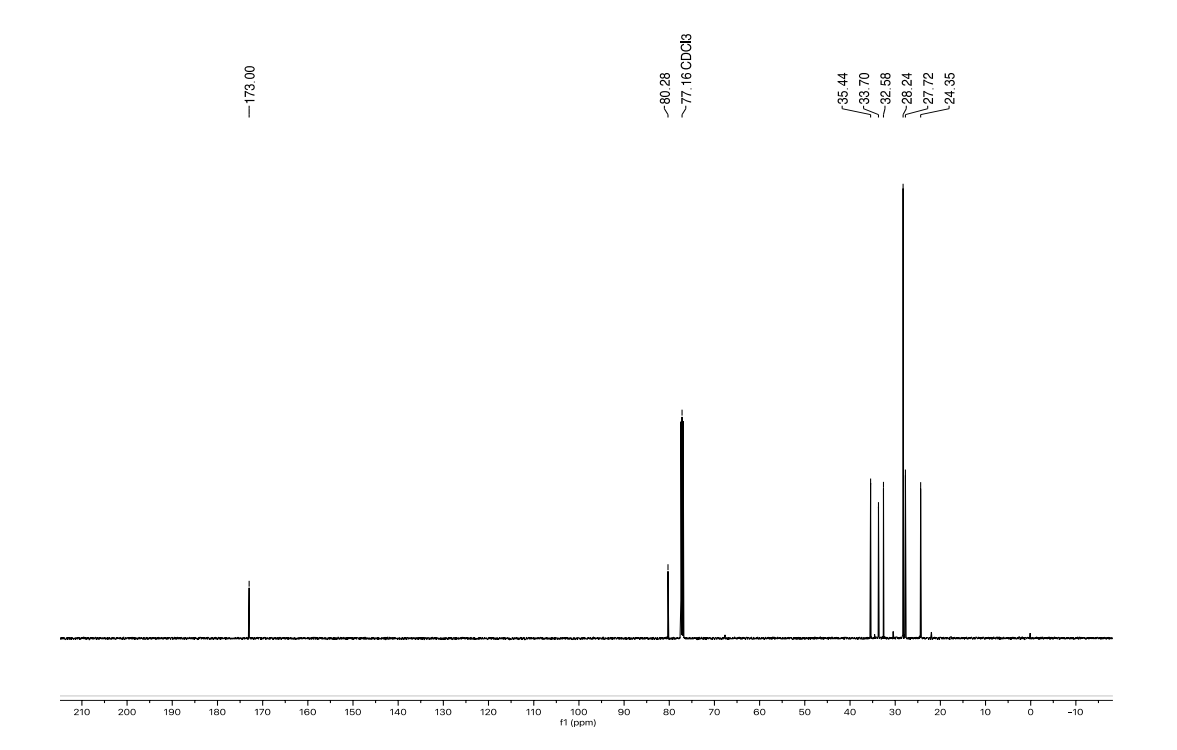


## C NMR spectroscopic data from Chapter 4

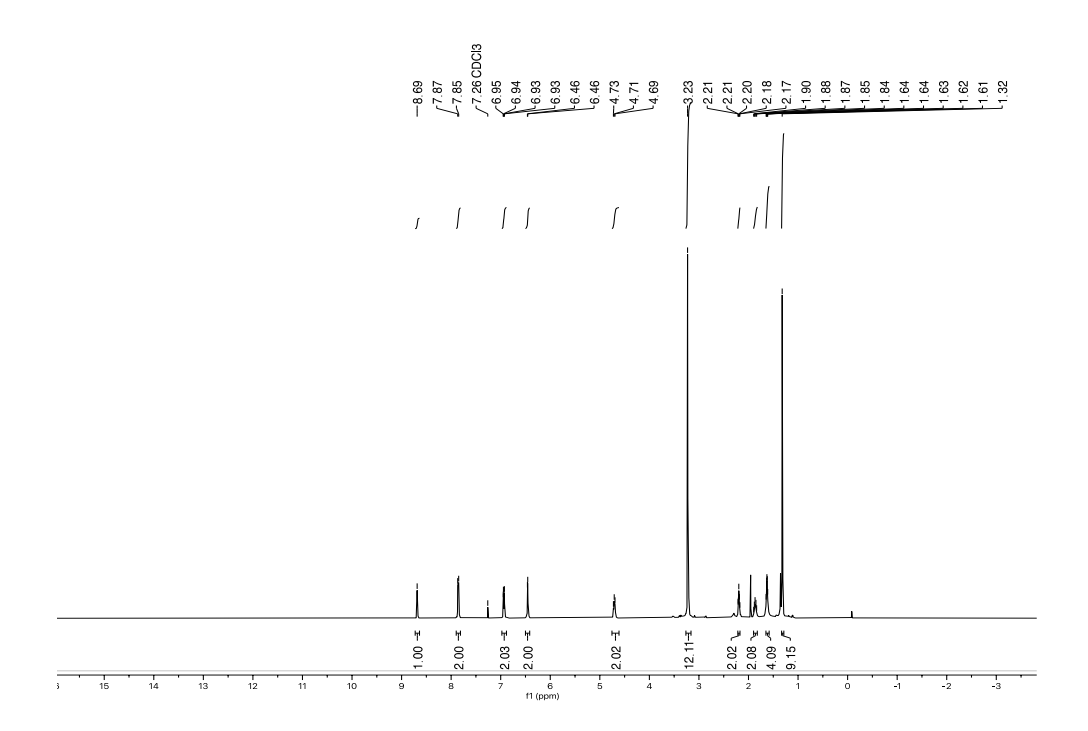
#### Compound 2

<sup>1</sup>H NMR (500 MHz, CDCl<sub>3</sub>)

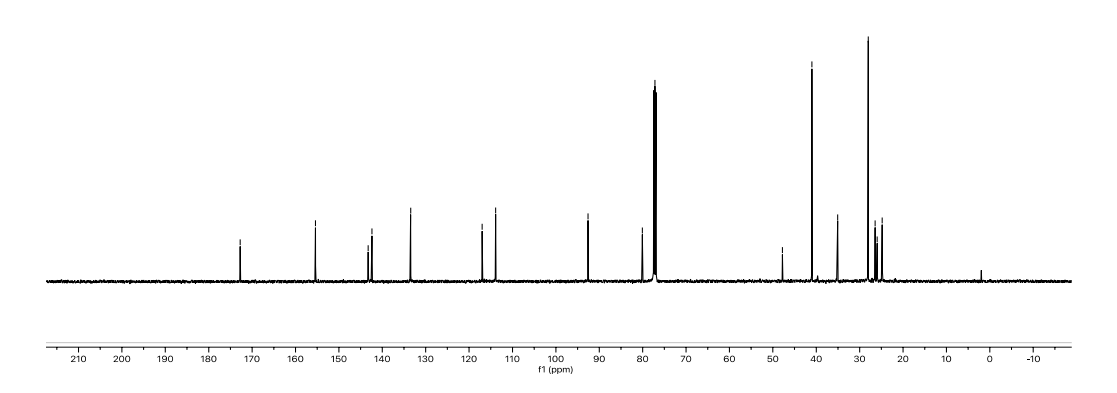




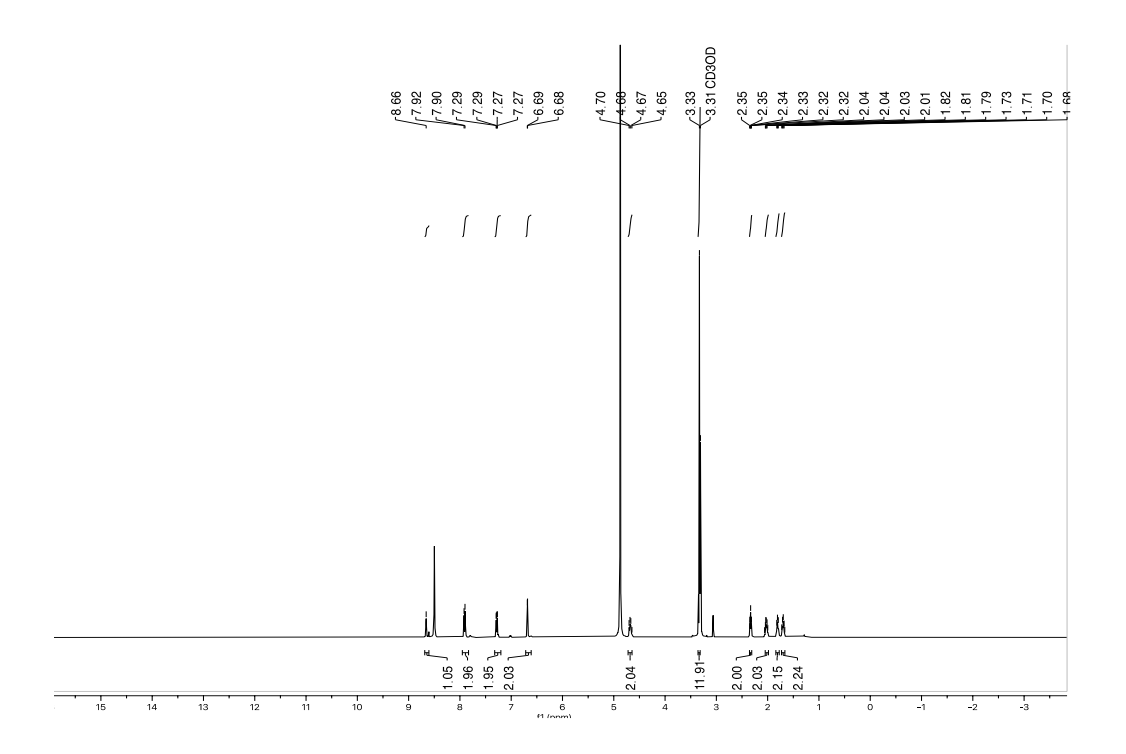
# <sup>1</sup>H NMR (500 MHz, CDCl<sub>3</sub>)



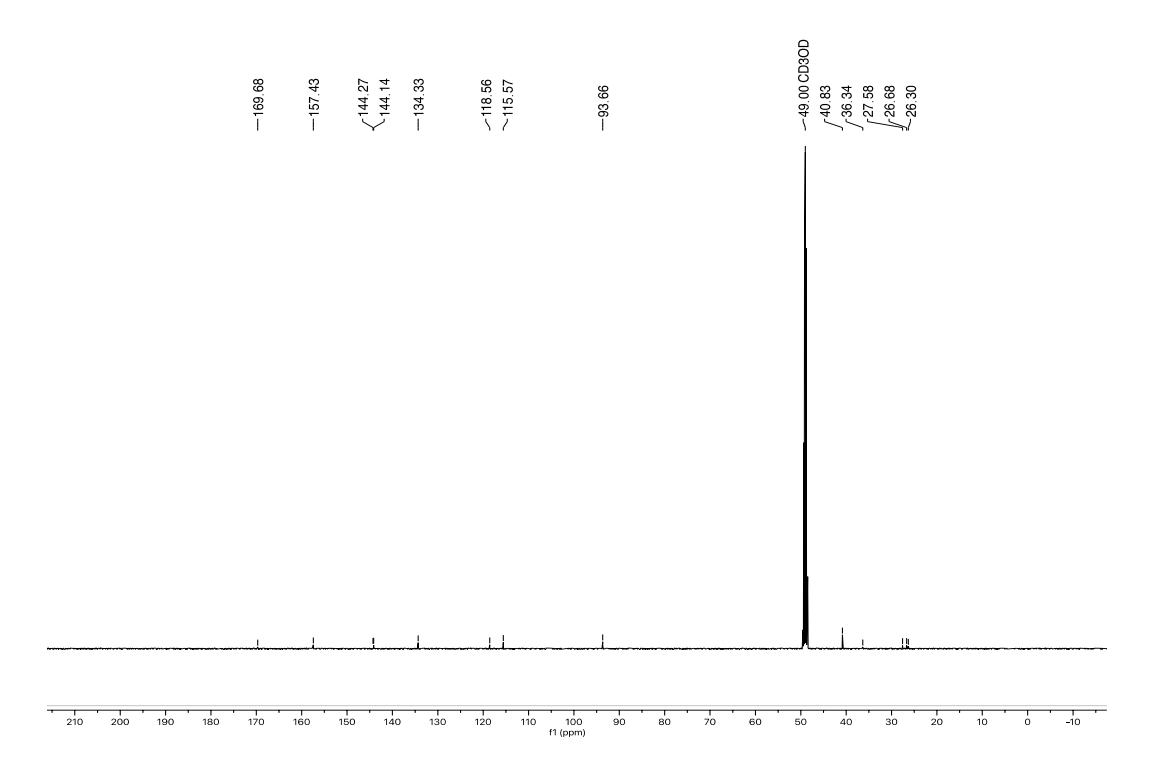




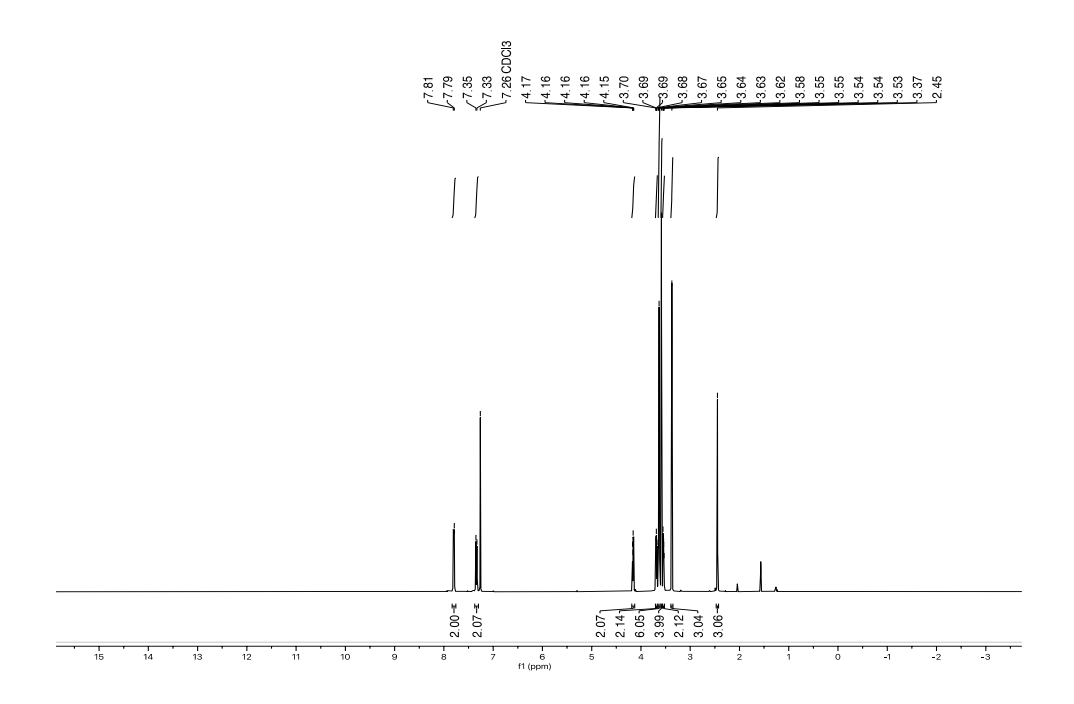
# <sup>1</sup>H NMR (500 MHz, MeOD)

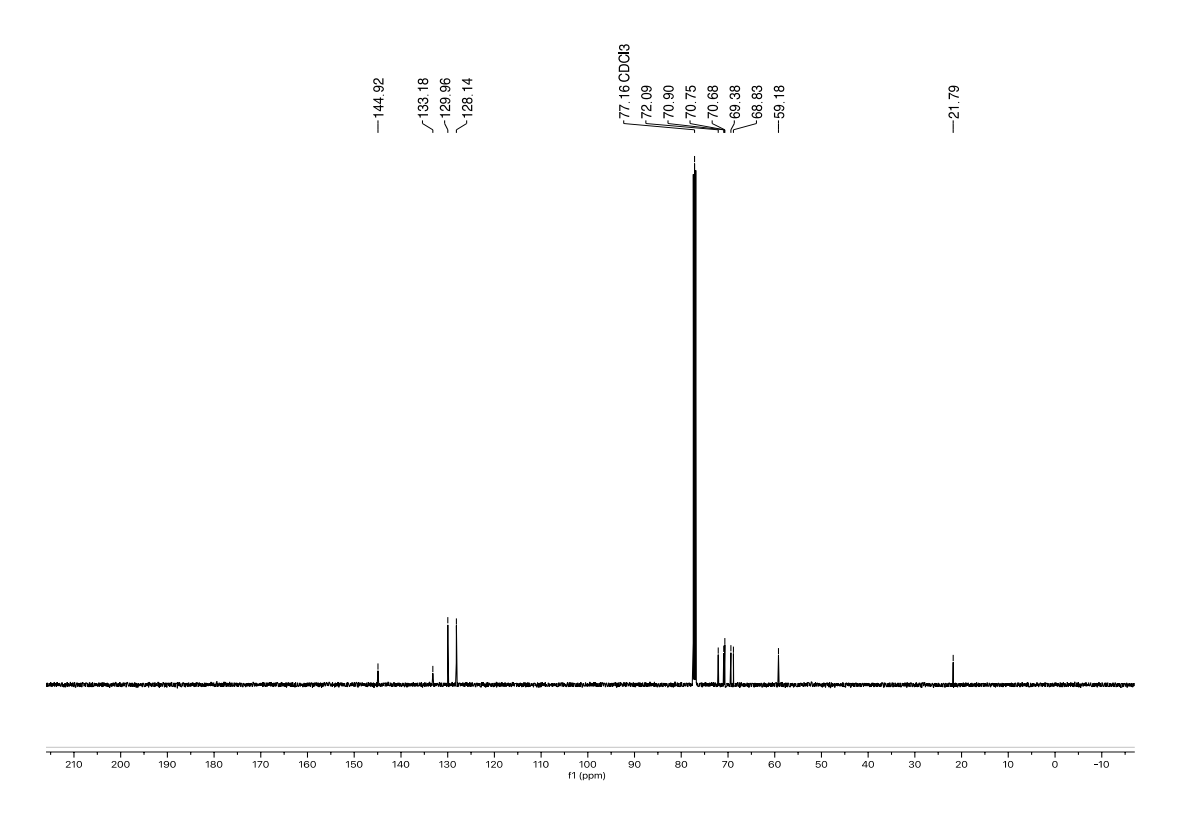


# <sup>13</sup>C NMR (126 MHz, MeOD)

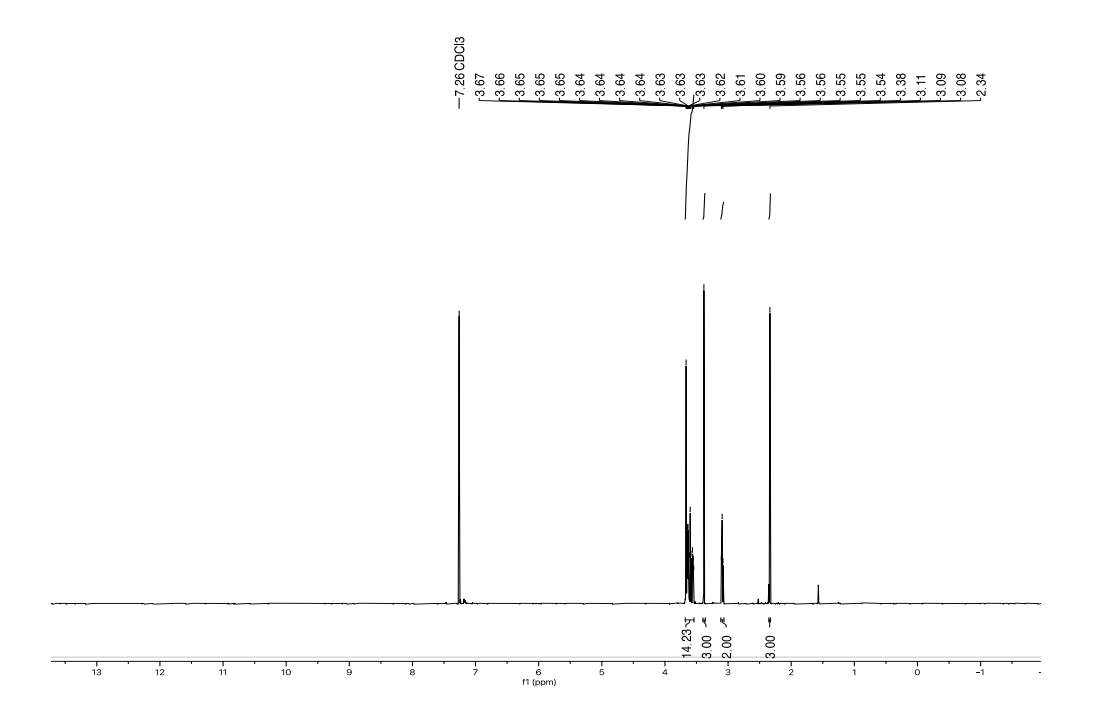


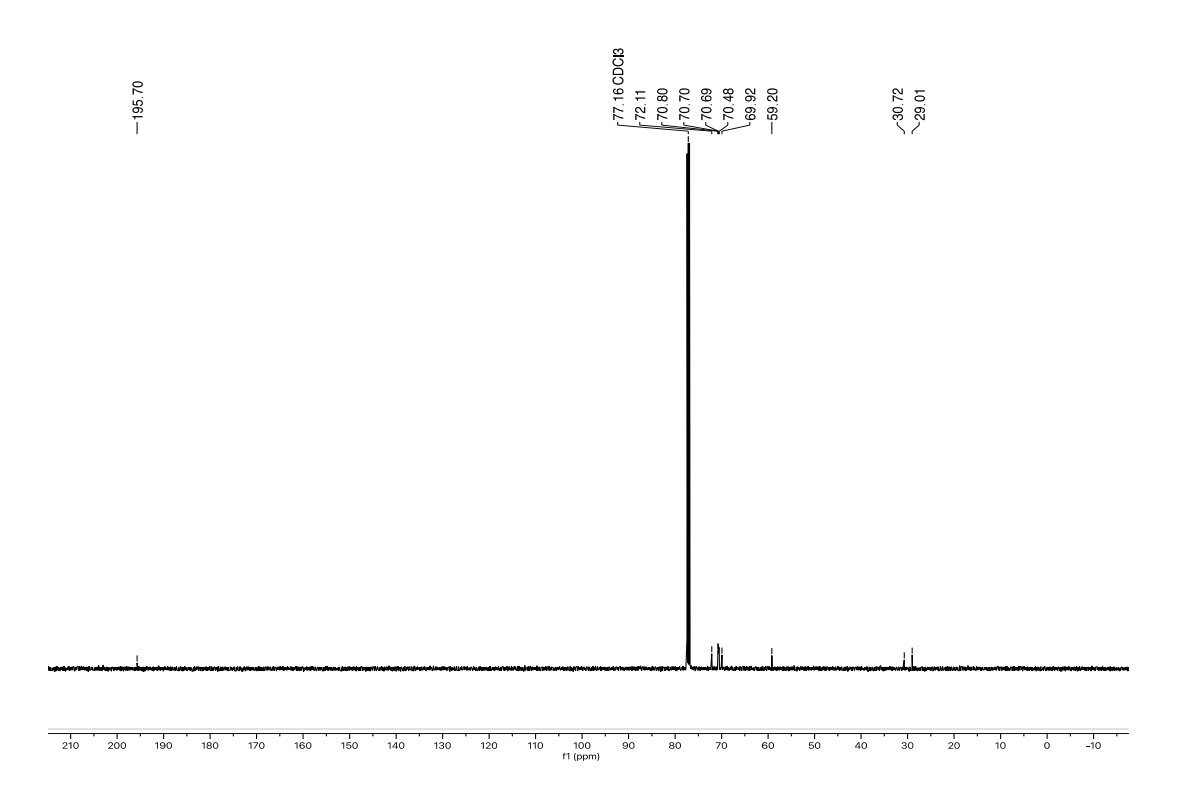
# <sup>1</sup>H NMR (400 MHz, CDCl<sub>3</sub>)

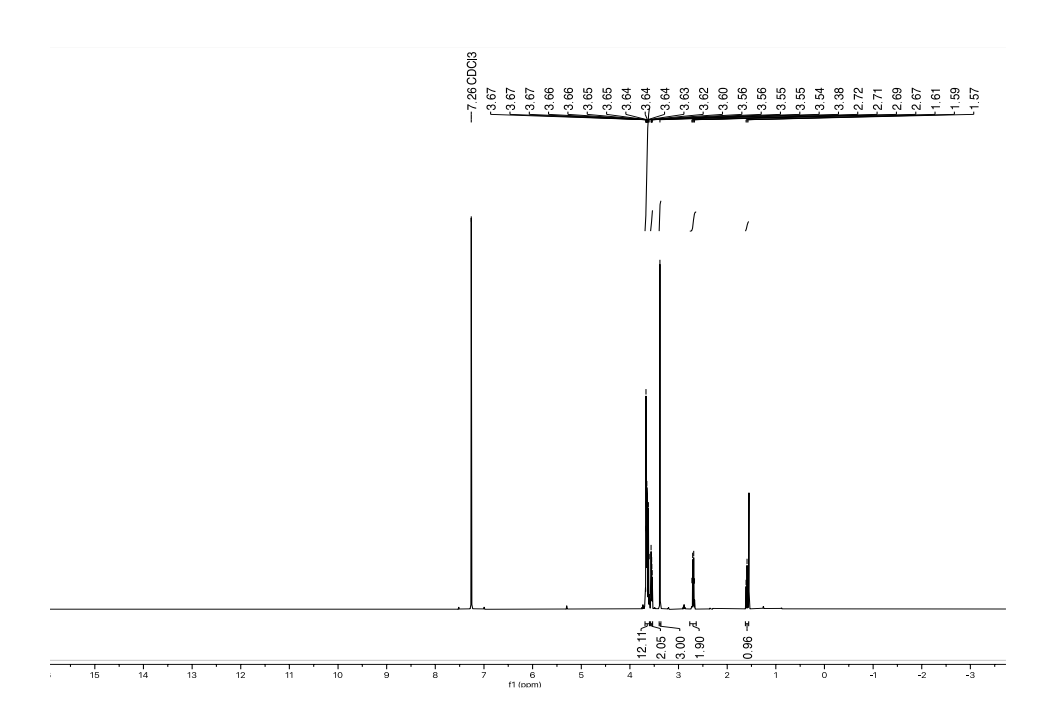




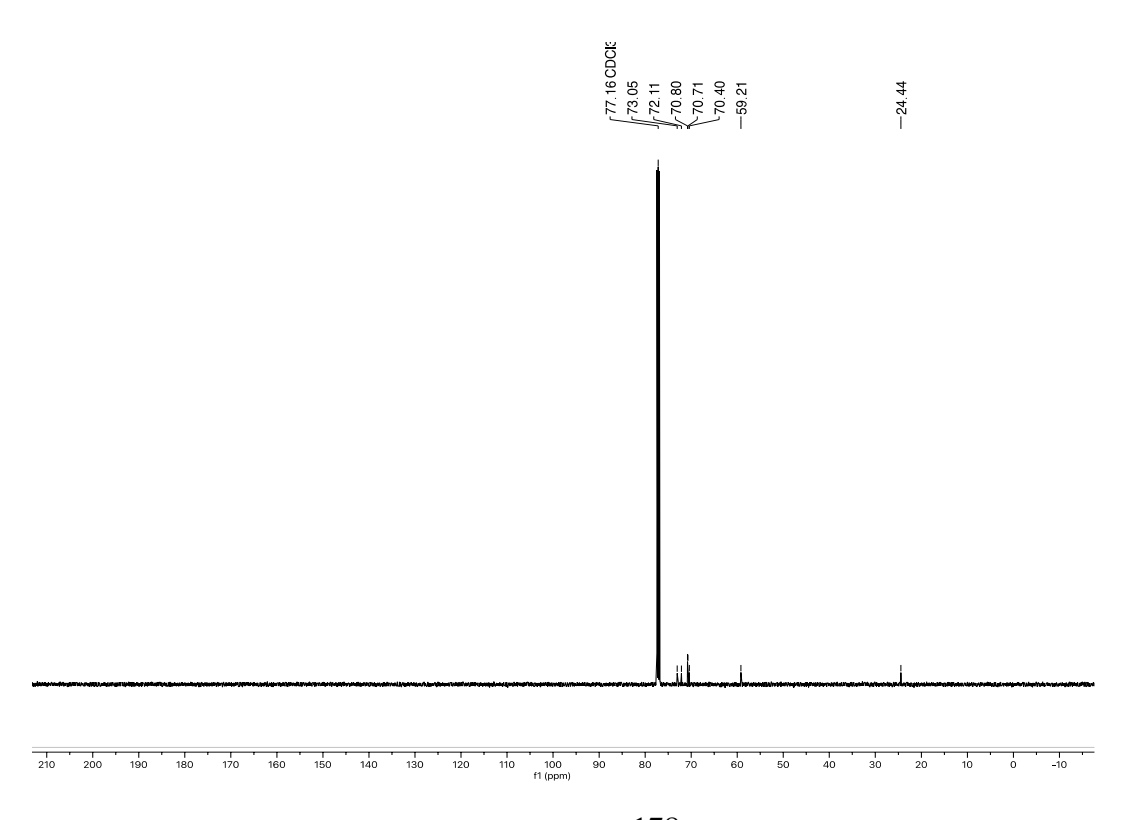
# <sup>1</sup>H NMR (500 MHz, CDCl<sub>3</sub>)





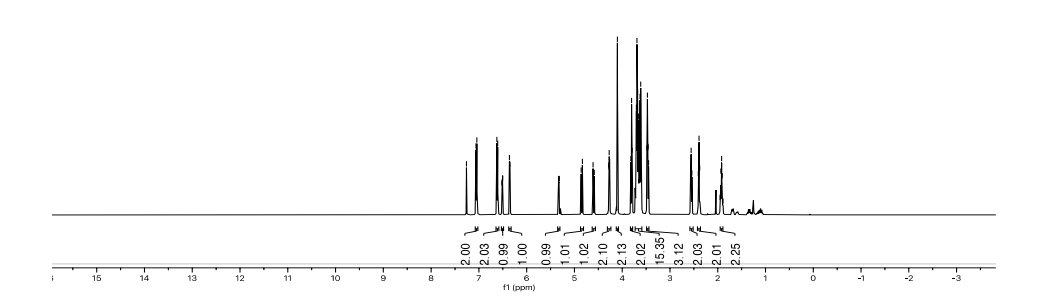


<sup>13</sup>C NMR (126 MHz, CDCl<sub>3</sub>)

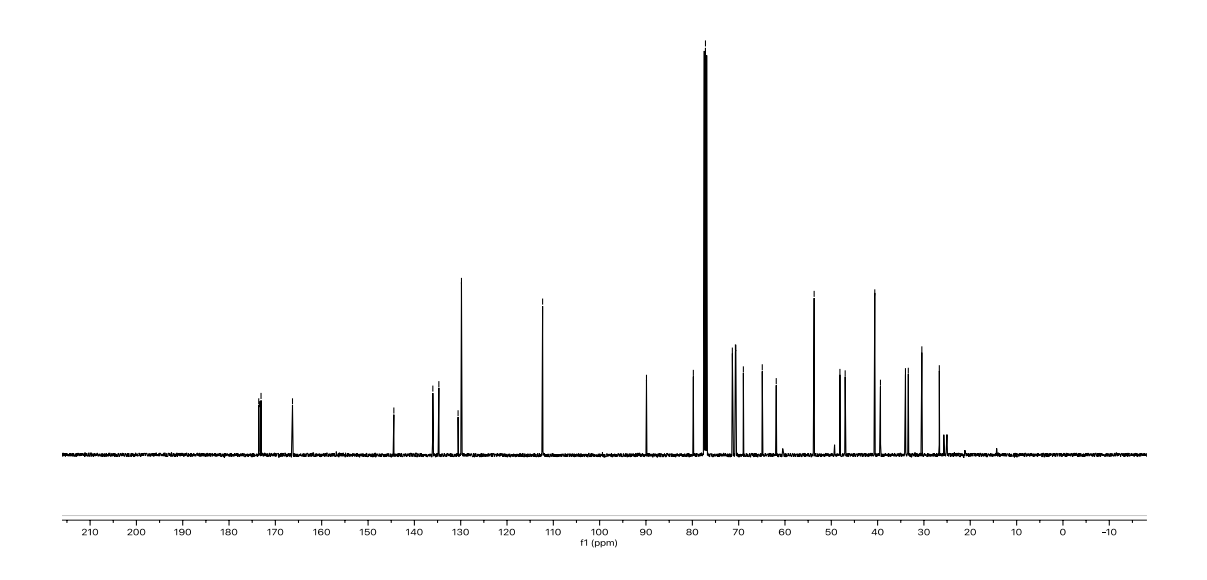


# <sup>1</sup>H NMR (500 MHz, CDCl<sub>3</sub>)









# <sup>1</sup>H NMR (400 MHz, CDCl<sub>3</sub>)

